

WL-TR-96-2129

COMBUSTION AND MIXING STUDIES IN  
COMPRESSIBLE FLOWS



T.H. CHEN, A. CREESE, S. DASGUPTA,  
R.P. FULLER AND P.K. WU

TAITECH INC  
3675 HARMELING DRIVE  
BEAVERCREEK, OH 45440-3568

SEPTEMBER 1996

FINAL REPORT FOR 11/18/93-05/31/96

APPROVED FOR PUBLIC RELEASE; DISTRIBUTION IS UNLIMITED.

19970113 084

AEROPROPULSION AND POWER DIRECTORATE  
WRIGHT LABORATORY  
AIR FORCE MATERIEL COMMAND  
WRIGHT PATTERSON AFB OH 45433-7251

DTIC QUALITY INSPECTED 1

# NOTICE

WHEN GOVERNMENT DRAWINGS, SPECIFICATIONS, OR OTHER DATA ARE USED FOR ANY PURPOSE OTHER THAN IN CONNECTION WITH A DEFINITE GOVERNMENT-RELATED PROCUREMENT, THE UNITED STATES GOVERNMENT INCURS NO RESPONSIBILITY OR ANY OBLIGATION WHATSOEVER. THE FACT THAT THE GOVERNMENT MAY HAVE FORMULATED OR IN ANYWAY SUPPLIED THE SAID DRAWINGS, SPECIFICATIONS, OR OTHER DATA, IS NOT TO BE REGARDED BY IMPLICATION, OR OTHERWISE IN ANY MANNER CONSTRUED, AS LICENSING THE HOLDER, OR ANY OTHER PERSON OR CORPORATION; OR AS CONVEYING ANY RIGHTS OR PERMISSION TO MANUFACTURE, USE, OR SELL ANY PATENTED INVENTION THAT MAY IN ANY WAY BE RELATED THERETO.

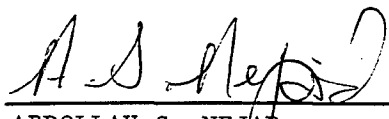
## LICENSE RIGHTS LEGEND

Contract Number:

Contractor:

For a period of four (4) years after the delivery and acceptance of the last deliverable item under the above contract, this technical data shall be subject to the restrictions contained in the definition of "Limited Rights" in DFARS clause at 252.227-7013. After the four-year period, the data shall be subject to the restrictions contained in the definition of "Government Purpose License Rights" in DFARS clause 252.227-7013. The Government assumes no liability for unauthorized use or disclosure by others. This legend, together with the indications of the portions of the data which are subject to such limitations, shall be included on any reproduction hereof which contains any portions subject to such limitations and shall be honored only as long as the data continues to meet the definition on Government purpose license rights.

This technical report has been reviewed and is accepted under the provisions of the Small Business Innovation Research Program.

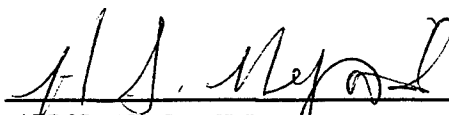


ABDOLLAH S. NEJAD

Program Monitor

Experimental Research Branch

Advanced Propulsion Division

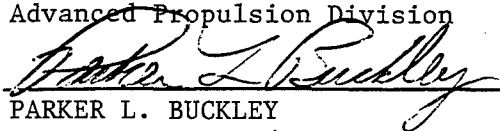


ABDOLLAH S. NEJAD

Acting Chief, WL/POPT

Experimental Research Branch

Advanced Propulsion Division



PARKER L. BUCKLEY

Deputy Chief, WL/POP

Advanced Propulsion Division

Publication of this report does not constitute approval or disapproval of the ideas or findings. It is published in the interest of scientific and technical information exchange.

Copies of this report should not be returned unless return is required by security considerations, contractual obligations, or notice on a specific document.

**SUPPLEMENTARY**

**INFORMATION**



## DEPARTMENT OF THE AIR FORCE

WRIGHT LABORATORY (AFMC)  
WRIGHT-PATTERSON AIR FORCE BASE OHIOERRATA  
AD-A319698MEMORANDUM FOR Defence Technical Information Center  
8725 John J. Kingman Road, Suite 0944  
Ft. Belvoir, VA 22060-6218

18 Mar 97

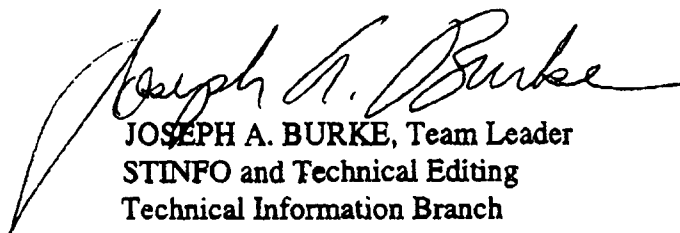
FROM: WL/DORT, Bldg 22  
2690 C St Ste 4  
Wright-Patterson AFB, OH 45433-7411SUBJECT: Notice of Changes in Technical Report(s) WL-TR-96-2129 [ADA319 698]

Please change subject report(s) as follows:

Please add the following authors to this report:

A.S. Nejad  
Mark Gruber  
Diana Glawe

Thank you.

  
JOSEPH A. BURKE, Team Leader  
STINFO and Technical Editing  
Technical Information Branch



# DISCLAIMER NOTICE



**THIS DOCUMENT IS BEST  
QUALITY AVAILABLE. THE  
COPY FURNISHED TO DTIC  
CONTAINED A SIGNIFICANT  
NUMBER OF PAGES WHICH DO  
NOT REPRODUCE LEGIBLY.**

REPORT DOCUMENTATION PAGE			Form Approved OMB No. 0704-0188	
Public reporting burden for this collection of information is estimated to average 1 hour per response, including the time for reviewing instructions, searching existing data sources, gathering and maintaining the data needed, and completing and reviewing the collection of information. Send comments regarding this burden estimate or any other aspect of this collection of information, including suggestions for reducing this burden, to Washington Headquarters Services, Directorate for Information Operations and Reports, 1215 Jefferson Davis Highway, Suite 1204, Arlington, VA 22202-4302, and to the Office of Management and Budget, Paperwork Reduction Project (0704-0188), Washington, DC 20503.				
1. AGENCY USE ONLY (Leave blank)	2. REPORT DATE SEP 1996	3. REPORT TYPE AND DATES COVERED FINAL 11/18/93--05/31/96		
4. TITLE AND SUBTITLE COMBUSTION AND MIXING STUDIES IN COMPRESSIBLE FLOWS		5. FUNDING NUMBERS C F33615-93-C-2300 PE 61102 PR 2308 TA B1 WU 01		
6. AUTHOR(S) T.H. CHEN, A. CREESE, S. DASGUPTA, R.P. FULLER AND P.K. WU				
7. PERFORMING ORGANIZATION NAME(S) AND ADDRESS(ES) TAITECH INC 3675 HARMELING DRIVE BEAVERCREEK, OH 45440-3568		8. PERFORMING ORGANIZATION REPORT NUMBER TI96RE-100		
9. SPONSORING / MONITORING AGENCY NAME(S) AND ADDRESS(ES) AEROPROPULSION AND POWER DIRECTORATE WRIGHT LABORATORY AIR FORCE MATERIEL COMMAND WRIGHT PATTERSON AFB OH 45433-7251 POC: A.S. NEJAD (937)255-9991		10. SPONSORING / MONITORING AGENCY REPORT NUMBER WL-TR-96-2129		
11. SUPPLEMENTARY NOTES				
12a. DISTRIBUTION / AVAILABILITY STATEMENT APPROVED FOR PUBLIC RELEASE; DISTRIBUTION IS UNLIMITED.		12b. DISTRIBUTION CODE		
13. ABSTRACT (Maximum 200 words)  Single- and two-phase fuel injection into compressible flows was studied. Mixing was measured under a variety of injection conditions as governed by injector geometry and fuel chemistry, phase, velocity, temperature and pressure. The impact of flow conditions on the state of mixing was also investigated. Several diagnostic methods were used, including optical diagnostic techniques and mechanical probing. Combinations of mechanical probe measurements were used to calculate such flow properties as Mach number, velocity, static temperature, and species concentration. For mixing studies, both the scalar and vector quantities were measured to assess the Schmidt number effect. Information obtained using laser diagnostic techniques was compared with the probe measurements. Results of the comparisons suggest that data obtained through laser diagnostic techniques and probe measurements can complement each other, contributing to the development of a broad understanding of the physical processes of mixing under a variety of conditions. These basic mixing studies have led to the successful development of several mixing enhancement schemes, which have been tested and reported elsewhere.				
14. SUBJECT TERMS		15. NUMBER OF PAGES 230		16. PRICE CODE
17. SECURITY CLASSIFICATION OF REPORT UNCLASSIFIED	18. SECURITY CLASSIFICATION OF THIS PAGE UNCLASSIFIED	19. SECURITY CLASSIFICATION OF ABSTRACT UNCLASSIFIED	20. LIMITATION OF ABSTRACT SAR	

## Table of Contents

List of Figures .....	iv
1. Abstract.....	1
2. Introduction .....	2
3. Experimental Studies .....	5
A. Facilities for Gas Fuel Injection Studies.....	5
B. Injection From Wall-Mounted Injectors Into A Supersonic Cross-Flow .....	6
C. Parallel Fuel Injection Study.....	13
1. Comparison of Jet Nozzle Geometries.....	13
2. Study Of The Effects Of Nozzle-To-Freestream Air Static Pressure Ratios.....	15
D. Mixing Enhancement Schemes .....	16
1. Ramp Schemes.....	16
2. High Aspect-Ratio Ramp Injector .....	19
E. Liquid Fuel Injection In Subsonic Crossflows.....	22
F. Injection Of Supercritical Ethylene In Nitrogen.....	25
G. Ethylene Mixing Studies.....	29
4. HT11 Software Development.....	30
5. Conclusions.....	32
6. Acknowledgments.....	34
7. References.....	35
8. Appendices .....	39

## List of Figures

Figure 1. Injector configurations for wall-mounted injection study.....	7
Figure 2. Schematic of jet with principal vortices and shock structures.....	8
Figure 3. Supersonic wind tunnel -- parallel fuel injection apparatus.....	13
Figure 4. Aero-ramp injector model.....	18
Figure 5. Physical ramp injector model.....	18
Figure 6. Predicted and experimental results for jet breakup process.....	24
Figure 7. Supercritical fuel injection chamber.....	27

## 1. Abstract

In this three-year research program, single- and two-phase fuel injection into compressible flows was studied. The main thrust of this project is the measurement of mixing and the definition of mixing mechanisms under a variety of injection conditions as governed by injector geometry and fuel chemistry, phase, velocity, temperature, and pressure. The impact of flow conditions on the state of mixing in a flow has also been examined. These basic mixing studies have led to the successful development of several mixing enhancement schemes, which have been tested and reported (see Appendix).

To quantify the mixing states of various flows, several diagnostic techniques, including optical diagnostic methods and mechanical probes, were employed. The laser diagnostic techniques implemented in this study include Laser Doppler Velocimetry (LDV), Phase Doppler Particle Analysis (PDPA), Laser Induced Fluorescence (LIF), Particle Imaging Velocimetry (PIV), Raman Scattering, and Rayleigh/Mie Scattering. Mechanical probes for measuring concentration, total temperature, cone-static pressure, and pitot pressure were developed and used. Combinations of mechanical probe measurements were used to calculate such flow properties as Mach number, velocity, static temperature, static pressure, pressure loss, and species concentration. For the mixing studies, both scalar and vector quantities were measured to assess the Schmidt number effect. Information obtained using laser diagnostic techniques was compared with the probe measurements. Results of the comparisons suggest that data obtained through laser diagnostic techniques and probe measurements can compliment each other, contributing to the development of a broad understanding of the physical processes of mixing under a variety of conditions.

## 2. Introduction

This report covers work performed during the period 19 November 1992 to 31 May 1996, under Air Force Contract F33615-93-C-2300, entitled "Combustion and Mixing Studies in Compressible Flows." Taitech personnel contributing to this effort were Dr. Tzong H. Chen, Dr. Samhita Dasgupta, Dr. Raymond P. Fuller, Gary L. Haines, Kevin A. Kirkendall, Mark L. Landrum, David G. Schommer, Charles R. Smith, and Dr. Pei-Kuan Wu. The work described was completed at the supersonic combustion facility of the Aero Propulsion and Power Directorate of Wright Laboratories (WL/POPT), at Wright-Patterson Air Force Base. The facility is fully described elsewhere [Gruber and Nejad, 1994].

The three-year study supported under this project was designed to 1) establish the utility of laser diagnostics in supersonic propulsion research and development, and 2) yield a better understanding of fuel injection, mixing and combustion processes under high speed propulsion conditions. The research program focuses on the physical processes involved in single- and two-phase fuel injection. It is expected that the data obtained will make significant contributions to the improvement of SCRAM/RAMJET configurations, fuel injection system designs and of film cooling system designs for gas turbine combustors and turbine blades.

Several related experimental programs were developed and carried out under this contract. The programs varied in scope, and ranged in experimental time from several months to three years, but each program has contributed in meaningful ways to the fulfillment of the two goals listed above. The research programs will be discussed separately as follows: 1) Mixing studies on transverse fuel injection into a supersonic crossflow, 2) Mixing studies on parallel injection into a supersonic crossflow, 3) Study of several mixing enhancement schemes for fuel injection into a supersonic freestream, 4) Study of the breakup processes of liquid jets in subsonic

cross-flows, and 5) Study of ethylene injection into a nitrogen atmosphere under supercritical conditions.

The flowfield created by the introduction of a gaseous fuel jet into a supersonic flow is of both fundamental and practical interest to the hypersonic propulsion community, as well as to those interested in the study of reaction control systems on high speed vehicles. In the propulsion sector, an understanding of the mechanisms that govern the fuel dispersion and fuel/air mixing in compressible shear flows is crucial for the development of an air-breathing supersonic combustion engine, such as the supersonic combustion ramjet (SCRAMJET). In this type of engine, the fuel mixing and combustion processes must take place in the supersonic air stream, because of the undesirable effects associated with decelerating a supersonic flow ( $M=6-8$ ) to appropriate speeds for subsonic combustion. Residence times within such supersonic combustors will necessarily be short, especially because of the prohibitive weight penalty of a long combustion chamber.

From a practical standpoint, transverse injection into a supersonic air stream represents one of the most interesting fuel injection concepts for these supersonic air-breathing engines. A second basic injection concept under consideration involves parallel injection. Each configuration presents distinct advantages and difficulties. In parallel injection, the compressible free shear layer formed between the oxidizer and fuel streams suffers from a suppressed growth rate and relatively slow mixing [Papamoschou and Roshko, 1988; Goebel and Dutton, 1991]. However, parallel injection produces the maximum thrust due to injection since the fuel stream is aligned with the combustor axis. Wall-mounted injector concepts, on the other hand, provide significant fuel penetration, which is vital for near-field mixing. However, transverse injection creates a strong disturbance in the freestream and requires that freestream momentum be used to turn the jet. Thus, gains due to near-field mixing are tempered by freestream losses. More complex injection schemes have been developed to effectively inject and disperse the fuel for efficient mixing and combustion using variations on parallel or transverse injection, and

usually involve a trade-off between rapid mixing and total pressure recovery. Thus, a fundamental understanding of the basic injection concepts will enhance the ability to incorporate them into more complex configurations, ultimately leading to more efficient combustor designs, which will provide rapid mixing, stable combustion and minimal pressure losses.

Two-phase flows, which may also play an important role in hypersonic flight vehicles, pose some slightly different problems. Liquid jet breakup patterns are as yet not well understood; research performed under this program has made a major contribution in this area by defining the jet breakup height. Similar fundamental problems are posed by injection under supercritical conditions, which may be typical of SCRAMJET operating conditions.

This research program has developed a significant body of knowledge, experience, and data on fuel injection into high speed flows. The results produced by the component studies in the program will serve as a foundation and background for the next generation of research in fuel injection and mixing studies, and specifically for the design and development of SCRAMJET engine technology.



### 3. Experimental Studies

#### A. Facilities for Gas Fuel Injection Studies

The Supersonic Combustion Facility of the Aero Propulsion and Power Directorate at Wright Laboratory, WPAFB, was used for all of the gas fuel injection experiments described below (3.B-D). The supersonic combustion facility is a continuous running, open-loop supersonic wind tunnel with a rectangular test section measuring 12.7-cm high, 15.2-cm wide, and 76.2-cm long. A pair of compressors capable of providing up to 15 kg/sec of air with total pressures and temperatures up to 48.6 atm and 922 K, respectively, were used to supply air to the facility. A massive exhaust system was used to lower and maintain the back pressure for smooth starting and safe operation. Complete details regarding this supersonic flow facility have been presented by Gruber and Nejad [1994]. The liquid fuel injection studies were performed in separate facilities, which are described in sections (3.E-G).

## **B. Injection From Wall-Mounted Injectors Into A Supersonic Cross-Flow**

A number of general studies of transverse injection of gas into a supersonic crossflow have been performed in the last thirty years; a comprehensive review of the studies of down-stream mixing produced by transverse jets and wall jets in supersonic flows was presented by Schetz et al. [1991]. It has been shown that as the injection angle decreases, the near-field mixing decreases, while pressure losses also decrease. In the far field, injection angle was found to have little effect on the overall mixing [Mays et al. 1989]. Fuller et al. [1992] extended this work to include injector yaw (angle of injector offset from wind tunnel centerline) as well as low transverse angles. It was observed that while injector yaw did not increase the rate of decay of maximum concentration, it did cause an increase in the overall injectant plume cross section, thus increasing the size of the mixing region. In both studies, it was shown that matched pressure injection produced greater fuel concentration decay rates when compared to an underexpanded case.

These studies have provided general surveys of the flow field, and data on the far-field mixing effects of injection. In order to facilitate the application of these observations to the development of mixing enhancement schemes, however, the fundamental physics of jet injection, and especially of the details of the near-field mixing processes, require closer study. The transitional mixing phenomena in the near-field are particularly important in propulsion applications, where flame stabilization must be achieved near the injector in order to minimize the length and weight of the combustor chamber.

In the near-field, close to the injection point, the flow is in a transitional stage. The large scale structures and unsteadiness introduced by the jet will eventually transition into smaller scale turbulence, but the rate of this transition will depend on various factors, including the size of the flame holder, the size of the injector, and the flow conditions of the fuel jet and freestream. The large scale flow facility at

Wright Laboratory used in this program provides an ideal site for the type of detailed observation required for the mapping of near-field mixing processes.

In order to develop a detailed understanding of the physics of mixing in the near field of gas injection, this section of the research program concentrates on the vortices which form around the injection point and strongly influence the entrainment of freestream fluid into the jet (or the dispersion of the jet fluid into the freestream). Also of significant interest are the influences of injectant molecular weight and compressibility on the structural and mixing characteristics associated with the jet/crossflow interaction. In addition, geometric effects which might lead to the development of a passive means of increasing the mixing rate while minimizing the total pressure losses were also studied. This work was reported in several papers by Gruber et al. [1994-1996]. These papers are attached (see Appendix); a summary of the results of the research is provided here.

The interaction of a supersonic cross-flow with sonic helium and air jets injected transversely through circular and elliptical nozzles was studied using shadowgraph photography and Planar Rayleigh Scattering (instantaneous and time-averaged).

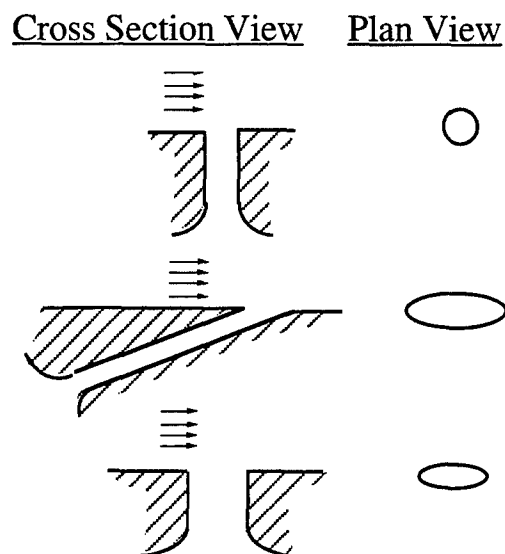


Figure 1. Injector configurations for wall-mounted injection study.

Results show a highly three-dimensional interaction which is dominated in the near-field by two types of large-scale vortical motions: shear layer eddies and a counter-rotating vortex pair.

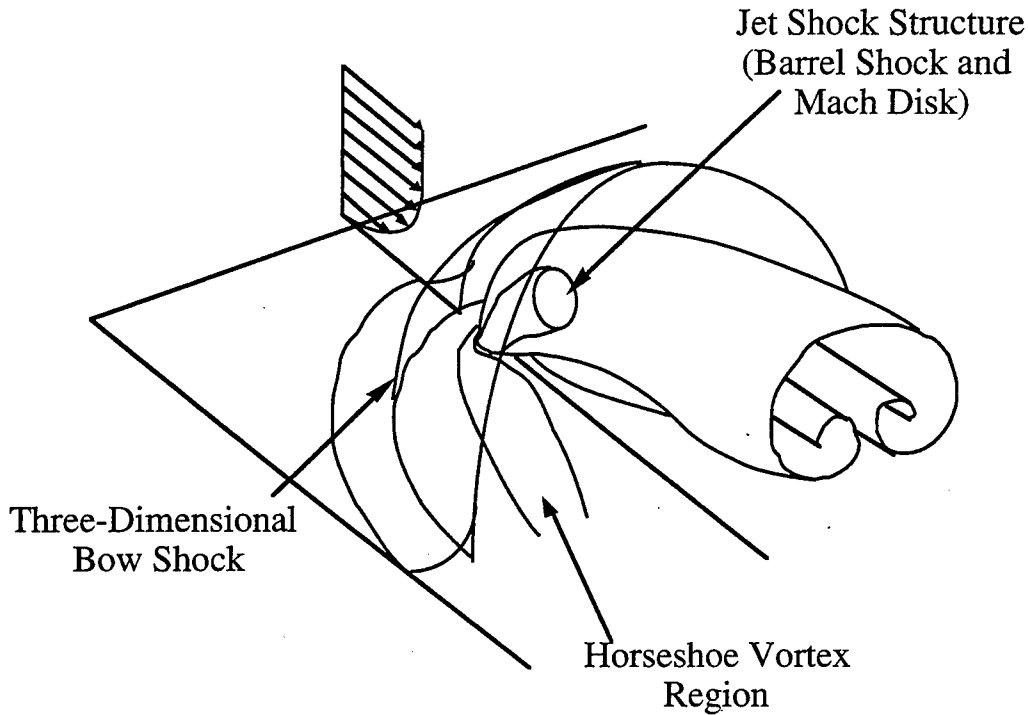


Figure 2. Schematic of jet with principal vortices and shock structures.

Helium and air injection were found to produce substantial differences in the shear layer structure and in the shock structures within the jets. Averaged face-on Rayleigh Scattering images show that the elliptical jet spreads more quickly in the lateral direction than does the circular jet, confirming that some axis-switching is present. The same data suggest that large-scale mixing for helium injection is slower than in the air injection cases. The freestream shock structure formed in the elliptical case suggests that the elongated geometry produces a smaller separated region upstream of the jet orifice than the relatively blunt circular case. Also, the bow shock appears weaker in the elliptical case. Near-field transverse penetration data collapse well with low speed scaling conventions, and the power law curve fits

obtained are consistent with previous results. Finally, analysis of mixing potential from standard deviation images of the jet cross-section indicates that the helium and air injection flow fields show significant differences.

#### Calculation of mixing potential

To quantify the large-scale mixing characteristics of the various injector and injectant combinations, analyses of the standard deviation contours in the Rayleigh Scattering images were performed. Large-scale fluctuations occurring in the shear layer entrain freestream fluid and increase the volume of fluid in the mixing zone. This, in turn, increases both the surface area between the jet and the freestream and the perimeter of the mixing region. Therefore, the relationship between these two parameters can be used to define an indicator of mixing potential. A shape parameter ( $S$ ), can be defined in terms of the area of the mixing zone cross section ( $A_\sigma$ ):

$$S = \frac{P}{2\pi r_o} \text{ where } r_o = \sqrt{\frac{A_\sigma}{\pi}}.$$

This shape parameter describes the relationship between the perimeter and the area of a given standard deviation contour by comparing them to the perimeter and the area of a perfectly circular contour of radius  $r_o$ . If the contour of interest were a perfect circle, the value of  $S$  would be its minimum value of unity. Contours that yield shape parameters greater than unity are considered to have a greater mixing potential than those having values of  $S$  near unity, by virtue of increased mixing area and the presence of large-scale structures.

#### Effects of injector geometry and injection angle

Injector exit geometry was found not to substantially affect the transverse penetration of the jet in the near field, while the orientation of the injector with respect to the free-stream (transverse vs. oblique) was found to have dramatic effects. Experimental results indicate that the lateral spread of the jet from the elliptical transverse injector is roughly 25% greater in the near field than that

associated with the circular transverse injector. This is attributed to the axis switching phenomenon commonly observed in elliptical jets.

Injector orientation plays an important role in the strength of the bow shock, with the shocks created by the oblique injector being substantially weaker than those created by the transverse injectors, given equal cross-sectional areas and pressures. This implies a smaller expected total pressure loss in the oblique injector flowfield. However, no large-scale vortices develop along the jet/freestream interface in the near-field region. As a result, the oblique injector produces relatively slow mixing in the near field as compared to transverse injectors.

#### Bow shock/jet interaction

Another dominant feature in flowfields created by transverse injection into supersonic crossflows is the shock wave structure, which consists of bow and separation shocks forming upstream of the injectant plume. The interaction between these features and the large-scale eddies that develop at the jet/freestream interface was examined. Results indicate that the large structures strongly influence the near-wall behavior of the bow shock, often resulting in severe curvature changes and position fluctuations. Lifting of the bow shock has been observed when the approaching boundary layer is relatively thick. In these instances, injectant and freestream fluid mix subsonically upstream of the injector orifice, thereby exacerbating the hot-spot phenomenon found in reacting transverse injection flowfields. The injector geometry was found to strongly affect the upstream separation zone, the bow shock standoff distance, and the strength of the bow shock. Elliptical injection with the major-axis aligned with the freestream flow was found to result in a smaller separation zone and standoff distance, and a weaker bow shock as compared to circular injection.

#### Convection velocity of large scale structures

Dependence of the convection velocity of large scale structures on mixing layer compressibility and injector geometry was also investigated. Convection

characteristics obtained from temporally correlated image pairs show a strong dependence on both mixing layer compressibility and injector geometry. For a given injector geometry, the near-field convection velocities are larger for cases with high compressibility (helium injection) than for cases with low compressibility (air injection). In the near-field, after the jet plume has been bent downstream, the eddies tend to convect with velocities that are closer to the freestream velocity, and convection angles decay rapidly toward the freestream flow direction.

The convection angles are shallower for elliptical injection than for circular injection. The near field convection velocities from the elliptical injection cases are skewed toward the freestream velocity.

#### Role of large scale structures

The large scale structures at the interface between the jet and freestream appear to be strongly influenced by the properties of the injectant gas, with helium giving rise to "clumpier" eddies as compared to the more distinct roll-up of long, pronounced eddies visible in the air injection cases. These eddies strain the interface between them and serve the engulfment process well, while structures at the interface of the helium jet appear more amorphous. This observation and the mixing measurements confirm that the large scale mixing in helium flowfields is slower than in air injection cases. Air injection yields better mixing potential than helium in both circular and elliptical injector cases.

#### Compressibility Effects

The large-scale vortices that develop at the jet/freestream interface generally roll into the freestream, which indicates that the injectant fluid below the mixing layer moves faster than does the crossflow fluid directly above it.

Compressibility plays an important role in the development and break-up of large-scale eddies: injection in high compressibility cases (helium) results in amorphous shear layer eddies with thin braid regions, as compared to well-defined vortices with

pronounced braid regions in low compressibility (air) cases. Poorer entrainment characteristics develop in high compressibility injection cases. Indeed, the mixedness analysis described above indicates that the mixing potential afforded by injection at low compressibility is larger than that of high compressibility cases.



## C. Parallel Fuel Injection Study

### 1. Comparison of Jet Nozzle Geometries

This section of the research program addresses the problems of fuel-air mixing in supersonic flows through an investigation of parallel fuel injection. Fuel was injected from the base of a two-dimensional extended strut into a nominal Mach 2 freestream in order to determine the fundamental characteristics of the injection scheme and to explore passive mixing enhancement through the use of different injector geometries. The experimental apparatus and results are described in detail in Glawe et al. [1995] (see Appendix) and Glawe [1995]; a summary is provided here.

A 1.27-cm-thick strut was extended approximately 7 cm into the wind tunnel test section, with the injection nozzle mounted in the base of the strut at the center-line of the wind tunnel.

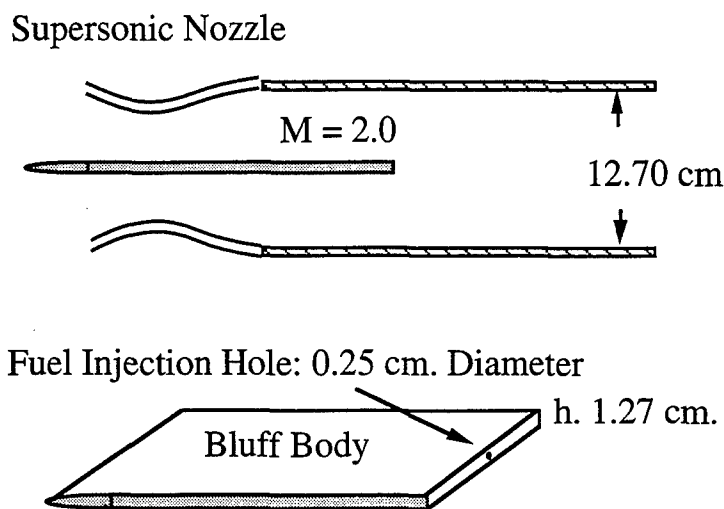


Figure 3. Supersonic wind tunnel -- parallel fuel injection apparatus.

Three nozzles were used in this study; a circular nozzle, a circular nozzle with vortex-generating tabs on opposite sides of the exit circumference, and an elliptic nozzle. Helium was used as the injectant to simulate gaseous hydrogen fuel.

Without injection, a two-dimensional wake flow exists behind the base of the strut. When fuel is injected parallel to the freestream, a highly three-dimensional complex flowfield results.

Flow visualization was performed by schlieren photography, planar Rayleigh/Mie scattering, and acetone Planar Laser-Induced Fluorescence (PLIF). Velocity profiles were obtained through two-component Laser Doppler Velocimetry (LDV). The flow field without injection was examined to establish a reference case against which the flow field with helium injection from the various nozzle geometries could be evaluated. LDV measurements show that the incoming boundary layer is fully developed and that the freestream flow is uniform and symmetric above and below the strut. The mixing interaction between the jet and the primary flow occurs within the confines of the strut wake. Thus, the jet spread is limited in the transverse direction, which in turn limits mixing between the jet and the primary freestream flow.

The various nozzle geometries create different jet/freestream interaction dynamics, which affect the overall mixing of the injectant with the freestream. The axis-switching phenomenon apparent in free jets issued from oblong nozzles is apparent for the jets issuing from the elliptical nozzle in this study. However, the speed and degree to which the axis-switch takes place seems to vary depending on the orientation of the ellipse with respect to the mixing layers produced by the strut. Likewise, bifurcation similar to that occurring in free jets issuing from a nozzle with two tabs is clearly seen in the case of the circular-with-tabs nozzle with the tabs oriented normal to the strut span. The orientation of the nozzle relative to the mixing layers seems to dictate whether the mixing layers reinforce or suppress jet dynamics induced by different nozzles and subsequent jet development.

Visual inspection of the instantaneous and averaged Rayleigh/Mie scattering images, particularly those of the face-on plane of view, suggests that the jet emanating from the circular nozzle with tabs oriented normal to the span of the

extended strut exhibited the best mixing. The second best mixing was exhibited by the elliptic nozzle with its major axis normal to the strut. In agreement with the LDV streamwise velocity profiles, the Rayleigh/Mie images show the elliptic case to spread the most in the spanwise direction, but to remain more coherent than the circular-with-tabs case.

## **2. Study Of The Effects Of Nozzle-To-Freestream Air Static Pressure Ratios**

Using the extended strut described above (see Figure 3), helium was injected at sonic velocity from a circular injector nozzle into a nominal Mach 2 freestream air flow at three different nozzle-to-freestream air static pressure ratios. Planar Rayleigh/Mie scattering and acetone PLIF flow visualization along with CFD results are presented in Glawe et al. [1994].

Jet spread was found to be insignificant for all three pressure cases, as the jet fluid remains primarily confined in the wake of the strut, but large scale, spatially periodic and organized structures were observed to reach into the freestream, particularly in the under-expanded cases. The jet was found to spread along the spanwise direction, creating an oblong jet contour with large scale structures evident along the transverse axis of the jet. These structures appear to be spatially periodic and more organized in the underexpanded cases than in the pressure matched case. The jet interaction with the freestream was found to be markedly three dimensional, as shown by highly irregular helium jet contours and the appearance of a conical shock in the highly under-expanded case.

The numerical simulation performed in this study [M.-H. Chen et al. 1995] was found to capture the essential features of the flow field, namely the barrel shock, Mach disk, recirculation region, and expansion zone. In addition, the Mach disk location and jet spread predicted by the CFD results compare reasonably well with the experimental planar Rayleigh/Mie scattering and the acetone PLIF images.

## D. Mixing Enhancement Schemes

### 1. Ramp Schemes

Numerous investigations have considered wall ramp injectors as a viable means of providing enhanced fuel-air mixing in supersonic flows [Hartfield et al., 1994; Riggins et al., 1995]. Ramps provide vortex shedding off the edges and local separation at the base (see Figure 5). The fuel is generally injected through the base and into the counter-rotating vortex pattern, creating a very dynamic mixing distribution. Furthermore, the ramp shock will reflect off the opposite wall and impinge on the plume/vortex structure, resulting in possible vortex breakdown and further enhancement of mixing. The reflected shock should also create a baroclinic torque where it intersects the plume resulting in additional vorticity. Finally, the recirculation zone caused by separation at the base of the ramp should provide flameholding capabilities similar to those of a backward-facing step. The major drawback to this design is its dependency on maintaining pristine geometry in the extremely harsh environment of a high-enthalpy combustor. Its physically intrusive nature will necessarily create "hot spots" with temperatures exceeding the thermal limits of most practical materials. Furthermore, the added drag and loss of thrust potential resulting from the intrusive presence of the ramp may be unacceptable in certain engine design configurations.

A recently introduced alternative to the physical ramp is the "aerodynamic ramp" or simply "aero-ramp" (see Figure 4). The aero-ramp was first presented by Cox et al. [1994] after a preliminary investigation involving both experiments and computational fluid dynamics. This injector design consists of a three-by-three array of closely spaced, flush-wall jets with various transverse and yaw angles. The jets were geometrically arranged so as to generate multiplicative fuel-vortex interactions which should lead to enhanced mixing. These fuel-vortex interactions include skew induced vortex generation, shock induced vortex generation, and vortex breakdown, all of which have been shown to be effective mixing enhancement mechanisms. Furthermore, the flush-wall design coupled with low angle injection

avoids the excessive pressure losses, drag, and hot-spots associated with conventional vortex generators.

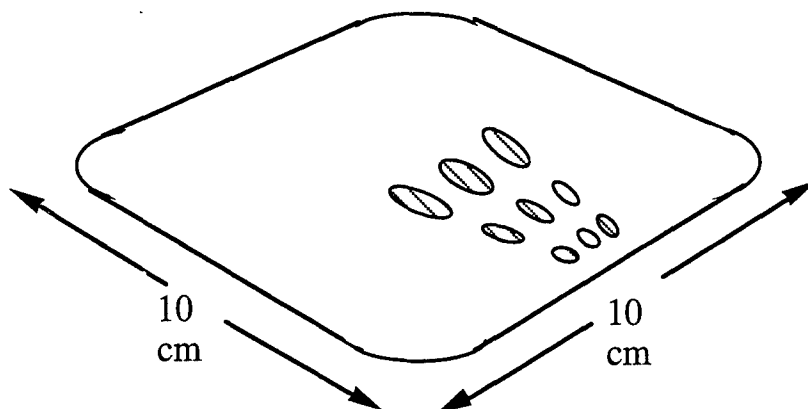


Figure 4. Aero-ramp injector model.

In this section of the research program, an experimental investigation was conducted to compare the supersonic mixing performance of an aerodynamic ramp injector with that of a physical ramp injector. The physical ramp injector is based on the design concept first introduced by Northam et al. [1992]. The design used in the present experiments has a  $10.3^\circ$  compression surface and contains a sonic injection orifice such that the injection axis is parallel to the compression surface.

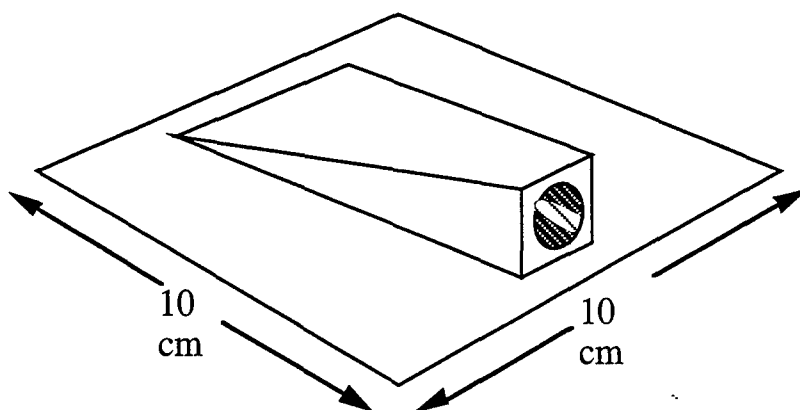


Figure 5. Physical ramp injector model.

The investigation focused on jet penetration, mixing characteristics, and total pressure losses; a parameter was defined to quantify the total pressure losses without

complex analysis or facility dependence. A full description of experimental set-up, procedures and results is presented in Fuller et al. [1996] (see Appendix); a summary is presented here.

Tests were conducted in a Mach 2.0 turbulent air crossflow. Freestream conditions were set for a total pressure of 3.06 atm and total temperature of 295 K, producing a freestream Reynolds number of  $3.63 \times 10^7$  per meter. Pure helium was used as the injectant to simulate hydrogen fuel. Species concentration measurements were obtained using an intrusive sampling probe and gas analyzer designed specifically for use in supersonic flow [Ninnemann et al., 1992]. Aerothermodynamic measurements were performed using a Pitot probe, cone-static pressure probe and a total temperature probe. These three measurements are combined with species composition sampling to estimate all aerothermodynamic variables of interest. Data reduction consist of an iterative scheme utilizing the isentropic flow relations, perfect gas relations, the Rayleigh-Pitot formula and the Taylor-McColl cone flow equation. Details regarding the data reduction techniques have been presented by Fuller et al. [1992]. The various analysis techniques applied to the mixing characteristics were found to produce consistent results.

The results of the study may be summarized as follows:

The aero-ramp exhibited a significant increase in jet penetration when the jet-to-freestream momentum flux ratio was increased from 1.0 to 2.0, while the physical ramp showed very little change. As a result, the jet penetration of the aero-ramp was comparable to that of the physical ramp at the higher momentum flux ratio.

The mixing characteristics of the physical ramp injection were dominated by the counter-rotating vortices generated by the ramp. The fuel-air mixing produced by the aero-ramp was dominated by the multiplicative fuel-vortex interactions confined to the injector vicinity. Mixing effectiveness was defined based on maximum fuel mass fraction, plume area, mixing efficiency, and spatial mixedness.

An innovative method of calculating the state of mixing (mixedness) in a flow from light scattering images was developed. With a jet-to-freestream momentum flux ratio of 1.0, the aero-ramp produced superior mixing in the near field and slightly less than comparable mixing in the far field. With a momentum flux ratio of 2.0, the aero-ramp mixing was comparable to that of the physical ramp in the far field. The mixing enhancement produced by the aero-ramp can be attributed to the multiplicative fuel-vortex interactions in the near field as well as the multiple jet design; that is, several small jets should mix better than one single jet. The mixing enhancement produced by the physical ramp can be attributed to the counter-rotating vortex pair. Increased jet momentum was found to reduce the strength of the vortices produced by the physical ramp while it increased the strength of the interactions produced by the aero-ramp. Thus, the mixing performance decreased with increasing jet momentum for the physical ramp while it increased for the aero-ramp.

For the physical ramp, the total pressure losses were found to be concentrated around the centers of the two counter-rotating vortices. For the aero-ramp, the total pressure losses were concentrated around the core of the jet plume. The pressure losses induced by the physical ramp were more severe. With a jet-to-freestream momentum flux ratio of 1.0, the physical ramp exhibited a larger loss parameter over the entire axial range of measurements. When the momentum flux ratio was increased to 2.0, both injectors exhibited a reduction in losses, but the physical ramp losses were more severe.

These results suggest that, whether or not the aero ramp studied here can be made to outperform the physical ramp at particular operating conditions, comparable performance alone merits further studies. Future studies should include parametric optimization through combined computational and experimental efforts.

## 2. High Aspect-Ratio Ramp Injector

A complex mixing enhancement device, High Aspect-Ratio Ramp Injector (HARI), for use in supersonic propulsion applications was designed, manufactured, and tested. A new nozzle module which produces a Mach 4.5 freestream in the Supersonic Combustion Facility at the Aero Propulsion and Power Directorate was designed and manufactured, to permit the testing of mixing enhancement devices under high speed fuel injection conditions.

The High Aspect-Ratio Ramp Injector (HARI) is a hybrid ramp-hypermixing injector module designed to generate sharp pressure gradients and strong vorticity for mixing enhancement. The large flow capacity of the supersonic combustion facility permits the use of a thick strut and a large injector, so that the important features involved in strut injection can be identified.

A mechanical probe was designed to sample injectant concentrations downstream of the HARI injector. The probe is an aspirating type probe which extracts a gas sample from the supersonic mixing region and analyzes it externally using hot-wire anemometry in conjunction with pressure and temperature measurements. Parametric studies were performed to optimize the probe geometry for the test conditions of the HARI experiments. The basic geometry was then determined and the appropriate components were selected. Pitot-pressure and cone-static pressure probes were also developed and manufactured. A thermocouple was built into the pitot probe for measuring total temperature. Software for calibrating the probes and for acquiring and reducing the data was developed.

Schlieren and shadowgraph photography were used to determine the principal features of the flow field: among the most interesting features is a complex shock structure originating from the ramps and expansion surfaces. Probe measurements were made and initial reduction of the HARI data was performed. The experimental



procedures and results are described in a report which is currently in preparation at WL/POPT, Wright Laboratory, Wright-Patterson Air Force Base.

## E. Liquid Fuel Injection In Subsonic Crossflows

Liquid jet atomization in an air crossflow has important applications in propulsion systems, including fuel injection in turbojet augmentor sections and ramjet and SCRAMJET combustors (see, for example, Hojnacki, 1972; Wotel et al., 1991]. In these applications, liquid fuel jets are injected from the walls of combustors or bluff body flameholders into the air stream under crossflow conditions. The combustion efficiency of these combustors thus depends closely on the outcome of the jet breakup process. Furthermore, current developments in spray simulation techniques require a fundamental understanding of jet breakup mechanisms to construct more realistic spray atomization models.

The recent development of secondary breakup theories has to some extent improved the current understanding of liquid jet breakup processes. Aerodynamic secondary breakup processes have been found to exhibit four major breakup regimes: bag, multimode, shear, and catastrophic breakup. Small droplets were stripped along the edge of parent drops and correlations were obtained by approximating the final droplet sizes with the thickness of the boundary layer along the windward side of the droplet surface [Wu et al. 1995; Hsiang and Faeth, 1992; Krzeczkowski, 1980; Hinze, 1955]. Since the breakup processes of a liquid jet and a spherical droplet in an air flow are both caused by aerodynamic forces, it is reasonable to apply the general understanding of the aerodynamic secondary breakup to the problem of liquid jet breakup.

This section of the research program, which was performed in the Aero Propulsion and Power facility at Wright Laboratory, experimentally examined the breakup processes of liquid jets injected into subsonic air crossflows. Test liquids, injector diameters, and air Mach numbers were varied to provide a wide range of jet operation conditions. The results were published in Wu et al. [1996] (see Appendix). A summary will be provided here.

Liquid jets of water, ethyl alcohol, a 30% alcohol/water solution, and a 40% glycerol/water solution were injected vertically upward into a subsonic wind tunnel from a nozzle exit flush with the tunnel bottom wall. Three nozzles with exit diameters of 0.5, 1.0, and 2.0 mm were used. Injection velocities were varied from 8.8 to 38.5 m/s and the air Mach numbers were limited to 0.2, 0.3, and 0.4. The wind tunnel has a rectangular test section with a cross section of 125 mm  $\times$  75 mm and a length of 406 mm. Quartz windows were installed on the top and both sides of the test section for laser diagnostics and flow visualization. The tunnel was operated continuously and the air Mach number was controlled by adjusting a variable-area nozzle device to obtain the correct area ratios at the choked point and at the test section [Chen et al., 1993].



**WATER,  $M_{air} = 0.2$ ,  $v_j = 10$  m/s,  $\bar{q} = 10$ ,  $d = 0.5$  mm.**

Figure 6. Predicted and experimental results for jet breakup process.

Near-field structures and breakup properties were visualized and analyzed using a pulsed shadowgraph technique with a frequency-doubled Nd:YAG laser as the light source. The resulting images were digitized and analyzed to provide liquid column trajectories and the distances to the column fracture point.

The processes of liquid column breakup in a crossflow were found to be similar to those of the aerodynamic secondary breakup of a spherical droplet, with the column eventually breaking into several bag-shaped membranes, as in the multimode breakup of droplets. When the liquid/air momentum flux ratio is large, the liquid jet undergoes surface breakup as droplets are stripped off the deflected edges of the liquid column before the development of large-scale column waves.

Column trajectories were correlated using a momentum analysis; the predictions were found to agree reasonably well with the experimental results (see Figure 6). The comparison of column trajectory predictions with measured results also allowed drag coefficients to be inferred. Drag coefficients were found to be larger for jets of more viscous liquids, perhaps because of the thicker boundary layer on the windward surface of the liquid column.

The column fracture location represents the boundary between the liquid column and dispersed-phase regimes. Fracture locations were identified by measuring the distances from the nozzle exit to the fracture points. The distances to the column fracture point were found to be a constant for the range of test conditions studied. Liquid jets always break at a location of eight diameters downstream from the nozzle exit, independent of jet injection conditions.

## F. Injection Of Supercritical Ethylene In Nitrogen

For hypersonic flight, e.g., flight Mach numbers greater than eight, thermal management of the airframe and of on-board electronic components is a particularly challenging problem. Conventional cooling techniques using ambient air are not feasible at hypersonic speeds because the stagnation temperature of the air is higher than the high-temperature limit of existing aerospace materials. One possible solution to this problem would be regenerative fuel cooling of the airframe and the combustor components, perhaps using endothermic fuels [Edwards, 1993]. An endothermic fuel is one that can undergo an endothermic thermal cracking (pyrolysis) reaction with a very large reaction heat. It has been shown that the thermal cracking reaction of endothermic fuels occurs at very high temperatures; n-dodecane, for example, is stable to 1100 K, at which point thermal cracking starts to become significant. These reaction temperatures are generally much higher than the critical temperatures of hydrocarbon fuels, so that the heat management of future aircraft is expected to require use of supercritical fuels [Edwards, 1993].

For aircraft which achieve hypersonic speeds in flight, the combustor operating conditions differ vastly between the start-up, boost, cruise, and final approach phases. Since fuel is used to absorb heat from the combustor for all phases, broad ranges of fuel operating temperatures and pressures are encountered. Thus, the regenerative fuel cooling approach increases the complexity of the combustor system and strongly affects injection and mixing mechanisms. Fuel may be injected as liquid under subcritical conditions or as gas under supercritical conditions, depending on the extent of heating and the fuel's thermodynamic state at the nozzle exit. Furthermore, supercritical fuels exhibit unusual thermophysical and transport properties near their critical point: liquid-like density, zero latent heat, zero surface tension, and high compressibility. These fuels also exhibit large variations in specific heats and speeds of sound, and enhanced values of thermal conductivity, viscosity, and mass diffusivity [Nieto de Castro, 1991; Holland et al., 1983; Younglove, 1982].

This section of the research program studied the injection of a supercritical fuel at injection temperatures slightly higher than the fuel's critical temperature, with back pressures lower than the critical pressure. The objective was to elucidate the effects of thermophysical and transport properties near the critical point on jet appearance, shock structures, and choking. Test conditions were designed to simulate injection of an endothermic fuel at temperatures between the critical temperature and the point where thermal cracking becomes significant. Ethylene and nitrogen were used to simulate interactions between supercritical fuel and air. The experimental methods and results were published in Wu et al. [1996]; a summary is provided here.

The experimental apparatus for this research program, which is located in Test Cell 18 at the Wright Laboratory Aero Propulsion and Power Directorate, consist of a fuel tank, a solenoid valve, a fuel temperature control unit, a nozzle, and the injection chamber.

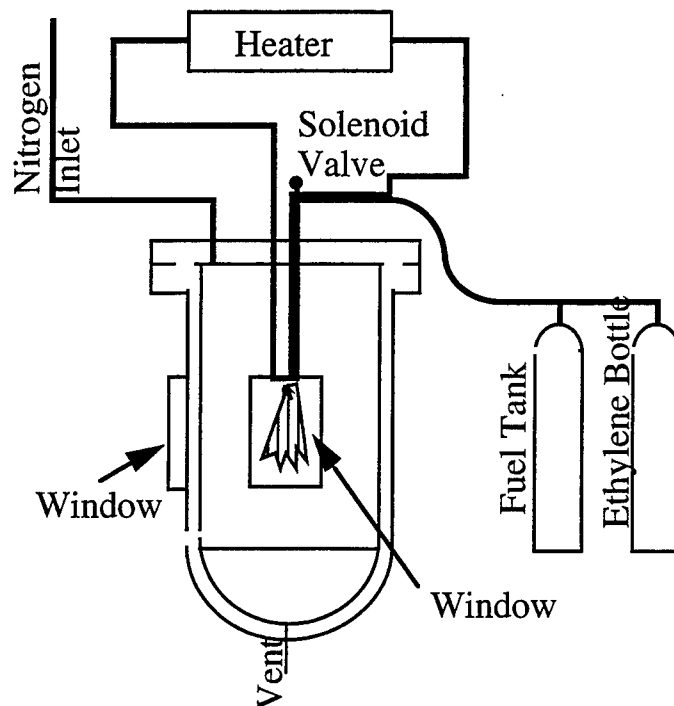


Figure 7. Supercritical fuel injection chamber.

The fuel tank assembly was designed to allow preset initial fuel pressures and temperatures and to provide a steady fuel supply during injection. A solenoid valve was installed in the fuel delivery line to control the injection duration. Supercritical fuel temperatures were monitored with thermocouples and controlled by flowing ethylene glycol outside the fuel pipe along the fuel delivery line for a distance of over 6 m upstream of the nozzle. In order to study the effects of ambient back pressure on the injection process, the fuel jet was enclosed in a large injection chamber. This chamber was designed to provide a high pressure, high temperature environment for the simulation of SCRAMJET and gas turbine combustor conditions and industrial injector atomization processes.

Long-exposure shadowgraphs were used to identify the thermodynamic phase (i.e., gas or liquid) of the injectant. Schlieren photographs were employed to resolve shock patterns and jet boundaries. The fuel mass flow rate was measured using a Coriolis-type mass flowmeter, with an uncertainty of less than  $\pm 1\%$ .

The fuel temperature and pressure were set to be slightly above the critical point in order to study the effect of near-critical-point thermophysical properties on the injection process. Ethylene was chosen as a test fuel because its critical temperature is near room temperature, which reduces system safety requirements. Nitrogen was used as the ambient gas because it is inert and has properties similar to those of air.

For ethylene injected at near room temperature, flow visualization showed an opaque region in the jet of up to 40 nozzle diameters, probably caused by condensation. This condensation will tend to cause ignition delay in propulsion systems. For higher injectant temperatures, the ethylene jet was found to exhibit shock structures similar to those of an underexpanded ideal-gas jet. Locations of Mach disks were compared to values predicted for ideal gases. Good agreement was obtained, which indicates that the Mach disk location is insensitive to fuel type. The shock structure of ethylene jets at lower injection temperatures is obscured by the

fuel condensation. For these higher injectant temperatures, mass flow rates were found to be insensitive to the variation of back pressure, indicating a choked flow.

The jet mass flow rate was found to increase as the injection conditions approach the thermodynamic critical point. Mass flow rates were 25 to 65% higher than the mass flow rates calculated according to the ideal-gas isentropic-flow approximation. A second isentropic approximation which takes into consideration the near-critical-point thermodynamic properties was developed for ethylene, and the predicted mass flow rates were found to be only about 15% lower than the measured values. This approximation produced a similar trend of mass flow rates vs. reduced temperature, which indicates that the increased mass flow rate at lower reduced temperatures was caused by the large density increase characteristic of fluid near its critical point.

Thermodynamic path analyses indicate that ethylene may pass through a liquid-gas regime for lower injection temperatures. This suggests the possible coexistence of liquid and gas phases at the nozzle exit. For higher injection temperatures, calculated choking pressures were found to be very close to the maximum ambient chamber pressure.



## G. Ethylene Mixing Studies

In work related to the supercritical fuel injection study described above, a brief study of ethylene injection into a nitrogen atmosphere was performed in order to identify the mixing characteristics of ethylene injection. A pressure cell which allowed varying pressure and gaseous species concentrations was used, and Raman spectroscopy was used to determine the number densities of the mixing species. Experiments were performed in the sub-critical regime, in order to study mixing behavior near the supercritical regime and to validate the experimental setup utilized in these experiments. The results of these experiments show that the Raman Scattering signal levels are acceptable and are sensitive to pressure, so that 2D planar imaging is feasible. The experimental techniques utilized, and the results obtained, are detailed in Dasgupta et al. [1995] (see Appendix).

#### 4. HT11 Software Development

In this section of the research program, a computer program was developed to predict the performance of heat exchangers using the endothermic fuel methylcyclohexane (MCH,  $C_7H_{14}$ ) as well as the performance of propulsion components cooled by MCH. The program, HT11, is written in FORTRAN 77, to run on IBM-compatible desktop computers. The program was used to analyze test data and validate the code. The program is described in detail, with case studies, in "HT11 - A Computer Program to Determine Performance of Heat Exchangers Using Endothermic Methylcyclohexane Fuel: Formulation and User Guide" [Taitech Special Report 95-1-1]; a summary is provided here.

HT11 is a performance code designed to estimate the exit properties of the hot and cold streams of a heat exchanger of specified dimensions and core properties. A performance code can be used to solve a design problem by adjusting core dimensions through an iterative process until the desired exit conditions are achieved.

HT11 is intended to handle pure counterflow or multipass cross counterflow mixed and unmixed fluid cases for any core geometry which can be described by conventional Kays and London surface properties [Kays and London, 1954]. The heat exchanger may be divided into any number of calculation segments. HT11 can currently access properties subroutines for air and for MCH. For MCH, thermal and transport properties are called as functions of pressure, temperature, and fraction of MCH reacted. An option exists to use fixed values of fluid properties. A subroutine is also available to calculate external free convection and radiative heat loss from the uninsulated test article.

To run HT11, an ASCII input file must be provided using a self-explanatory template. The program functions in accordance with the Kays and London effectiveness-NTU (e-NTU) method of estimating heat exchanger performance.

Within each calculation segment the code iterates on an assigned effectiveness value until the effectiveness used in calculated film coefficients agrees with the effectiveness calculated from the e-NTU exponential relations. The calculated effectiveness successively replaces the assigned effectiveness until the two agree.

To obtain convergence of the solution between segments, the computed exit temperatures of each fluid in a segment must agree with the entrance temperatures to adjacent segments. After one pass is made through each segment, the estimated exit temperatures of each fluid are assigned as new values of the entrance temperatures to the adjacent downstream segments. This process is repeated until the temperature to be assigned no longer differs from the value used in the previous iteration.

## 5. Conclusions

This three-year research program has produced a large set of data on fuel injection in high speed flows. Fundamental studies of gas and liquid-phase injection into subsonic and supersonic crossflows were carried out. The supersonic studies of single-jet parallel and transverse fuel injection will provide useful data for the future development of more complex mixing-enhancing injectors, and will contribute to the verification of future computational fluid dynamics programs. The results of these studies were used in the development of an innovative method of calculating the state of mixing (mixedness) in a flow from light scattering images. This calculation method will allow visual diagnostic techniques to provide quantitative mixing measurements.

More complex mixing enhancement schemes were also explored in the supersonic regime. These schemes introduced geometric effects into the flow, and provided a field for comparison with some of the more fundamental transverse and parallel studies. In the course of both groups of studies, innovative diagnostic and measurement techniques were developed, refined, and applied. In particular, the use of multiple techniques (combinations of laser-based diagnostics and mechanical probing, for instance) for the characterization of a single flow field has been shown to be very powerful. These types of combination are especially important in the challenging environments typical of supersonic research and applications.

In the subsonic regime, the studies described here have shown that liquid jets always break up into droplets at the same point -- eight diameters from the jet exit. The characterization of liquid jet breakup and supercritical jets will be of crucial importance for the design of future propulsion systems.

The results of the research described in this report are already in use in successor studies, including heat transfer measurement and boundary layer studies. More

detailed mixing enhancement studies are contributing to the development of a prototype design for a SCRAMJET fuel injector, which is also in progress.

Thus, the research program described here can be seen to have made major contributions to the ongoing study of high speed fuel injection issues, in both fundamental and applications contexts. Future research, building on the results described here, will carry the field further toward a basic understanding of the physics of fuel injection into high speed flows, and toward the application of this knowledge in the design and development of high speed aircraft.

## 6. Acknowledgments

This project was supported by and performed at the Aero Propulsion and Power Directorate, Wright Laboratory, at Wright-Patterson Air Force Base under contract F33615-93-C-2300. The authors are very grateful for support and technical guidance from Dr. A. S. Nejad. Technical contributions by Dr. D. Glawe and M. Gruber, and Mr. J. Donbar have played an essential role in the success of this project. The support of the Wright Laboratory Aero Propulsion and Power air facility crew and contracting personnel are also highly appreciated, as is the editorial assistance of Dr. Anna E. S. Creese.

## 7. References

- Barber, M.J., Roe, L.A., and Schetz, J.A., "Simulated Fuel Injection Through a Wedge-Shaped Orifice Into Supersonic Flow," AIAA Paper 95-2559, July 1995.
- Chen, T. H., Smith, C. R., Schommer, D. G., and Nejad, A. S., "Multi-Zone Behavior of Transverse Liquid Jet in High-Speed Flow," AIAA Paper 93-0453, Jan. 1993.
- Cox, S.K., Fuller, R.P., Schetz, J.A., and Walters, R.W., "Vortical Interactions Generated by an Injector Array to Enhance Mixing in Supersonic Flow," AIAA Paper 94-0708, Jan. 1994.
- Dasgupta, S., Vuppuladhadiam, R., Wu, P.K., Chen, T.H., Carter, C., and Nejad, A.S., "Raman Scattering Study of Ethylene Under Varying Pressure," AIAA Paper 95-2551, July 1995.
- Edwards, T., "USAF Supercritical Hydrocarbon Fuels Interests," AIAA Paper 93-0807, Jan. 1993.
- Fric, T. F., and Roshko, A., "Vortical Structure in the Wake of a Transverse Jet," *Journal of Fluid Mechanics*, Vol. 279 (1994) 1-47
- Fuller, E.J., Thomas, R.H., and Schetz, J.A., "Mixing Studies of Helium in Air at High Supersonic Speeds," AIAA Journal, Vol. 30, No. 9 (1992).
- Glawe, D.D., "Effect of Nozzle Geometries on Parallel Injection from the Base of an Extended Strut into Supersonic Flow," Ph.D. dissertation, Ohio State University, 1995.
- Glawe, D.D., Samimy, M., Nejad, A.S., and Chen, T.H., "Effects of Nozzle Geometry on Parallel Injection from Base of an Extended Strut into a Supersonic Flow," AIAA Paper 95-0522, Jan. 1995.
- Glawe, D.D., Samimy, M., Nejad, A.S., and Chen, T.H., "Effects of Nozzle Geometry on Parallel Injection from Base of an Extended Strut into a Supersonic Flow," AIAA Paper 95-0522, Jan. 1995.
- Goebel, S.G., and Dutton, J.C., "Experimental Study of Compressible Turbulent Mixing Layers," *AIAA Journal*, Vol. 29, No. 4 (1991) 538-546.
- Gruber, M.R. and Nejad, A.S., "Development of a Large-Scale Supersonic Combustion Research Facility," AIAA Paper 94-0544, Jan. 1994.

- Gruber, M.R., Nejad, A.S., and Dutton, J.C., "Circular and Elliptical Transverse Injection into a Supersonic Cross-flow -- The Role of Large-Scale Structures," AIAA Paper 95-2150, June 1995.
- Gruber, M.R., Nejad, A.S., Chen, T.H., and Dutton, J.C., "Mixing and Penetration Studies of Sonic Jets in a Mach 2 Freestream," *Journal of Propulsion and Power*, Vol. 11, No. 2 (1995) 315-323.
- Hartfield, R.J., Hollo, S.D., and McDaniel, J.C., "Experimental Investigation of a Supersonic Swept Ramp Injector Using Laser-Induced Iodine Fluorescence," *Journal of Propulsion and Power*, Vol. 10, No. 1 (1994) 129-135.
- Heiser, W.H., Pratt, D.T., Daley, D.H., and Mehta, U.B., "Hypersonic Airbreathing Propulsion," in *AIAA Education Series*, Przemieniecki, J. S. (Edit.) AIAA, Washington, D.C., 1994.
- Hinze, J. O., "Fundamentals of the Hydrodynamic Mechanism of Splitting in Dispersion Processes," *AIChE Journal*, Vol. 1, No. 3, 1955, pp. 289-295.
- Hojnacki, J. T., "Ramjet Engine Fuel Injection Studies," AFAPL-TR-72-76, Aero Propulsion Laboratory, Wright-Patterson AFB, 1972.
- Holland, P. M., Eaton, B. E., and Hanley, H. J. M., "A Correlation of the Viscosity and Thermal Conductivity Data of Gaseous and Liquid Ethylene," *J. Phys. Chem. Ref. Data*, Vol. 12 (1983) 917-932.
- Hsiang, L.-P. and Faeth, G. M., "Near-Limit Drop Deformation and Secondary Breakup," *International Journal of Multiphase Flow*, Vol. 18, No. 5 (1992) 635-652.
- Kays, W.M., and London, A.L., "Compact Heat Exchangers," Stanford University, 1954.
- Krzeczkowski, S. A., "Measurement of Liquid Droplet Disintegration Mechanisms," *International Journal of Multiphase Flow*, Vol. 6, No. 2, 1980, pp. 227-239.
- Mays, R.B., Thomas, R.H., and Schetz, J.A., "Low Angle Injection into a Supersonic Flow," AIAA Paper 89-2461, July 1989.
- Nieto de Castro, C. A., "Thermal Conductivity and Thermal Diffusivity in Supercritical Fluids," *Supercritical Fluid Technology: Reviews in Modern*



*Theory and Applications*, ed. T. J. Bruno and J. F. Ely, CRC Press, Boca Raton, 1991, Chapter 9.

Ninnemann, T.A. and Ng, W.F., "A Concentration Probe for the Study of Mixing in Supersonic Shear Flows," *Experiments in Fluids*, Vol 13 (1992) 98-104.

Northam, G.B., Greenburg, I., Byington, C.S., and Capriotti D.P., "Evaluation of Parallel Injector Configurations for Mach 2 Combustion," *Journal of Propulsion and Power*, Vol. 8, No. 2 (1992) 491-499.

Papamoschou, D., and Roshko, A., "The Compressible Turbulent Shear Layer: An Experimental Study," *Journal of Fluid Mechanics*, Vol. 197, No. 1988, pp. 453-477.

Riggins, D.W., and Vitt, P.H., "Investigation of Scramjet Strategies for High Mach Number Flows," *Journal of Propulsion and Power*, Vol. 11, No. 3 (1995) 419-425.

Riggins, D.W., McClinton, C.R., Rogers, R.C., and Bittner, R.D., "Investigation of Scramjet Strategies for High Mach Number Flows," *Journal of Propulsion and Power*, Vol. 11, No. 3 (1995) 409-418.

Rogers, R.C., Weidner, E.H., and Bittner, R.D., "Quantification of Scramjet Mixing in the Hypervelocity Flow of a Pulse Facility," AIAA Paper 94-2518, June 1994.

Samimy, M., and Lele, S.K., "Motion of Particles with Inertia in a Compressible Free Shear Layer," *Physics of Fluids A*, Vol. 3, No. 8 (1991) 1915-1923.

Schetz, J.A. and Billig, F.S., "Penetration of Gaseous Jets Injected into a Supersonic Stream," *Journal of Spacecraft and Rockets*, Vol.3, No. 11 (1966) 1658-1665.

Schetz, J.A., "Interaction Shock Shape for Transverse Injection," *Journal of Spacecraft and Rockets*, Vol. 7, No. 2 (1970) 143-149.

Schetz, J.A., Hawkins, P.F., and Lehman, H., "Structure of Highly Underexpanded Transverse Jets in a Supersonic Stream," *AIAA Journal*, Vol. 5, No. 5 (1967) 882-884.

Schetz, J.A., Thomas, R.H., and Billig, F., "Mixing of Transverse Jets and Wall Jets in Supersonic Flow," in *Separated Flows and Jets*, V. V. Kozlov and A. V. Dovgal (Edits.), Springer-Verlag, Berlin, 1991.

- Schetz, J.A., Weinraub, R.A., and Mahaffey, R.E. Jr., "Supersonic Transverse Injection into a Supersonic Stream," *AIAA Journal*, Vol. 6, No. 5 (1968) 933-934.
- Wotel, G. J., Gallagher, K. E., Caron, S. D., Rosfjord, T. J., Hautman, D. J., and Spadaccini, L. J., "High Speed Turboramjet Combustor Technology Program," WL-TR-91-2043, Wright Laboratory, Wright-Patterson AFB, OH., 1991.
- Wu, P.-K., Chen, T. H., Nejad, A. S., and Carter, C. D., "Injection of Supercritical Ethylene in Nitrogen," *Journal of Propulsion and Power*, Vol. 12, No. 4, (1996) 770-777.
- Wu, P.-K., Hsiang, L.-P., and Faeth, G. M., "Aerodynamic Effects on Primary and Secondary Breakup," *Liquid Rocket Engine Combustion Instability*, ed. V. Yang and W. Anderson, Vol. 169, Progress in Astronautics and Aeronautics, AIAA, Washington, DC, 1995, pp. 247-279.
- Younglove, B. A., "Thermophysical Properties of Fluids: I. Argon, Ethylene, Parahydrogen, Nitrogen, Nitrogen Trifluoride, and Oxygen," *J. Phys. Chem. Ref. Data*, Vol. 11, Suppl. 1 (1982) 58-96.

## 8. Appendices

- Chen, M.-H., Gaffney, R., Wu, P.-K., Nejad, A.S., "Numerical Simulations of Axisymmetric Sonic He and H<sub>2</sub> Injections into a Mach 2 Airstream," AIAA Paper 95-0873, Jan. 1995.
- Dasgupta, S., Vuppuladhadiam, R., Wu, P.-K., Chen, T.H., Carter, C., Nejad, A.S., "Raman Scattering Study of Ethylene Under Varying Pressure," AIAA Paper 95-2551, July 1995.
- Fuller, R.P., Wu, P.-K., Nejad, A.S., and Schetz, J.A., "Fuel-Vortex Interactions for Enhanced Mixing in Supersonic Flow," AIAA Paper 96-2661, July 1996.
- Glawe, D.D., Donbar, J.M., Nejad, A.S., Sekar, B., Chen, T.H., Samimy, M., and Driscoll, J.F., "Parallel Fuel Injection from the Base of an Extended Strut into a Supersonic Flow," AIAA Paper 94-0711, Jan. 1994.
- Glawe, D.D., Samimy, M., Nejad, A.S., and Chen, T.H., "Effects of Nozzle Geometry on Parallel Injection from the Base of an Extended Strut into a Supersonic Flow," AIAA Paper 95-0522, Jan. 1995.
- Gruber, M.R., Nejad, A.S., and Dutton, J.C., "Circular and Elliptical Transverse Injection into a Supersonic Crossflow--The Role of Large-Scale Structures," AIAA Paper 95-2150, June 1995.
- Gruber, M.R., Nejad, A.S., Chen, T.H., and Dutton, J.C., "Compressibility effects in supersonic transverse injection flowfields," (submitted to *Physics of Fluids*, 1996).
- Gruber, M.R., Nejad, A.S., Chen, T.H., and Dutton, J.C., "Large Structure Convection Velocity Measurements in Compressible Transverse Injection Flowfields," AIAA Paper 96-0203, Jan. 1996.
- Gruber, M.R., Nejad, A.S., Chen, T.H., and Dutton, J.C., "Mixing and Penetration Studies of Sonic Jets in a Mach 2 Freestream," *Journal of Propulsion and Power*, Vol. 11, No. 2 (1995): 315-323.
- Gruber, M.R., Nejad, A.S., Chen, T.H., and Dutton, J.C., "Observations of the Bow Shock-Jet Interaction in Compressible Transverse Injection Flowfields," (accepted for publication in the *AIAA Journal*).

Wu, P.-K., Kirkendall, K.A., Fuller, R.P., and Nejad, A.S., "Breakup Processes of Liquid Jets in Subsonic Crossflows," AIAA Paper 96-3024, July 1996 (accepted for publication in *Journal of Propulsion and Power*).



**AIAA 95-0873**

**Numerical Simulations of  
Axisymmetric Sonic He and H<sub>2</sub>  
Injections into a Mach 2 Airstream**

**Ming-Hsiung Chen**  
**Taitech Inc., Dayton, OH 45440**

**Rick Gaffney**  
**Analytical Services and Materials, Inc., Hampton, VA**

**Pei-Kuan Wu**  
**Tzong H. Chen**  
**Taitech Inc., Dayton, OH 45440**

**Abdollah S. Nejad**  
**Wright Laboratory, WPAFB, OH 45444**

**33rd Aerospace Sciences  
Meeting and Exhibit  
January 9-12, 1995 / Reno, NV**

# Numerical Simulations of Axisymmetric Sonic He and H<sub>2</sub> Injections into a Mach 2 Airstream

Ming-Hsiung Chen,<sup>1</sup> Rick Gaffney,<sup>2</sup> Pei-Kuan Wu,<sup>1</sup>  
Tzong H Chen,<sup>1</sup> Abdollah S. Nejad<sup>3</sup>

<sup>1</sup>Taitech Inc. 3675 Harmeling Drive, Beavercreek, OH 45440

<sup>2</sup>Analytical Services and Materials, Inc, Hampton, VA 23665

<sup>3</sup>Advanced Propulsion Division, Aero Propulsion and Power Directorate  
WPAFB, OH 45433

## Abstract

The main purpose of this investigation is to conduct a series of inviscid calculations capable of accurately predicting the non-reacting flow fields associated with underexpanded axisymmetric helium and hydrogen injections into a Mach 2 airstream. The flow fields exhibit complex shock structures of a Mach disk formation. The results show that Mach disks are observed for conditions of  $P_{jet}/P_{\infty}$  greater than 2.0. For higher pressure ratios, larger Mach disk formations are observed at a location farther downstream. The computed Mach disk locations agree favorably with in-house experimental data. The Mach disk formation apparently has a strong effect on fuel/air mixing processes. Injection of hydrogen is simulated and compared with the results of helium injection. The results of both air and nitrogen injection simulations are very consistent.

## Introduction

The design of hypersonic vehicles, such as the National Aero-Space Plane (NASP), requires accurate predictions of combustion processes within a high speed air-breathing propulsion system. Air breathing combustors utilizing supersonic combustion are currently under active development for the propulsion of future hypersonic vehicles. In the past, supersonic combustion flow fields have been studied by numerous investigators in order to optimize scramjet combustor performance [1-4]. The performance of a propulsion system is directly reflected in the fuel-air mixing. One commonly used configuration for fuel delivery is parallel fuel injection into a supersonic airstream. To characterize the flow features of this configuration, a

supersonic combustion test facility was designed and constructed at the Propulsion Laboratory, Wright-Patterson Air Force Base, Ohio [5]. Several fundamental issues involving supersonic fuel-air mixing have been investigated and reported [6-7]. Glawe et al. [7] used planar Rayleigh/Mie Scattering and acetone PLIF to study the mixing processes of helium injection into a Mach 2 airstream. Based on their measurements, the Mach disk for  $P_{jet}/P_{\infty} = 5.0$  was visualized and the location of the Mach disk was identified. However, only limited quantitative information on these complex flow fields is currently available; systematic studies are required to further our understanding of both the shock structures and the mixing process.

In the present study, parallel fuel injection at sonic speed from a circular nozzle into a Mach 2 airstream was chosen as a test model for two reasons. In the first place, numerical simulations can provide accurate predictions of complex shock structures and mixing processes. Secondly, numerical simulations are more economical than experimental approaches in terms of parametric studies. A series of systematic numerical simulations were therefore conducted to characterize the flow fields and to highlight supersonic mixing mechanisms. The knowledge obtained from present study will be important for designing efficient hypersonic combustors. In practice, hydrogen is used as a fuel for scramjet combustors. In the laboratory, because of safety considerations, hydrogen is generally replaced by helium. To date, however, there have been few studies comparing the flow fields of these two injectants. Therefore, the objectives of the current study are to identify the starting pressure match ratio for the appearance of a regular reflect and Mach reflect, and to compare the locations, sizes and shapes of the Mach disk for highly underexpanded jets with various injectants. The calculated results are validated with in-house experimental data, from coaxial helium injection

with  $P_{jet}/P_{\infty} = 2.0$  and  $5.0$ , produced by Glawe et al [7]. The discrepancies between the flow fields and complex shock structures in the helium and hydrogen injection cases are also compared.

### Governing Equations

The equations governing flow of a multiple species gas mixture are the Navier-Stokes equations augmented with species continuity equations. The Navier-Stokes equations, which represent conservation of mass, momentum and energy, are

$$\begin{aligned}\frac{\partial \rho}{\partial t} + \frac{\partial(\rho u_i)}{\partial x_i} &= 0 \\ \frac{\partial(\rho u_i)}{\partial t} + \frac{\partial}{\partial x_j} [\rho u_i u_j + \delta_{ij} P - \tau_{ij}] &= 0 \\ \frac{\partial(\rho E)}{\partial t} + \frac{\partial}{\partial x_j} [\rho u_j H + q_j - u_i \tau_{ij}] &= 0\end{aligned}$$

where  $\rho$  is the density,  $u_i$  is the velocity in the  $x_i$  direction,  $P$  is the static pressure,  $\tau_{ij}$  is the shear stress tensor and  $q_j$  is the heat flux vector. The total energy  $E$  is related to the total enthalpy  $H$  by

$$E = H - \frac{P}{\rho}$$

and the total enthalpy is related to the static enthalpy  $h$  and the velocity by

$$H = h + \frac{u_i u_i}{2}$$

The static enthalpy of the mixture is given by

$$h = \sum_{n=1}^{ns} f_n h_n$$

where  $h_n$  is the static enthalpy of species  $n$  and  $f_n$  is the mass fraction of species  $n$ . The species continuity equations written in terms of mass fractions are

$$\frac{\partial(\rho f_n)}{\partial t} + \frac{\partial}{\partial x_i} [\rho u_i f_n + \rho v_{ni} f_n] = \dot{\omega}_n$$

where the mass fraction is defined in terms of the species density  $\rho_n$  and the total density

$$f_n = \frac{\rho_n}{\rho}$$

Note that

$$\rho = \sum_{n=1}^{ns} \rho_n$$

which gives the property

$$\sum_{n=1}^{ns} f_n = 1$$

In the species continuity equations  $v_{nj}$  is the diffusion velocity of species  $n$  in the  $x_j$  direction and  $\dot{\omega}_n$  is the time rate of change of species  $n$  due to chemical reaction. Because the species densities sum to the total density, it is necessary to solve only  $ns-1$  species continuity equations in addition to the Navier-Stokes equations.

### Equation of State

The gas mixture can be described by the perfect gas law

$$p = \rho R T$$

where  $R$  is the gas constant of the mixture which is given by

$$R = \sum_{n=1}^{ns} R_n f_n$$

The gas constant of species  $n$  is given by

$$R_n = \frac{R_u}{W_n}$$

where  $R_u$  is the universal gas constant and  $W_n$  is the molecular weight of species  $n$ .

### Thermodynamic Model

The gas is assumed to be a mixture of thermally perfect gases so that the temperature and the static enthalpy of each species are related by

$$h_n = \int_{T_{ref}}^T C_{pn}(T) dT + h_n^0$$

where  $C_{pn}$  is the coefficient of specific heat at constant pressure and  $h_n^0$  is the heat of formation at  $T_{ref}$ . We further assume that the gas is always in thermal equilibrium and that  $C_{pn}$  can be described by a polynomial. McBride et al. [8] curve fit  $C_p$  for a number of species. They use polynomials of the form

$$\frac{C_p}{R} = a_0 + a_1 T + a_2 T^2 + a_3 T^3 + a_4 T^4$$

where  $T$  is the local dimensional temperature in degrees Kelvin.

### Solution Techniques

An axisymmetric FDSCHM code [9], was applied to simulate the flow fields of a coaxial fuel injection of helium and hydrogen into a Mach 2 airstream. The FDSCHM code is a 2D/axisymmetric, Euler/Navier-Stokes solver. The governing equations are discretized using a finite-volume method with the explicit multi-stage Runge-Kutta time integration approach of Jameson et al. [10]. The flow quantities are stored at the cell centers and the flux balancing reduces to a contour integral for the faces of each cell. The total

variation diminishing (TVD) schemes of Roe's flux-difference splitting [11] with different flux limiters are incorporated into the current computer program such that strong shocks can be captured without spurious oscillations, and non-physical solutions can also be eliminated by entropy correction. The  $\kappa$ - $\epsilon$  two equation turbulence model is available in the FDSCHM code. This code also supports several chemistry models, predominately covering helium-air and hydrogen-air chemistry. Furthermore, the equations of motion are integrated in time using a multi-stage fourth-order Runge-Kutta scheme with an implicit residual smoothing [12]. This enhancement can improve the overall convergence rate of the steady solutions.

### Boundary Conditions

Boundary conditions for inviscid, non-reacting coaxial jet flow field computations are summarized as follows:

#### *Inflow boundary*

Inflow conditions on the upstream boundaries can be divided into three regions:

- (1) region of sonic fuel injection ( $0 \leq y < 0.001778$  m)  
All the jet conditions are specified.
- (2) region of nozzle wall ( $0.001778 \leq y \leq 0.00635$  m)  
The tangency condition is imposed.
- (3) region of external supersonic airstream ( $0.00635 < y \leq 0.0635$  m).

All the freestream flow quantities are specified and held fixed during the solution procedure.

#### *Symmetry boundary*

The jet centerline is a line of symmetry with no mass or flux across it. The derivatives in the direction normal to the centerline are set to be zero.

#### *Outflow boundary*

The outflow boundary is chosen to be 56.2 nozzle radii away from the nozzle exit plane. The assumption that uniform static pressure is equal to the ambient pressure is likely to be true; all fluxes therefore are extrapolated from the interior points.

#### *Top wall boundary*

The top wall boundary is about 35.7 nozzle radii away from the centerline of the nozzle axis. This is consistent with the experimental set-up. Since the present calculation is limited to the inviscid case, a tangency condition is imposed on the top wall.

### Test Conditions

The test conditions for this simulation were based on the aforementioned supersonic nozzle experiments [7]. The pertinent operating conditions for the parallel sonic helium injection into a Mach 2 airstream are summarized in Table 1.

### Computational Grids

A geometric layout of the supersonic parallel fuel injection tunnel is shown in Fig.1. A computational grid system was generated in a domain of 0.1 m x 0.0635 m; the computational domain of the coaxial jet flow problem is shown in Fig.2. The grid system utilized 151 points in the axial direction and 101 points in the radial direction, with 25 points across the jet exit, 35 points across nozzle base region and 40 points cover the rest of external airstream region (see Fig. 3a). All grids used are nonuniform distributions in both directions. For a high-pressure jet (highly underexpanded) condition, a rapid expansion wave issues from the nozzle lip. In order to accurately model real physical behavior and to stabilize the solution procedure, refinement of the grid points near the nozzle wall is mandatory. The stretching transformation proposed by Roberts [13] was employed to cluster the grid points in both the axial and the radial directions adjacent to the nozzle base region. The detailed formulation of stretching function can be found in Ref [14]. In the current study, the minimum grid spacing in axial direction is  $1.358 \times 10^{-5}$  m, while a minimum radial spacing around  $y = 0.001778$  m (the location of nozzle lip) is  $3.5 \times 10^{-6}$  m and around  $y = 0.00635$  m (the location of external corner) is about  $8.61 \times 10^{-6}$  m. A close-up view of the 151 x 101 grid system is shown in Fig. 3b. It can be seen that the nozzle base region between the fuel injector and coaxial airstream are well resolved.

### Results

#### Sonic helium injection: the formation of the Mach disk

Fig. 4 shows results of the Mach contours of six different pressure ratios ( $P_{jet}/P_{\infty}$ ) ranging from 1 to 5 for helium injection. For the  $P_{jet}/P_{\infty} = 1$  case, the jet stream is almost parallel to the nozzle lip at  $y = 0.001778$  m (see Fig. 4a). For a slightly higher pressure ratio ( $P_{jet}/P_{\infty} = 1.2$ ), the expansion waves issuing from the nozzle lip are reflected as compression waves from the jet boundary. Subsequently these reflected compression waves coalesce and form a barrel shock (intercepting shock). Further downstream (0.0054 m,  $L/D = 1.54$ ), this barrel shock is reflected



off the centerline of symmetry, and the reflected shock emerges and interacts with the shear layer. This process is called regular reflection when the pressure ratio is still small (see Fig. 4b). When  $P_{jet}/P_{\infty} = 2.0$ , the embedded shock wave is strong enough that regular reflection from the centerline of symmetry cannot form, so the appearance of a Mach reflection begins to occur. Concurrently, there is a normal or nearly normal shock (Mach disk) that appears near the centerline of symmetry together with the barrel shock and reflected shocks to become a triple intersection point. Behind the Mach disk there is a region of subsonic flow bounded by a slip line (sonic line) emanated from that triple point. Figs. 4c-4f show that the size of Mach disk gradually grows and its location shifts farther downstream away from injector as the pressure ratio increases. The figures clearly show that the salient features of complex shock structures; namely the expansion wave, oblique recompression shocks, barrel shock, Mach disk and slip line, have been adequately captured and resolved. The computed locations and sizes of the Mach disks for various pressure ratios ranging from 2.0 to 5.0 are summarized in Table 3.

#### Detailed flow fields for $P_{jet}/P_{\infty} = 5.0$ case

Figs. 5a-5d show the contour plots of the density, Pressure, temperature, mass fraction of He, velocity vectors and streamlines for the  $P_{jet}/P_{\infty} = 5.0$  case, respectively. Since the density of air is 7.2 times larger than that of helium (cf. Table 2), the Mach disk is not quite visible in this density contour plot, and the density of air dominates the upper portion of figure (cf. Fig. 5a). On the contrary, the pressure contours are quite strong at the jet exit and the Mach disk is noticeable (Fig. 5b). It can also be seen that there is a high temperature region (see Fig. 5c) located at the upper portion of the recirculation zone adjacent to the nozzle base region when the highly underexpanded jet is exhausted from the nozzle. This is the reason the nozzle base region can serve as a flame holder. Fig. 5d shows that mass fraction of air/He occurs in the middle portion of nozzle base region. The close-up views of both velocity vectors and streamlines (Figs. 5e and 5f) show recirculation near the nozzle base region.

#### Centerline profiles of flow variables with helium injection

The centerline distributions of density, pressure, temperature, Mach number and axial velocity are displayed in Fig. 6. The overall centerline distribution of profiles show no overshoot or undershoot across the Mach disk except for the  $P_{jet}/P_{\infty} = 2.0$  case, where there is a kink in the temperature and Mach number

profiles. In general, the profiles across the shock only smear out one to two grid points; this indicates that sharp profiles for a wide range of pressure ratios are predicted well by the current simulation. These profiles provide an invaluable data base for studying highly underexpanded sonic jets.

#### The effect of grid refinement

The purpose of grid refinement is to ensure that the calculated solutions will be independent of grids. Figs. 7a - 7c show three different grid systems, namely, 151x101, 201x151 and 251x201, and Mach contour plots for helium injection with the  $P_{jet}/P_{\infty} = 5.0$  case for each grid system. The location of the Mach disk for 151x101 grid system is about 0.0076 meter (or  $L/D = 2.17$ ), while the Mach disks for both 201x151 and 251x201 cases are located at 0.0075 meter ( $L/D = 2.14$ ). The shape of the Mach disk is much crisper when the grids increasing in both axial and transverse directions. Moreover, the recompression wave, shear layer and jet boundary are much more distinct in the 201x151 and 251x201 grid systems (see Figs. 7b and 7c). Nevertheless, the computed solutions based on the 151x101 grid resolution are adequate to capture the essential flow features for highly underexpanded jet problems.

#### 0.5 mass fraction contour lines vs. mixing process

Fig. 8 shows the 0.5 mass fraction contour lines induced by various pressure ratios. This 0.5 mass fraction contour line can be viewed as an indicator of the air/helium mixture ratio. As pressure ratio increases, the 0.5 mass fraction contour lines gradually rise. This suggests that the mixing process of air/helium might also increase as the pressure ratios increase. The Fig. 8 also illustrates that the mixing process evolves and is quite active due to a strong recirculation in the region immediately after the nozzle base.

#### Comparison the location of the Mach disk between the measures and computed values

Fig. 9 shows the two schlieren photographs of sonic helium injection in the  $P_{jet}/P_{\infty} = 2.0$  and 5.0 cases. The corresponding locations of the Mach disks in the experimental data [7] are 0.0053 m and 0.0075 m, respectively. Computed values of the Mach disk locations for these two cases are 0.0056 and 0.0076 m, which are very close to the measured values. The percentages of error between the calculated and measured values are 5.6 % for  $P_{jet}/P_{\infty} = 2.0$  case and 1.3 % for  $P_{jet}/P_{\infty} = 5.0$  case (see Table 4 ). The calculated solutions thus agree very favorably with the experimental measurements.

### Sonic injection with hydrogen

With the FDSCHM code, the chemical model for hydrogen injection is also available. For hydrogen to be reacting, the required temperature is very high. However, in the present study the temperature used is based on the temperature condition of helium. Therefore the flow features of helium and hydrogen can be compared equally. Fig. 10 shows the Mach contours for hydrogen injection for  $P_{jet}/P_{\infty} = 1.0$  through 5.0. The Mach disk appears beginning with  $P_{jet}/P_{\infty} = 2.0$ . The size of Mach disk increases and the location of the Mach disk shifts farther downstream from the nozzle exit as the pressure ratio increases. This qualitative trend of the solutions is very similar to the helium case for each pressure ratio (cf. Fig. 4). However, quantitative measurements of Mach disk locations of hydrogen generally will appear at 1.4 to 21.6 % of upstream position from nozzle exit as compared with helium cases. The Mach disks are 4.2 to 34.7 % larger for the hydrogen than for the helium cases as the pressure ratio decreases from 5.0 to 1.0. (cf. Tables 3 and 5). Fig. 11 shows the centerline distribution profiles of density, pressure, temperature, Mach number and axial velocity for hydrogen injection. The pattern of distribution profiles is also very similar to those observed with helium injection. The profiles are very sharp across the shock except in the  $P_{jet}/P_{\infty} = 2.0$  case.

### The effect of different injectants

Figure 12a. shows the Mach and temperature contours of the  $P_{jet}/P_{\infty} = 5.0$  case with air injection. Fig. 12b shows the same contour plots with same pressure ratio, except that the injectant is nitrogen. As mentioned previously, the thermal properties (such as density, gas constant, specific heat ratio etc.) of air and nitrogen are very close (cf. Table 2). As a result, the flow features based on calculated solutions are almost identical, as expected. The centerline distribution of pressure and Mach number profiles (Figs. 12c and 12d) for both air and nitrogen are exactly the same. The positions of the Mach disk for both air and nitrogen are also the same, i.e. 0.0073 meter ( $L/D = 2.09$ ). The profiles across the shock do not show any wiggles. It is evident that the current predictions are very reliable and can provide further insight into the highly underexpanded sonic jet.

### Conclusions

The numerical simulations of axisymmetric sonic fuel injection from a nozzle into a Mach 2 airstream

with a wide range of pressure ratios have been conducted to capture the salient features of the flow fields. The specific conclusions and findings of the present study are summarized as follows:

- (1) This systematic study provides a comprehensive understanding of coaxial sonic fuel injection into a supersonic flow. The essential features of the current problem, namely the barrel shock, Mach disk, slip line (sonic line), triple point, and recompression waves have been captured adequately.
- (2) As pressure ratios increase over a range from 1.0 to 5.0, the detailed evolution of flow behaviors, namely regular reflect and Mach reflect, can be observed vividly. Furthermore, for higher pressure ratios, the size of the Mach disk increases gradually and the location of the Mach disk also shifts further downstream.
- (3) For sonic helium injection for  $P_{jet}/P_{\infty} = 2.0$  and 5.0 cases, the predicted locations of the Mach disk agreed well with the experimental results. The error is about 5.6 % for  $P_{jet}/P_{\infty} = 2.0$  and 1.3 % for  $P_{jet}/P_{\infty} = 5.0$  case.
- (4) The location of the Mach disk for hydrogen injection is slightly upstream of the location for helium injection with the same pressure ratio. However, the size of the Mach disk for the hydrogen case is larger than for the helium case.
- (5) The centerline distribution profiles of density, pressure, temperature, Mach number and axial velocity for both helium and hydrogen injection cases do provide an invaluable data base for studying the axisymmetric underexpanded sonic fuel injection into a Mach 2 airstream.
- (6) The calculated solutions for both air and nitrogen injections are very consistent. The location, size and shape of Mach disk are almost identical. It is evident that FDSCHM code is very reliable to simulate the complex flow problems like current study.

### Acknowledgments

This work was partially supported by and was performed at Wright Laboratory, Aero Propulsion and Power Directorate, Wright Patterson Air Force Base under contract No. F33615-93-C-2300. The present calculations were performed on CRAY YMP/C90 of DoD High Performance Computing Center at

Vicksburg, Mississippi. This support is gratefully acknowledged. Special thanks are given to Diana D. Glawe (WL/POPT) for providing schlieren photographs of underexpanded sonic helium injection with  $P_{jet}/P_{\infty} = 2.0$  and 5.0 cases, to Gary Haines (Taitech) for drawing Figure 2, and to Anna Creese (Taitech) for reviewing the manuscript and preparing the format of present paper.

### References

1. M. Takahashi and A.K. Hayashi, "Numerical Study on Mixing and Combustion of Injection Hydrogen Jet in a Supersonic Air Flow," AIAA Paper 91-0574.
2. J. Lee, "A Numerical Study of Mixing in Supersonic Combustors with hyper mixing Injectors," AIAA Paper 93-0215, 1993.
3. P.S. King, R.H. Thomas and J.A. Schetz, "Combined Tangential-Normal Injection into a Supersonic Flow," *J. Propulsion and Power*, Vol. 7, 1991, pp. 420-430.
4. G. Wadawadigi, J.C. Tannehill and P.E. Buelow and S.L. Lawrence, "Three-Dimensional Upwind Parabolized Navier-Stokes Code for Supersonic Combustion Flow fields," *J. Thermophysics and Heat Transfer*, Vol. 7, No. 4, 1993, pp. 661-667.
5. M.R. Gruber and A.S. Nejad, "Development of a Large-Scale Supersonic Combustion Research Facility," AIAA Paper 94-0544, 1994.
6. M.R. Gruber, A.S. Nejad, T.H. Chen and J. Dutton, "Mixing and Penetration Studies of Sonic Jets in Mach 2 Freestream," AIAA Paper 94-0790, 1994.
7. D.D. Glawe, J.M. Donbar, A.S. Nejad, B. Sekar, M. Samimy and J.F. Driscoll, "Parallel Fuel Injection from the Base of an Extended Strut into Supersonic Flow," AIAA Paper 94-0711, 1994.
8. B.J. McBride, S. HeimeI, J.G. Ehlers and S. Gordon, *Thermodynamic Properties to 6000 °K for 210 Substances Involving the First 18 Elements*, NASA SP-3001, 1963.
9. R.L. Gaffney Jr., J.A. White, S.S. Girimaji, and J.P. Drummond, "Modeling Turbulent/Chemistry Interactions Using Assumed PDF Methods," AIAA Paper 92-3638, 1992.
10. A. Jameson, W. Schmidt and E. Turkel, "Numerical Solution of the Euler Equations by Finite Volume Methods Using Runge-Kutta Time Stepping Schemes," AIAA Paper 81-1259, 1981.
11. P. Roe, "Approximate Riemann Solvers, Parameter Vectors, and Difference Schemes," *J. Comp. Phys.*, vol. 43, pp. 357-372, 1981.
12. A. Jameson and T.J. Baker, "Solution of the Euler Equations for complex Configurations," AIAA Paper 83-1929, 1983.
13. G.O. Robert, "Computational Meshes for Boundary Layer Problems," *Proc. 2nd ICNMF*, lecture Notes in Physics, vol 8, Springer-Verlag, N.Y. 1971, pp. 171-177.
14. S.A. Anderson, J.C. Tannehill and R.H. Pletcher, *Computational Fluid Mechanics and Heat Transfer*, Hemisphere Publishing Co., New York, 1984, pp. 249-251.

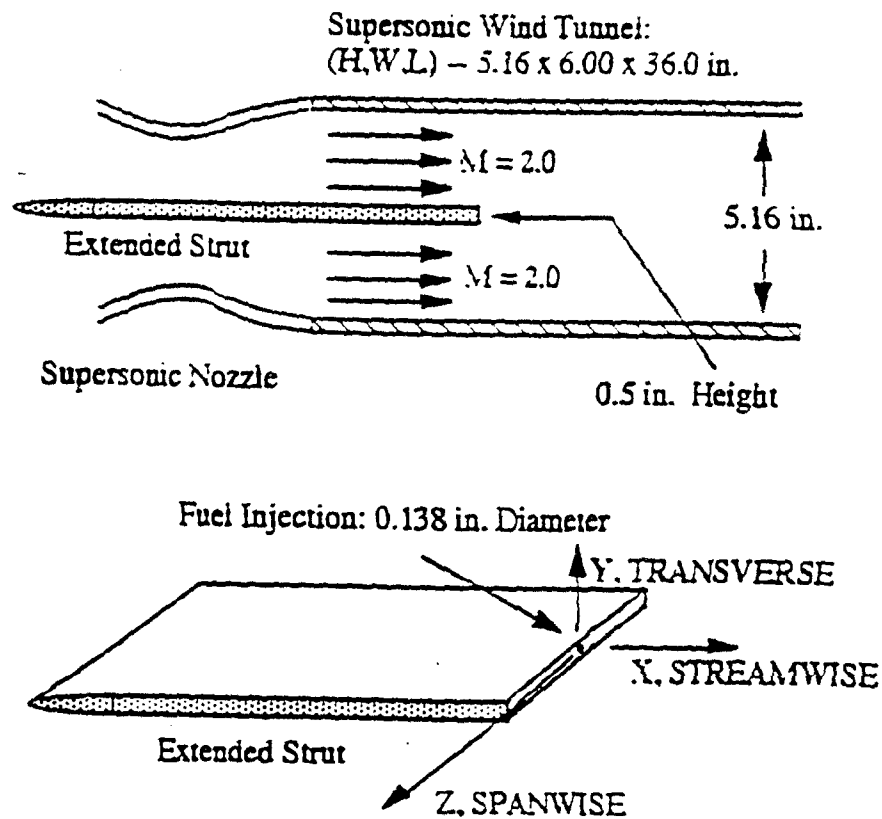


Fig. 1 Geometric layout of the supersonic parallel fuel injection tunnel.

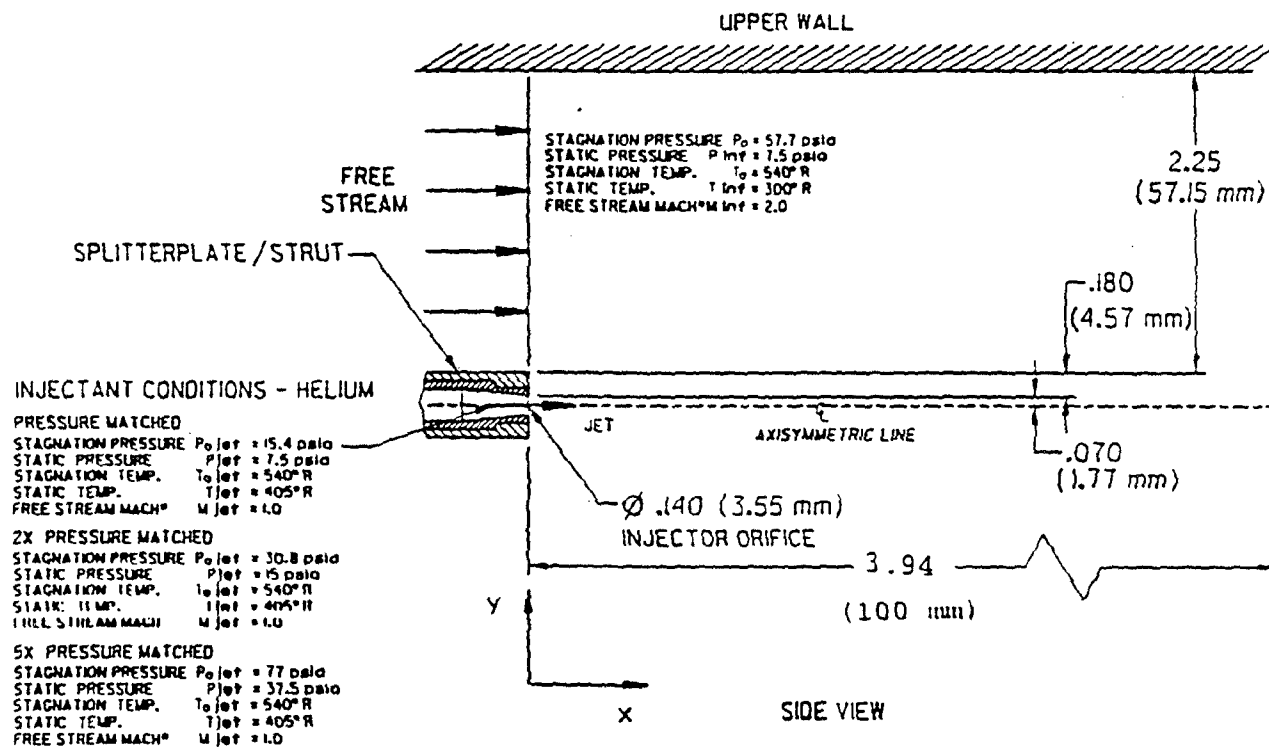
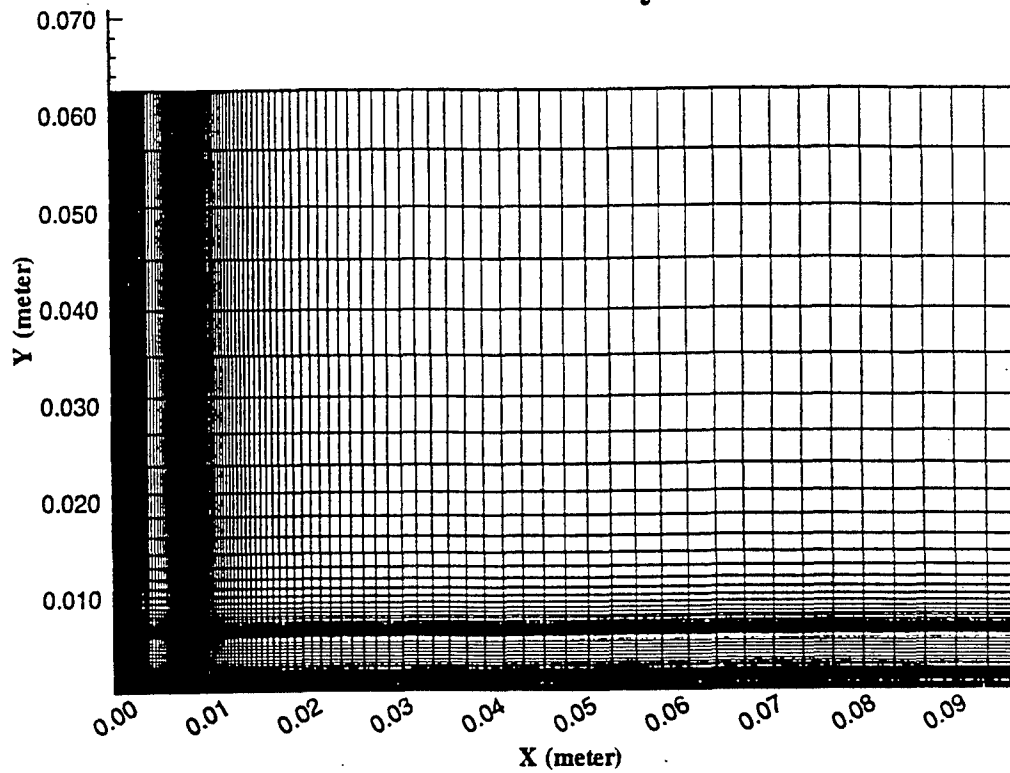


Fig. 2 Schematic representation of computational domain and operating conditions for sonic Helium injection into supersonic airstream.

## 151x101 Grid System



## Close-Up View of 151x101 Grid Systems

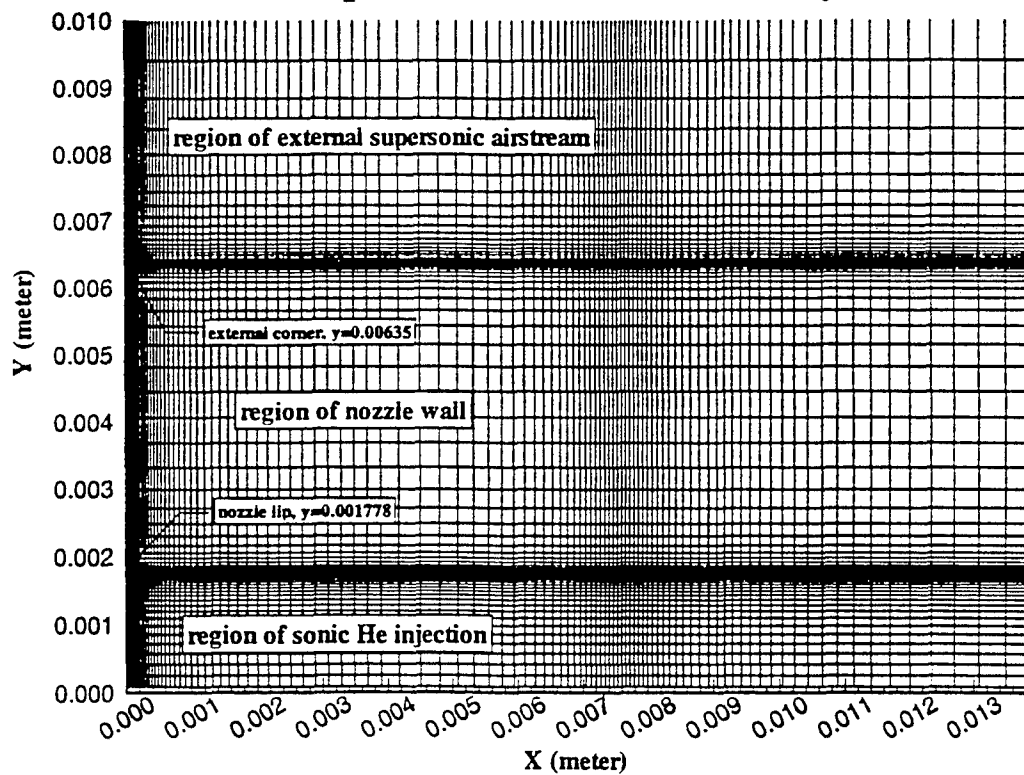


Fig. 3 151x101 grid system, (a) global view, (b) closed-up view.

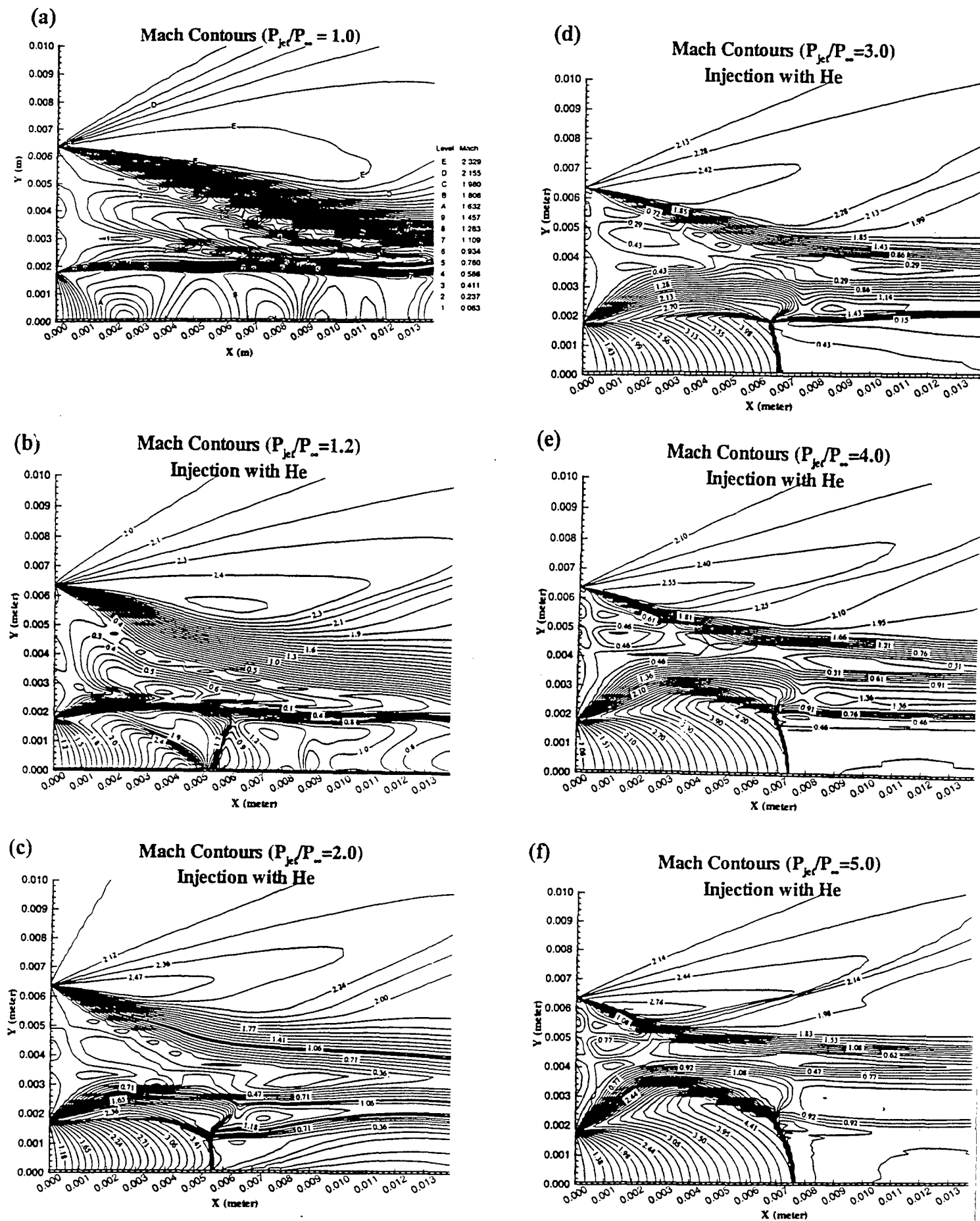
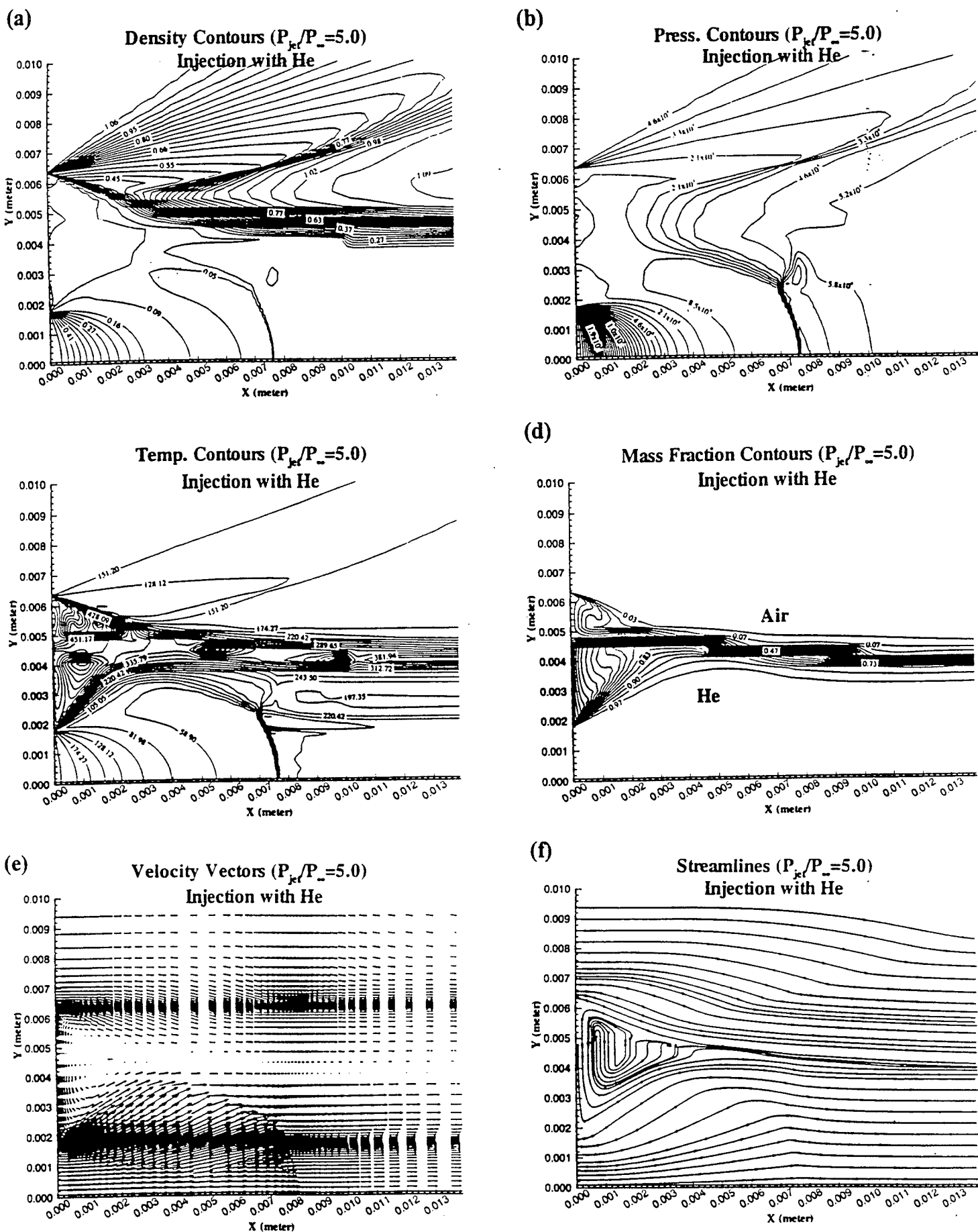


Fig. 4 Mach contours for sonic helium injection with (a)  $P_{jet}/P_{\infty} = 1.0$ , (b)  $P_{jet}/P_{\infty} = 1.2$ , (c)  $P_{jet}/P_{\infty} = 2.0$ , (d)  $P_{jet}/P_{\infty} = 3.0$ , (e)  $P_{jet}/P_{\infty} = 4.0$ , and (f)  $P_{jet}/P_{\infty} = 5.0$ .



**Fig. 5** Flowfields for sonic helium injection with the  $P_{jet}/P_{\infty} = 5.0$ , (a) density contours, (b) pressure contours, (c) temperature contours, (d) mass fraction contours, (e) velocity vectors and (f) streamlines.

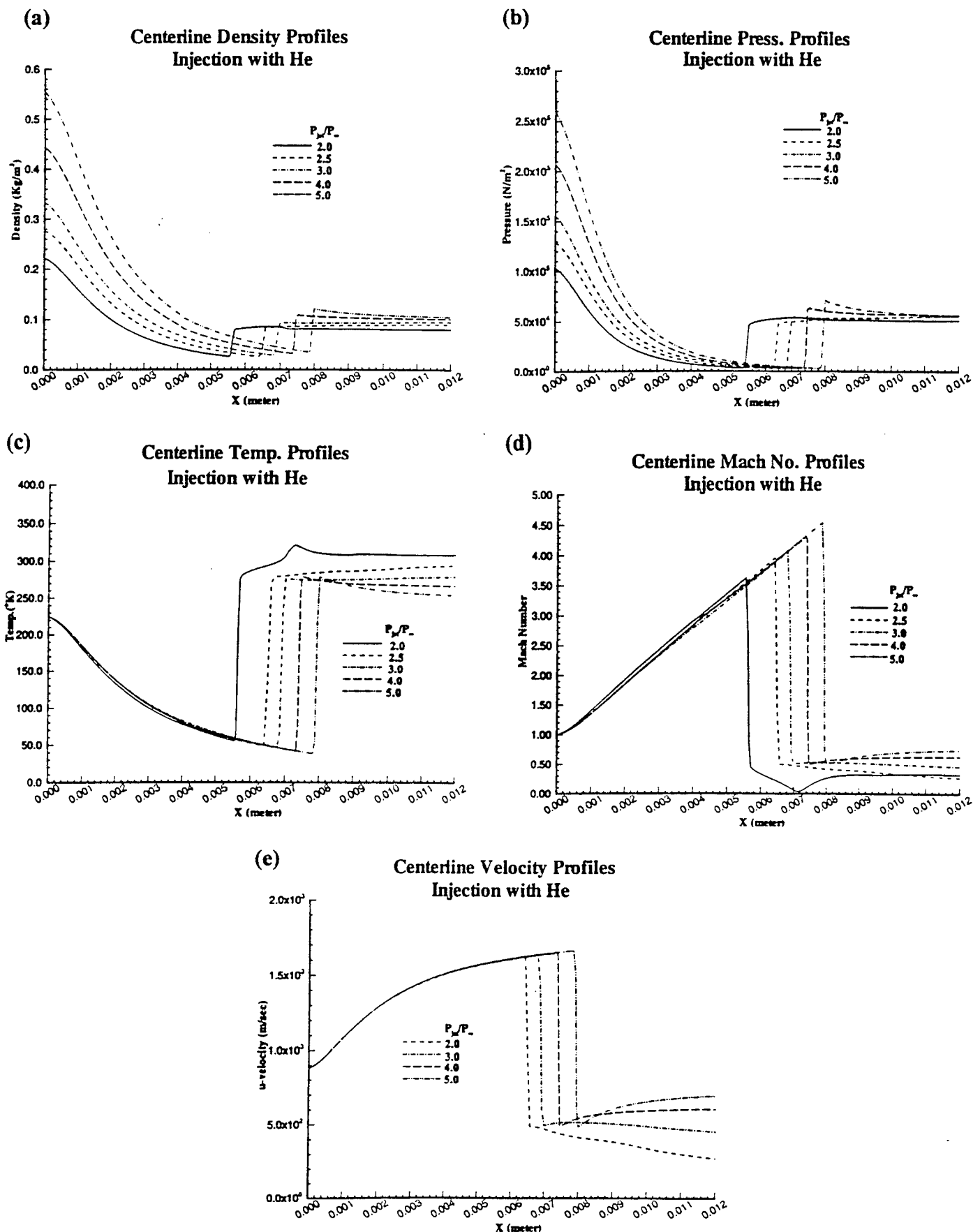


Fig. 6 Centerline profiles for sonic helium injection, (a) density, (b) pressure, (c) temperature, (d) Mach number, and (e) axial velocity.



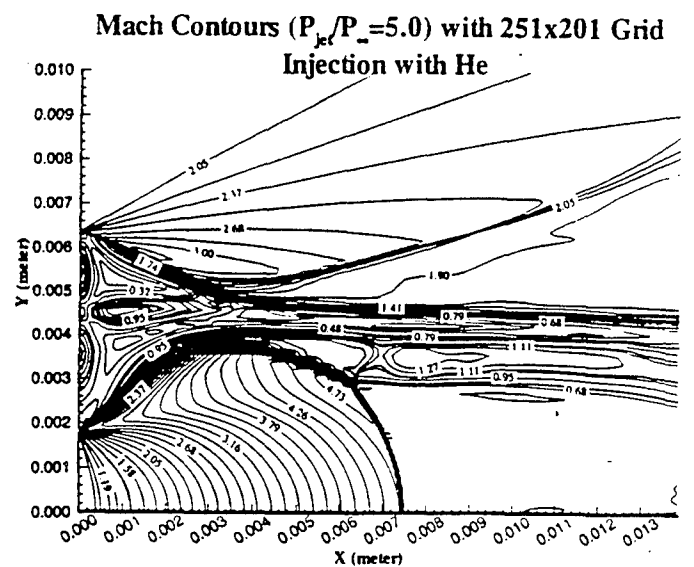
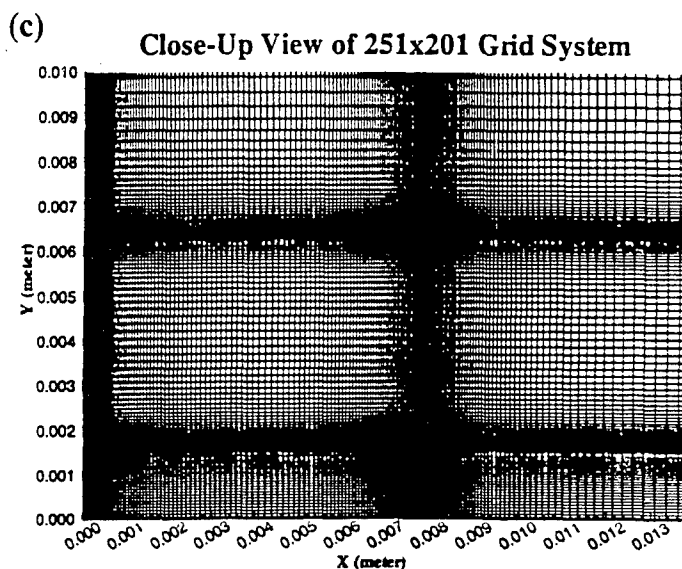
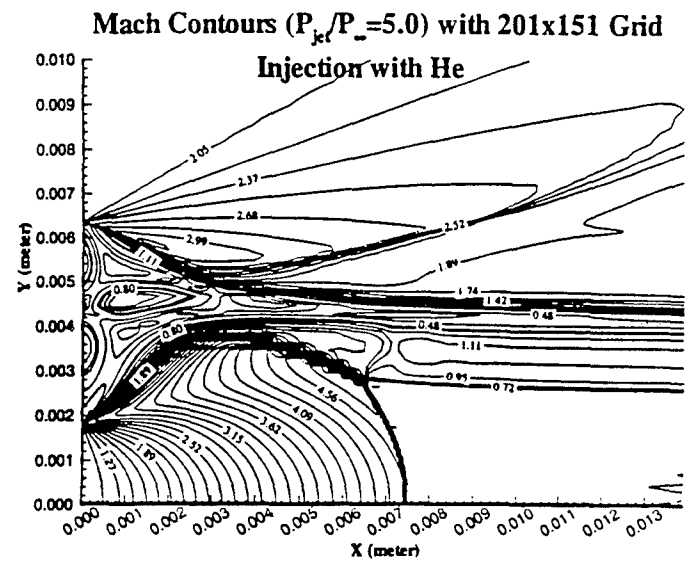
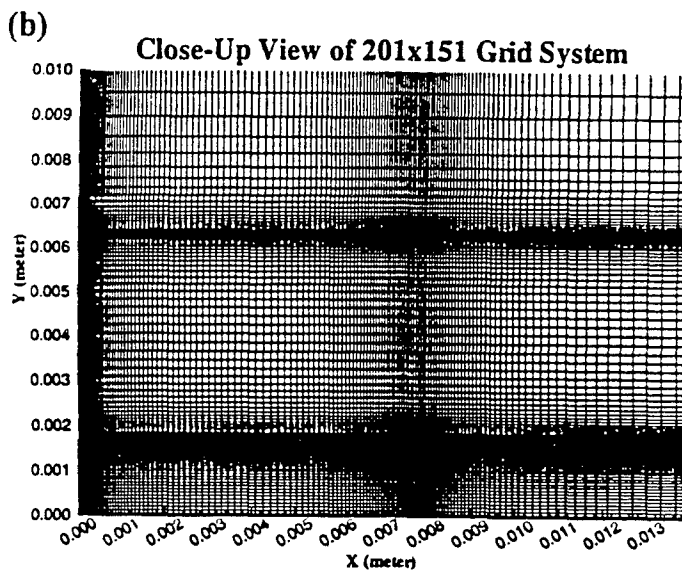
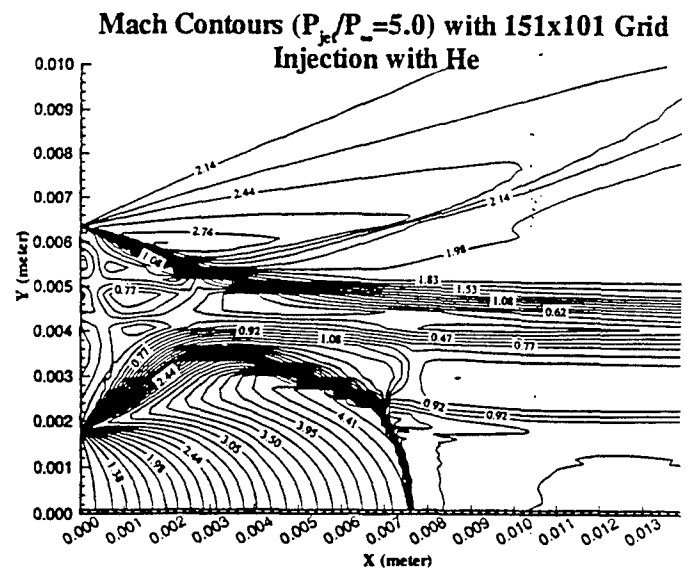
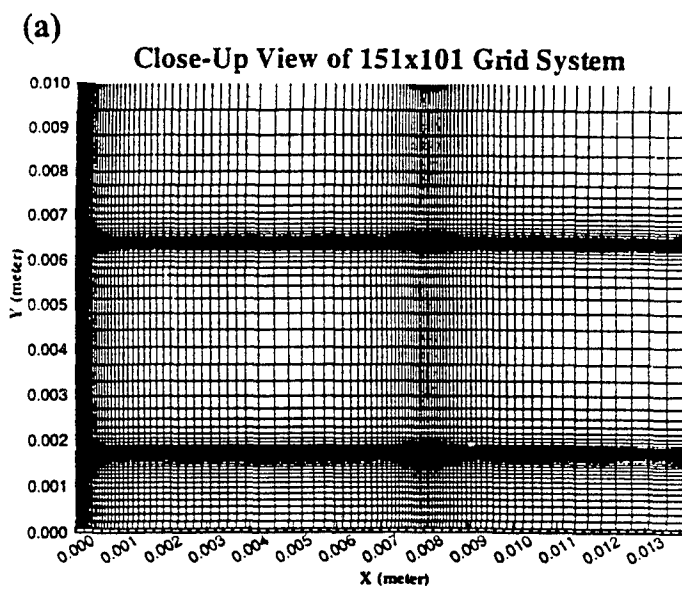


Fig. 7 Grid systems and Mach contours for sonic helium injection with the  $P_{jet}/P_{\infty} = 5.0$  case. (a) 151x101 grid, (b) 201x151 grid, and (c) 251x201 grid.

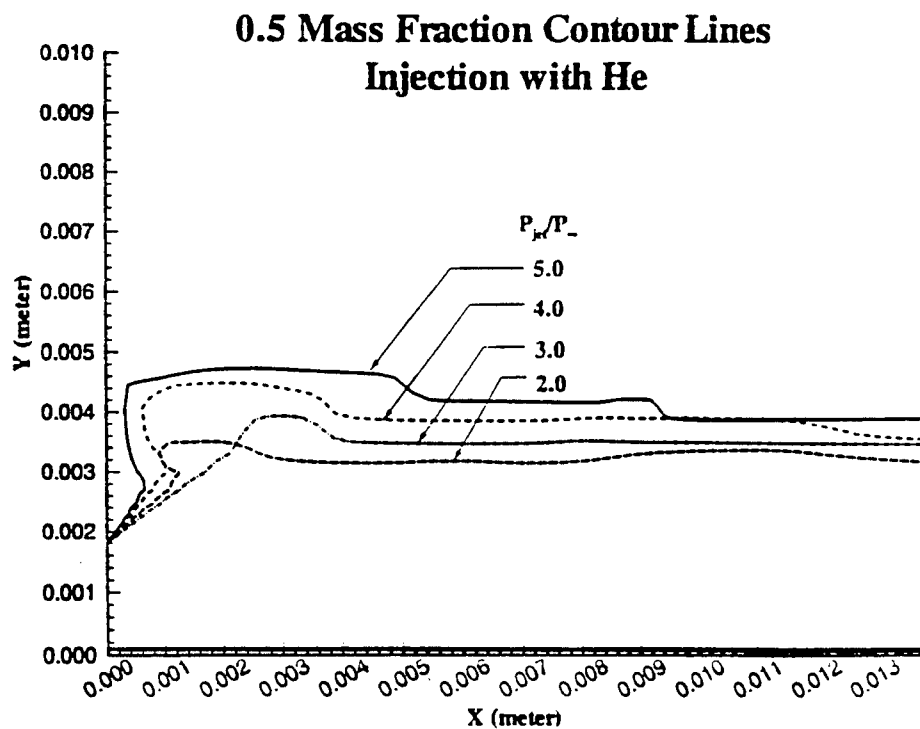


Fig. 8 0.5 mass fraction contour lines for sonic helium injection with the  $P_{jet}/P_{\infty} = 2.0$  and 5.0

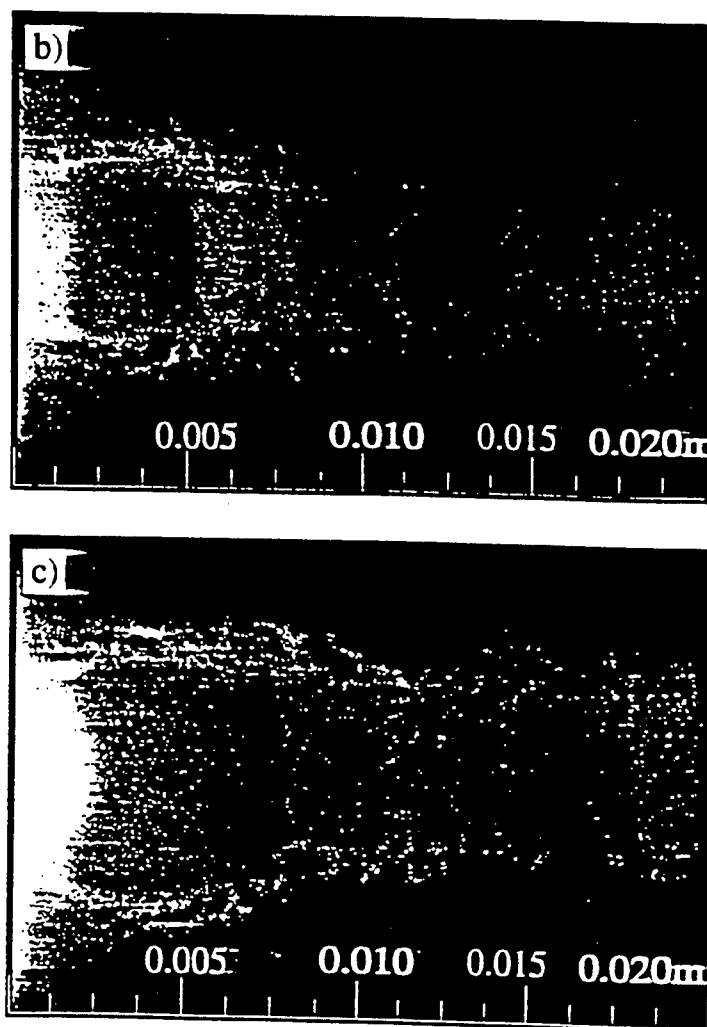


fig. 9 Schlieren photographs of sonic helium injection into a Mach 2 airstream with  
(a)  $P_{jet}/P_{\infty} = 2.0$  and (b)  $P_{jet}/P_{\infty} = 5.0$  case.

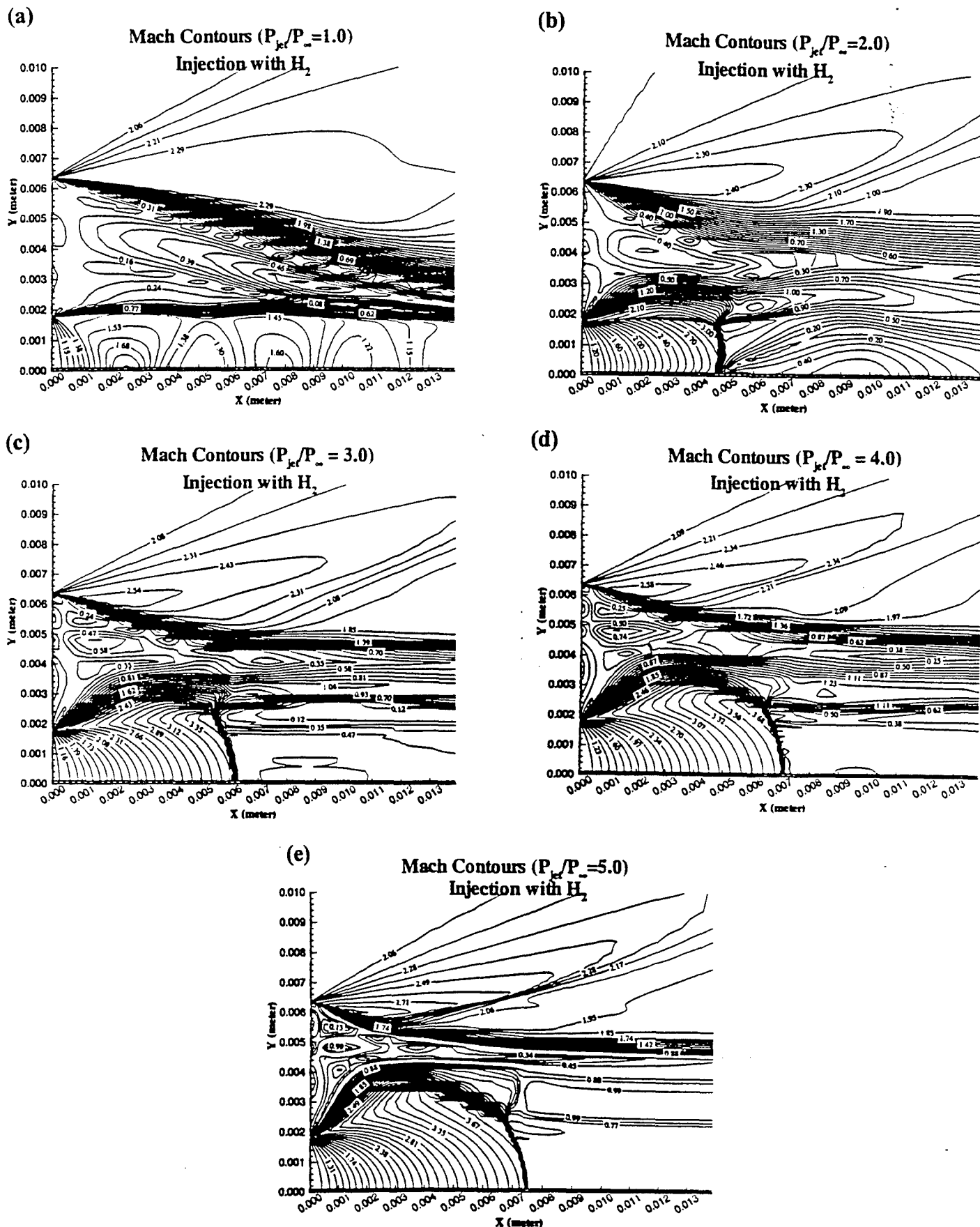


Fig. 10 Mach contours for sonic hydrogen injection with (a)  $P_{jet}/P_{\infty}=1.0$ , (b)  $P_{jet}/P_{\infty}=2.0$ , (c)  $P_{jet}/P_{\infty}=3.0$ , (d)  $P_{jet}/P_{\infty}=4.0$ , (e)  $P_{jet}/P_{\infty}=5.0$ .

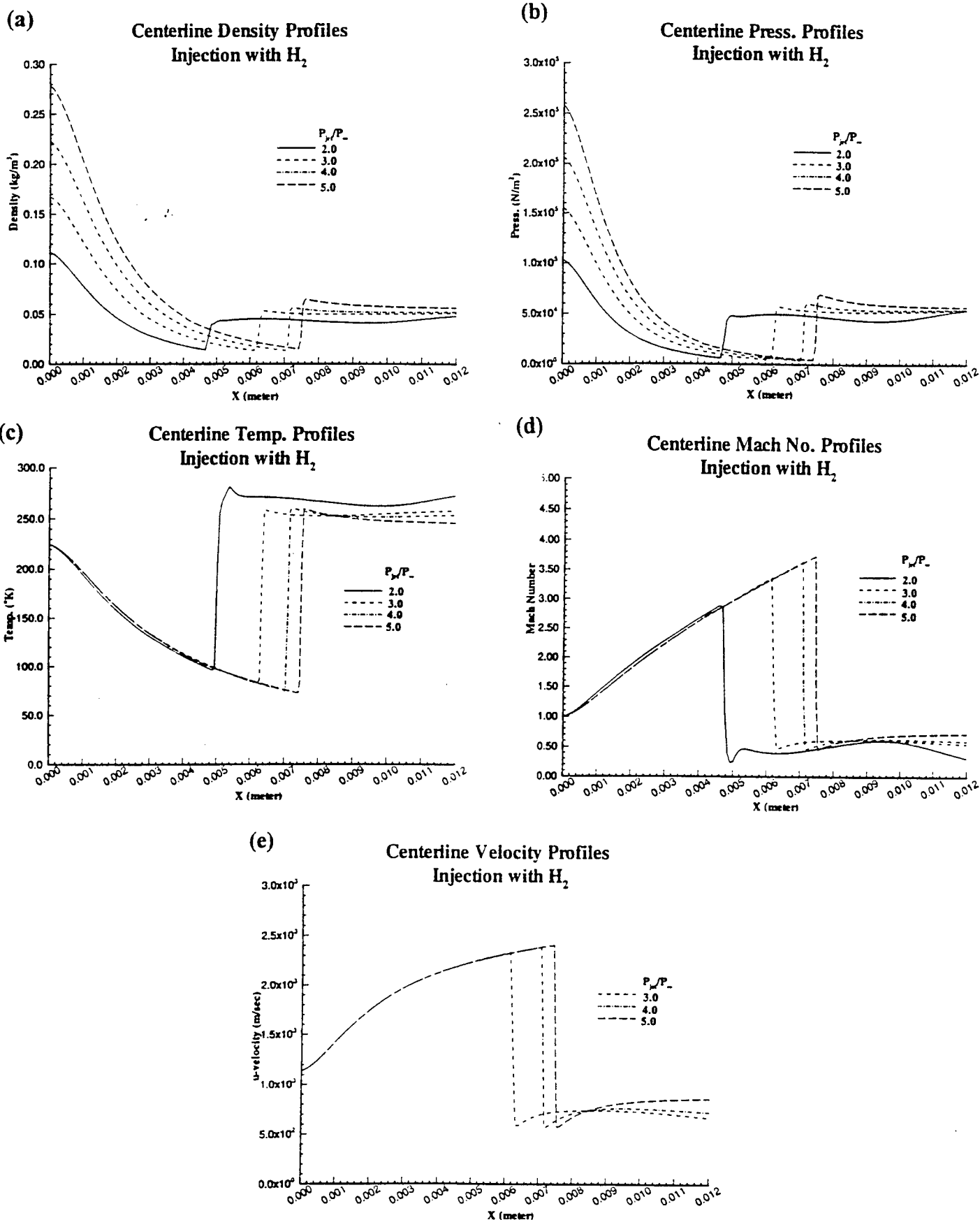


Fig. 11 Centerline profiles for sonic hydrogen injection, (a) density, (b) pressure, (c) temperature, (d) Mach number, (e) axial velocity.

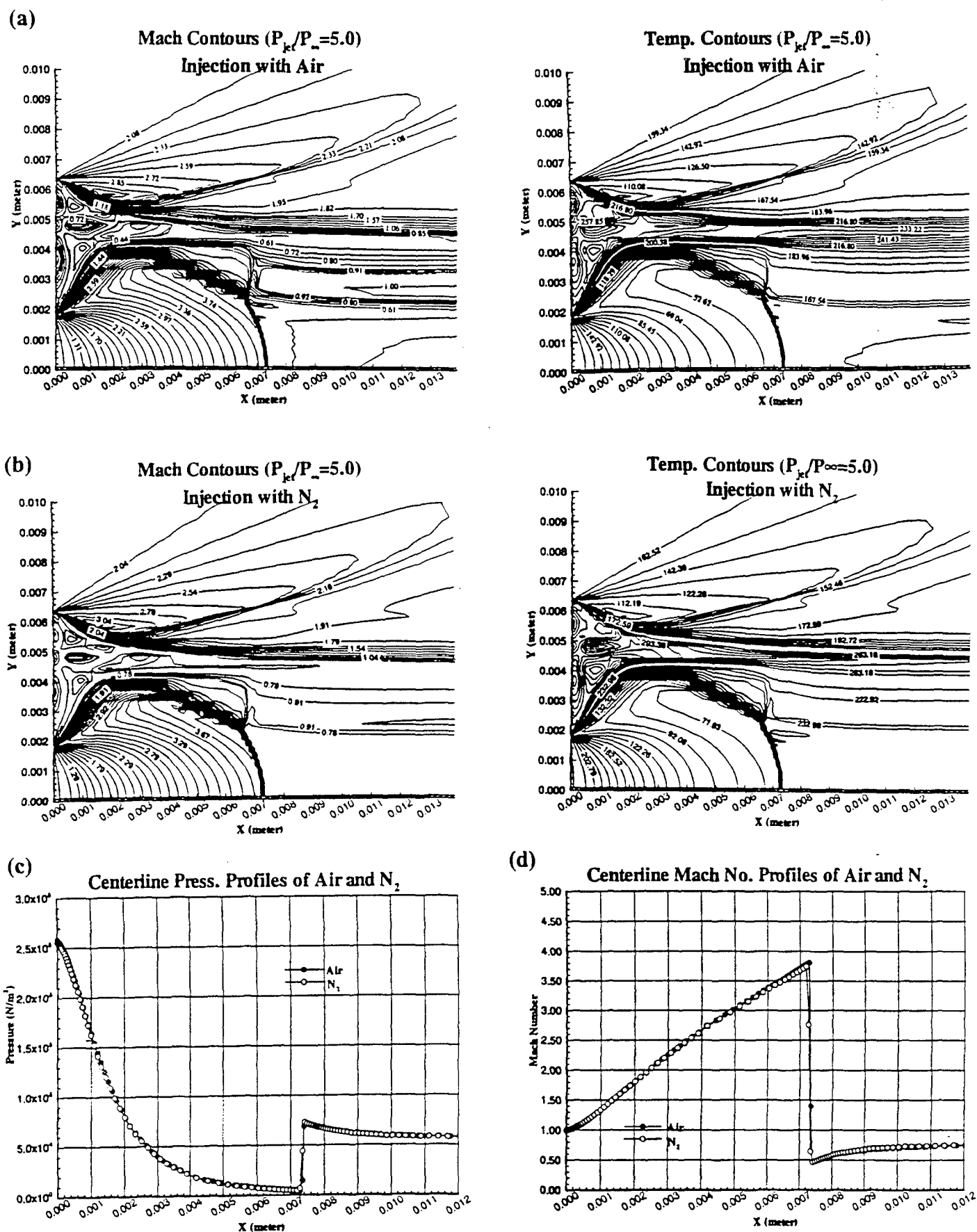


Table 1. The Operating Conditions for Sonic Helium Injection into a Mach 2 Airstream.

	$P_0$	$T_0$	Mach #	$P_\infty$	$T_\infty$	$\rho_\infty$	$u_\infty$
	Pa	K		Pa	K	kg/m <sup>3</sup>	m/s
air	295,442	300	2.0	37,758	167	0.7894	518
He case 1	92,755	339	1.0	45,181	254	0.8556	939
He case 2	164,898	339	1.0	80,322	254	0.1521	939
He case 5	398,503	339	1.0	194,111	254	0.3676	939

Table 2. Thermal Properties of Gases.

Gas	Density (kg/m <sup>3</sup> )	Molecular Weight	Gas Constant	Specific Heat Ratio
Helium	0.1640	4.000	2077.20	1.667
Hydrogen	0.0826	2.020	4126.00	1.406
Air	1.1900	28.960	287.03	1.402
Nitrogen	1.1650	28.013	296.80	1.401

Table 3. Computed Locations and Sizes of Mach Disks for Helium Case (D: nozzle diameter, 0.0035 m).

$P_{jet}/P_\infty$	Locations of the Mach Disk		Size of the Mach disk	
	(meter)	(L/D)	(meter)	(S/D)
5.0	0.0076	2.17	0.00239	0.68
4.0	0.0074	2.11	0.00218	0.62
3.0	0.0069	1.97	0.00186	0.53
2.5	0.0063	1.80	0.00138	0.39
2.0	0.0057	1.63	0.00112	0.32

Table 4. Computed and Experimental Mach Disk Locations for Helium case.

$P_{jet}/P_\infty$	Experimental Results	Numerical Results	Difference %
2.0	0.0053	0.0056	5.6
5.0	0.0075	0.0076	1.3

Table 5. Computed Locations and Sizes of Mach Disks for Hydrogen Case (D: nozzle diameter, 0.0035m).

$P_{jet}/P_\infty$	Locations of the Mach Disk		Size of the Mach disk	
	(meter)	(L/D)	(meter)	(S/D)
5.0	0.0075	2.14	0.00247	0.71
4.0	0.0071	2.03	0.00232	0.66
3.0	0.0062	1.77	0.00230	0.65
2.0	0.0047	1.34	0.00172	0.49



**AIAA 95-2551**

**Raman Scattering Study of Ethylene  
Under Varying Pressure**

**S. Dasgupta, R. Vuppuladhadiam, P.-K.  
Wu, T.H. Chen**

**Taitech, Inc.**

**Beavercreek, OH,**

**C. Carter**

**Systems Research Laboratories**

**Dayton, OH**

**and**

**A.S. Nejad**

**Advanced Propulsion Division**

**WPAFB, OH**

**31st AIAA/ASME/SAE/ASEE  
Joint Propulsion Conference and Exhibit  
July 10-12, 1995/San Diego, CA**

For permission to copy or republish, contact the American Institute of Aeronautics and Astronautics  
370 L'Enfant Promenade, S.W., Washington, D.C. 20024

# RAMAN SCATTERING STUDY OF ETHYLENE UNDER VARYING PRESSURE

S. Dasgupta,\* R. Vuppuladhadiam\*, P.-K. Wu,\* T.H. Chen,\* C. Carter\*\*, and A.S. Nejad\*\*\*

\* Taitech, Inc., 3675 Harmeling Drive, Dayton, Ohio 45440

\*\* System Research Laboratories, 2800 Indian Ripple Road, Dayton, Ohio 45440-3696

\*\*\* Advanced Propulsion Division

Wright Laboratory

Wright-Patterson Air Force Base, Ohio 45433

## ABSTRACT

Raman scattering studies of ethylene under varying pressure conditions have been performed. Experiments were performed using a pressure cell which allowed varying pressure and gaseous species concentrations. The experiments were performed to establish the behavior of ethylene in the sub-critical region to form a data base for future studies near the super critical state. Raman scattering will provide information on species concentration and its variation with pressure. The initial results obtained to date have showed that the vibrational Raman modes of ethylene at  $1342\text{ cm}^{-1}$ ,  $1623\text{ cm}^{-1}$  and  $3020\text{ cm}^{-1}$  all showed the characteristic increase in Raman signal intensity as a function of pressure indicating the feasibility of performing Raman imaging of ethylene fuel injection under supercritical conditions. Preliminary data of mixing was also obtained by injecting ethylene into a nitrogen atmosphere, which were consistent with expected behavior although time resolved measurements are required to get more detailed information. Some preliminary Raman images were taken which showed qualitative agreement with the Raman spectral data.

## INTRODUCTION

Fuel sprays and their behavior under various pressure and temperature conditions often dictate the nature of the ensuing combustion process. The quality of atomization and subsequent development of the size and velocity distributions of liquid fuel within the combustion chamber have a significant effect on the performance of the

combustion system. Factors such as ignition, flame stability, combustion efficiency, combustor durability, and pollutant emissions can be connected to fuel spray characteristics and fuel-air mixing. Furthermore, fuel under super-critical conditions have added complex characteristics which play an important role in the combustion process. The thermodynamic characteristics of fuel at or near super critical conditions are also not well understood. The goal of the overall research project is to study the mixing process of supercritical fuel with the surrounding gas.

Ethylene and nitrogen will be used as the fuel and the gas components in this research study. Spontaneous planar Raman scattering was used to detect changes in species concentrations as a function of pressure. This data provides the initial basis for further studies of the mixing process for ethylene injection in the super-critical regime and the comparison of concentration variations as a function of the fuel mixing ratio near supercritical conditions.

## OVERVIEW

Cooling of airframe under hypersonic flight conditions is an engineering challenge. The use of endothermic fuels have been proposed for regenerative cooling of the airframe components. This approach increases the fuel temperature and pressure and the fuel is found to be in the supercritical state prior to injection [1]. In order to better understand the supercritical fuel mixing properties, initial studies of species concentration as a function of pressure will be carried out with the pressure approaching the supercritical limit.



For supercritical fluids, thermodynamic and transport properties exhibit unusual behavior near the supercritical point, e.g. zero surface tension, liquid like density, gas like diffusivities, etc. [1,2,3]. Near the critical point, the gradient of fluid density with respect to temperature and pressure is very large. These properties affect the atomization and the mixing process of the fuel. Chen [4] recently studied the atomization processes of supercritical SF<sub>6</sub> injected into quiescent gases and found the supercritical fluid exhibited an opaque core which persisted for a long distance before disappearing as a result of mixing and/or phase change. However, core lengths observed were much smaller than those produced by sub critical liquids injected under the same test conditions. Hermanson et al. [5] studied the supercritical (cryogenic) nitrogen injection into supersonic flow streams and attributed a reduction in penetration height, when compared to sub critical ethanol injection, to a larger degree of superheat. These studies indicate that the atomization and mixing processes of supercritical fluids are very different from those observed under sub critical conditions. Nevertheless, the results obtained from studying the mixing properties of fluids in sub critical conditions will be used as a frame of reference for further study on supercritical fluid injection processes.

### EXPERIMENTAL APPROACH

Raman scattering was used to perform studies on species concentration as a function of pressure. The initial studies were carried out with fluids in the sub critical regime in order to better understand the mixing behavior near the supercritical regime and to validate the experimental setup utilized in these experiments. A schematic of the experimental setup is shown in Figure 1. A Nd:YAG laser operating at its frequency doubled output line at 532 nm was used as the excitation source. In the experiments detailed in this paper, only time averaged measurements were performed as a precursor to future time resolved measurements. The Nd:YAG laser was operated at 20 Hz with an average power of 1 Watt. The laser pulse width was around 7 - 9 nsec. The average power of the laser was kept low in order to prevent air breakdown in the scattering volume. A 300 mm focusing lens was used to focus the incident laser light into a pressurized gas cell shown in Figure 2 that was used to perform the concentration

studies as a function of pressure. The pressure test cell provided optical access in three different directions. Quartz windows were utilized for the optical access although all the tests were carried out in the visible wavelength regime. The test cell consisted of one gas inlet line and an outlet line placed in the same vertical plane as the scattering probe volume. The pressure cell has the capability of being pressurized up to 69 MPa which is well above the critical pressure of 51.13 MPa at 283K. Scattered light at an angle of 90 degrees to the incident beam was collected using a 75 mm focusing lens into an ISA-Spex spectrometer in order to observe the behavior of the scattered light. A notch filter centered at the 532 nm laser line was used to filter out most of the Rayleigh scattered light at the entrance of the spectrometer.

The spectrometer used was a 0.46 m imaging system which was used with a grating which had 1200 grooves/mm and blazed at 500 nm. A CCD camera was used to detect the scattered light. The detector consisted of 578 x 385 pixels with each pixel size being 22 microns in width and 27 microns in height. The detector was cooled with liquid nitrogen to increase its signal to noise capability. The operation of the spectrometer and the detector were controlled using a Pentium computer system. The pressure in the test chamber was monitored throughout the experiment using a pressure gauge. The accuracy of the pressure gauge was  $\pm 0.5$  psi. A thermocouple was also used to monitor the temperature in the cell during the experiments in order to ensure that localized warming was not taking place due to the laser beam.

Some preliminary Raman images were also taken using a Princeton intensified CCD camera and an interference filter designed for the 3020 cm<sup>-1</sup> ethylene Raman line. The images were taken with an exposure time of 0.2 sec. The pressure inside the test cell was varied during the imaging process. Time resolved Raman imaging analysis will next be performed to better understand the mixing process during ethylene fuel injection. A description of the results obtained in these initial experiments is now presented.

### RESULTS AND DISCUSSION

The overall setup was initially tested to determine proper operation of the experiment.

The first tests of the experiment were performed with nitrogen gas in the test cell only. The  $2331\text{ cm}^{-1}$  ( $607\text{ nm}$ ) line of nitrogen was detected with the pressure in the test cell being fixed at atmospheric pressure, i.e.  $0.1\text{ MPa}$ . Once the nitrogen line was detected, the pressure in the cell was increased up to  $0.772\text{ MPa}$  in order to observe the changes on the Raman signal intensity. Figure 3 shows a plot of the  $2331\text{ cm}^{-1}$  mode of nitrogen taken as a function of the pressure in the test cell. The Raman signal was collected over a 10 second duration, i.e. 200 laser shots from the  $20\text{ Hz}$  laser with an average power of  $1\text{ Watt}$ . In these experiments shot to shot variation in signal intensity was not monitored, so only qualitative assessment of the behavior of the signal can be made. The data shows a definite increase in Raman signal intensity as a function of increased pressure in the test cell as expected. The sample volume was approximately  $1\text{ cu mm}$ . The Raman signal intensity is considerably lower in the  $0.1\text{ MPa}$  case. This is attributed to the design of the test cell which has the inlet and outlet for the gas flow situated directly in line with the optical measurement volume.

Following this initial verification, ethylene was introduced into the test cell (following a nitrogen purge) and the spectrometer scanned and the  $1342\text{ cm}^{-1}$  ( $573\text{ nm}$ ),  $1623\text{ cm}^{-1}$  ( $582\text{ nm}$ ) and the  $3020\text{ cm}^{-1}$  ( $633\text{ nm}$ ) vibrational Raman modes of ethylene were detected. Figure 4 a, and b are plots of the  $573\text{ nm}$  and the  $633\text{ nm}$  peaks taken as a function of increasing ambient pressure. As is clearly evident from the figures the Raman signal intensity increases with increasing pressure, i.e. increasing number density of the gaseous species. The signal at  $0.1\text{ MPa}$  is considerably weaker compared to the signals at higher pressures. This is consistent with the observation with nitrogen also and is attributed to the presence of a constant gas flow in the optical measurement volume. Careful observation of the signal in Figure 4a ( $573\text{ nm}$  line) shows that there is a definite increase in the baseline counts at the higher pressure readings. This is due to the increase in Rayleigh scattering intensity at higher pressure levels. This effect is not visible in the  $633\text{ nm}$  spectra due to its separation from the incident laser light wavelength. The data showed qualitative agreement with the expected results, i.e. increase in Raman signal with increase in cell pressure, but due to the averaged measurements performed actual calculations of number density were not

done. In future experiments, single shot measurements will be performed in order to accurately predict number densities. The scattering cross section for the  $633\text{ nm}$  ( $3020\text{ cm}^{-1}$ ) line was considerably better than the  $573$  ( $1342\text{ cm}^{-1}$ ) line. Due to the better scattering cross section at the  $633\text{ nm}$  line, future studies of ethylene with pressures approaching the super critical regime will be concentrated at this band. The full width at half maximum (FWHM) were plotted for the ethylene spectra as a function of increasing pressure. Figure 5 depicts a plot of the FWHM of the two lines as a function of pressure. The plot shows that the experimental uncertainty of the measurements were in the acceptable range and that there were no significant temperature rise during the measurements..

The next set of experiments that were attempted involved the injection of ethylene into a nitrogen environment and then re-injecting nitrogen back to study the effect of mixing. Due to the limitations of the experimental setup, qualitative variations in the data were studied. Figure 6 shows a plot of the nitrogen line and the ethylene line under mixed conditions. The test chamber was initially pressurized with nitrogen up to  $0.2\text{ MPa}$ . Ethylene was then injected in steps so that the total pressure was near  $0.47\text{ MPa}$ ; and then nitrogen was re-injected up to a total pressure of  $0.6\text{ MPa}$ . As seen from the plot, the relative cross sections for the two interactions are different and the ethylene Raman line demonstrates larger changes with small changes in pressure. The drop in the ethylene signal at the high end of the pressure scale is attributed to local changes in species concentration during the measurement process.

Following these preliminary spectral studies, Raman imaging was attempted. An interference filter designed for the  $633\text{ nm}$  ( $3020\text{ cm}^{-1}$ ) line was used along with a Princeton instruments intensified camera. The  $20\text{ Hz}$  Nd:YAG laser was once again used to excite the Raman process in ethylene. Images were taken at varying pressures with an exposure time of  $0.2\text{ sec}$ . Figure 7 shows Raman images of ethylene for pressure readings of  $0.15\text{ MPa}$  and  $0.46\text{ MPa}$ . The increase in signal intensity with increase in pressure is evident from these images.

The results presented in this paper were a precursor to performing 2D planer Raman scattering studies of ethylene fuel injection near

super critical conditions. Time resolved measurements are the next step to the initial experiments presented here. The experimental setup required to perform the fuel injection studies under high pressure are currently operational in the research facilities [6]. Time resolved measurements will involve the usage of a fully automated pressure chamber and fuel injection system which will significantly improve the quantification process. The general conclusion from the above results is that planar Raman scattering can be used as a tool for studying fuel injection and mixing. Overall feasibility of the desired goal has been established with the set of experimental results presented here.

## CONCLUSIONS

In conclusion, the ability to use Raman scattering to detect changes in number densities of species as a function of pressure was demonstrated. The preliminary experiments performed demonstrated that the signal levels available were reasonable so that 2D planar imaging is feasible. The signal level variation was also in accordance with the expected signal levels showing that the experimental setup is very sensitive to the Raman signal. It is expected that with further increase in pressure in future experiments, Rayleigh scattering intensity will go up but not significantly reduce the signal to noise ratio. Preliminary Raman images were also taken and showed the expected variation in signal intensity with pressure. In future experiments time resolved measurements will also be carried out to quantify the mixing and fuel injection process.

## ACKNOWLEDGMENTS

This study is supported by and performed at Wright-Patterson Air Force Base, under contract No. F33615-93-C-2300 and F33615-94-C-2470. The authors wish to acknowledge the great help provided by William Terry in the set up and the execution of the experiments.

## REFERENCES

1. Edwards, T., "USAF Supercritical Hydrocarbon Fuel Interests," AIAA 93-0807, 1993.
2. McHugh, M. and Krokons, V., *Supercritical Fluid Extraction: Principle and Practice*, Butterworths Pub., 1-5, 1993.
3. Holland, P.M., Eaton, B.E., and Hanley, H.J.M., "A Correlation of the Viscosity and Thermal Conductivity Data of Gaseous and Liquid Ethylene," J. of Phys. Chem. Ref. Data, 12, 917-932, 1983.
4. Chen, L.D., "Supercritical Atomization Studies," AFOSR Supercritical Fuels/Combustion Workshop, WPAFB, Ohio, February 1994.
5. Hermanson, T.C., Papas, P., and Kay I.W., "Structure and Penetration of a Traverse Fluid Jet Injected at Supercritical Pressure into Supersonic Flow," AIAA 92-3652, 1992.
6. Wu P.-K., Chen, T.H., Nejad, A.S., and Carter, C., "Injection of Super Critical Ethylene in Nitrogen," AIAA Paper #95-0382, presented in the AIAA Conference in Reno, Nevada, January 1995.

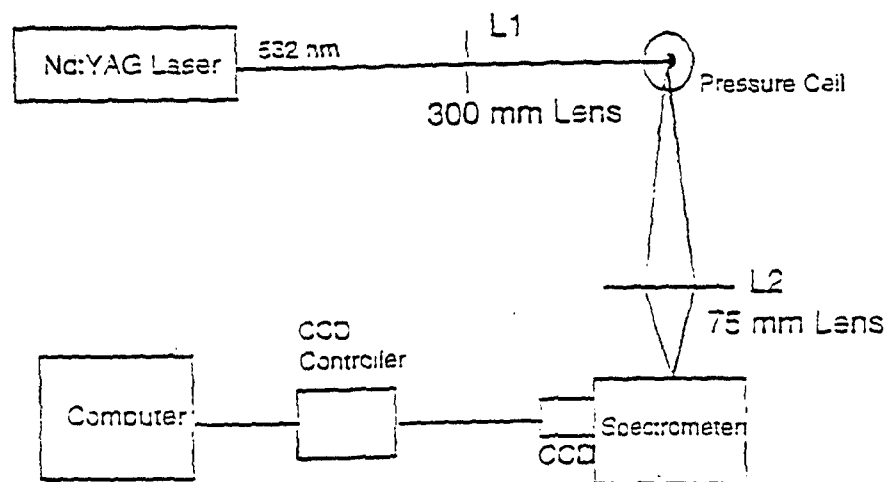


Figure 1. Schematic of Raman Scattering setup.

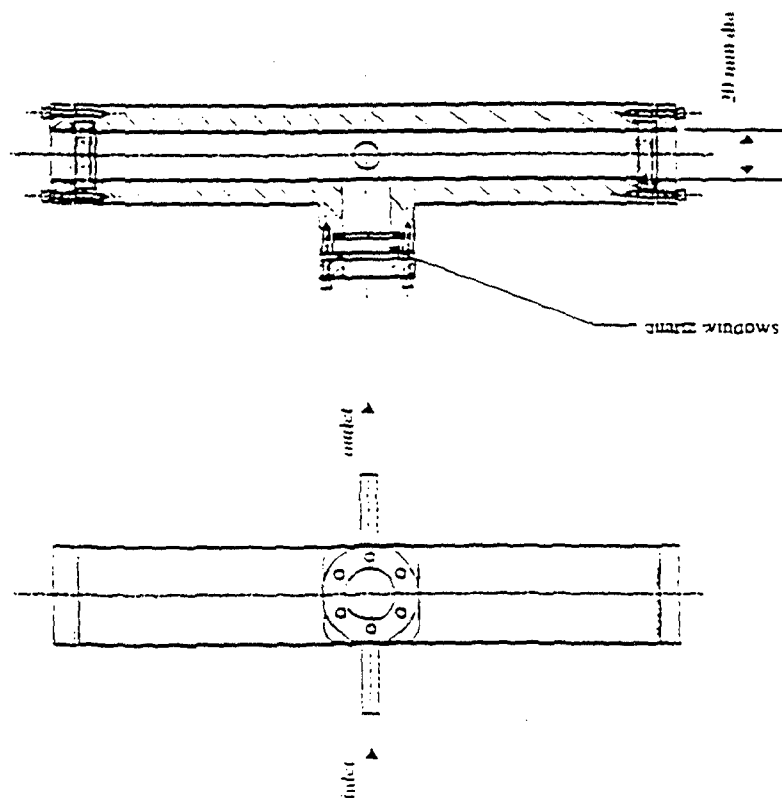


Figure 2. Schematic of Pressure Cell for Raman Studies on ethylene.

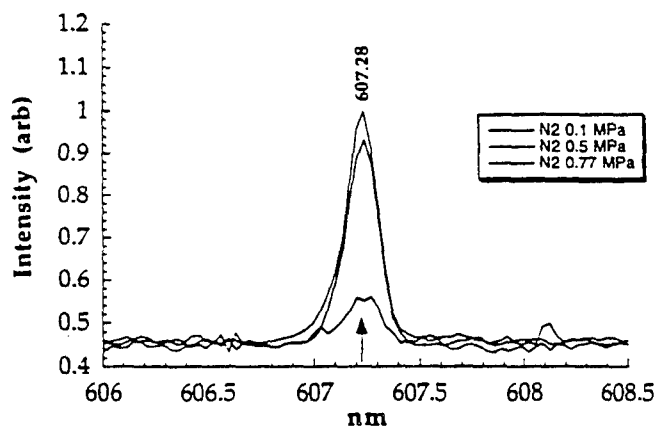


Figure 3. Raman Spectra of Nitrogen taken at different pressures.

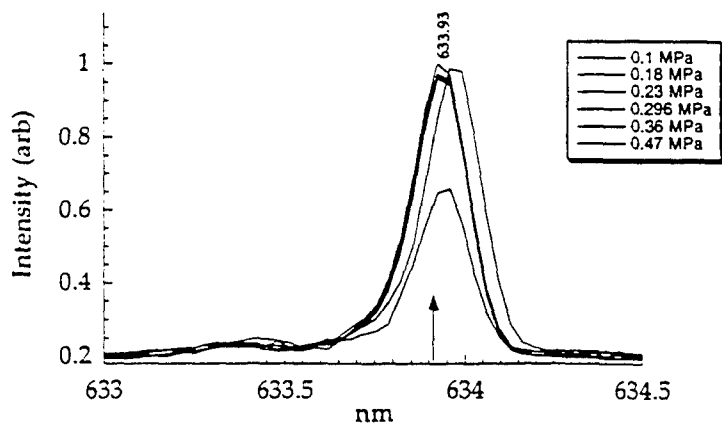
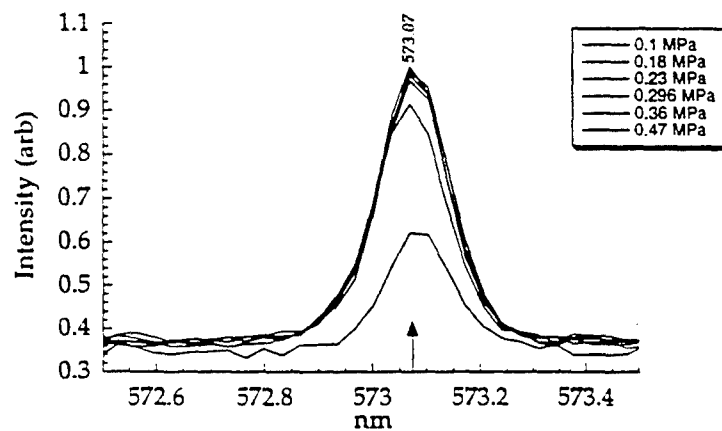


Figure 4a and 4b. Ethylene Raman spectra shown as a function of pressure. The 573 nm and the 633 nm modes are shown.

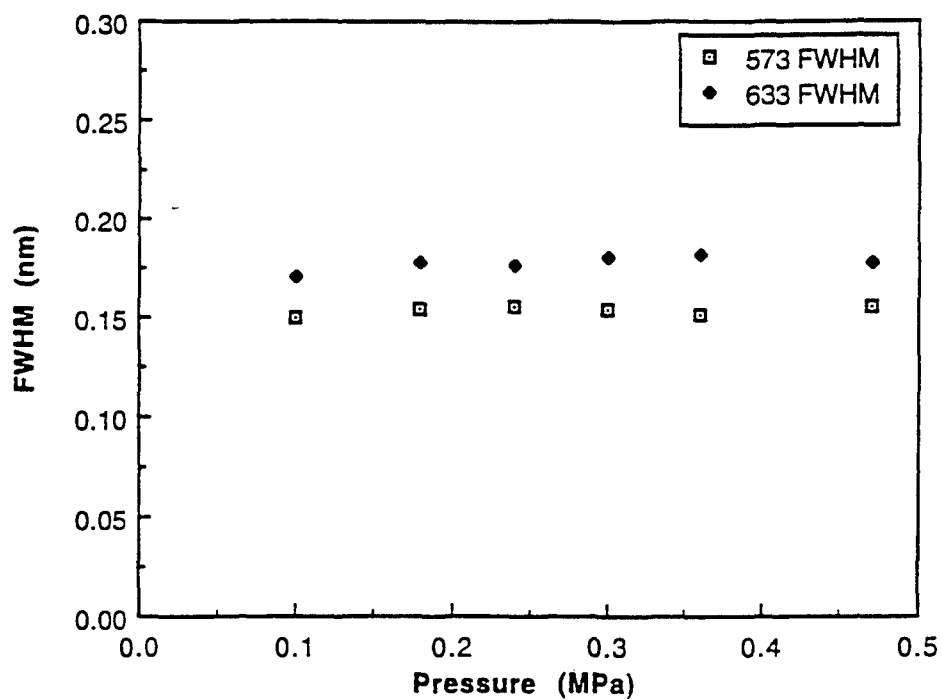


Figure 5. Plot of the Full Width at Half Maximum of the 573 nm and the 633 nm vibrational Raman modes of ethylene as a function of pressure.

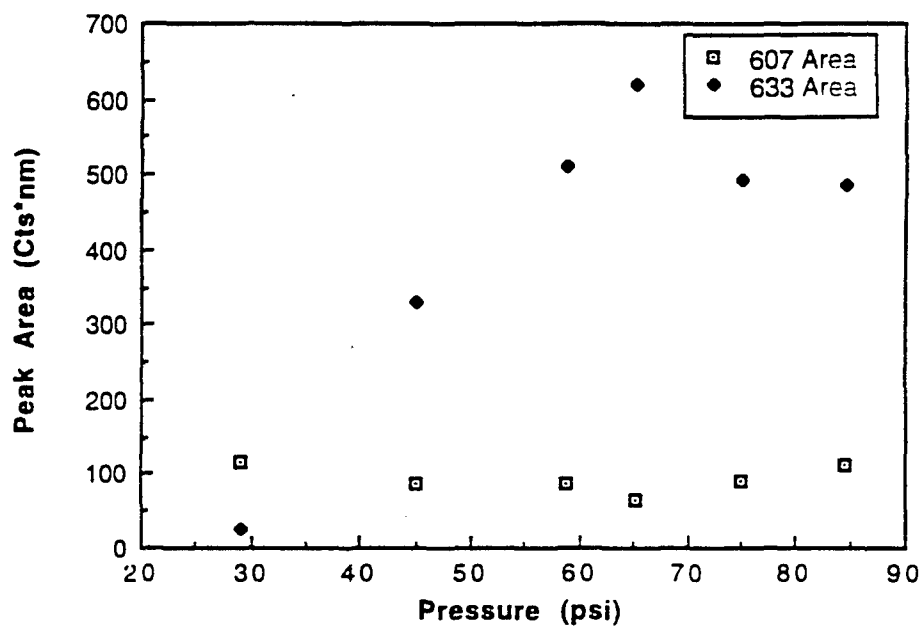


Figure 6. Raman Spectra Depicting Mixing Characteristics between nitrogen and ethylene.



Figure 7. Raman images of ethylene taken at 0.15 MPa pressure and 0.45 MPa pressure.



**AIAA 96-2661**

**Fuel-Vortex Interactions for Enhanced Mixing  
in Supersonic Flow**

R.P. Fuller, P.-K. Wu

Taitech, Inc.

AMC P.O. Box 33830

WPAFB, Ohio 45433

A.S. Nejad

Wright-Laboratory

Aero Propulsion and Power Directorate

WPAFB, Ohio 45433

J.A. Schetz

Virginia Polytechnic Institute and State University

Department of Aerospace and Ocean Engineering

Blacksburg, Virginia 24061

**32nd AIAA/ASME/SAE/ASEE**

**Joint Propulsion Conference**

**July 1-3, 1996 / Lake Buena Vista, FL**

# Fuel-Vortex Interactions for Enhanced Mixing in Supersonic Flow

R.P. Fuller\*, P.-K. Wu\*

Taitech, Inc., Beavercreek, Ohio 45440

A.S. Nejad†

Wright Laboratory, Wright-Patterson Air Force Base, Ohio 45433

and

J.A. Schetz‡

Virginia Polytechnic Institute and State University, Blacksburg, Virginia 24061

An experimental investigation was conducted to compare the supersonic mixing performance between a novel aerodynamic ramp injector and a physical ramp injector. The aerodynamic ramp injector consisted of nine, flush-wall jets arranged to produce fuel-vortex interactions for mixing enhancement in a supersonic crossflow. Test conditions included a Mach 2.0 freestream with a Reynolds number of  $3.63 \times 10^7$  per meter and jet-to-freestream momentum flux ratios of 1.0 and 2.0. Conventional probing techniques including species composition sampling were employed to interrogate the flow field at several downstream locations. Results show that with increasing jet momentum, the aero-ramp exhibited a significant increase in penetration while the physical ramp showed no discernible change. The near-field mixing of the aero-ramp was superior to that of the physical ramp. At the higher jet momentum, the far-field mixing of the aero-ramp was comparable to the physical ramp. In all cases, the total pressure losses suffered with the aero-ramp were less than those incurred with the physical ramp. For both injectors, the total pressure losses decreased with increasing jet momentum. It is concluded that these results merit further studies and parametric optimization of the aero-ramp or similar configurations.

## Nomenclature

$A$	= cross-sectional area
$\alpha_{He}$	= helium mass fraction
$\alpha_{max}$	= maximum helium mass fraction
$\alpha_s$	= $H_2$ -air stoichiometric mass fraction, 0.0292
$\beta$	= decay coefficient
$C_d$	= injector discharge coefficient
$d_{eff}$	= effective jet diameter, $\sqrt{C_d} d_j$
$d_{eq}$	= equivalent jet diameter, $2\sqrt{\sum A_j/\pi}$
$d_j$	= jet diameter
$\gamma$	= ratio of specific heats
$h$	= plume penetration height
$\lambda$	= mass flux ratio, $(\rho u)_j/(\rho u)_\infty$
$M$	= Mach number
$n$	= decay rate of $\alpha_{max}$
$\eta_m$	= mixing efficiency
$p$	= static pressure
$p_c$	= cone-static pressure
$p_t$	= total pressure
$\Pi$	= total pressure loss parameter
$\bar{q}$	= momentum flux ratio, $(\rho u^2)_j/(\rho u^2)_\infty$

$Re$	= Reynolds number
$\rho$	= static density
$T_t$	= total temperature
$u$	= flow speed
$U_s$	= spatial unmixedness
$x$	= streamwise coordinate
$x_{fm}$	= fully-mixed distance
$X_{He}$	= helium mole fraction
$y$	= spanwise coordinate
$z$	= vertical coordinate

## Subscripts

$\infty$	= freestream property
$j$	= jet exit property

## Introduction

The role of supersonic injection and mixing enhancement is vital to the development of a successful hypersonic air-breathing propulsion system. A successful system will be one capable of providing the thrust required to accelerate an aero-space plane or missile from supersonic to hypersonic speeds within the Earth's atmosphere. For flight Mach numbers above 5, the adverse effects associated with decelerating the flow to subsonic speeds for combustion prohibit the use of conventional ramjets.<sup>1</sup> Consequently, the use of supersonic combustion ramjets (scramjets) has been proposed as a necessary alternative. Scramjet combustor velocities can be on the order of several thousand meters per second, resulting in severely restricted fuel resi-

\*Research Scientist, Member AIAA

†Senior Research Scientist, Aero Propulsion & Power Directorate, Member AIAA

‡J. Byron Maupin Professor, Department of Aerospace and Ocean Engineering, Fellow AIAA

Copyright © by Raymond Fuller. Published by the American Institute of Aeronautics and Astronautics, Inc. with permission.



dence times. It is a primary concern in hypersonic aircraft development to limit the engine length and therefore the combustor length to a reasonable size. This requires an effective injection scheme producing enhanced mixing and rapid combustion. A typical scramjet design configuration may include a pilot flame combustor system with hydrogen as the injected fuel. While hydrogen can provide the necessary heat release to produce sufficient thrust levels, its low molecular weight inhibits penetration and rapid dispersion. Injection and mixing augmentation schemes have been developed to effectively inject and disperse the fuel for efficient mixing and combustion. However, there usually exists a trade-off between rapid mixing and total pressure recovery. Hence, the goal here is to develop an injection and mixing augmentation scheme capable of providing rapid mixing, stable combustion and minimal pressure losses.

The subject of transverse injection of a foreign gas into a supersonic crossflow has been studied extensively in the past.<sup>2-6</sup> A comprehensive review of the mixing of transverse jets and wall jets in supersonic flow has been presented by Schetz et al.<sup>7</sup> Mays et al.<sup>8</sup> studied the effects of low angle injection into a supersonic flow. It was shown that as the injection angle decreases the near-field mixing also decreases. However, this decrease in mixing is accompanied by a desirable reduction in pressure losses. In the far field, injection angle was found to have little effect on the overall mixing. Fuller et al.<sup>9</sup> extended this work to include injector yaw as well as low transverse angles. It was observed that while injector yaw did not increase the rate of decay of maximum concentration, it did cause an increase in the overall injectant plume cross section, thus increasing the size of the mixing region. In both studies, it was shown that a matched pressure injection produced greater fuel concentration decay rates when compared to an underexpanded case.

It has been previously postulated and shown that mixing enhancement may be achieved through the addition of three-dimensional vorticity. Based on experiments performed in the subsonic and transonic regimes, Swithenbank et al.<sup>10</sup> proposed that substantial increases in mixing rates might be obtained by introducing a swirling motion to the fuel. It was postulated that the increase in fuel-air mixing rates resulted from the creation of radial and axial pressure gradients in the swirling flow. Povinelli et al.<sup>11</sup> investigated the penetration and spreading of helium injected into the vortex pattern generated by a delta wing in a Mach 2 airstream. Results were compared to a flat-plate injector with the same projected frontal area and angle of attack. It was concluded that the vortex motion generated by the delta wing injector led to substantial increases in the penetration and spreading rates in supersonic flow. In a subsequent study, Hersh et al.<sup>12</sup> obtained similar results for fuel injected into a counter-rotating vortex structure also generated by delta wings. While these studies demonstrated the effects on penetration and spreading, no experimental data confirming accelerated mixing rates due to swirl in a supersonic stream had been produced.

In fact, studies conducted by Povinelli et al.<sup>13</sup> and Schetz et al.<sup>14</sup> concluded that for co-axial jets in supersonic flow, jets with swirl produced no discernible effect on the mixing when compared to non-swirling jets. However, it is suspected that the tangential velocities were too small to create radial and axial pressure gradients sufficient for mixing enhancement. The experimental investigation of Tillman et al.<sup>15</sup> concluded that the axial vortex mechanism previously shown to be responsible for rapid mixing in low-speed, subsonic flows is indeed effective in the supersonic jet environment. Naughton et al.<sup>16</sup> conducted an experimental study of the effect of streamwise vorticity on supersonic turbulent mixing. A Mach 3 streamwise vortex was generated using a strut-mounted swirl injector exhausting into a Mach 3.5 freestream. Results were compared with a baseline, swirl-free jet. It was found that with the addition of streamwise vorticity, increases in mixing rates of up to 34% are possible.

Much interest has recently been given to mechanisms leading to enhanced mixing through the interaction of shock waves with fuel-vortex structures. Marble et al.<sup>17</sup> first proposed the mechanism of shock-induced vorticity generation for supersonic combustion. It was argued that the interaction of a shock wave with a jet of light gas surrounded by an ambient heavy gas would generate vorticity around the perimeter of the jet. This vorticity is caused by the so-called "baroclinic torque" which is essentially a misalignment of the pressure and density gradients at a point in the flow. An excellent review of this process was given by Waitz et al.,<sup>18</sup> and a detailed model has been presented by Yang et al.<sup>19</sup> Marble et al.<sup>20</sup> later showed that this phenomena can indeed lead to a considerable and rapid enhancement of the mixing process. He also concluded that some mechanism for destabilizing the vortex must be incorporated into the injector design to ensure complete mixing of the light gas with air. This agrees with the proposal of Naughton et al.,<sup>16</sup> that a streamwise vortex can enhance supersonic mixing if the vortical flow is passed through a shock wave of sufficient strength to cause vortex breakdown. Metwally et al.<sup>21</sup> showed that a strong shock/vortex interaction leading to vortex breakdown is characterized by unsteady upstream shock propagation, apparent flow recirculation, and the appearance of a recompression shock downstream. It was reasoned that such behavior should lead to increased turbulence levels downstream and therefore enhanced fuel-air mixing.<sup>16</sup>

Numerous investigations<sup>22-27</sup> have looked at wall ramp injectors as a viable means of providing enhanced fuel-air mixing. Ramp designs attempt to make full use of the various mixing enhancement mechanisms previously discussed. The ramp should provide vortex shedding off the edges and a local separation at the base. The fuel is injected through the base and into the counter-rotating vortex pattern. This situation creates a very dynamic mixing distribution. Furthermore, the ramp shock will reflect off the opposite wall and impinge on the plume/vortex structure resulting in possible vortex breakdown and further enhancement of the mixing. The reflected shock should also

create a baroclinic torque where it intersects the plume resulting in additional vorticity. Finally, the recirculation zone occurring due to flow separation at the base of the ramp should provide flameholding similar to a rearward-facing step. The major drawback to this design is its dependency on maintaining pristine geometry in the extremely harsh environment of a high-enthalpy, scramjet combustor. Its physically intrusive nature will necessarily create "hot spots" with temperatures exceeding the thermal limits of most practical materials. Furthermore, the added drag and loss of thrust potential resulting from its intrusive presence may be unacceptable in certain engine design configurations.

The results of the previously described studies form the database of knowledge which was applied in the development of the novel injector design given the term "aerodynamic ramp" or simply "aero-ramp." The aero-ramp was first presented by Cox et al.<sup>28</sup> after a preliminary investigation involving both experiments and CFD. This injector design consists of a three-by-three array of closely spaced, flush-wall jets with various transverse and yaw angles. The jets were geometrically arranged so as to generate multiplicative fuel-vortex interactions which should lead to enhanced mixing. These fuel-vortex interactions were to include skew induced vortex generation, shock induced vortex generation, and vortex breakdown, all of which have been shown to be effective mixing enhancement mechanisms. Furthermore the flush-wall design coupled with low angle injection avoids the excessive pressure losses, drag, and hot-spots associated with conventional vortex generators.

### Test Facilities

The Supersonic Combustion Facility of the Aero Propulsion and Power Directorate at Wright Laboratory, WPAFB, was used for all experiments documented herein. Complete details regarding this facility have been presented by Gruber et al.<sup>29</sup> This facility is a continuous running, open-loop supersonic wind tunnel with a rectangular test section measuring 12.7-cm high, 15.2-cm wide, and 76.2-cm long. A pair of compressors capable of providing up to 15 kg/sec of air with total pressures and temperatures up to 48.6 atm and 922 K, respectively, were used to supply air to the facility. A massive exhaust system was used to lower and maintain the back pressure for smooth starting and safe operation.

### Injector Models

#### Physical Ramp Injector

The physical ramp injector used in these experiments is based on the design concept first introduced by Northam et al.<sup>22</sup> In the present studies, the physical ramp injector, shown in Fig. 1, has a 10.3° compression surface with a leading-edge width of 403 mm, a trailing-edge width of 152 mm, and a length of 610 mm. The ramp base is canted at 10.3° and contains a 95.3-mm sonic injection orifice such

that the injection axis is parallel to the ramp compression surface.

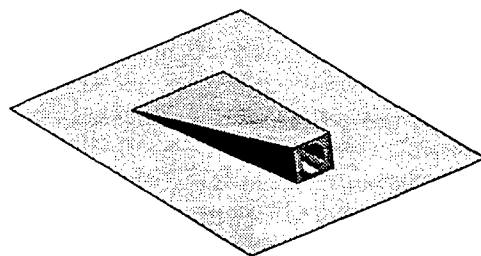


Fig. 1 Physical ramp injector model.

#### Aero-Ramp Injector

Figure 2 shows the three-by-three array of jet orifices comprising the aerodynamic ramp injector model. Each sonic jet orifice has an exit diameter of 3.18 mm. The first upstream row of injectors consisted of three ports with a spanwise spacing of 9.53 mm, transverse angle of 15°, and no yaw. The second row of injectors was located 22.2 mm downstream of the first row with a spanwise spacing of 7.94 mm, transverse angle of 30°, and respective yaw angles of -15°, 0°, and 15°. The third row of injectors was located 44.4 mm downstream of the first row with a spanwise spacing of 6.35 mm, transverse angle of 45°, and respective yaw angles of -30°, 0°, and 30°. The injection insert was designed to be mounted flush with the bottom wall surface of the tunnel test section.

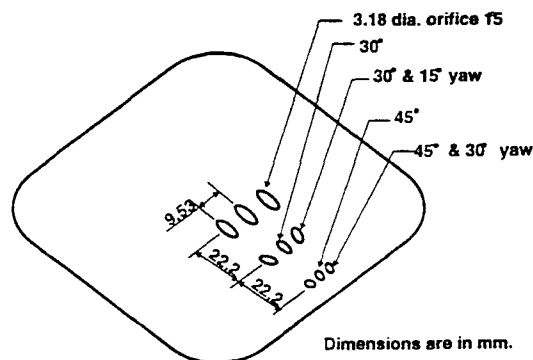


Fig. 2 Aero-Ramp injector model.

### Test Matrix

Tests were conducted with a Mach 2.0 turbulent crossflow. Freestream conditions were set for a total pressure of 3.06 atm and total temperature of 295 K, producing a freestream Reynolds number of  $3.63 \times 10^7$  per meter. Pure helium was used as the injectant to simulate hydrogen fuel. The jet-to-freestream momentum flux ratio,  $\bar{q}$ , was set at either 1.0 or 2.0 as indicated. Recall that the jet-to-freestream momentum flux ratio is defined by

$$\bar{q} = \frac{(\rho u^2)_j}{(\rho u^2)_\infty} = \frac{(\gamma p M^2)_j}{(\gamma p M^2)_\infty} \quad (1)$$

Neglecting discharge coefficients, this corresponded to an injection total pressure of 2.69 atm for  $\bar{q} = 1.0$  and 5.38 atm for  $\bar{q} = 2.0$ . For all cases, the injectant total temperature was subject to ambient temperature which averaged approximately 295 K.

A right-handed, Cartesian coordinate system was chosen with the origin placed at the leading edge of the injector on the wall surface along the test section centerline. The positive x-axis was in the freestream direction, the positive z-axis was in the vertical direction perpendicular to the wall surface, and the y-axis spanned the test section. All lengths were nondimensionalized by an effective diameter,  $d_{eff}$ , defined as follows:

$$d_{eff} = C_d^{0.5} d_j \quad (2)$$

where  $C_d$  is the injector discharge coefficient and  $d_j$  is the jet diameter. For the aero-ramp injector an equivalent jet diameter,  $d_{eq}$ , was defined as the diameter of a single circular orifice having the same area as the combined area of all nine orifices. This equivalent diameter of the aero-ramp was equal to the single jet diameter of the physical ramp. The injector discharge coefficients for the physical ramp operating at  $\bar{q} = 1.0$  and  $\bar{q} = 2.0$  were 0.75 and 0.84, respectively. The injector discharge coefficients for the aero-ramp operating at  $\bar{q} = 1.0$  and  $\bar{q} = 2.0$  were 0.89 and 0.92, respectively. For the physical ramp injector, measurements were taken at axial distances of 80, 118, 213, 518, and 700 mm. For the aero-ramp injector, measurements were taken at axial distances of 65, 103, 198, 503, 674 mm. With  $\bar{q} = 1.0$ , these distances corresponded to  $x/d_{eff} = 9.7, 14.3, 25.9, 62.8, 83.6$  for the physical ramp and  $x/d_{eff} = 7.2, 11.4, 22.0, 56.0, 75.0$  for the aero-ramp. With  $\bar{q} = 2.0$ , measurements were taken at the furthest downstream distance only corresponding to  $x/d_{eff} = 79.0$  for the physical ramp and  $x/d_{eff} = 73.8$  for the aero-ramp.

### Test Procedures

#### Species Composition Sampling

Species concentration measurements were obtained using an intrusive sampling probe and gas analyzer designed specifically for use in supersonic flow. The fundamental concepts have been presented by Ninnemann et al.<sup>30</sup> The sampling probe consisted of a small Pitot tube with a conical tip and an internal divergence. This geometry was used so that an isokinetic sample could be extracted from the flow. Isokinetic sampling is ensured in supersonic flow by swallowing the shock into the probe. With a swallowed shock, there is no disturbance upstream of the probe and no distortion of the streamtube entering the probe inlet. The gas analyzer consisted of a hot-film sensor operating in a channel with a pressure tap and a thermocouple. The sample was drawn into the analyzer via the sampling probe and exhausted out through a choked orifice. The flow through the channel is of very

low Mach number – typically 0.05. This allows for the approximate measurement of total pressure and total temperature within the sampling channel. The gas analyzer is calibrated to measure the helium concentration uniquely related to a given pressure, temperature and heat transfer sensed at the hot-film operating plane.

#### Aerothermodynamic Probing

Aerothermodynamic measurements were performed using a standard set of probes. This set included a Pitot probe, cone-static pressure probe and a total temperature probe. The Pitot probe was a simple round stainless steel tube with an outer diameter of 3.18 mm and an inner diameter of 2.37 mm, indicating a capture area of 4.29 mm<sup>2</sup>. The cone-static pressure probe consisted of a 3.18-mm stainless steel tube with a closed-end, 10° half-angle conical tip. The cone had four pressure taps, each of 0.51-mm diameter, located approximately 7.44 mm from the cone vertex. These pressure taps were spaced azimuthally at 90° intervals. All taps emptied into a common chamber to reduce error due to flow angularity. The total temperature probe was based on an original design of Winkler<sup>31</sup>. The probe consisted of a 3.18-mm stainless steel Pitot tube with a ceramic diffuser tip. A type-K thermocouple with a 0.38-mm bead was mounted within the ceramic diffuser tip. The diffuser tip has an inlet diameter of 1.60 mm and two side vent holes with diameters of 0.51 mm each. Geometries were chosen such that the flow entering the probe inlet would be effectively stagnated around the thermocouple bead. This design yielded a temperature recovery factor of approximately 0.98 with a response time constant (time to reach 63% of a step input) of approximately 0.01 seconds.

These three measurements are combined with species composition sampling to estimate all aerothermodynamic variables of interest. Data reduction consist of an iterative scheme utilizing the isentropic flow relations, perfect gas relations, the Rayleigh-Pitot formula and the Taylor-Mccoll cone flow equation. Details regarding the data reduction have been presented by Fuller et al.<sup>9</sup>

### Results and Analysis

#### Shadowgraphs

Figures 3 through 6 show shadowgraph images of the physical ramp and aero-ramp injectors operating with jet-to-freestream momentum flux ratios of 1.0 and 2.0 as indicated. The flow is left-to-right and the injector is at the bottom of the image. The thin shocks crossing at the extreme left of the images are weak disturbances originating at the interface between the nozzle and test sections. Their angle with respect to the freestream is approximately that of a Mach wave in a Mach 2.0 flow. It is important to bear in mind that these flows are highly three-dimensional and one must exercise caution in interpreting the shock structures.

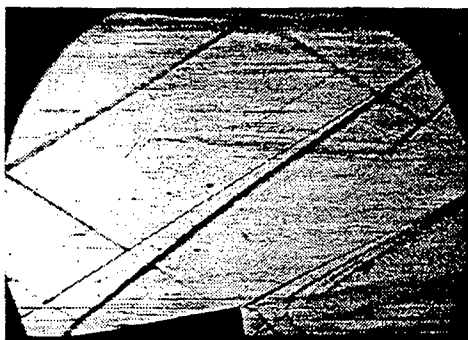


Fig. 3 Shadowgraph image of physical ramp injection with  $\bar{q} = 1.0$ .

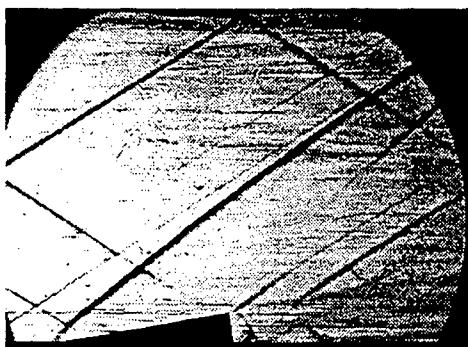


Fig. 4 Shadowgraph image of physical ramp injection with  $\bar{q} = 2.0$ .

In both Figs. 3 and 4, the oblique shock wave originating at the leading edge of the ramp is clearly seen. The angle of this shock is approximately  $38^\circ$  which is slightly less than that predicted for a  $10.3^\circ$  wedge in a Mach 2.0 flow. This is a result of the three-dimensional relieving effect. Just downstream of the top edge of the ramp base, a recompression shock, similar to a lip shock on a rearward facing step, is observed in both cases. As the flow expands over the ramp base it encounters the jet plume and must negotiate an upward deflection which results in a recompression wave originating at the fuel-air interface. Further downstream along the fuel-air interface the shock wave originating at the upper edge of the jet Mach disk is clearly seen. Note, the barrel shock and Mach disk may not be clearly seen in these photographic reproductions. In the case of  $\bar{q} = 1.0$ , shown in Fig. 3, two subsequent compression waves following the one formed at the upper edge of the Mach disk can be observed. In the case of  $\bar{q} = 2.0$ , shown in Fig. 4, only the wave originating at the Mach disk is observed, however it is stronger than that observed in the previous case. Various weak shocks appear in the jet plume, however these shocks are outside the centerline plane and are a result of three-dimensional effects. For background information on the structure of underexpanded jets in a supersonic crossflow, the reader should refer to Ref. 5. Finally, note that the observed plume height does not change appreciably when  $\bar{q}$  is increased from 1.0 to 2.0. This should be expected since most of the jet momentum is in the freestream direction, however some increase in height should result from a greater jet expansion.

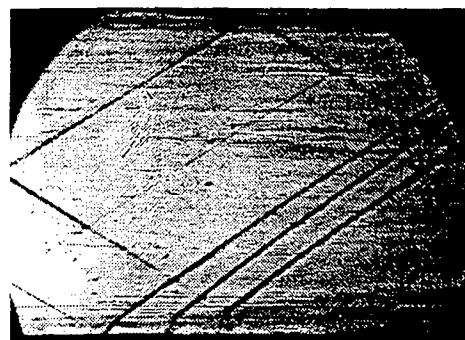


Fig. 5 Shadowgraph image of aerodynamic ramp injection with  $\bar{q} = 1.0$ .

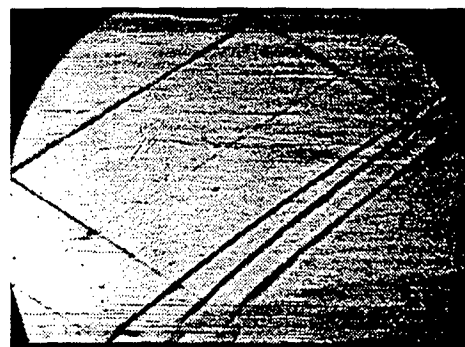


Fig. 6 Shadowgraph image of aerodynamic ramp injection with  $\bar{q} = 2.0$ .

In both Figs. 5 and 6, the nine jet interaction shocks appear as three composite shock structures forming over each of the three rows of jets. In the case of  $\bar{q} = 1.0$  shown in Fig. 5, the shocks are curved near the wall and become nearly straight just above the jet plume. The initial angles near the wall upstream of the first, second, and third rows are approximately  $48^\circ$ ,  $40^\circ$ , and  $38^\circ$ , respectively. All shocks reach a final angle of approximately  $35^\circ$ . In the case of  $\bar{q} = 2.0$ , shown in Fig. 6, the shocks appear to be stronger and the jet penetration has increased significantly when compared to the previous case. Indeed the shocks are stronger with initial angles near the wall upstream of the first, second, and third rows of approximately  $55^\circ$ ,  $42^\circ$ , and  $41^\circ$ , respectively. Again all shocks reach a final angle of approximately  $35^\circ$ .

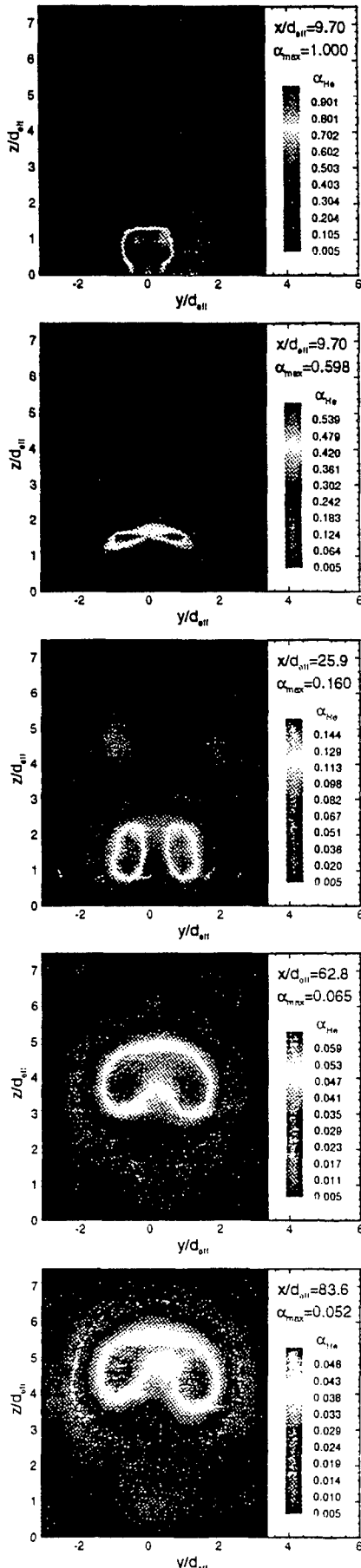


Fig. 7 Helium mass fraction contours for physical ramp injection with  $\bar{q} = 1.0$ .

### Species Composition Sampling

Figure 7 shows the profiles of helium mass fraction at each of the five stations sampled for the physical ramp injector operating with a jet-to-freestream momentum flux ratio of 1.0. Note that the contour color-scales are not consistent between plots. While the minimum value indicating the plume boundary is fixed at a mass fraction value of one-half of one percent, the maximum value corresponds to the local station maximum. This was done to preserve structural details of the plume as the mass fractions vary over three orders of magnitude. At  $x/d_{eff} = 9.7$ , the jet potential core ( $\alpha_{He} = 1$ ) still persists in the plume. On the left and right sides of the plume there are small triangular structures of low-concentration helium. These are the effect of the two counter-rotating vortices stripping helium away from the sides of the plume. At  $x/d_{eff} = 14.3$  the plume shape changed dramatically. The helium has begun to wrap around the vortices and lift away from the wall surface at the centerline. At  $x/d_{eff} = 25.9$  the helium has now completely enveloped the vortex structure with the maximum concentration occurring at the two vortex cores. At  $x/d_{eff} = 62.8$  the vortex pattern convected upwards into the freestream and carried the fuel plume with it. The maximum helium mass fraction is still found at each of the vortex cores. At  $x/d_{eff} = 83.6$  it is clear that the mixing distribution is no longer dominated by the vortex structure and diffusive mechanisms have taken over. The overall structure of the plume is very similar to that observed in the previous plot. The overall area of the plume increased and the maximum helium mass fraction decreased. Again the maximum helium concentration is located in what remains of the two vortex cores.

Figure 8 shows the profile of helium mass fraction at the fifth station sampled for the physical ramp injector operating with a jet-to-freestream momentum flux ratio of 2.0. Here the plume is much fuller, however there is no discernible change in the penetration. Furthermore there is only one single maximum in the helium concentration occurring near the plume center indicating a weaker effect of the dual-vortex structure on the mixing distribution. This should be expected since the higher jet momentum will tend to weaken the vortex structure.

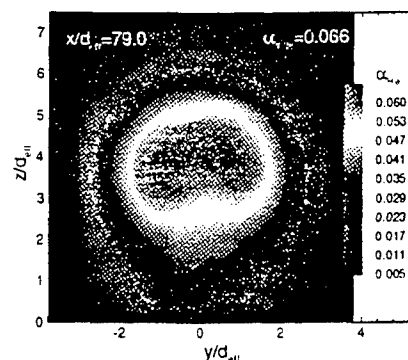


Fig. 8 Helium mass fraction contours for physical ramp injection with  $\bar{q} = 2.0$ .

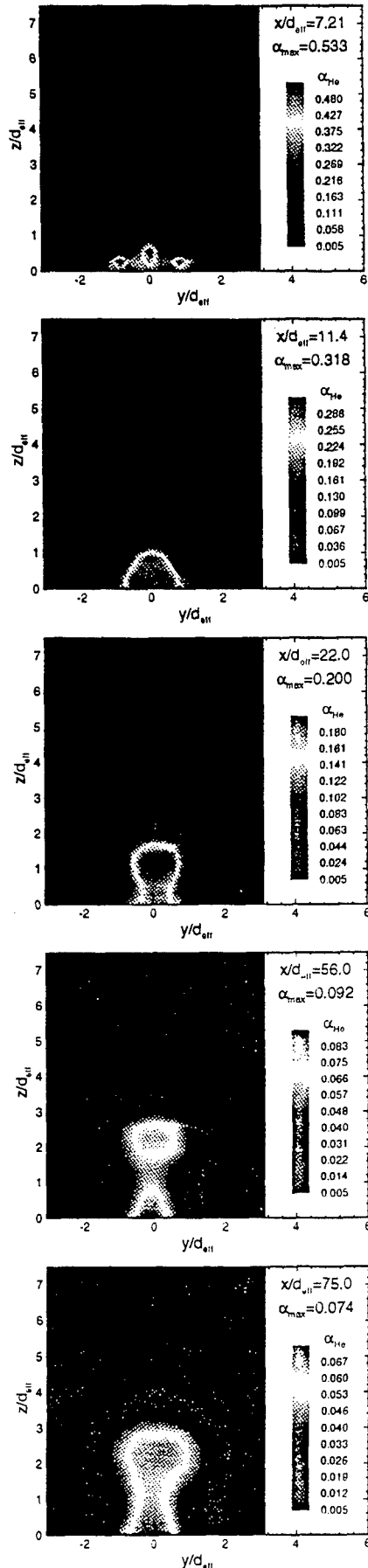


Fig. 9 Helium mass fraction contours for aero-ramp injection with  $\bar{q} = 1.0$ .

Figure 9 shows the profiles of helium mass fraction at each of the five stations sampled for the aero-ramp injector operating with a jet-to-freestream momentum flux ratio of 1.0. Again the contour color-scales are not consistent between plots so as to preserve plume structural detail. At  $x/d_{eff} = 7.21$  three distinct jet cores appear in the single composite plume produce by the entire nine-jet array. These jet cores are produced by the furthest downstream row of jets. The maximum helium concentration is nearly half of the value produced by the physical ramp at  $x/d_{eff} = 9.7$  where the potential core still persists. The diameter of each individual jet comprising the aero-ramp is one-third the size of the single orifice of the physical ramp, therefore the multiple potential cores of the aero-ramp will be much shorter than the single potential core of the physical ramp. This will result in a substantially larger decay rate of the helium concentrations in the near-field. At  $x/d_{eff} = 11.4$  the three previously distinct jet cores have now merged into a single core at the center with the maximum mass fraction occurring near the wall. At  $x/d_{eff} = 22.0$  the jet core lifted away from the wall and penetrated farther into the freestream. At  $x/d_{eff} = 56.0$  the jet core split into two leaving behind a secondary core in the boundary layer. This was originally identified by Cox et al.<sup>28</sup> as being the effect of two large counter-rotating vortices generated by the aero-ramp in the very near field. These vortices induce an upward motion at the centerline, disperse helium outward at the top, and entrain air inward near the bottom. This results in the apparent bottlenecking of the plume. At  $x/d_{eff} = 75.0$  the plume has become more rounded and the two cores are beginning to merge as diffusive mechanisms take control.

Figure 10 shows the profile of helium mass fraction at the fifth station sampled for the aero-ramp injector operating with a jet-to-freestream momentum flux ratio of 2.0. Like the physical ramp case higher  $\bar{q}$  produces a fuller profile. However unlike the physical ramp case the penetration increased significantly with  $\bar{q}$ . Furthermore the added jet momentum seems to enhance the vorticity generation as indicated by the increased bottlenecking and separation of the primary and secondary cores.

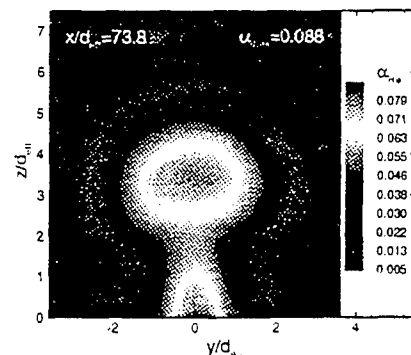


Fig. 10 Helium mass fraction contours for aero-ramp injection with  $\bar{q} = 2.0$ .

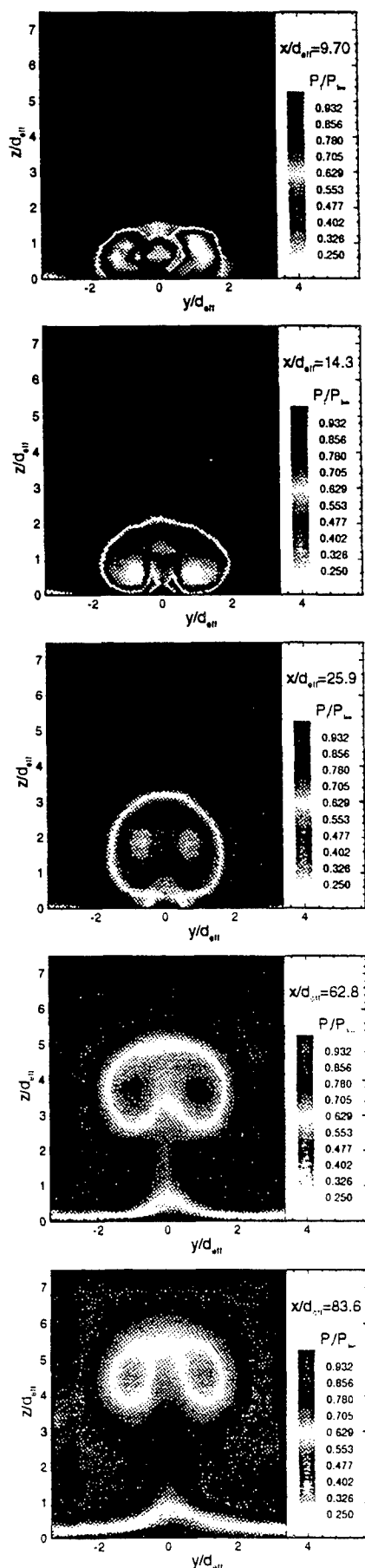


Fig. 11 Total pressure contours for physical ramp injection with  $\bar{q} = 1.0$ .

### Aerothermodynamic Probing

Figure 11 shows the profiles of total pressure at each of the five stations sampled for the physical ramp injector operating with a jet-to-freestream momentum flux ratio of 1.0. In each of the plots shown, the contour color-scales are consistent so that plot-to-plot comparisons may easily be made. At  $x/d_{eff} = 9.7$  the effects of the ramp and jet are clearly visible in the plot. Three local minima occur in the plot corresponding to the two vortex cores and the jet. The local minimum of total pressure occurring in the jet results from shock losses through the Mach disk. The outer minima clearly identify the location of the two vortices where the apparent reduction in total pressure results from a transfer of kinetic energy to the transverse directions. Note the ramp shock is not apparent in this plot since it was above the vertical extent of measurement. However the lip shock can be identified just above the fuel-vortex structure. At  $x/d_{eff} = 14.3$  the losses in the jet core have been distributed over a larger area encompassing the plume and a certain amount of pressure recovery has been realized. The vortices have retained their strength and position as indicated by the total pressure. The recompression shock downstream of the lip shock can be identified over the fuel-vortex structure. The resolution of this shock results from an undesirable interaction with the cone-static pressure probe leading to slight inaccuracies over the range of impingement. This is why the shock appears as a wide band rather than a discreet step. At  $x/d_{eff} = 25.9$  the vortex structures have convected upwards carrying the plume with them. At  $x/d_{eff} = 62.8$  the losses are less concentrated indicating a dissipation of the streamwise vorticity. At  $x/d_{eff} = 83.6$  the profile is similar to the previous plot with smaller gradients and a larger distribution of losses.

Figure 12 shows the profile of total pressure at the fifth station sampled for the physical ramp injector operating with a jet-to-freestream momentum flux ratio of 2.0. As was mentioned earlier, the added jet momentum tends to lessen the vorticity generated by the ramp. This is evidenced by the contours where only a single core exists and the gradients are less severe. Of course, the added jet momentum will also tend to alleviate the losses associated with flow separation and add to the total pressure sensed downstream.

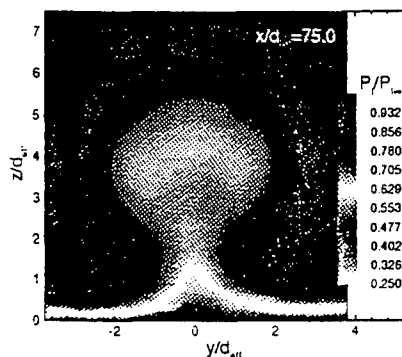


Fig. 12 Total pressure contours for physical ramp injection with  $\bar{q} = 2.0$ .

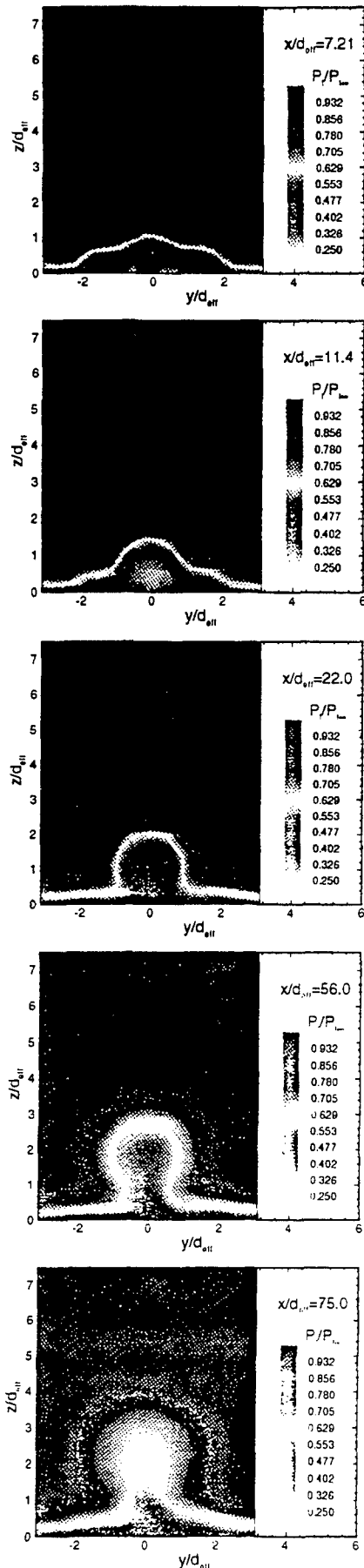


Fig. 13 Total pressure contours for aero-ramp injection with  $\bar{q} = 1.0$ .

Figure 13 shows the profiles of total pressure at each of the five stations sampled for the aero-ramp injector operating with a jet-to-freestream momentum flux ratio of 1.0. The contour color-scales are consistent between plots. At  $x/d_{eff} = 7.2$  the losses are confined to the boundary layer very near the wall surface. The aero-ramp does not appear to separate the boundary layer – at least not to the same extent as was observed with the physical ramp. This will most certainly contribute less drag and minimize the occurrence of “hot spots” in the scramjet combustor. The center jet imparts added total pressure to the boundary layer as indicated by the small local maximum just above the wall at  $y/d_{eff} = 0$ . The three composite shock patterns forming over each of the three rows of jets can be identified. As explained earlier, the resolution of these shocks results from an undesirable interaction between the jet shock and the cone-static pressure probe shock. Thus, it is an effect of the jet shocks which appears in the plots and not the measurement of a true pressure difference. The actual shock locations are at the lower edge of these bands where the jet shock first impinges on the cone-static pressure probe. At  $x/d_{eff} = 11.4$ , where the three jets have now merged to form one single core of helium, the total pressure losses are more severe and cover a larger area. The three composite jet interaction shocks can still be identified as they have moved upward with axial distance. At  $x/d_{eff} = 22.0$  some of the total pressure has been recovered within the helium core as the losses have been distributed over a larger region. At  $x/d_{eff} = 56.0$  the jet plume finally emerges from the boundary layer as a secondary boundary layer is developing near the wall surface. At  $x/d_{eff} = 75.0$  the gradients have become less severe and the pressure losses are distributed over a greater area. Note that no strong vortex patterns persist downstream of the first station. Hence, the mixing downstream of the first station is not dominated by large scale vorticity as is the physical ramp.

Figure 14 shows the profile of total pressure at the fifth station sampled for the aero-ramp injector operating with a jet-to-freestream momentum flux ratio of 2.0. Note that while the pressure losses are distributed over a greater area the magnitude of the losses have been lessened by the added jet momentum.

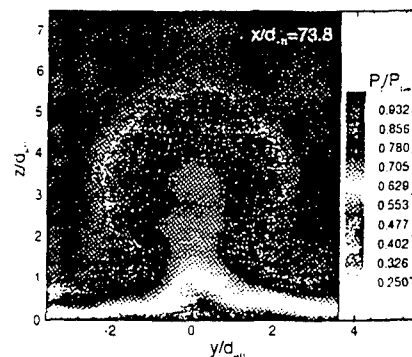


Fig. 14 Total pressure contours for aero-ramp injection with  $\bar{q} = 2.0$ .



## Penetration Trajectory

Overall plume penetration is defined here as the vertical height from the wall surface to the edge of the mixing region where the fuel mass fraction is 0.5%. The penetration trajectory is then defined as the variation with downstream distance of the plume penetration in the vertical centerline plane. The penetration trajectories of both injectors are quite complicated in the near field and appear to jump almost discontinuously between  $12 < x/d_{eff} < 22$ . To predict penetration accurately in far-field region, where the trajectories are more well behaved, curve fits were constructed correlating penetration height with downstream distance for  $\bar{q} = 1.0$ . Past studies<sup>7,8,30</sup> have shown the penetration height to vary exponentially with axial distance in the far-field region. Power-law curve fits were constructed using only the data obtained from the last three axial locations. These predictions are shown in Fig. 15 along with the measured penetration heights at each axial location. Also shown are the penetration heights for each injector at the furthest downstream location with  $\bar{q} = 2.0$ .

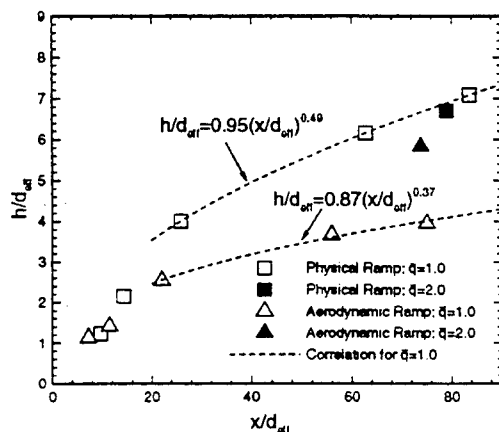


Fig. 15 Injectant penetration trajectory.

Note that when  $\bar{q}$  is increased to 2.0 the normalized penetration for the aero-ramp increases while for the physical ramp it decreases. Recall that, the penetration is nondimensionalized by the effective diameter which is a function of the injector discharge coefficient. The increase in  $\bar{q}$  resulted in an increase in the injector discharge coefficient and therefore the effective diameter as well. The absolute penetration does indeed increase in both cases, however they are scaled by larger effective diameters. In any event, these results suggest that with further increases in  $\bar{q}$  the penetration height for the aero-ramp may surpass that of the physical ramp.

## Decay of Maximum Concentration

The decay of maximum concentration with downstream distance for the injectors is presented in Fig. 16. In general, the decay of maximum concentration proceeds exponentially with downstream distance so that it may be correlated using an appropriate power law. The following

form will be used to obtain a decay rate,  $n$ .

$$\alpha_{max} = \beta (x/d_{eff})^{-n} \quad (3)$$

A larger value of  $n$  indicates a faster overall rate of decay. Using the data obtained in the experiments, correlations were constructed using a least squares approach.

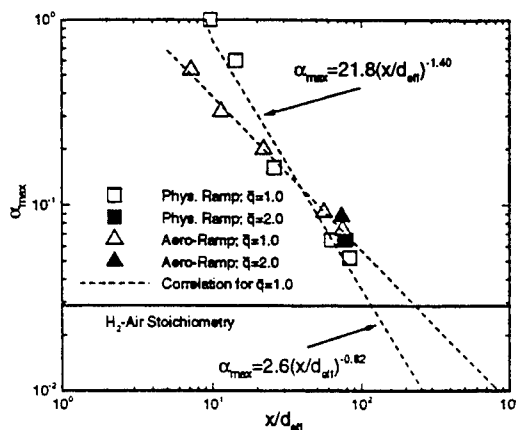


Fig. 16 Decay of maximum concentration.

The decay rate for the physical ramp injector was 1.40 and for the aero-ramp injector it was 0.82. The physical ramp injector exhibits a very high rate of decay when compared to the average rate of 0.8 determined through an extensive review study conducted by Schetz et al.<sup>9</sup> However, note that in the near-field region the initial decay produced by the aero-ramp upstream of the first measurement station is far superior to that of the physical ramp injector. As a result, the far-field values of maximum concentration are comparable despite the large decay rate produced by the physical ramp downstream of the first measurement station. Setting  $\alpha_{max} = 0.0292$ , the stoichiometric mass fraction of hydrogen in air, and solving for  $x/d_{eff}$  gives the distance at which all of the mixture is at or below the stoichiometric mass fraction of hydrogen in air. At this distance, denoted as  $x_{fm}$ , the injectant is considered "fully mixed." For the physical ramp, the fully mixed distance is  $113 d_{eff}$  and for the aero-ramp, it is  $240 d_{eff}$ . While these fully-mixed distances are quite different, the near-field fuel concentrations will certainly have a strong impact on flame ignition and combustion.

When plotting  $\alpha_{max}$  for different values of  $\bar{q}$  it is appropriate to account for the added fuel mass by rescaling the axial distance with the square-root of the jet-to-freestream mass flux ratio. This is essentially the same as correcting for the discharge coefficient by considering the effective jet diameter when nondimensionalizing the axial distance. Figure 17 shows the maximum helium mass fraction plotted against this variable. As a result of the correlation, when  $\bar{q}$  was increased to 2.0, the maximum fuel mass fraction is nearly equal to that predicted for the case of  $\bar{q} = 1.0$ .

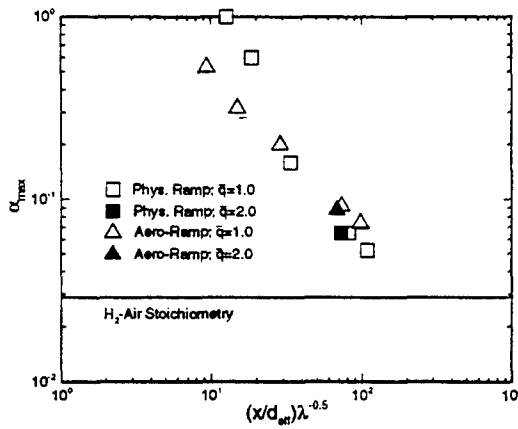


Fig. 17 Correlated decay of maximum concentration.

### Plume Area

The overall plume area is defined by that area enclosed by the outermost contour representing a fuel mass fraction of 0.5%. Figure 18 shows the overall plume area versus axial distance for each case tested. The plume areas are nondimensionalized by that area to which a segregated jet (a perfectly unmixed jet) would expand if allowed to reach a uniform static pressure equal to the freestream. This area is denoted by  $A_u$ . Thus  $A/A_u$  is a measure of the degree to which the plume has expanded.  $A_u$  will vary with the jet operating conditions. An increase in  $\bar{q}$  will result in a linear increase  $A_u$ . Therefore a constant value of  $A/A_u$  with increasing  $\bar{q}$  means the plume is growing in proportion to  $\bar{q}$ .

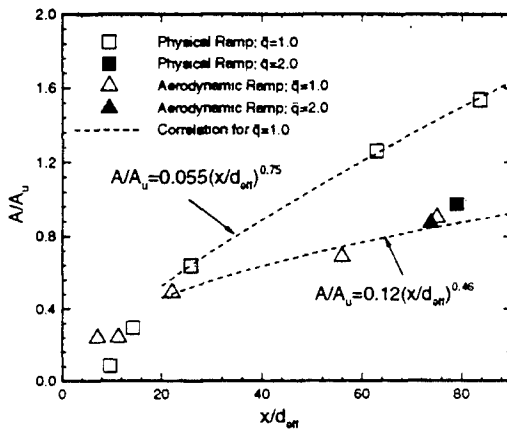


Fig. 18 Overall plume area.

In the near-field, the plume area produced by the aero-ramp is larger than that produced by the physical ramp. In the far-field region the plume produced by the physical ramp quickly grows and surpasses the aero-ramp plume in terms of size. However note that when the jet-to-freestream momentum flux ratio is increased to 2.0, the nondimensional plume area decreases significantly for the physical ramp while it remains approximately the same size for the aero-ramp. That is, the plume produced by the physical ramp does not grow much with increasing  $\bar{q}$

whereas the plume produce by the aero-ramp grows significantly. These results suggest that further increases in  $\bar{q}$  may lead to a larger plume area with the aero-ramp when compared to the physical ramp.

### Mixing Efficiency

The mixing efficiency used here is based on the traditional definition as expressed by Mao et al.<sup>32</sup> The mixing efficiency is defined as that fraction of the least available reactant which would react if the fuel-air mixture were brought to chemical equilibrium without additional local or global mixing. Thus in fuel rich regions, all of the local air is considered mixed, while in fuel lean regions all of the local fuel is considered mixed. A two-part definition for mixing efficiency is required depending on whether the flow is globally fuel rich or fuel lean. In this study of single injectors in a relatively large duct, the flow is globally fuel lean and the mixing efficiency is defined as follows.

$$\eta_m \equiv \frac{\dot{m}_{f,mix}}{\dot{m}_{f,tot}} = \frac{\int \alpha_r \rho u dA}{\int \alpha \rho u dA} \quad (4)$$

where

$$\alpha_r \equiv \begin{cases} \alpha & \alpha \leq \alpha_s \\ \left(\frac{1-\alpha}{1-\alpha_s}\right)\alpha_s & \alpha > \alpha_s \end{cases} \quad (5)$$

and

- $\alpha$  fuel mass fraction
- $\alpha_s$   $H_2$ -air stoichiometric mass fraction
- $A$  plume area
- $\dot{m}_{f,mix}$  mixed fuel mass flow rate
- $\dot{m}_{f,tot}$  total fuel mass flow rate

So that  $\eta_m = 0$  corresponds to a perfectly segregated jet and  $\eta_m = 1$  corresponds to a perfectly mixed jet.

Figure 19 shows the integrated mixing efficiencies versus axial distance for both injectors tested. Fitting a power law to the three downstream points yields predictions for the far-field mixing efficiencies of each injector.

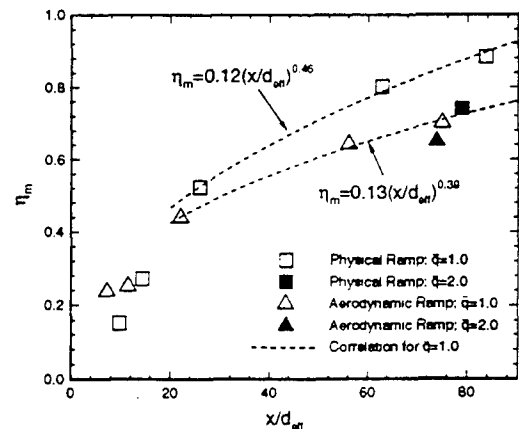


Fig. 19 Integrated mixing efficiency.

In the near-field, the mixing efficiency produced by the aero-ramp is superior to that produced by the physical ramp. In the far-field, however the mixing efficiency

produced by the physical ramp prevails. This is consistent with the results of the maximum fuel concentration and fuel plume area measurements. As the maximum concentration goes down and the plume area goes up the mixing efficiency must necessarily go up. Furthermore, if the maximum fuel concentration is lower and the fuel plume area is larger in one case when compared to another, the mixing efficiency will necessarily be higher. When  $\bar{q}$  was increased to 2.0, the mixing efficiencies were reduced in both cases. However the reduction was more severe for the physical ramp. Both injectors rely heavily on streamwise vorticity for mixing enhancement. As stated earlier, the physical ramp vorticity is reduced with increasing jet momentum while for the aero-ramp it appears to increase. As a result, further increases in jet momentum will most likely cause the physical ramp to suffer more than the aero-ramp in terms of mixing efficiency.

Finally note that when  $\alpha_{max} \leq \alpha_s$ , the mixing efficiency,  $\eta_m$ , equals unity. Thus, the fully-mixed distance,  $x_{fm}$ , also corresponds to that distance when then mixing efficiency first reaches unity. The predictions were used to compute the fully-mixed distances. For the physical ramp,  $x_{fm} = 100 d_{eff}$  and for the aero-ramp,  $x_{fm} = 187 d_{eff}$ . These distances are comparable, in terms of relative magnitude, to those computed based on the maximum fuel concentration predictions. The fully-mixed distance for the aero-ramp is approximately twice the fully-mixed distance for the physical ramp. Again bear in mind that the near-field behavior will most certainly dominate flame definition characteristics and the reacting flow will most likely alter the "fully-mixed" distance.

### Spatial Mixedness

An unmixedness parameter that quantifies mixing rates based on the variance of the concentration distribution was defined by Liscinsky et al.<sup>33</sup> as,

$$U_s = \frac{\alpha_{var}}{\alpha_{eq}(1 - \alpha_{eq})} \quad (6)$$

where,

$$\alpha_{var} = \frac{1}{n} \sum_{i=1}^n (\bar{\alpha}_i - \alpha_{eq})^2 \quad (7)$$

$$\alpha_{eq} = \frac{\dot{m}_j}{\dot{m}_j + \dot{m}_\infty} \quad (8)$$

$$\bar{\alpha}_i = \alpha_i \alpha_{eq} \left[ \frac{1}{n} \sum_{i=1}^n \alpha_i \right]^{-1} \quad (9)$$

A value of zero for  $U_s$  corresponds to a perfectly mixed system and a value of unity corresponds to a perfectly segregated system. The value of this parameter is that it requires fuel concentration measurements only and does not rely on aerothermodynamic measurements. It was originally developed for planar-laser fuel plume imaging. Here we have chosen to plot  $1 - U_s$ , so as to be consistent with the information provided by the plume area and mixing efficiency (i.e. a larger value indicates better mixing).

Figure 20 shows the computed spatial mixedness ( $1 - U_s$ ) versus axial distance along with the predictions for both injectors tested.

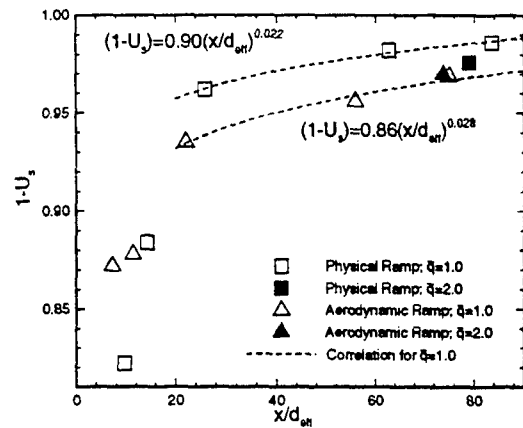


Fig. 20 Spatial mixedness.

The fully mixed distances ( $U_s = 0$ ) based on the predictions are  $x_{fm} = 120 d_{eff}$  for the physical ramp and  $x_{fm} = 218 d_{eff}$  for the aero-ramp. Again the distances are comparable to those previously computed using the maximum concentration and mixing efficiency predictions. When  $\bar{q}$  was increased to 2.0 the spatial mixedness decreased with the physical ramp while it slightly increased for the aero-ramp. Yet again indicating better mixing performance with increasing  $\bar{q}$  for the aero-ramp.

### Total Pressure Losses

The total pressure losses due to fuel injection can seriously affect the thermodynamic efficiency of a scramjet engine. Therefore, the evaluation of a given injector must include some quantification of losses. The total pressure of the incoming air is reduced by viscous forces in the boundary layer, shock waves, flow separation, and fuel-air mixing. Unfortunately these losses are often very difficult to assess in the cold-flow situation. Previous studies conducted by Fuller et al.<sup>9</sup> and Mays et al.<sup>33</sup> have defined quantitative measures for such assessments. In each case, losses were quantified by examining the mass-weighted field values of the total pressure normalized by the freestream conditions. However, the area over which the integration takes place is often facility dependent or based on a complex analysis of data not readily available. In order to simplify these measures, an adaptation of those previously defined forms was developed. A total pressure loss parameter was defined as follows:

$$\Pi = \frac{\int \rho u (p_{t,\infty} - p_t) dA}{\rho_\infty u_\infty p_{t,\infty} A_s + \rho_j u_j p_{t,j} A_j} \quad (10)$$

where

$$A_s = \frac{\lambda}{\alpha_s} A_j \quad (11)$$

That is,  $A_s$  is the area required for a uniformly stoichiometric jet given the jet-to-freestream mass flux ratio and jet exit area. A parameter value of  $\Pi = 0$  indicates no

losses. However the total pressure parameter is essentially unbounded and a value of unity does not indicate total loss. The computed total pressure parameter versus axial distance for each injector is plotted in Fig. 21. Again, power-law curve fits have been constructed using the last three data points.

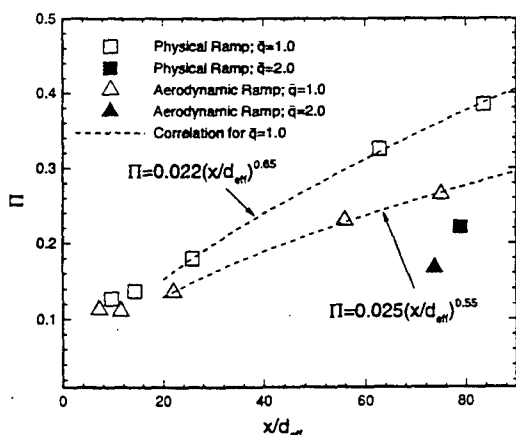


Fig. 21 Total pressure loss parameter.

The pressure loss incurred with the physical ramp injector is more severe than that exhibited by the aero-ramp injector for both cases of  $\bar{q}$  equal to 1.0 and 2.0. Note that when  $\bar{q}$  is increased from 1.0 to 2.0 there is a reduction in total pressure loss parameter as was indicated in the total pressure contours. These reductions result from the added momentum in the freestream direction. Furthermore, the reduction in the case of the physical ramp is greater. This should be expected since a much greater part of the jet momentum is directed into the freestream.

### Summary and Conclusions

An experimental investigation was conducted to compare the performance of the aero-ramp injector with a physical ramp injector previously shown to enhance mixing in supersonic flow. The scope of the investigation focused on jet penetration, mixing characteristics, and total pressure losses. Several analysis techniques were applied to evaluate the mixing characteristics and all provided consistent results. Furthermore, a parameter was defined to quantify the total pressure losses without complex analysis or facility dependence.

The aero-ramp exhibited a significant increase in jet penetration when the jet-to-freestream momentum flux ratio was increased from 1.0 to 2.0, however, the physical ramp showed very little change. As a result, the jet penetration of the aero-ramp was comparable to that of the physical ramp at the higher momentum flux ratio.

The mixing characteristics of the physical ramp injection were dominated by the counter-rotating vortices generated by the ramp. The fuel-air mixing produced by the aero-ramp was dominated by the multiplicative fuel-vortex interactions confined to the injector vicinity. Mixing effectiveness was based on maximum fuel mass fraction, plume area, mixing efficiency, and spatial mixedness. With a jet-to-freestream momentum flux ratio of 1.0, the

aero-ramp produced superior mixing in the near field and slightly less than comparable mixing in the far field. With a momentum flux ratio of 2.0, the aero-ramp mixing was comparable to that of the physical ramp in the far field. The enhanced mixing of the aero-ramp can be attributed to the multiplicative fuel-vortex interactions in the near field as well as the multiple jet design. That is, several small jet should mix better than one single jet. The enhanced mixing of the physical ramp can be attributed to the counter-rotating vortex pair. The increased jet momentum reduced the strength of the vortices produced by the physical ramp while it increased the strength of the interactions produced by the aero-ramp. Thus, the mixing performance decreased with increasing jet momentum for the physical ramp while it increased for the aero-ramp.

For the physical ramp, the total pressure losses were concentrated around the centers of the two counter-rotating vortices. For the aero-ramp, the total pressure losses were concentrated around the core of the jet plume. The pressure losses induced by the physical ramp were more severe. With a jet-to-freestream momentum flux ratio of 1.0, the physical ramp exhibited a larger loss parameter over the entire axial range of measurements. When the momentum flux ratio was increased to 2.0, both injectors exhibited a reduction in losses with the physical ramp losses still being more severe.

The key point to be made here is that, regardless of whether the current ramp can be made to outperform the physical ramp at certain operating conditions, comparable performance alone merits further studies. Future studies should include parametric optimization through combined efforts of CFD and experiments. Furthermore, the fundamental effects of impinging jets in a supersonic crossflow and their uses in creating fuel-vortex mixing mechanisms need to be studied.

### Acknowledgments

This work was sponsored by and performed at Wright Laboratory, Wright-Patterson AFB, Ohio, under contract numbers F33615-93-C-2300 and F33615-96-C-2625. This experimental work was made possible through the efforts of Dr. T. Chen, G. Haines, M. Landrum, and D. Schommer of Taitech and Dr. M. Gruber of Wright Laboratory. Technical monitoring was provided by J. Donbar and Dr. D. Glawe of Wright Laboratory. A sincere thanks is given to the Air Facilities Group at the Wright Laboratory Aero Propulsion and Power Directorate.

### References

- Heiser, W.H., Pratt, D.T., Daley, D.H., and Mehta, U.B., "Hypersonic Airbreathing Propulsion," in AIAA Education Series, Przemieniecki, J. S. (Edit.) AIAA, Washington, D.C., 1994.
- Schetz, J.A. and Billig, F.S., "Penetration of Gaseous Jets Injected into a Supersonic Stream," *Journal of Spacecraft and Rockets*, Vol. 3, No. 11, November 1966, pp. 1658-1665.
- Schetz, J.A., Hawkins, P.F., and Lehman, H., "Structure of Highly Underexpanded Transverse Jets in a Supersonic Stream," *AIAA Journal*, Vol. 5, No. 5, May 1967, pp. 882-884.

- <sup>4</sup>Schetz, J.A., Weinraub, R.A., and Mahaffey, R.E.Jr., "Supersonic Transverse Injection into a Supersonic Stream," *AIAA Journal*, Vol. 6, No. 5, May 1968, pp. 933-934.
- <sup>5</sup>Schetz, J.A., "Interaction Shock Shape for Transverse Injection," *Journal of Spacecraft and Rockets*, Vol. 7, No. 2, February 1970, pp. 143-149.
- <sup>6</sup>Barber, M.J., Roe, L.A., and Schetz, J.A., "Simulated Fuel Injection Through a Wedge-Shaped Orifice Into Supersonic Flow," AIAA Paper 95-2559, July 1995.
- <sup>7</sup>Schetz, J.A., Thomas, R.H., and Billig, F., "Mixing of Transverse Jets and Wall Jets in Supersonic Flow," in *Separated Flows and Jets*, V. V. Kozlov and A. V. Dovgal (Eds.), Springer-Verlag, Berlin, 1991.
- <sup>8</sup>Mays, R.B., Thomas, R.H., and Schetz, J.A., "Low Angle Injection into a Supersonic Flow," AIAA Paper 89-2461, July, 1989.
- <sup>9</sup>Fuller, E.J., Thomas, R.H., and Schetz, J.A., "Mixing Studies of Helium in Air at High Supersonic Speeds," *AIAA Journal*, Vol. 30, No. 9, September 1992.
- <sup>10</sup>Swithenbank, J. and Chigier, N.A., "Vortex Mixing for Supersonic Combustion," *12th Symposium (International) on Combustion*, 1968, pp. 1153-1162.
- <sup>11</sup>Povinelli, L.A., Povinelli, F.P., and Hersch, M., "A Study of Helium Penetration and Spreading in a Mach 2 Airstream Using a Delta Wing Injector," NASA TN D-5322, 1969.
- <sup>12</sup>Hersch, M., and Povinelli, L.A., "Effect of Interacting Vortices on Jet Penetration into a Supersonic Stream," NASA TM-X-2134, November 1970.
- <sup>13</sup>Povinelli, L.A. and Ehlers, R.C., "Swirling Base Injection for Supersonic Combustion Ramjets," *AIAA Journal*, Vol. 10, No. 9, September 1972, pp. 1243-1244.
- <sup>14</sup>Schetz, J.A. and Swanson, R.C., "Turbulent Jet Mixing at High Supersonic Speeds," *Zeitschrift Für Flugwissenschaften*, Vol. 21, 1973, pp. 166-173.
- <sup>15</sup>Tillman, T.G., Patrick, W.P., and Paterson, R.W., "Enhanced Mixing of Supersonic Jets," *Journal of Propulsion and Power*, Vol. 7, No. 6, November-December 1991, pp. 1006-1014.
- <sup>16</sup>Naughton, J.W., Cattafesta, L.N., and Settles, G.S., "An Experimental Study of the Effect of Streamwise Vorticity on Supersonic Mixing Enhancement," AIAA Paper 92-3549, July 1992.
- <sup>17</sup>Marble, F.E., Hendricks, G. J., and Zukoski, E.E., "Progress Toward Shock Enhancement of Supersonic Combustion Processes," AIAA Paper 87-1880, June 1987.
- <sup>18</sup>Waitz, I.A., Marble, F.E., and Zukoski, E.E., "Vorticity Generation by Contoured Wall Injectors," AIAA Paper 92-3550, July 1992.
- <sup>19</sup>Yang, J., Kubota, T., and Zukoski, E.E., "A Model for Characterization of a Vortex Pair Formed by Shock Passage Over a Light-Gas Inhomogeneity," *Journal of Fluid Mechanics*, Vol. 258, January 1994, pp. 217-244.
- <sup>20</sup>Marble, F.E., Zukoski, E.E., Jacobs, J.W., Hendricks, G.J., and Waitz, I.A., "Shock Enhancement and Control of Hypersonic Mixing and Combustion," AIAA Paper 90-1981, July 1990.
- <sup>21</sup>Metwally, O., and Settles, G., "An Experimental Study of Shock Wave/Vortex Interaction," AIAA Paper 89-0082, January 1989.
- <sup>22</sup>Northam, G.B., Greenburg, I., Byington, C.S., and Capriotti D.P., "Evaluation of Parallel Injector Configurations for Mach 2 Combustion," *Journal of Propulsion and Power*, Vol. 8, No. 2, March-April 1992, pp. 491-499.
- <sup>23</sup>Davis, D.O. and Hingst, W.R., "Progress Toward Synergistic Hypermixing Nozzles," AIAA Paper 91-2264, June 1991.
- <sup>24</sup>Waitz, I.A., Marble, F.E., and Zukoski, E.E., "Investigation of a Contoured Wall Injector for Hypervelocity Mixing Augmentation," *AIAA Journal*, Vol. 31, No. 6, June 1993, pp. 1014-1021.
- <sup>25</sup>Hartfield, R.J., Hollo, S.D., and McDaniel, J.C., "Experimental Investigation of a Supersonic Swept Ramp Injector Using Laser-Induced Iodine Fluorescence," *Journal of Propulsion and Power*, Vol. 10, No. 1, January-February 1994, pp. 129-135.
- <sup>26</sup>Riggins, D.W., McClinton, C.R., Rogers, R.C., and Bittner, R.D., "Investigation of Scramjet Strategies for High Mach Number Flows," *Journal of Propulsion and Power*, Vol. 11, No. 3, May-June 1995, pp. 409-418.
- <sup>27</sup>Riggins, D.W., and Vitt, P.H., "Investigation of Scramjet Strategies for High Mach Number Flows," *Journal of Propulsion and Power*, Vol. 11, No. 3, May-June 1995, pp. 419-425.
- <sup>28</sup>Cox, S.K., Fuller, R.P., Schetz, J.A., and Walters, R.W., "Vortical Interactions Generated by an Injector Array to Enhance Mixing in Supersonic Flow," AIAA Paper 94-0708, January 1994.
- <sup>29</sup>Gruber, M.R. and Nejad, A.S., "Development of a Large-Scale Supersonic Combustion Research Facility," AIAA Paper 94-0544, January 1994.
- <sup>30</sup>Ninnemann, T.A. and Ng, W.F., "A Concentration Probe for the Study of Mixing in Supersonic Shear Flows," *Experiments in Fluids*, Vol. 13, 1992, pp. 98-104.
- <sup>31</sup>Winkler, E.M., "Design and Calibration of Stagnation Temperature Probes for Use at High Supersonic Speeds and Elevated Temperatures," *Journal of Applied Physics*, Vol. 25, 1954, p. 231.
- <sup>32</sup>Mao, M., Riggins, D.W., and McClinton, C.R., "Numerical Simulation of Transverse Fuel Injection," NASP CR 1089, May 1990.
- <sup>32</sup>Liscinsky, D.S., True, B., and Holdeman, J.D., "Effects of Initial Conditions on a Single Jet in Crossflow," AIAA Paper 95-2998, July 1995.



**AIAA 94-0711**

**Parallel Fuel Injection from the Base  
of an Extended Strut into Supersonic Flow**

D.D. Glawe, J.M. Donbar, A.S. Nejad, B. Sekar  
T.H. Chen (Taitech Group)  
Aero Propulsion and Power Directorate  
Wright-Patterson Air Force Base, OH

M. Samimy  
Mechanical Engineering Department  
The Ohio State University

J. F. Driscoll  
Aerospace Engineering Department  
University of Michigan

**32nd Aerospace Sciences  
Meeting & Exhibit**  
**January 10-13, 1994 / Reno, NV**

# Parallel Fuel Injection from the Base of an Extended Strut into Supersonic Flow

D.D. Glawe, J.M. Donbar, A.S. Nejad, B. Sekar  
T.H. Chen (Taitech Group)  
Aero Propulsion and Power Directorate  
Wright-Patterson Air Force Base, OH 45433

M. Samimy  
Mechanical Engineering Department  
The Ohio State University, 43210

J. F. Driscoll  
Aerospace Engineering Department  
University of Michigan, 48109

## Abstract

Planar Rayleigh/Mie scattering and acetone PLIF flow visualizations along with CFD results are presented for helium injected at sonic velocity into a nominal Mach 2 freestream air flow. The helium is injected parallel to the freestream from an extended strut with three different nozzle-to-freestream air static pressure ratios. Jet spread is insignificant for all three pressure cases. However, large scale, spatially periodic and organized structures are observed primarily in the under-expanded cases. The jet interaction is markedly three dimensional as exhibited by the irregular helium jet contour and the appearance of a conical shock in the highly under-expanded case. The Mach disk, jet spread, barrel shock and recirculation zone shown in the CFD results compare reasonably well to the planar Rayleigh/Mie scattering and the acetone PLIF images.

## Introduction

Gaseous fuel injection into a supersonic airstream will be used in air-breathing hypersonic planes with supersonic combustion engines such as the National Aerospace Plane (NASP) and its derivatives. Several methods of injecting fuel into supersonic combustion ramjet (scramjet) engines have been proposed; among them is injection from a strut located in the upstream portion of the combustor.<sup>1-3</sup> This concept of strut injection leads to the experimental configuration outlined below. The engineering challenge for injection of fuel, either normal or parallel, into a supersonic freestream air flow is to produce optimal mixing with minimal losses within the space and time constraints of the combustor. Normal injection produces better mixing but causes major thrust losses primarily due to strong bow shocks.<sup>4</sup> Therefore, it would be advantageous to increase the extent of mixing in parallel injection to that of normal injection without incurring the associated thrust losses.

Passive means such as modified nozzle geometry,<sup>5-9</sup> selective initial conditions,<sup>12</sup> and acoustic excitation<sup>13</sup>

have been shown to enhance mixing in subsonic parallel injection. However, injection and combustion in scramjets occurs at supersonic speeds (e.g., combustor Mach numbers of approximately 2 for flight Mach numbers of 7 or 8), and mixing characteristics are conceivably different under supersonic conditions compared to subsonic conditions. Although the effects of fluid compressibility encountered in supersonic flow can inhibit mixing,<sup>14-17</sup> shock waves can be generated to enhance mixing.<sup>18-20</sup> Continued studies through experiments and computational fluid dynamics (CFD) will cultivate a better understanding of mixing phenomenon in supersonic flows. The CFD results provide useful information for the design of experiments and the experimental results provide a detailed data base for future CFD work and to gage the accuracy of the CFD results.

The objective of this research is to investigate supersonic parallel injection and mixing through observation and measurements of flow parameters using acetone Planar Laser Induced Fluorescence (PLIF), planar Rayleigh/Mie scattering, and comparison to CFD results. The first consideration in this research is the injection model. The injection nozzle needs to be mounted inside the supersonic tunnel with minimal upstream disturbances to eliminate extraneous factors from the experiments. A strut provides rigid support for the nozzles and the added benefit of a recirculation zone for flame holding in combustion applications. This strut is similar to a typical splitter plate used in shear layer studies except that the flow velocity is the same on both sides of the strut and the base of the strut is blunt rather than tapered to a knife edge. By extending the strut upstream through the nozzle into the settling chamber and using the method of characteristics to design the nozzles, shock waves are eliminated in the free stream before reaching the end of the strut. Although the strut and injection nozzle are of a simple geometry, the two-dimensional expansion of the freestream over the base, combined with the axisymmetry of the jet result

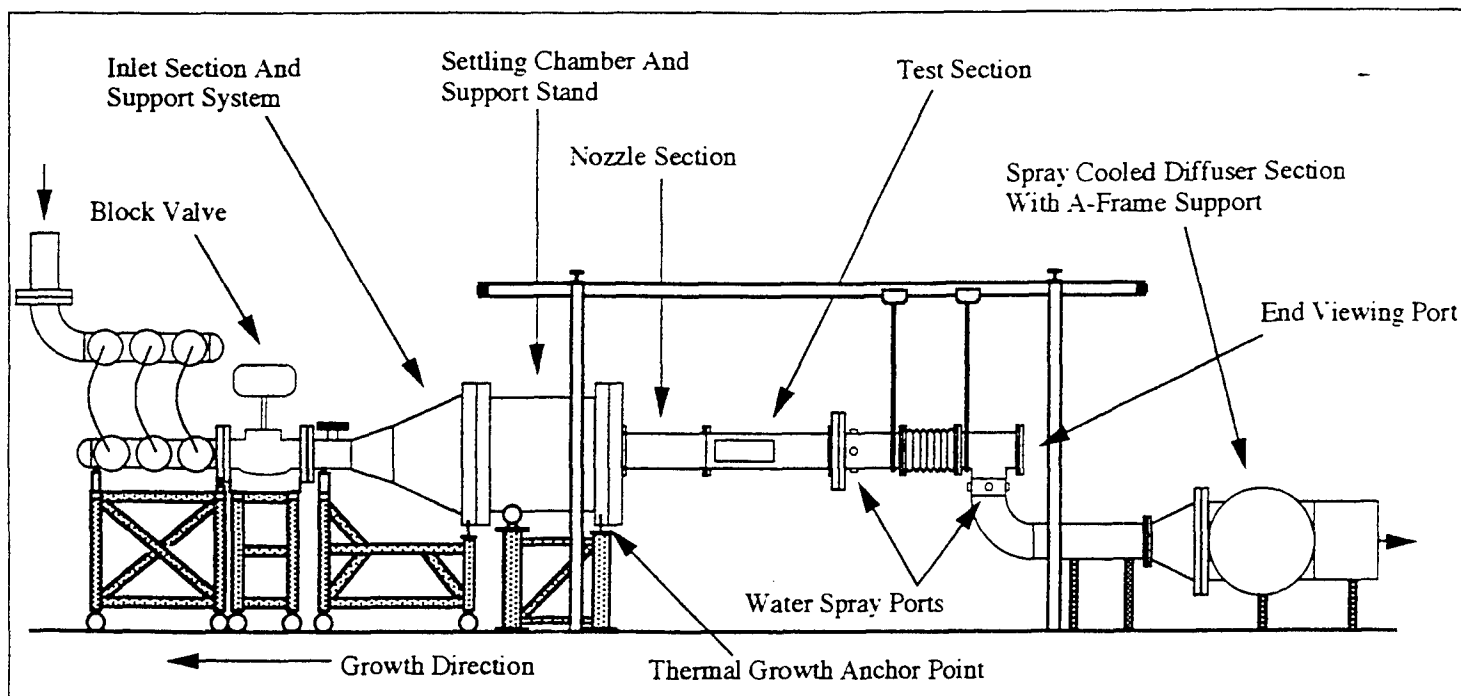


Figure 1 Schematic of supersonic combustion tunnel

in a complex three-dimensional flow field. The flow characteristics of this design are intermediate between two-dimensional slot injection from a base and parallel injection from an axisymmetric configuration.

### Experimental Facility

This research was conducted in the newly built supersonic combustion research facility at the Aero Propulsion and Power Directorate, Wright Patterson Air Force Base.<sup>21</sup> The wind tunnel is capable of continuous flow operation at maximum stagnation conditions of 400 psia (2.75 MPa) and 1660 R (889 K) at a peak flow rate of 34 lbm/s (15.5 kg/s) with the test section design static condition being 7.35 psia (51 KPa) and 525 R (292 K). The test section temperature and pressure conditions are adjusted by mixing air from hot and cold supply lines in controlled quantities. The nominal 5 by 6 in. (12.70 x 15.24 cm) test section has optical access from three sides and from the downstream end. A tunnel schematic is shown in Figure 1.

The 0.5 in. (1.27 cm) thick strut extends from the settling chamber, through the nozzle section and into the test section, thus avoiding leading edge shock waves. The Mach 2 nozzle (Figure 2) was designed by the method of characteristics to eliminate shock waves and provide a uniform, nominal Mach 2.0 freestream flow before reaching the end of the extended strut where injection occurs. The plumbing for the injector runs through the sidewall of the tunnel into the strut and is directed through a 90

degree bend to enter a circular converging nozzle. The nozzle is inserted into the center of the trailing end of the strut. The nozzle is directly preceded by a straight section that is over 40 injector diameters in length. Helium is used as the injectant to simulate hydrogen which will be used in future hydrogen/air combustion tests. Helium exits at sonic velocity from a 0.138 in. (3.5 mm) diameter converging circular nozzle (Figure 2).

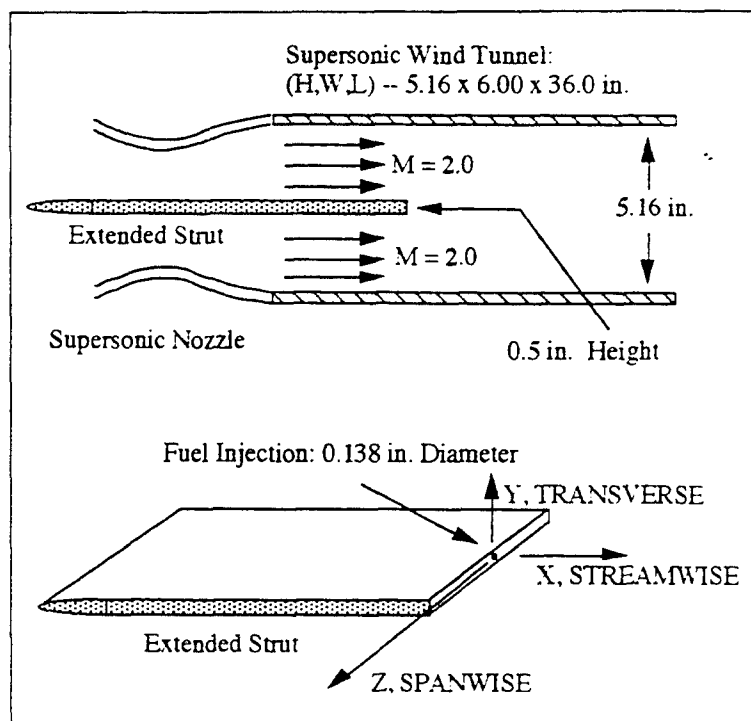


Figure 2 Schematic of extended strut and reference coordinate system



## Flow Diagnostics

### Planar Rayleigh/Mie Scattering

A Lambda Physik EMG 150 Excimer laser produced the 248 nm wavelength ultra-violet radiation used for Rayleigh/Mie scattering. The laser beam was transformed into a sheet, approximately 0.5 mm thick, and projected through the test section by a series of lenses and prisms as shown in Figure 3. A Princeton Instrument Intensified Charge Coupled Device (ICCD) camera with forced cooling captured images of the flow on command and stored them in a central processing unit (CPU) for subsequent analysis. The signal was collected through a Nikon UV-Nikkor 105 mm f/4.5 telephoto lens and was imaged onto the 578 by 384 pixel array of the ICCD camera. The effective gate width of approximately 10 ns, which is the laser temporal pulse width, is sufficiently short in duration to consider the images instantaneous. To keep the plane of interrogation in focus, the ICCD camera was mounted on the same three axis transverse table as the optics so that the laser sheet and camera moved in unison.

Naturally occurring moisture in the wind tunnel condenses to form an ice "fog" that effectively scatters the UV radiation. The resulting scattering highlights shock waves in the freestream and the mixing of the freestream air with the injected helium jet. Figure 4 a,b,c are schematic representations of the flow field as seen using the planar Rayleigh/Mie scattering technique. They are provided to outline the features of the flow field for reference when viewing the actual Rayleigh/Mie images. This visualization method with naturally occurring moisture has previously been used in supersonic boundary layers<sup>22,23</sup> and mixing layers.<sup>24</sup> Likewise, condensed droplets of ethanol added to the freestream flow have previously been used in visualizing supersonic mixing layers<sup>25</sup> and a transverse sonic jet.<sup>26,27</sup> However, these particles are not conserved scalars throughout the flow since the fluid temperature changes as it passes through shock waves, expansion waves, and viscosity dominated regions (i.e., boundary layer), possibly creating or destroying particles by condensation and evaporation respectively. A change in scattered light due to temperature change (particles being created/destroyed) cannot be discerned from an increase/decrease in scattered light due to existing particles amassing in a particular region.

The information contained in these images is analogous whether the scattering is Rayleigh or Mie. As long as the particles follow the flow, their size is not of critical importance. Because the particles are formed through a homogeneous nucleation process,<sup>28</sup> they are probably small. Evaluation of particle size by Elliot<sup>24</sup> in nominal Mach 2 and 3 freestream showed the particles to scatter light in the

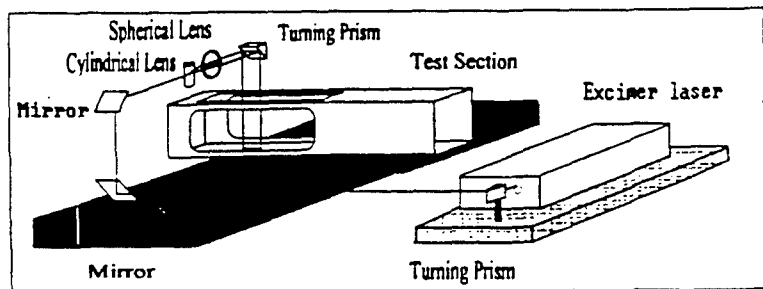


Figure 3 Mie scattering optical arrangement

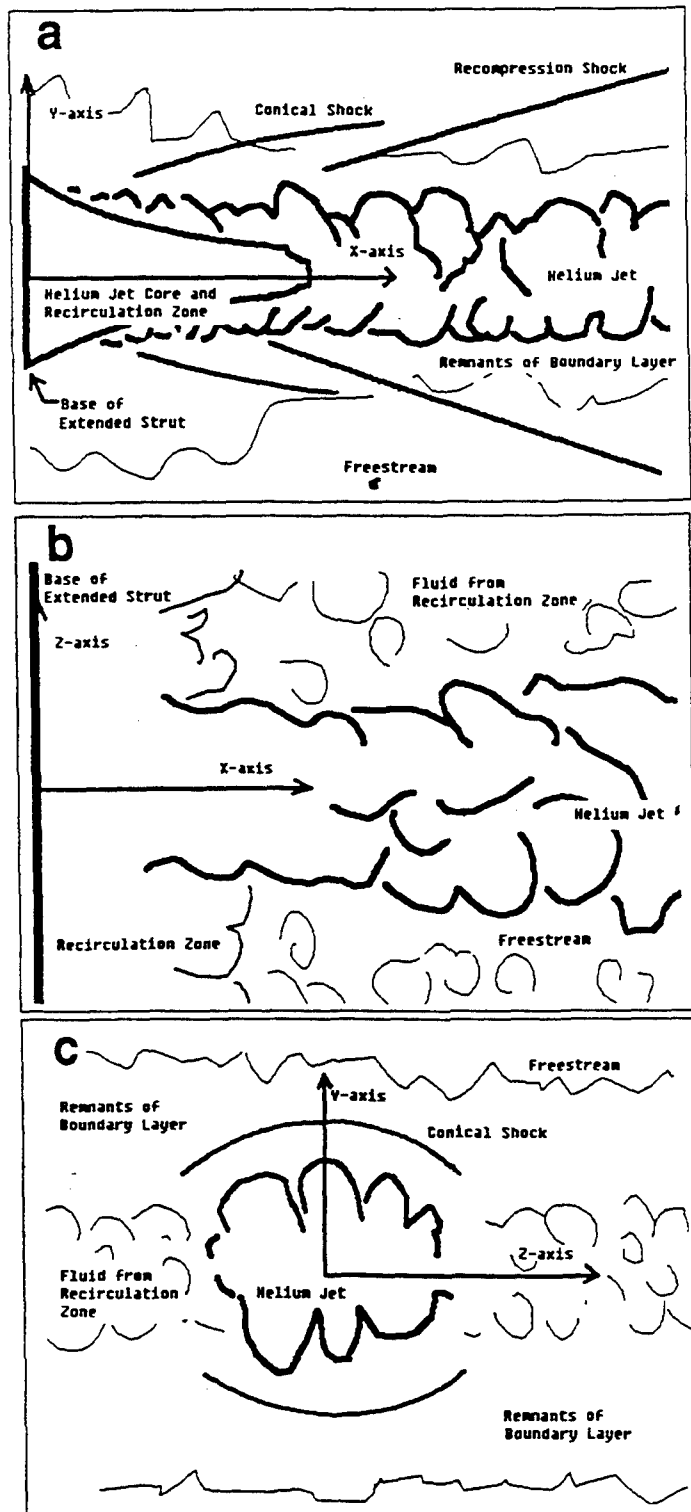


Figure 4 Schematic of planar Rayleigh/Mie images  
a) streamwise b) planar and c) face-on views

Rayleigh regime for a wavelength of 532 nm. The particles of the present study seem to follow the flow as represented by ligaments of freestream fluid, which contains particles, entrained in the helium jet (discussed in the Results portion of this paper). Future work will include measurements of the particle size.

### Acetone PLIF

A frequency doubled Spectra-Physics Quanta-Ray DCR-4 Nd:YAG laser (532 nm wavelength beam) in conjunction with a Quanta-Ray wavelength extender (WEX-1) produced the ultra-violet radiation (266 nm) for acetone PLIF. The acetone added to the helium jet was regulated and metered along with the helium gas flow rate. The same optical system as shown in Figure 3 was used except that the Excimer laser was replaced by the YAG/WEX system. Likewise, the same imaging system was used as in the Rayleigh/Mie set-up except that a Nikon Nikkor 60 mm f/2.8 Micro lens replaced the UV telephoto lens. Because of the visible fluorescence, an ordinary camera lens can be used; an added advantage of an ordinary lens is that it effectively blocks the strong particle scattering at 266 nm.

The acetone PLIF images show the internal shock structure of the injected helium jet (see the schematic in Figure 5). Acetone has proven to be superior to

other molecular tracers because of its high signal to noise ratio, non-toxic nature, and an excitation frequency that is easily accessible by different lasers.<sup>28</sup> Acetone ( $\text{CH}_3\text{-CO-CH}_3$ ) has a molecular weight of 58.08, a specific gravity of 0.79, and a vapor pressure of 3.48 psia (24 KPa) at 527 R (293 K). It absorbs light and is excited from a ground singlet state to a first excited singlet state in the 225-320 nm wavelength band. Most of the excited acetone molecules in the singlet state are transferred to the triplet state and almost all of the remaining excited singlet molecules fluoresce in the 350-600 nm wavelength band with a lifetime of a few nanoseconds. The triplet state molecules undergo phosphorescence which is shifted toward the red with respect to the singlet-state fluorescence, with a natural lifetime of approximately 200  $\mu\text{s}$ .<sup>29,30</sup> However, the triplet state is effectively quenched by  $\text{O}_2$ . The limited gate width of the camera captures only the fluorescence signal. The aforementioned acetone characteristics are included in a more detailed description by Lozano et al.<sup>28</sup>

### CFD Code and Conditions

All numerical results presented here were obtained through the use of the General Aerodynamic Simulation Program (GASP). All numerical results are three-dimensional and include the combustion tunnel nozzle solution starting from the subsonic portion of the nozzle, the throat area, subsequent expansion in the supersonic portion in the nozzle and the mixing regions starting at the base of the extended strut. All results were obtained using the flux-differencing scheme of Roe. In addition, Sutherland's law is used to determine individual laminar species viscosity while Wilke's rule is used to determine the mixture viscosity. The Baldwin-Lomax eddy viscosity model accounts for turbulence. Perfect gases are assumed and binary diffusion can occur under the presence of mass fraction gradients. The binary diffusion coefficient is calculated using a constant Schmidt number of 0.5.<sup>31</sup> Air and helium input conditions for the code were chosen to match

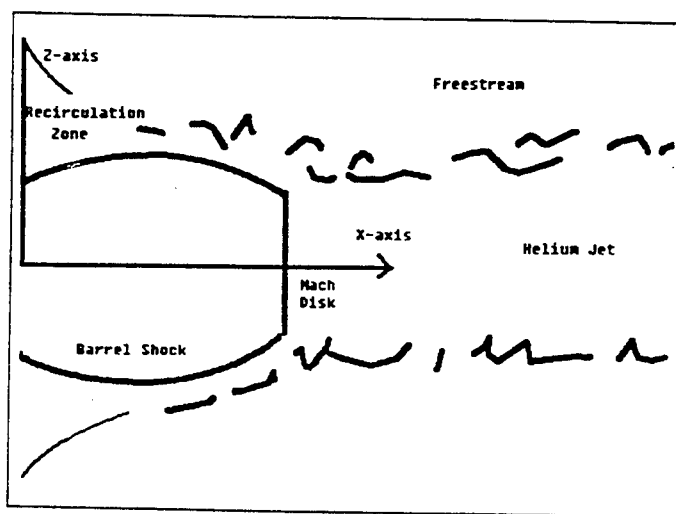


Figure 5 Schematic of PLIF image, streamwise view

Table 1 Operating conditions for helium injection into Mach 2 air freestream

	Po	To	Mach #	P $\infty$	t $\infty$	$\rho\infty$	u $\infty$
	Pa	K		Pa	K	kg/m <sup>3</sup>	m/s
Freestream	295,442	300	2.0	37,758	167	0.7894	518
He Case 1x	92,755	339	1.0	45,181	254	0.8556	939
He Case 2x	164,898	339	1.0	80,322	254	0.1521	939
He Case 4x	398,503	339	1.0	194,111	254	0.3676	939

the experimental operating conditions listed in Table 1.

The calculations were carried out in a multi-zone fashion with two zones in the nozzle region, one upstream of the base edge of the strut and two downstream of the injection point. For the two mixing zones, complete Reynolds averaged Navier-Stokes equations are solved. Locally, 3rd order computations of inviscid flux contributions in the streamwise and transverse directions are used in conjunction with 1st order accurate contributions of inviscid terms in the spanwise direction. Viscous contributions are second order accurate. Wall boundaries are treated as adiabatic, and first order computation of gradients at the wall are used.

Due to symmetry, only one quarter of the injector configuration was modeled. The near field around the injector is an unsteady and complex flow field. The goal of the CFD investigation was to capture the bulk characteristics of the mean flow to compliment the instantaneous experimental images. Note that the individual instantaneous experimental images are

representative of the relevant time-averaged experimental images of the flowfield, thus making direct comparison between CFD and experimental results meaningful.

## Results and Discussion

The helium is injected at nozzle-to-freestream air static pressure ratios of 1, 2, and 4 (denoted as cases 1x, 2x and 4x); these operating conditions are summarized in Table 1. Figure 4 shows schematic drawings of the three orthogonal planes of view for the Rayleigh/ Mie scattering technique: streamwise, planar, and face-on. Both the streamwise and the planar images represent a 1.7 by 1.1 in. field of view, with the flow direction being left to right. With the 578 by 384 pixel array of the camera, this corresponds to an apparent resolution of 0.0030 in. (76.2  $\mu$ m) per pixel. However, the overall resolution is limited by the laser sheet thickness of about 0.5 mm. The face-on view has a 1.2 by 0.8 in.

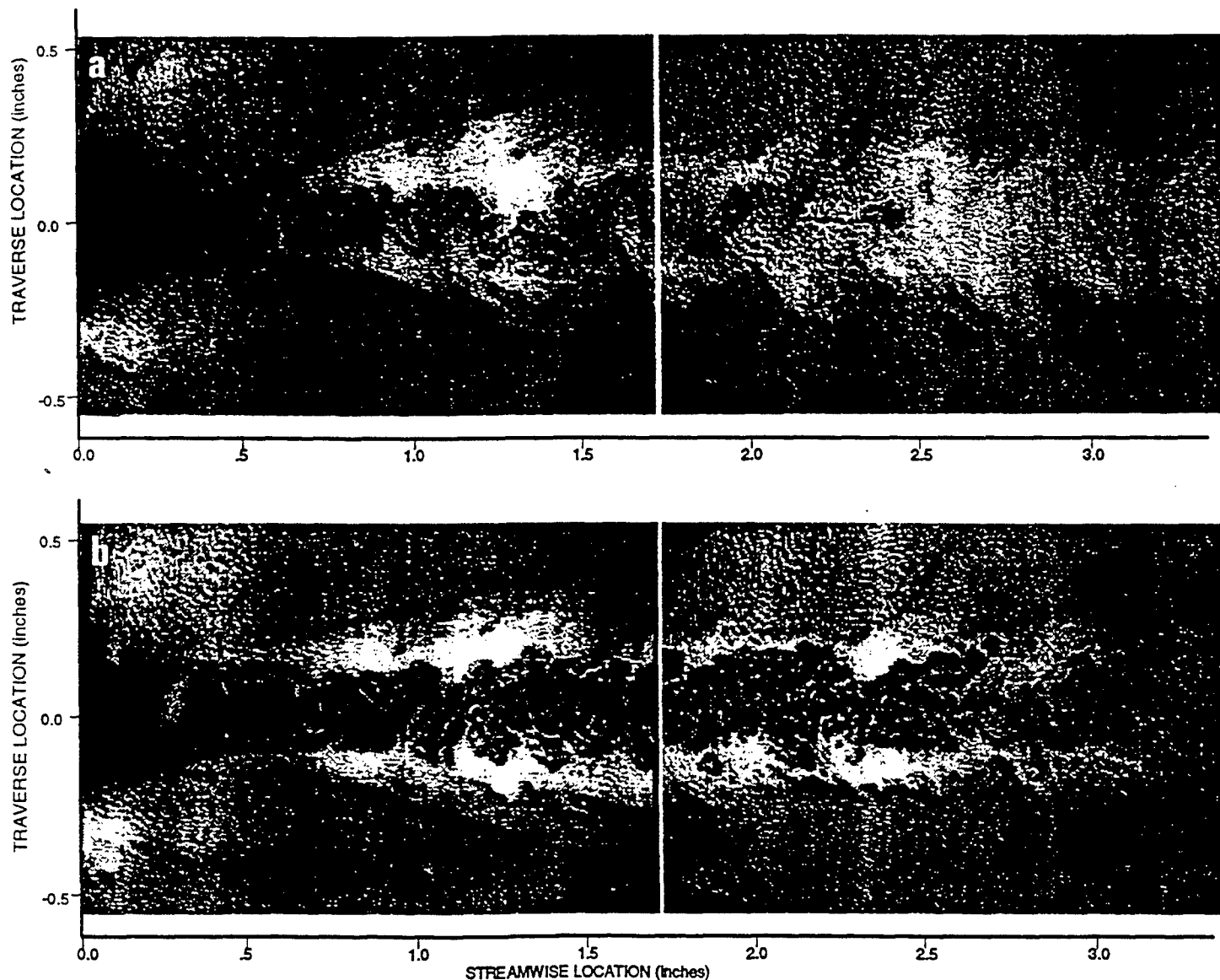


Figure 6 Streamwise views on centerline of a) no-injection and b) 1x pressure matched cases

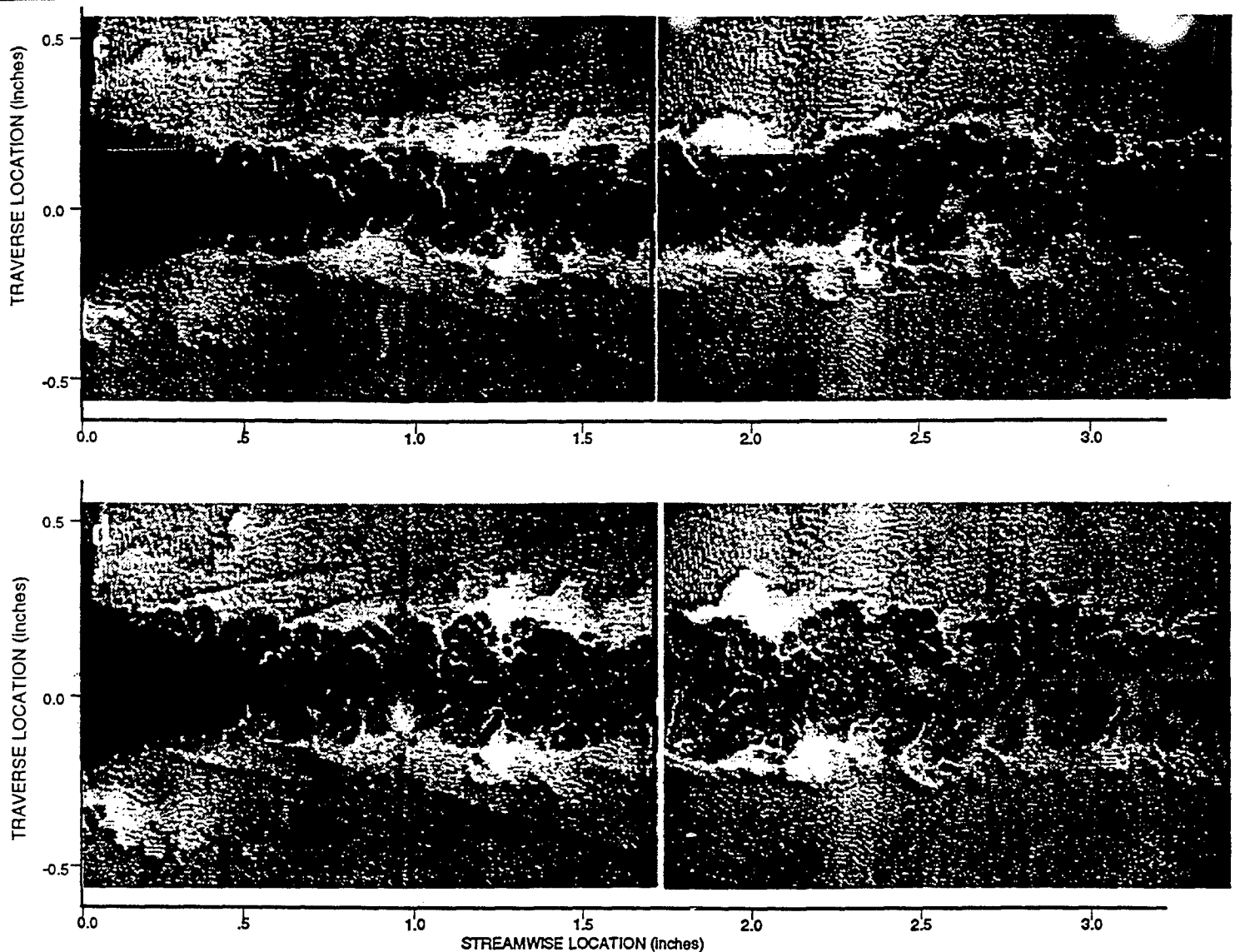


Figure 6 Streamwise views on centerline of c) 2x and d) 4x pressure matched cases

field of view with the flow direction being out of the plane of the page. Figure 5 shows the schematic drawing for the streamwise view for acetone PLIF, which has a 0.80 by 0.53 in. field of view.

Figure 6 shows Mie scattering images for all four cases studied: no injection, 1x, 2x, and 4x. This figure includes upstream and downstream views (taken during different laser pulses), separated by a white line, for each pressure condition. The images are not corrected for laser intensity variation or background, but the contrast is adjusted for print quality. The jet does not penetrate transversely beyond the strut 'boundary layer remnants' (i.e., fluid downstream of the strut base that was initially in the boundary layer), except for some structures in the 2x and 4x cases. The 'boundary layer remnants' are identified in the images as the most intense region of the freestream that borders the helium jet (Figures 4 and 6). This is similar to observations made in a comparable normal injection case where these 'boundary layer remnants' appear to 'ride' atop the injectant fluid.<sup>32</sup>

The field of view presented is limited to 25 jet diameters downstream of injection. Jet behavior may differ further downstream. The temperature and pressure of the 'boundary layer remnants' change with passage through the expansion fan and shock wave(s). This may decrease/increase the scattering signal intensity as previously discussed. The images show the boundary layer to be approximately 0.17 in. (4.3 mm) thick before reaching the base of the extended strut, while CFD results predict a 0.13 in. (3.3 mm) thick boundary layer.

From the streamwise views similar to Figure 6, average jet core lengths and recompression shock angles can be estimated. Conventional definitions of the jet core are based on injectant gas concentration measurements. Since the intensity change is not a known function of concentration in these images, determination of the core length is an approximation. The recirculation zone for the no injection case was observed to extend approximately 0.40 in. beyond the base of the strut in the direction of flow. The 0.40 in.

length of the recirculation zone relative to the 0.50 in. strut width is similar to observations in subsonic flow.<sup>33</sup> The recirculation/jet-core zone extends about 0.25 to 0.35 in. beyond this in all three injection cases. The recompression shock angles remain about the same for all three injection pressures and the no injection case. The slight variation between 12 and 16 degrees, measured with respect to the streamwise axis, indicates that the near-field injection plume does not significantly alter the freestream recompression shock angle. The large density and pressure gradients associated with the recompression shock are difficult to locate precisely in the CFD results because of the limited resolution of the three-dimensional CFD generation grid. However, the CFD results do show an increase in density and pressure across a region surrounding the presumed location of the recompression shock.

Figure 7 shows corresponding face-on Rayleigh/Mie images and CFD results for the 1x and 4x cases at a streamwise location of 0.5 in. (1.27 cm). Note that the face-on spanwise images are elongated along the

spanwise axis due to a 27 degree angle between the camera axis and the flow axis. After calculating trigonometric corrections for this distortion, the jet contour is still oblong with the major axis along the spanwise axis. The eccentricity ( $e = \sqrt{1 - b^2/a^2}$  where a, b are the semi-major and semi-minor axes, respectively) of the jet core region is greater than 0.86 for all injection cases.

The large scale mixing with the freestream fluid occurs primarily in the transverse direction as illustrated by the 'lobed' structures along the periphery of the jet contour in the transverse direction. These lobes are most visible in the 4x case (Figure 7b), but can be seen in the 2x and 1x cases (Figure 7a) as well. For the under-expanded cases where the structures are distinctly visible, the structures appear in the same position on the 5 images recorded at each location. Therefore, a time averaged image, corresponding to the CFD results, would show structures similar to those on the instantaneous images. The corresponding CFD plots of helium mole fraction (Figures 7c,d) show protuberances similar in appearance to the lobed

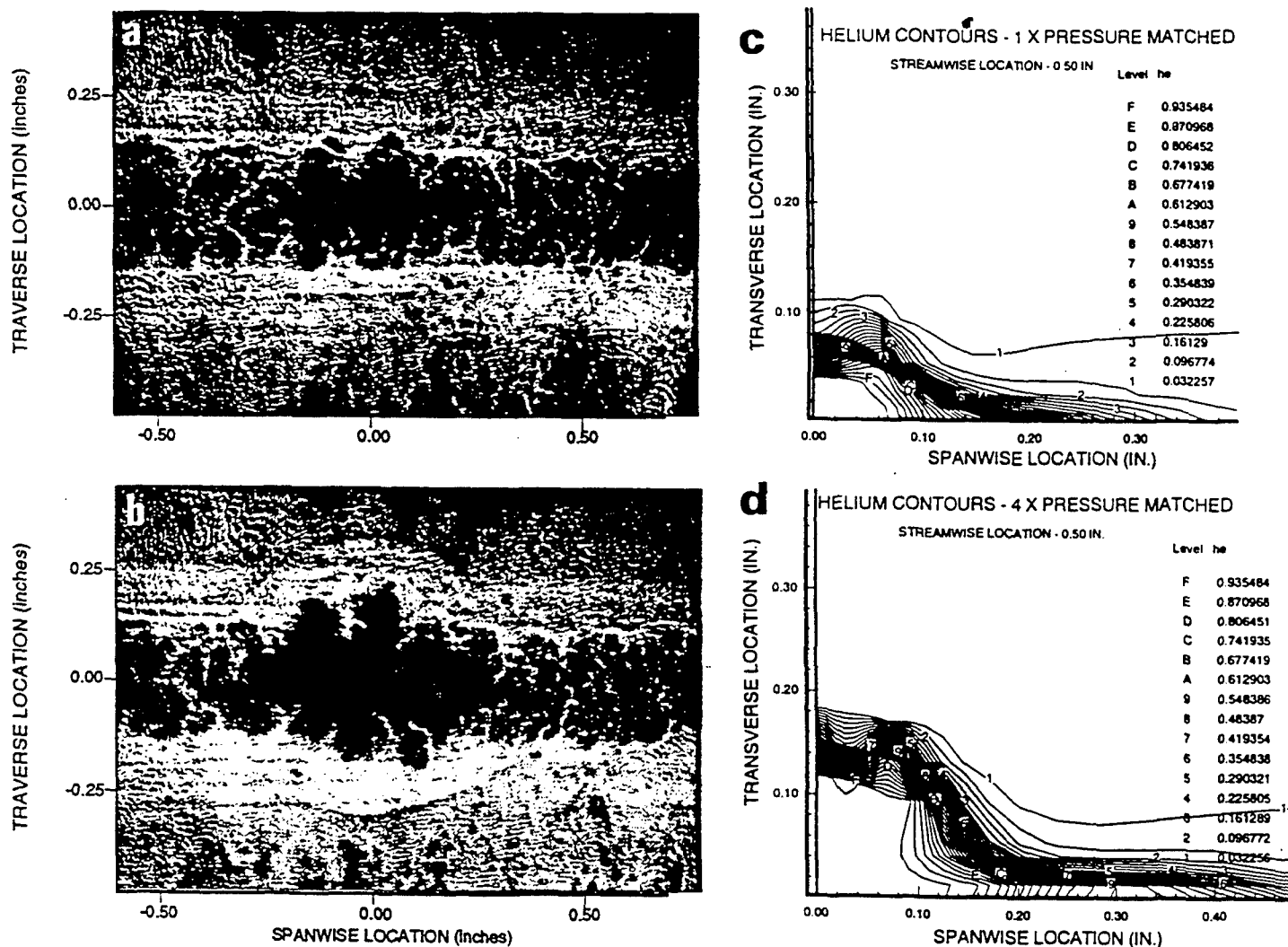
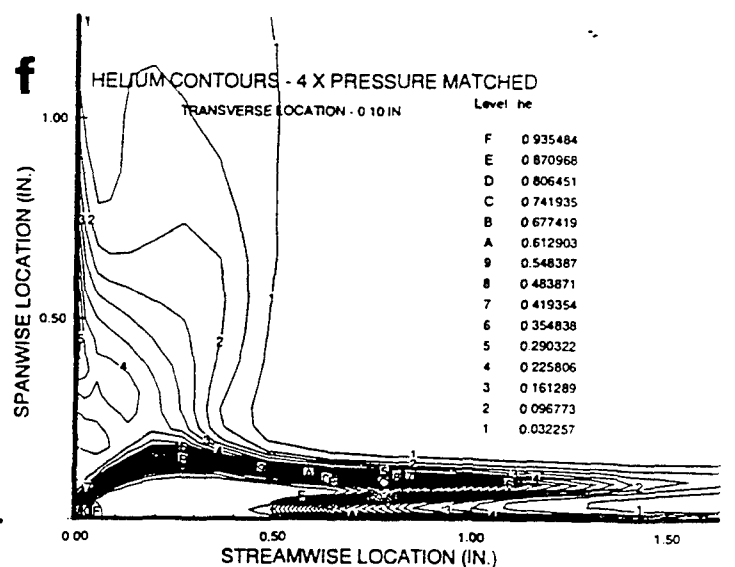
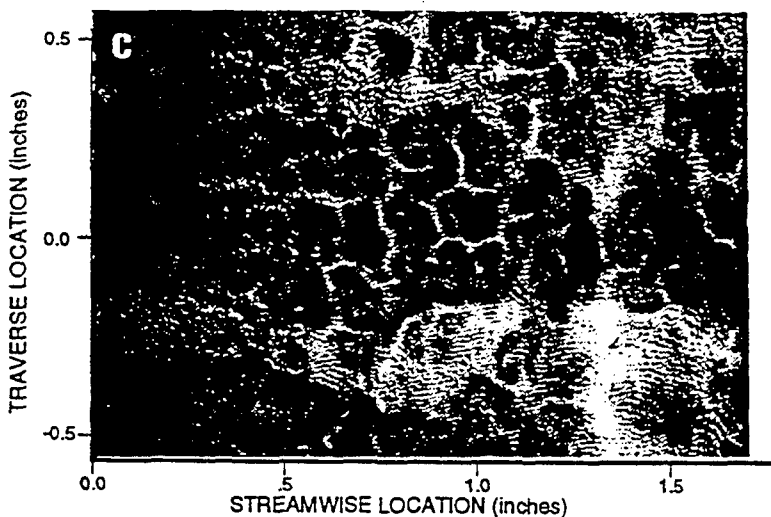
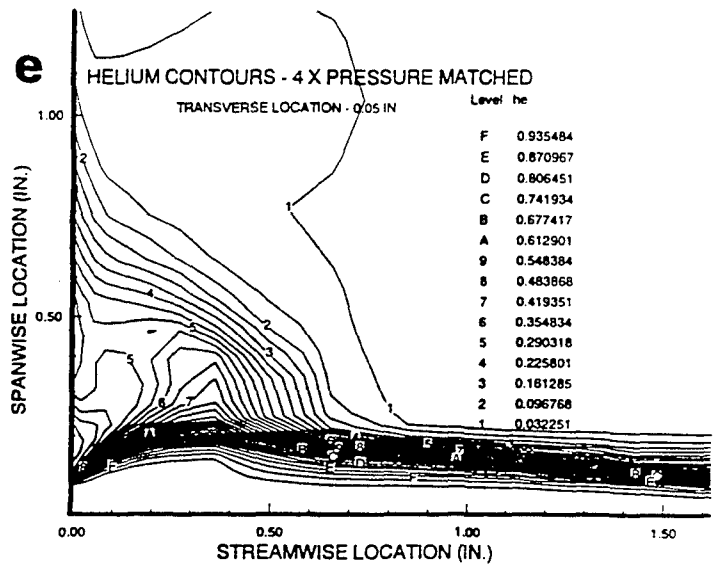
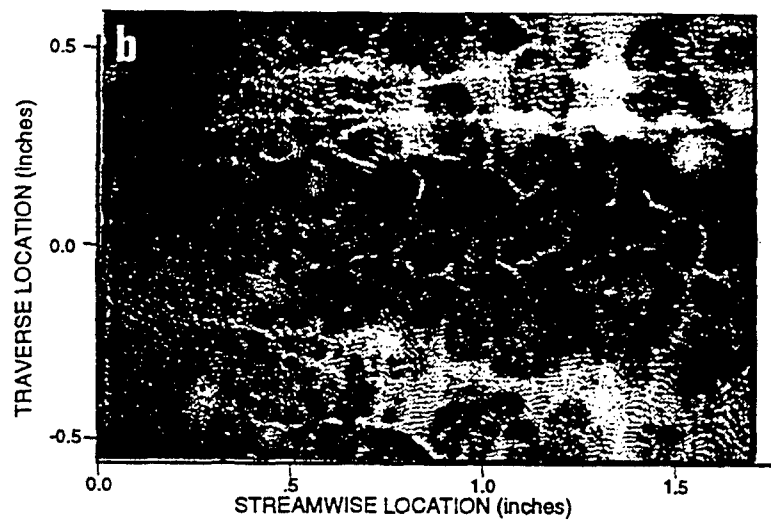
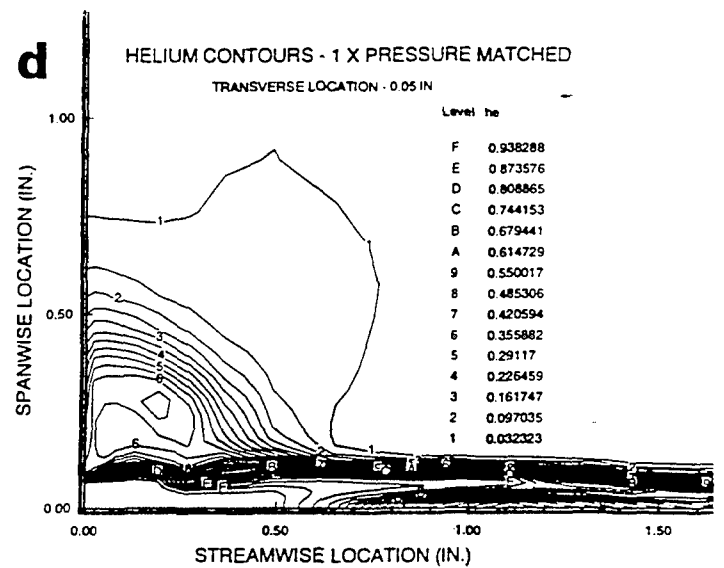
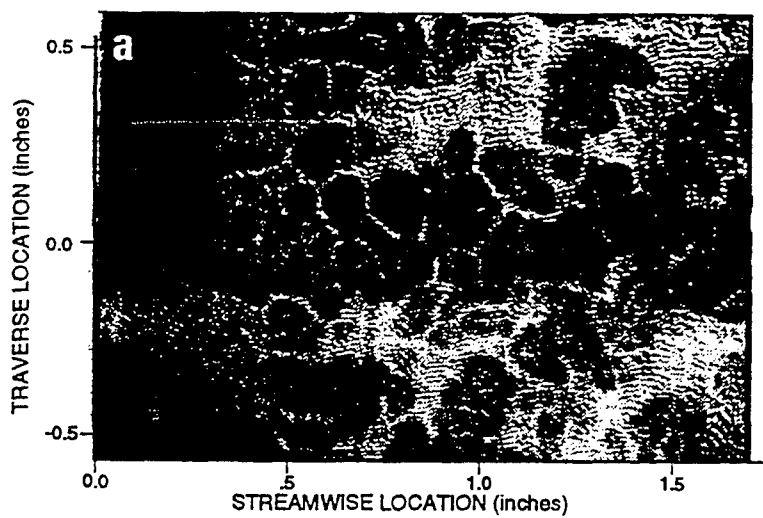
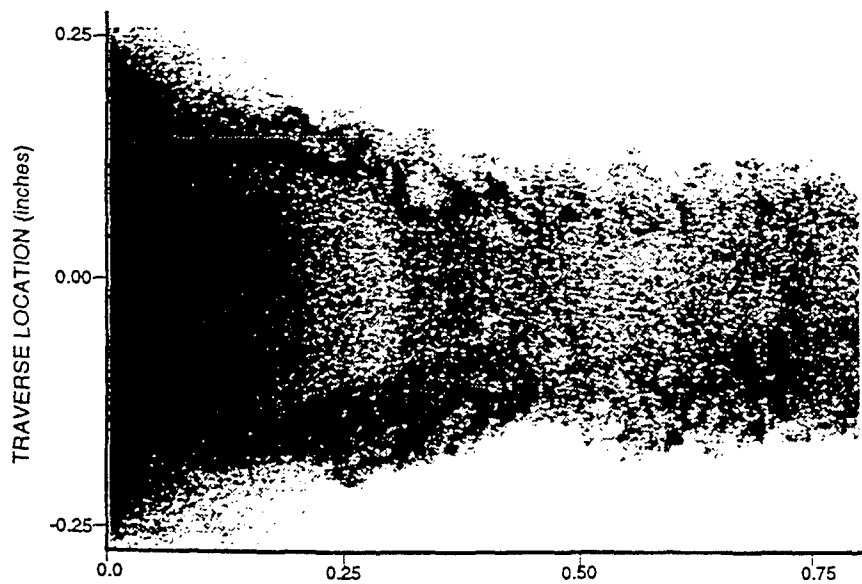


Figure 7 Face-on views at 0.5 in. downstream of extended strut base for a) 1x and b) 4x case using Rayleigh/Mie scattering and c) 1x d) 4x pressure matched case using results of CFD



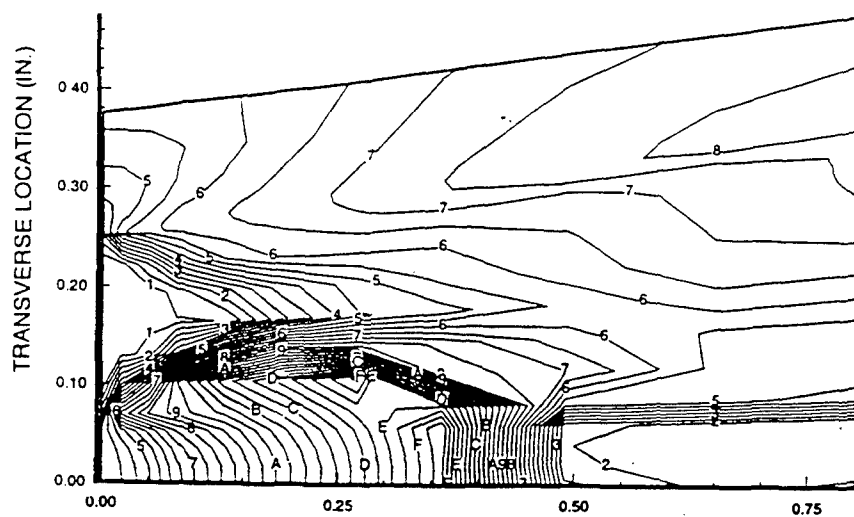
**Figure 8** Planar views for a) 1x and b) 4x cases at 0.05 in. off centerline and c) 4x case at 0.10 in. off centerline in the transverse direction using Rayleigh/Mie scattering the corresponding helium concentration profiles are shown in plots d, e, and f.



**Figure 9**

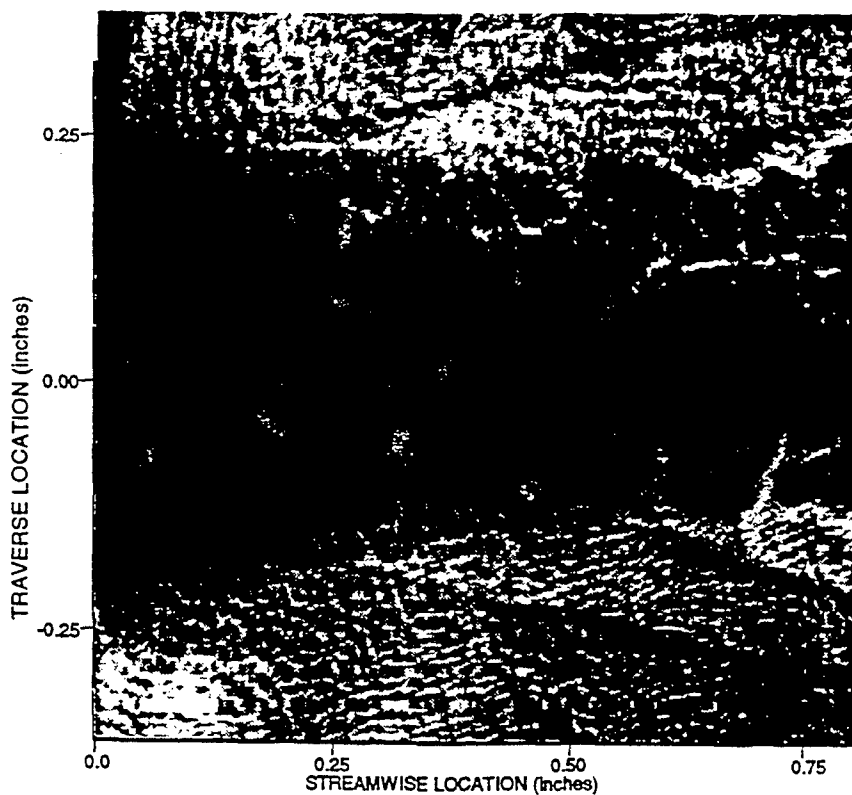
Streamwise views on centerline for  
4x pressure matched case:

- a) Acetone PLIF
- b) CFD generated Mach contours
- c) Planar Rayleigh/Mie scattering



Level M

F	4.95652
E	4.61504
D	4.27356
C	3.93209
B	3.59061
A	3.24913
9	2.90765
8	2.56617
7	2.2247
6	1.88322
5	1.54174
4	1.20026
3	0.858782
2	0.517304
1	0.175826



structures. Note that the CFD scale is more than twice the size of the image scale for better visibility of the protuberances.

Images taken in the other two orthogonal planes of view show these large scaled structures as well. Figure 8a,b shows planar cut images at a transverse location 0.05 in. (1.27 mm) above the centerline for the 1x and 4x cases. This view reveals consecutive sets of helium lobes propagating downstream (dark regions) and the entrained freestream fluid layer between them (bright ligaments). The lobes in the 4x case are not as distinct as the 1x case at this transverse location. The corresponding CFD plots (Figure 8d,e) of helium concentration show similar results. The CFD plot for the 1x case shows noticeable spacial fluctuations of helium concentration across the jet, whereas the plot of the 4x case is more uniform. This concentration difference corresponds to the appearance of more distinct bright freestream ligaments in the image of the 1x case. However a planar cut at 0.10 in. (2.54 mm) above the centerline for the 4x pressure case (Figure 8e) shows the same type of separation between structures as the 1x case at 0.05 in. This indicates that structures reach further in the transverse direction for the 4x case. Comparison of the corresponding CFD images (Figure 8d,f) supports the above observation.

Figure 9 displays close-up, streamwise views using PLIF, CFD, and Rayleigh/Mie data for the region immediately downstream of the injector for the 4x case. Upon leaving the injector, the under-expanded helium continues to accelerate until a barrel shock/Mach disk mechanism acts to raise the pressure to the required freestream value. This acceleration is captured in the PLIF images as a significant decrease in signal intensity (Figure 9a). The CFD results (Figure 9b) predict the location of the Mach disk reasonably well by comparison to the PLIF images, and estimate the final expansion Mach number to be approximately 5 for the 4x case. Similar results for the 1x and 2x cases indicate final expansion Mach numbers of 3.5 and 4, respectively. It is believed that the bending of the freestream fluid as it flows off the end of the extended strut and encounters the side region of the barrel shock causes a second shock to appear upstream of the recompression shock (Figure 9c). This shock also appears as a shadow-like outline of a bright ellipse surrounding the helium jet in the face-on view (Figure 7b). Comparing these two views reveals that the shock wave is cone shaped. This conical shock, however, does not appear in the 1x or 2x cases. One possible explanation is that the conical shock coalesces with the recompression shock in the 2x case. Another more likely explanation is that the influence of the barrel shock for the 2x case does not extend beyond the buffer region of the recirculation zone. The 1x case is pressure matched and has no barrel shock.

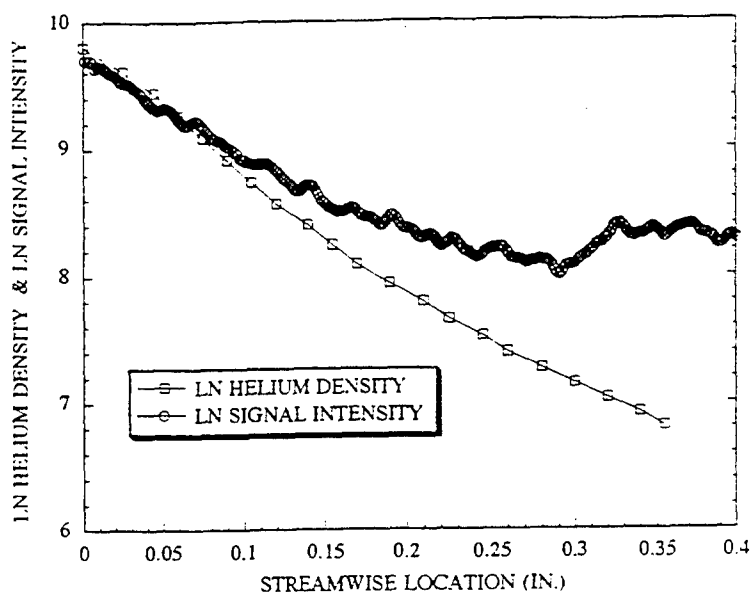


**Figure 10** Natural log (LN) of helium density compared to natural log of signal intensity

The use of acetone for injectant concentration measurements, as demonstrated in Figure 9a, is promising. However, the lack of signal intensity inside the barrel shock, where the helium and air have not yet mixed, indicates the signal intensity is not solely a function of mixture fraction. Instead, the fluorescence intensity apparently follows the helium number density. This behavior is expected when the spontaneous emission rate is much greater than the quenching rate.<sup>28</sup> Figure 10 shows a logarithmic plot comparing collected signal intensity to CFD calculated helium density for the near field region of Figure 10. The curves agree in the extreme near field but begin to diverge further downstream. This difference may be due to several factors which include, but are not limited to, laser sheet variations, the effects of unidentified flow phenomena on the fluorescence signal, and possible CFD inaccuracies. Until further studies have been completed and this relationship is completely understood, direct mixture fraction measurements from the PLIF signal are not possible.

## Conclusions

The sonic helium jet that was injected coaxially into a Mach 2 airstream did not spread significantly for any of the three pressure cases considered. The jet fluid remains within the remnants of the splitter plate boundary layer with the exception of some large scale structures reaching into the freestream (particularly for the 4x case). However, the jet does spread predominantly along the spanwise direction creating an oblong jet contour with large scale structures evident along the transverse axis of the jet. These structures appear to be spatially periodic and more organized in the under-expanded cases as compared to the pressure matched case. The jet spread is markedly three-dimensional as



seen by the irregular jet contours downstream of injection and by the conical shock in the highly under-expanded case.

The numerical simulation captures the essential features of the flow field, namely the barrel shock, Mach disk, recirculation region, and expansion zone. In addition, the Mach disk location and helium jet spread predicted by these numerical simulations agree reasonably well with the Rayleigh/Mie scattering and acetone PLIF images from experiments.

Future studies will involve other appropriate measurement techniques and mixing enhancement schemes. Laser Doppler Velocimetry (LDV) measurements will allow more precise determination of the jet width and the boundary layer thickness in addition to providing statistical velocity information. Acetone PLIF, with refinement, will provide more detailed information about the extent of mixing. Passive mixing enhancement by the use of different nozzle geometries and stationary impinging shock waves will be explored. When concentration and velocity information become available, the GASP code will be tested further.

### Acknowledgements

The support of Dr. Julian Tishkoff and the Air Force Office of Scientific Research is greatly appreciated. Special thanks to Dave Schommer, Charles Smith, and Campbell Carter for their technical assistance.

### References

- <sup>1</sup>Jacobs, P.A., Rogers, R.C., Weidner, E.H., and Bittner, R.D., "Flow Establishment in a Generic Scramjet Combustor," AIAA Paper 90-2096, 1990.
- <sup>2</sup>Northam, G.B., Trexler, C.A., and McClinton, C., "Flame-holding Characteristics of a Swept Strut Hydrogen Fuel Injector for Scramjet Application," NASA TR A81-10711, 1981.
- <sup>3</sup>Anderson, G.Y., Reagon, P.G., Gooderum, P.B., and Russin, W.R., "Experimental Investigation of a Swept Strut Fuel Injector concept for Scramjet Application," NASA TN D-8454, 1977.
- <sup>4</sup>King, P.S., Thomas, R.H., Schetz, J.A., Billig, F.S., "Combined Tangential-Normal Injection Into a Supersonic Flow," AIAA Paper 89-0622, 1989.
- <sup>5</sup>Ho, C.M., and Gutmark, E., "Vortex Induction and Mass Entrainment in a Small-Aspect-Ratio Elliptic Jet," *J. Fluid Mech.*, Vol. 179, 1987, pp. 383-405.
- <sup>6</sup>Gutmark, E., Schadow, K.C., and Wilson, K.J., "Subsonic and Supersonic Combustion Using Non-Axisymmetric Injectors," AIAA Paper 88-3141, 1988.
- <sup>7</sup>Gutmark, E., Schadow, K.C., and Wilson, K.J., "Noncircular Jet Dynamics in Supersonic Combustion," *J. Propulsion*, Vol. 5, No. 5, 1989, pp. 529-533.
- <sup>8</sup>Quinn, W.R., "On Mixing in an Elliptic Turbulent Free Jet," *Phys. Fluids A*, Vol. 1, No. 10, 1989, pp. 1716-1722.
- <sup>9</sup>Samimy, M., Zaman, K.B.M.Q., and Reeder, M.F., "Effect of Tabs on the Flow and Noise Field of an Axisymmetric Jet," *AIAA Journal*, Vol. 31, No. 4, 1993, pp. 609-619.
- <sup>10</sup>Wlezien, R.W., and Kibens, V., "Influence of Nozzle Asymmetry on Supersonic Jets," *AIAA Journal*, Jan. 1988, pp. 27-33.
- <sup>11</sup>Longmire, E.K., Eaton, J.K., and Elkins, C.J., "Control of Jet Structure by Crown-Shaped Nozzles," *AIAA J.*, Vol. 30, No. 2, 1992, pp. 505-512.
- <sup>12</sup>Hussain, A.K.M.F., and Zedan, M.F., "Effects of the Initial Condition of the Axisymmetric Free Shear Layer: Effects of the Initial Momentum Thickness," *Phys. Fluids*, Vol. 21, no.7, 1978, pp. 1100-1112.
- <sup>13</sup>Hussain, A.K.M.F., and Zedan, M.G., "Effects of the Initial Condition on the Axisymmetric Free Shear Layer: Effect of the Initial Fluctuation Level," *Phys. Fluids*, Vol. 21, No. 9, 1978, pp. 1475-1481.
- <sup>14</sup>Gutmark, E., Schadow, K.C., and Wilson, K.J., "Mixing Enhancement in coaxial Supersonic Jets," AIAA Paper 89-1812, 1989.
- <sup>15</sup>Papamoschou, D., and Roshko, A., "The compressible turbulent mixing layer: an experimental study," *J. fluid Mech.*, Vol. 197, 1988, pp. 453-477.
- <sup>16</sup>Samimy, M., and Elliot, G.S., "Effects of Compressibility on the characteristics of free shear layers," *AIAA J.*, vol. 28, 1990, pp. 439-445.
- <sup>17</sup>Samimy, M., Reeder, M.F., and Elliott, G.S., "Compressibility effects on Large Structures in Free Shear Flows," *Phys. Fluids A*, Vol. 4, 1992, pp. 1251-1258.
- <sup>18</sup>Marble, F.E., Zukoski, E.E., Jacobs, J.W., Hendricks, G.J., and Waitz, I.A., "Shock Enhancement and Control of Hypersonic Mixing and Combustion," AIAA Paper 90-1981, 1981.
- <sup>19</sup>Budzinski, J.M., Zukoski, E.E., and Marble, F.E., "Rayleigh Scattering Measurements of Shock Enhanced Mixing," AIAA Paper 92-3546, 1992.
- <sup>20</sup>Jacobs, J.W., "Shock-induced mixing of a light-gas cylinder," *J. Fluid Mech.*, Vol. 234, 1992, pp. 629-649.
- <sup>21</sup>Gruber, M.R., and Nejad, A.S., "Development of a Large-Scale Supersonic Combustion Research Facility," AIAA Paper 94-0544, 1994.
- <sup>22</sup>Miles, R. and Lempert W., "Two-Dimensional Measurement of Density, Velocity and Temperature in Turbulent High-Speed Air Flows by UV Rayleigh Scattering," *Appl. Phys. B*, Vol. 51, 1990, pp.1-7.
- <sup>23</sup>Arnette, S.A., Samimy, M., and Elliot, G.S., "The Effect of Expansion on the Large Scale Structure of a Compressible Turbulent Boundary Layer," AIAA Paper 93-2991, 1993.
- <sup>24</sup>Elliott, G.S., Samimy, M., and Arnette, S.A., "Filtered Rayleigh Scattering Based Measurements in Compressible Mixing Layers," AIAA Paper 92-3543, 1992.
- <sup>25</sup>Clemens, N.T. and Mungal, M.G., "A Planar Mie Scattering Technique for Visualizing Supersonic Mixing Flows," *Exp. in Fluids*, Vol. 11, 1991, pp.175-185.

- <sup>26</sup>Hermanson, J.C. and Winter M., "Imaging of a Transverse, Sonic Jet in Supersonic Flow," AIAA Paper 91-2269, 1991.
- <sup>27</sup>Hermanson, J.C., and Winter M., "Mie Scattering Imaging of a Transverse, Sonic Jet in Supersonic Flow," AIAA J., Vol. 31, No. 1, 1993, pp.129-132.
- <sup>28</sup>Lozano, A., Yip, B., and Hanson, R.K., "Acetone: a Tracer for Concentration Measurements in Gaseous Flows by Planar Laser-Induced fluorescence," *Exp. in Fluids*, Vol. 13, 1992, pp. 369-376.
- <sup>29</sup>Greenblatt, G.D., Ruhman, S., and Haas, Y., "Fluorescence Decay Kinetics of Acetone Vapor at Low Pressures," *Chem. Physics Letters*, Vol. 112, No. 3, 1984, pp. 200-206.
- <sup>30</sup>Copeland, R.A., and Crosley, D.R., "Radiative, Collisional and Dissociative Processes in Triplet Acetone," *Chem. Physics Letters*, Vol. 115, No. 4, 1985, pp. 362-368.
- <sup>31</sup>Balu, S., Donbar, J.M., and Nejad, A.S., "Numerical Study of Mixing in High and low Enthalpy Supersonic Test Facility", JANNAF Propulsion Meeting and 30th JANNAF Combustion Subcommittee Meeting, Monterey, California, Nov. 1993.
- <sup>32</sup>Gruber, M.R., Nejad, A.S., Chen, T., and Dutton, J. "Mixing and Penetration Studies of Sonic Jets in a Mach 2 Freestream," AIAA Paper 94-0709, 1994.
- <sup>33</sup>Raffoul, C., and Nejad, A., Chen, T., and Dutton, J., "Entrainment and Mixing Characteristics of Bluff Body Flameholders; An Experimental and Numerical Study," AIAA Paper 94-0710, 1994.

THIS PAGE LEFT BLANK INTENTIONALLY



**AIAA 95-0522**

**Effects of Nozzle Geometry on Parallel  
Injection from Base of an Extended Strut  
into a Supersonic Flow**

**Diana D. Glawe, Mo Samimy,**  
Department of Mechanical Engineering  
The Ohio State University  
Columbus, OH 43210

**Abdollah S. Nejad**  
Wright Laboratory/POPT  
Wright-Patterson AFB, OH 45433-6563

and

**Tzong H. Chen**  
Taitech, Inc.  
3675 Harmeling Drive  
Beavercreek, OH 45440-3568

**33rd Aerospace Sciences  
Meeting and Exhibit  
January 9-12, 1995 / Reno, NV**

# Effects of Nozzle Geometry on Parallel Injection from the base of an Extended Strut into a Supersonic Flow

Diana D. Glawe\* and Mo Samimy<sup>+</sup>  
Department of Mechanical Engineering  
The Ohio State University  
Columbus, OH 43210

Abdollah S. Nejad\*\*  
Wright Laboratory/POPT  
Wright-Patterson AFB, OH 45433-6563

and

Tzong H. Chen<sup>++</sup>  
Taitech, Inc.  
3675 Harmeling Drive  
Beavercreek, OH 45440-3568

## Abstract

Fuel injection from the base of a two-dimensional extended strut bounded above and below by Mach 2 freestreams was investigated. Fuel, simulated with helium, was injected parallel to the Mach 2 freestreams before expansion and various injector nozzle geometries were investigated. Without injection, a nominally two-dimensional recirculation zone is set up behind the base of the strut. When fuel is injected at the strut base, a highly three-dimensional complex flowfield results. The behavior of the flowfield generated by a circular injection nozzle was characterized using LDV and Rayleigh/Mie scattering. Results were compared to those obtained with two other nozzle geometries - an elliptic nozzle and a circular nozzle with vortex-generating tabs. For comparing the relative merits of the various geometries from the perspective of enhancing mixing, a novel Total Mixing Evaluation methodology was developed. This approach evaluates the mixing potential of the flowfield by employing the large-scale mixing parameters such as perimeter, area, and shape factor. For quantifying the mixing effectiveness, a small-scale mixing parameter referred to as the mixedness was defined and computed. Although detailed data were obtained, only preliminary results are currently available. The preliminary results indicate the circular-with-tabs nozzle provided the most desirable large- and small-scale mixing enhancement characteristics.

## 1.0 Introduction

Gaseous injection into supersonic flows has many engineering applications. One application of primary interest to the aerospace community is the injection of gaseous hydrogen or hydrocarbon fuels in supersonic combustion ramjet (SCRAMJET) engines. It has been argued that airbreathing supersonic combustion engines offer the best performance for a single-stage-to-orbit flight vehicle. However, the challenges involved in realizing such a vehicle are still beyond present capabilities.

Designing an injection scheme to produce optimal fuel-air mixing and combustion within the space and time constraints of a supersonic combustor remains a daunting challenge. Enhancement and control of fuel-air mixing in supersonic flows suffers from very short time scales and inherently low mixing rates at higher Mach numbers. Parallel, normal, and oblique injection have all been investigated. Normal injection produces the best mixing but a greater total pressure loss primarily due to the generation of a strong bow shock [King et al., 1989]. Parallel injection of fuel can provide a significant component of the engine thrust in high flight Mach numbers, but typically provides limited mixing capability. To enhance mixing associated with parallel injection, many investigators have employed discrete ramp injectors designed to enhance mixing by vortex shedding, flow separation, and shock impingement. An advantageous consequence of injection from ramps and struts is the formation of a recirculation zone capable of flameholding. Continuous progress has been made in characterizing and optimizing ramp injectors [Bogdanoff, 1994, Waitz et al., 1992]. Injection at oblique angles to the flow has shown an improved total pressure recovery relative to normal injection and an improved mixing and fuel distribution relative to parallel injection [Fuller et al., 1992,

\* Senior knight Student, AIAA Member

<sup>+</sup> Professor, AIAA Senior Member

<sup>\*\*</sup> AIAA Member

<sup>++</sup> AIAA Senior Member

This paper is declared a work of the U.S. Government and is not subject to copyright protection in the United States.

McClinton, 1972]. However, as in normal injection, penetration is limited to the near wall region.

Fuel penetration and fuel distribution are of major concern in the design of injectors for supersonic combustors. To date, some of the practical injector designs employ in-flow struts for even fuel placement and distribution within the combustor flowfield. In subsonic flows many investigators have studied parallel injection of fuel behind bluff-bodied flameholders. Both passive (injector geometry effects) and active (acoustic excitation) forcing have been used to enhance mixing. However, very limited data is available for this type of injection into supersonic flows. The objectives of this investigation were to determine the fundamental characteristics of parallel fuel injection into a supersonic freestream from the base of an extended strut and to explore passive mixing enhancement through the use of different injector nozzle geometries.

## 2.0 Facility

This research was conducted in the supersonic combustion research facility at the Aero Propulsion and Power Directorate, Wright-Patterson Air Force Base [Gruber & Nejad, 1994]. The tunnel is capable of continuous operation at maximum stagnation conditions of 2.75 MPa and 890 K at a peak flow rate of 15.5 kg/s. The test section temperature and pressure conditions are adjusted by mixing air from hot and cold supply lines in controlled quantities. The test section, which is depicted schematically in Fig. 1, is 15.2 cm-wide by 13.1 cm-high, and has optical access from three sides and from the downstream end.

A 1.27-cm-thick strut provides rigid support for the injection nozzles and also provides a recirculation zone for flame holding in combustion studies. By extending the strut upstream through the nozzle into the settling chamber, as shown in Fig. 1, and using the method of characteristics to design the Mach 2 nozzles, the presence of strong waves in the freestream was avoided. LDV profiles show very symmetric and uniform nominal Mach 2 flow on each side of the strut. The mean velocity and turbulence profiles show the freestreams above and below the strut to be very uniform with turbulence intensities of about 1%. An example of the LDV profiles obtained is shown in Fig. 2. This profile is located in the test section at  $x = 2.54$  cm (where  $X = 0$  at the base of the strut). LDV measurements acquired in the boundary layers on the surfaces of the strut ( $X = -1.27$  cm) give a boundary layer thickness of approximately  $\delta = 5.6$  mm. In addition, the boundary layer turbulence intensities lie within the expected range for fully developed boundary layers when compared to data from previous studies [Kuntz et al., 1987].

In this study, the three injection nozzle geometries shown in Fig. 3 -- circular, circular-with-tabs, and elliptic -- were employed. The nozzles were rigidly

mounted in the base of the strut at the center-line of the tunnel. All three nozzles were machined (by electrical discharge machining) to converge to a minimum cross-sectional area at the nozzle exit. The exit area of all three nozzles was  $9.6 \text{ mm}^2$ . The diameter of the circular and circular-with-tabs nozzles was 3.5 mm. The width of the tabs was 0.86 mm and the tabs extended into the flow with a projected length of 0.38 mm. The tabs were at an angle of 135 degrees with respect to the jet axis, the configuration which has been shown to have the greatest mixing effect [Zaman et al., 1995]. The ellipse had a semi-major diameter of 6.15 mm and a semi-minor diameter 2.05 mm, resulting in an equivalent diameter of 3.5 mm and an aspect ratio of 3:1. The elliptic and circular-with-tabs nozzles were rotated to examine the effects of different angular orientations. Injection from the nozzles with the orientations shown in Fig. 4 will hereafter be referred to by the symbols C, T1, T2, T3, E1, E2, E3. The no injection case will be denoted as N.

Helium, used as the injectant to simulate hydrogen fuel, exited the converging nozzles at sonic velocity. The helium mass flow rate was varied so that the ratio of the static pressure of the helium jet at the nozzle exit to the static pressure of the freestream air was approximately  $\psi = P_{\text{nozzle}} / P_{\text{freestream}} = 4$ . The operating conditions are listed in Table 1. The  $\psi = 4$  ratio was chosen to obtain a highly underexpanded jet. This most accurately mimics operational fuel injection in scramjets, where the injected fuel is typically at supercritical conditions. As hydrogen fuel will probably be used to cool the external vehicle surface in scramjet applications, the fuel will achieve high temperatures and pressures -- likely into the supercritical thermodynamic range.

## 3.0 Experimental Techniques

Flow visualization was obtained by schlieren photography and planar Rayleigh/Mie scattering techniques, and velocity profiles were obtained with two-component Laser Doppler Velocimetry (LDV).

Schlieren images were acquired using a mercury arc lamp and 20-cm-diameter plano-concave transmitting mirrors. Images were captured on 10.2 x 12.7 cm Polaroid film using a 1/400 second shutter speed.

The optical arrangement for the planar Rayleigh/Mie scattering visualizations is given in Fig. 5. A Lambda Physik EMG 150 Excimer laser provided ultraviolet light ( $\lambda = 248 \text{ nm}$ ). The laser beam was transformed into a sheet, approximately 50 mm wide and 0.3 mm thick at the waist, and projected through the test section by a series of lenses and prisms. Three separate configurations were used to obtain laser sheets in the X-Y, X-Z, and Y-Z planes. The system configuration for streamwise (X-Y) view is shown in Fig. 5.

The scattered light signal was collected through a Nikon UV-Nikkor 105-mm  $f/4.5$  telephoto lens and imaged onto the 578 x 384 pixel array of a Princeton Instrument Intensified Charge Coupled Device (ICCD) camera. The temporal duration of the laser pulse, approximately 20 ns, is sufficiently short to consider the images instantaneous.

The Rayleigh/Mie scattering images were obtained by the "scalar transport" technique. The incident UV radiation was scattered off ice crystals from the condensed moisture naturally present in the wind tunnel supply air. As air passed through the supersonic tunnel nozzle, the moisture condensed to form an ice "fog" that scatters incident laser light. As in other investigations which have used this method of marking a supersonic flow, whether the scattering is in the Rayleigh or Mie regime is not important so long as the particles accurately track the flow. Previous investigations have shown that these particles are small enough to follow the large scale turbulent fluctuations in the flow [Elliott et al., 1992, Wegner & Pouring, 1964].

The ice crystals mark the freestream air. The injectant helium, on the other hand, was free of condensation. This, combined with helium's small scattering cross section, resulted in negligible scattering from the helium relative to the air containing condensation. Thus, the Rayleigh/Mie images appear bright where air is present and dark where helium is present. Regions of mixed fluid fall between the bright and dark extremes.

A set of 20 instantaneous images was recorded for selected locations and operating conditions. Both the streamwise (sheet in the X-Y plane) and the spanwise (sheet in the X-Z plane) images represent a 4.32 x 2.79 cm field of view, with the flow direction being left to right. The face-on images (sheet in the Y-Z plane) represent a 3.05 x 2.03-cm field of view with the flow direction out of the plane of the page. The camera was located approximately 30 degrees off of the X-axis in the face-on images. As a result, the images are elongated approximately 15% in the spanwise (Z) direction.

For the two-component LDV measurements, the 488 nm and 514.5 nm wavelength lines of an argon-ion laser were used. The measurement volume for each wavelength was approximately 4 mm in length and 130  $\mu\text{m}$  in width, with 16 fringes spaced approximately 7.9  $\mu\text{m}$  apart. The collecting optics unit was positioned at approximately 21 degrees off the forward scattering axis. The LDV system recorded approximately 5,000 acceptable bursts per measurement location. LDV profiles were obtained along the transverse (Y) and spanwise (Z) axes at several streamwise (X) locations.

#### 4.0 Results and Discussion

Modern computational techniques and knowledge derived from past experimental research can be used to

predict turbulent phenomena in simple flows. However, in a complex three-dimensional flow as is studied here, computation methods are not available and gaining solid understanding of the underlying physics is very difficult. In the current flow, the injected jet of helium and the mixing layers shed from both surfaces of the strut undergo complex interactions. Given these interactions, it is expected that data obtained in basic flows such as turbulent mixing layers and jets is of limited use in the present investigation. We have obtained detailed data, however, only some preliminary results will be discussed in this paper.

The flowfield with no injection, N, was examined to establish a reference case against which the injector nozzle geometries could be evaluated. A schlieren image of the no-injection case is given in Fig. 6. The boundary layers on the top and bottom strut surfaces are visible. The Mach 2 freestream and boundary layers expand around the base of the strut and encircle a recirculation zone. At the trailing edge of the expansion regions, recompression shock waves are formed where the two mixing layers shed from the strut surfaces meet and interact. In the freestream, the shock waves appear as a half dark/half light stripe on the Rayleigh/Mie image of the streamwise view (Fig. 7a). The dark strip shows the region where the ice crystals melt and evaporate as they pass through the temperature gradient associated with the shock. This two-dimensional recompression shock wave, typical of a base flow, appeared in all cases.

For the no-injection case (Fig. 7a), the Rayleigh/Mie images show the recirculation zone behind the base of the strut. The static temperature of the recirculation zone is approximately equal to the stagnation temperature (300 K). This drives the water condensation back into the vapor state. This destruction of the scattering condensation is why the recirculation zone appears dark in Fig. 7a.

Injecting helium with nozzles located in the base of the strut creates a highly three dimensional flowfield. A streamwise image on the centerline of the injector nozzle for the circular nozzle helium injection ( $\psi = 4$ ) is given in Fig. 7b. For this and the other injection cases, the dark regions in the image are largely a result of the presence of helium (and corresponding lack of water condensation). Unfortunately, as cited previously, condensation present in the air captured in the recirculation zone is destroyed. Although the evaporated moisture in the recirculating air recondenses as it mixes with freestream air further downstream, the Rayleigh/Mie scattering technique cannot be used to study the detailed evolution of the helium jet in the recirculation zone. This ambiguity is confined to the recirculation zone.

Similar to the no-injection case, recompression shocks emanate from the interaction of the mixing layers shed from the top and bottom strut surfaces. However, two other shock waves are present upstream

of the two-dimensional recompression shocks. These shock waves are also recompression shocks. They result from the intersection of the helium jet mixing layer and the mixing layers shed from the strut surfaces. Since the helium jet is highly underexpanded, the mixing layer surrounding the jet diverges outward from the nozzle exit, resulting in the interaction with the nominally two-dimensional mixing layers. Given that the injector nozzle is circular, it is not surprising that the "jet/mixing layer" recompression shock is not two-dimensional. For this reason and for the sake of clarity, these initial shock waves are referred to as "conical shock". The three-dimensional conical shock wave coalesces with the two-dimensional recompression shock between  $X = 2.2$  and  $3.5$  cm depending on which nozzle is in place.

A schematic of the main features of the circular injection flowfield is given in Fig. 8. Figure 8a gives a streamwise view which is analogous to the Rayleigh/Mie visualization of Fig. 7b. Figure 8b gives a plan view through the nozzle centerline. The three-dimensionality of the conical shock is shown in Fig. 8c, where the flow is out of the plane of the page.

Streamwise Rayleigh/Mie visualizations on the injector nozzle centerlines are given for the other injector geometries in Figs. 7c-h. Recall that  $\psi$  equals 4 for all of the injection cases. The conical shocks are clearly present for all cases except the elliptical nozzle whose major axis is oriented parallel to the streamwise laser sheet (E1 case). This is likely a result of the axis-switching effect commonly observed in oblong jets. The two-dimensional recompression shocks are present for all of the injection cases as would be expected. Schlieren photographs confirmed that the expansion fans and two-dimensional recompression shocks are very similar for the injection and no-injection cases.

Figure 9 gives instantaneous Rayleigh/Mie scattering images of the face-on view located at  $X = 2.54$  cm. These images show the jet contour, the fluid previously in the boundary layer, and the conical shock waves as outlined in Fig. 8. The streamwise location of  $X = 2.54$  cm is far enough upstream that only the conical shock waves are visible. The three-dimensional conical shock waves appear in the images of Fig. 9 as an arc, above and below the strut, enclosing a bright region. This conical shock waves are more visible in the average face-on Rayleigh/Mie images at the same location, which are given in Fig. 10.

Mixing is initiated by large-scale structures, which entrain large quantities of fluid into the mixing region. This "fuels" the cascading process which generates smaller scale turbulence down to the micro-scales. Micro-scale mixing is a necessary component of the combustion process, since the fuel and oxidizer must be mixed on a molecular level in order to obtain efficient combustion. Therefore, when one speaks of mixing, it is important to differentiate between large-scale and small-scale mixing.

The following discussion is divided into two sections. First, the flow dynamics which govern the evolution of the different injected flows will be considered. Second, the comparative large-scale and small-scale mixing performance of the seven injection configurations will be discussed.

Since the air in the recirculation zone behind the strut is of relatively low velocity and at a lower pressure than that at the injector nozzle exit, the injected jet is expected to behave much like an underexpanded free jet until it interacts with the mixing layers shed from the top and bottom of the strut. The underexpanded helium jet forms a barrel shock and a Mach disk. The geometry of the shock structure is different for the different nozzle geometries. When the jet interacts with the mixing layers, the flow dynamics become very complex. However, given that flows establish equilibrium by pressure and vorticity redistribution, insight may be gained by considering pressure gradients and vorticity vector orientations.

It is obvious from the face-on images of the jet that the mixing layers shed from the strut restrict jet spread in the transverse direction. This is certainly true for the case of the circular injector nozzle (Fig. 10b) and the circular-with-horizontal-tabs injector nozzle (Fig. 10e). For the circular case, an oblong jet is encountered where a round jet would be expected for the free jet case. For the injector with horizontal tabs, T3, growth in the transverse direction would be expected to be more pronounced than the growth in the spanwise direction [Reeder, 1994]. Restriction of transverse jet growth by the shed mixing layers is also suggested by Figs. 10f and 10h, where the transversely-oriented elliptical jet has spread much more in the spanwise direction than the spanwise-oriented elliptical jet has spread in the transverse direction.

Previous studies have shown that tabs in subsonic and supersonic free jets generate a pair of counter-rotating vortices which engulf ambient fluid. The generation of these vortices has been attributed to a pressure "hill" upstream of the tab and a lower pressure downstream of the tab. The strength of the pressure gradient was seen to increase with increasing jet-to-freestream pressure ratio [Zaman et al., 1995]. As a result, it was expected that the circular-with-tab nozzle cases (T1, T2, and T3) would generate counter-rotating vortices. The mixing layers shed from the strut surfaces appear to either reinforce or degrade these vortices depending on the orientation of the nozzle with respect to the wake flow. For example, in the T1 case, the mixing layer reinforces the effect of counter-rotating vortices to engulf freestream air and the jet quickly bifurcates into two adjacent cores. Bifurcation is clear in the face-on views at  $X = 2.54$  cm (Figs. 9c and 10c). The bifurcation is so pronounced that the streamwise view on injector nozzle centerline for the T1 case (Fig. 7c) looks nearly identical to the no injection N case (Fig. 7a). The separation into two cores is so complete



that freestream fluid is allowed to flow between the cores, almost as if there were no jet on the ejector nozzle centerline. For the T2 case, it is evident that the pair of streamwise vortices created by the tabs is distorted by the mixing layer to form the "S" like jet contour of Fig. 10d. This distortion can be understood by considering the free jet dynamics for a two-tab nozzle case and a superimposed no-injection flowfield around the base of the strut. Secondary to the flow along the axis of injection, the jet fluid is seen to flow predominantly outward along a line perpendicular to a nozzle diameter connecting two tabs [Reeder, 1994]. For the T1 case, this motion is directed along the spanwise axis of the tunnel (horizontal in Figs. 9c and 10c). This same motion of jet fluid for the T2 case is directed at an angle into the mixing layers on top and bottom of the strut. A noticeably larger conical recompression shock wave is generated at the point of intersection between the jet and the mixing layer relative to other points around the jet (See Fig. 10d). Large conical shocks occur for other cases as well (Figs. 10 d, e, g, h). The two-dimensional mixing layers seem to suppress the action of the tab vortices in the T3 case (Fig. 10e). Virtually no evidence of stationary streamwise vortices is encountered and the jet remains compact in a cross-sectional area similar to that of the circular jet.

Jets emanating from elliptic nozzles evolve significantly differently from those emanating from circular (and circular-with-tabs) nozzles. The elliptic jets begin with different dynamics. The large azimuthal curvature variation of elliptic vortical structures causes non-uniform self-induction and subsequent complex three-dimensional deformation. The most notable phenomenon of an oblong jet is axis-switching in which the jet cross-section contracts in the direction of the major-axis and expands along the minor-axis, so that the two axis are eventually interchanged [Hussain & Husain, 1989]. This phenomenon is believed to be intimately related to momentum thickness around the jet perimeter. The face-on images for injection from the elliptic nozzles (E1, E2, and E3) are shown in Figures 9f-h and 10f-h. The elliptic jet in the E1 orientation goes through one axis switch by  $X = 2.54$  cm and appears to continue spreading along the new major axis. The mixing layer didn't seem to hinder the axis switch and perhaps even induced subsequent jet spread in the spanwise direction. A plan view image (not included here) shows that the jet core has bifurcated (albeit less completely than in the T1 case) and that each core appears to be traveling away from the centerline. This bifurcation is explained in the subsonic case by a connecting type action of adjacent sides of the elliptic vortical structure [Hussain & Husain, 1989]. If the "connection" becomes complete, the elliptic jet separates into two adjacent, almost circular jets. A distorted axis-switch is seen for the E2 case. The elliptic jet at the ends of the major axis was distorted by

the wake flow in a manner similar to the T2 case and also formed an "S" shaped jet cross-sectional area. The T3 case does not achieve an axis switch. Instead it becomes rather compact. This jet displays "curls" at the plan view sides of the jet relative to the strut. These are presumably caused by streamwise vortices. They appear to be spatially stationary judging from the presence of engulfed air between the location of the curls seen on the average image (Fig. 10h).

The different nozzle geometries and orientations indeed create different jet shapes. The question now arises -- which nozzle configuration promotes the best mixing? Mixing can be approached from two sides: large-scale mixing involving large scale structure and small-scale mixing down to the molecular level necessary for efficient combustion. Large-scale mixing can be viewed by considering overall jet parameters such as the cross-sectional jet area and the mixing layer perimeter of the jet. To determine these parameters, the mixing region must first be identified. The RMS intensity from 20 images was calculated to identify the mixing region. The two primary regions of the jet are the core and the mixing layer. The core is the portion of the jet that remains unmixed (i.e. 100% helium). The jet mixing layer is the portion of the jet that contains helium mixed with air. The mixing region is characterized by high RMS intensity values. Figure 11 shows RMS images for the different nozzle configurations. The high intensity RMS values arise from the helium and air engulfed in the jet mixing layer intermittently passing the plane of view. The maximum RMS values around the jet can be loosely compared to the neutral (or saddle) point about which the shear layer structures seem to rotate.

The region of highest RMS values was used to define a contour line of the mixing layer to compare jet spread between injection cases. Using a computer graphics program, a contour was visually interpolated to approximate the curve of maximum RMS surrounding the injected helium jet (Fig. 12). The resulting contours are shown in Fig. 13. Near the base of the strut, the condensation destruction in the recirculation zone must be kept in mind.

In order to evaluate the mixing potential of the different injector geometries, one needs to consider the interfacial surface area between the jet fluid and the air per unit volume of jet fluid available for mixing. This is calculated as the ratio of the jet perimeter ( $p$ ) to the cross-sectional area ( $A$ ) of the enclosed region. This quality is given by the shape parameter, defined as,

$$S = \frac{p}{2\pi R_o}$$

where  $R_o$  is the effective radius defined as

$$R_o = \sqrt{\frac{A}{\pi}}$$

A, p,  $R_o$  and S were calculated from the face-on images located at  $X = 1.27, 2.54$ , and  $5.08$  cm for all the nozzle configuration (Table 2). The area and shape factor are shown graphically in Figures 14 and 15. A large shape factor and a large area are desired for a favorable mixing situation. This data in Table 2 clearly indicate that the circular-with-tabs nozzles, especially the T1 case, produce the largest mixing areas and shape factors. At the  $X = 2.54$  cm location, the T1 case produces an area which is 36% larger than that obtained with the circular injector (case C), with a shape factor only 15% higher than that of case C. Although T3 produces an area which is also 36% larger than that of case C, the T3 shape factor (1.22) is smaller than that of case C (1.28). Based on the data for the  $X = 2.54$  cm location, T1 is the favored configuration. For the case of the elliptic nozzle, configuration E3 generates larger area but E1 generates larger shape factor. Both T3 and E3 yield very low shape factors.

At the  $X = 5.08$  cm location, the tabbed nozzle again produces greater mixing areas than the other nozzle geometries. The shape factor of T1 (1.82) is 58% higher than that of case C (1.15). The area for T1 is 35% larger than for C, similar to the results obtained at  $X = 2.54$  cm. Interestingly, the shape factor of C, T3, and E3 are very similar (1.15). This outcome suggests that the T3 and E3 configurations do not enhance mixing appreciably.

Once the area of interest is defined, an evaluation of mixedness quality in this region can be performed. A mixedness parameter was developed to give a figure of merit for the small scale mixing. The mixedness parameter is defined by

$$M = 1 - \frac{\left(\overline{I^2}\right)^{\frac{1}{2}}}{\left[(I_1 - \bar{I})(\bar{I} - I_2)\right]^{\frac{1}{2}}}$$

where  $I_1$  is maximum intensity of scattering in air and  $I_2$  is minimum scattering in helium. Thus M equals zero for no mixing and one for fully mixed. The mixedness calculated using this parameter closely resembled the mixedness values calculated from two other established mixedness equations [Pratt, 1975, Konrad, 1976]. However, the above defined mixedness equation requires less computation. Mixedness plots for the T1 case are shown as a sample set of face-on mixedness images located at  $X = 1.27, 2.54, 5.08$  cm (Fig. 16). Unlike the average images which show a smooth transition across the mixing layer, the

mixedness maps highlight the area where mixing occurred. At the  $X=1.27$  cm location, the jet flow is clearly beginning to bifurcate. At the center of the jet core and outside the jet area, little mixing has occurred. Mixing occurs in the mixing layer of the jet; the mixedness map is not uniform due to the under sampling.

Comparison of Figs. 16a and 16b show an increase in the mixing layer of the jet and in the jet cross-sectional area between  $X=1.27$  cm and  $X=2.54$  cm. Note that the mixing intensity is less at  $X = 2.54$  cm than at  $X = 1.27$  cm downstream. This indicates the mixing strength is dissipated with the progress of mixing. At the  $X = 5.08$  cm location, the growth of the mixing region and shear layer thickness continues and the mixing intensity drops correspondingly.

In light of the above discussion, it seems that the within the same nozzle geometry (i.e. elliptic, circular-with-tabs), the orientation that allows the natural (free jet) spreading to occur would support the best mixing. A more detailed description of the results presented here as well as an accounting of results which have been collected but not presented because of space limitations will be available in the near future. [Glawe, 1995].

## 5.0 Conclusions

A supersonic windtunnel facility capable of providing continuous high Mach number flow with large fuel mass injection capacity has been utilized for an investigation of mixing enhancement with various parallel injector nozzle geometries. To simulate strut fuel injection, a strut was designed to generate a nominally two-dimensional recirculation zone into which the fuel could be injected. Without fuel injection, the key flow elements in the vicinity of the strut base are the expansion fan, the recirculation zone and the nominally two-dimensional mixing layers shed from the top and bottom of the strut. With the sonic fuel injection, the flow near the base of the strut had the added complexities associated with underexpanded jets, three-dimensional "conical" recompression shocks, barrel shocks, Mach discs, slip lines, etc. To eliminate the possible complications of a shock wave/jet interaction, the strut was extended into the settling chamber and a shock-free freestream flow both above and below the strut was established.

The large flow facility allows for a large strut and a large injection port so that many important features could be identified with imaging techniques such as Rayleigh/Mie scattering and PLIF. The continuous flow facility allows the momentum transport to be characterized with LDV. Only with these two important advantages was this extensive experimental investigation possible.

Helium was injected to simulate hydrogen fuel. Nozzle geometry effects on the mixing behavior were investigated. In addition to a circular injector nozzle,

elliptic and circular-with-tabs nozzles were investigated. The Total Mixing Evaluation (TME) approach was developed to determine both the potential and the quality of mixing. In this approach, the mixing potential (large-scale mixing) was characterized by computing the area and perimeter of mixing region and the quality (small-scale mixing) was quantified with a mixedness parameter. This approach was used to determine the best mixing enhancement configuration. Based on the analyses of the acquired data, the following conclusions can be made:

1. The LDV data not presented in this paper indicate the nominally two-dimensional strut generates a recirculation zone-dominated mixing region. The fuel jet will lose its identity at the downstream location of  $x/H \sim 1.0$ . The dominance of the strut wake explains why struts are favorable flame stabilizers in supersonic combustion applications.
2. The bifurcation behavior of the tabbed nozzle jets was observed similar to free jet studies. The mixing layers shed from the strut influence the action of the counter-rotating streamwise vortices produced by the tabs.
3. The axis-switching behavior of the elliptic nozzle jet flows was observed similar to free jet studies. The mixing layer shed from the top and bottom strut surfaces influences the axis-switching.
4. The mixing layer shed from the strut tend to suppress jet spread in the transverse direction.
5. The TME approach developed in this study proves capable of identifying the best mixing configuration. For all the configurations compared in this investigation, the circular nozzle with tabs oriented in the lateral direction was the best in terms of both large scale and small scale mixing.

## 6.0 Acknowledgments

This work was supported by the Palace Knight Program and by the Aero Propulsion and Power Directorate of the Wright Laboratory under Contract No. F33615-93-C-2300. The authors are indebted to M. Gruber, C. Carter and L. P. Goss for helpful discussions, and D. G. Schommer, C. R. Smith, K. A. Kirkendall and G. Haines for technical assistance, S. A. Arnette for technical editing, and Jan Solari for graphic layout.

## 7.0 References

- Bogdanoff, D.W. (1994) "Advanced Injection and Mixing Techniques for Scramjet Combustors," *J. Propulsion & Power*, Vol. 10, No. 2, pp. 183-190.
- Elliott, G.S., Samimy, M., and Arnette, S.A. (1992) "A Study of Compressible Mixing Layers Using Filtered Rayleigh Scattering Based Visualizations," *AIAA Journal*, Vol. 30, pp. 2567-2569.
- Fuller, E.J., Mays, R.B., Thomas, R.H., and Schetz, J.A. (1992) "Mixing Studies of Helium in Air at High Supersonic Speeds", *AIAA Journal*, Vol. 30, No. 9, pp. 2234-2243.
- Glawe, D.G. (to be completed Summer 1995) The Effects of Nozzle Geometry on Parallel Injection from the Base of an Extended Strut into a Supersonic Freestream. Ph.D Dissertation, OSU Department of Mechanical Engineering.
- Gruber, M.R., and Nejad, A.S. (1994) "Development of a Large-Scale Supersonic Combustion Research Facility," AIAA Paper 94-0544.
- Hussain, F., and Husain, H.S. (1989) "Elliptic Jets. Part 1. Characteristics of Unexcited and Excited Jets," *J. Fluid Mech.*, Vol. 208, pp. 257-320.
- Konrad, J.H. (1976) An Experimental Study of Mixing in Two-Dimensional Turbulent Shear Flows with Applications to Diffusion Limited Chemical Reactions. Project SQUID Tech. Rep. CIT-8-PU.
- King, P.S., Thomas, R.H., Schetz, J.A., Billig, F.S. (1989) "Combined Tangential-Normal Injection Into a Supersonic Flow," AIAA Paper 89-0622.
- Kuntz, D.W., Amatucci, V.A., and Addy, A.L. (1987) "Turbulent Boundary-Layer Properties Downstream of the Shock-Wave/ boundary-Layer Interaction," *AIAA Journal*, Vol. 25, No. 5, pp. 668 - 675.
- McClinton, C.R. (1972) The Effects of Injection Angle on the Interaction Between Sonic Secondary Jets and a Supersonic Free Stream. NASA Tech. Rep. TN D-6669.
- Pratt, D.T. (1975) "Mixing and Chemical Reaction in Continuous Combustion," reprinted in *Energy and Combustion Science*, Pergamon Press, New York (Chigier, N. Ed.), pp. 75 - 88.
- Reeder, M.F. [1994] An Experimental Study of Mixing Enhancement in Jets with Vortex Generating Tabs. Ph.D. Dissertation, OSU Department of Mechanical Engineering.
- Waitz, I.A., Marble, F.E., and Zukoski, E.E. (1992) "A Systematic Experimental and Computational Investigation of a Class of Contoured Wall Fuel Injectors," AIAA Paper 92-3550.
- Wegner, P.P., and Pouring, A.A. (1964) "Condensation of Water by Homogeneous Nucleation in Nozzles," *Physics of Fluids*, Vol. 7, No. 3, pp. 352-361.
- Zaman, K.B.M.Q., Reeder, M.F., and Samimy, M. (1995) "Control of an Axisymmetric Jet Using Vortex Generators," *Phys. Fluids*, Vol. 6, No. 2, pp. 778-793.

**Table 1:** Operating condition for helium injection into Mach 2 air freestream

	$P_o$	$T_o$	Mach #	$P_\infty$ or $P_{exit}$	$T_\infty$ or $T_{exit}$	$P_\infty$ or $P_{exit}$	$U_\infty$ or $U_{exit}$
	KPa	K		KPa	K	kg/m <sup>3</sup>	m/s
Freestream	344	301	2	44	167	0.918	518
Helium	414	292	1	201	219	0.443	871

\* Note the  $T_o$  for the helium accounts for pressure losses in the fuel that result in an actual lower exit pressure closer to 180 KPa as opposed to the theoretically calculated 210 KPa

**Table 2:** Measured Parameters for Large Scale Mixing

X (cm)	Nozzle	Area (square pixels)	Perimeter (pixel units)	Effective Radius	Shape Factor
1.27	c	26368.00	695.12	91.61	1.208
1.27	t1	25166.00	807.00	89.50	1.435
1.27	t2	26373.00	759.80	91.62	1.320
1.27	t3	30597.00	711.10	98.69	1.147
1.27	e1	23355.00	685.60	86.22	1.266
1.27	e2	22945.00	688.30	85.46	1.282
1.27	e3	27035.00	645.00	92.77	1.107
2.54	c	25533.00	730.00	90.15	1.289
2.54	t1	34193.00	974.00	104.33	1.486
2.54	t2	28209.00	729.00	94.76	1.224
2.54	t3	34943.00	796.00	105.46	1.201
2.54	e1	22674.00	786.00	84.96	1.472
2.54	e2	24613.00	792.00	88.51	1.424
2.54	e3	28978.00	693.00	96.04	1.148
5.08	c	26415.00	662.89	91.70	1.151
5.08	t1	34807.00	1204.50	105.26	1.821
5.08	t2	32160.00	1039.00	101.18	1.634
5.08	t3	34414.00	767.75	104.66	1.167
5.08	e1	29532.00	950.70	96.96	1.561
5.08	e2	19352.00	752.20	78.49	1.525
5.08	e3	31456.00	721.70	100.06	1.148
8.64	c	19530.00	560.84	78.85	1.132
8.64	t1	40487.00	1090.00	113.52	1.528
8.64	t2	27371.00	677.20	93.34	1.155
8.64	t3	25763.00	697.95	90.56	1.227
8.64	e1	29690.00	965.60	97.21	1.581
8.64	e2	18932.00	569.30	77.63	1.167
8.64	e3	36531.00	850.85	107.83	1.256
12.7	c	22121.00	589.09	83.91	1.117

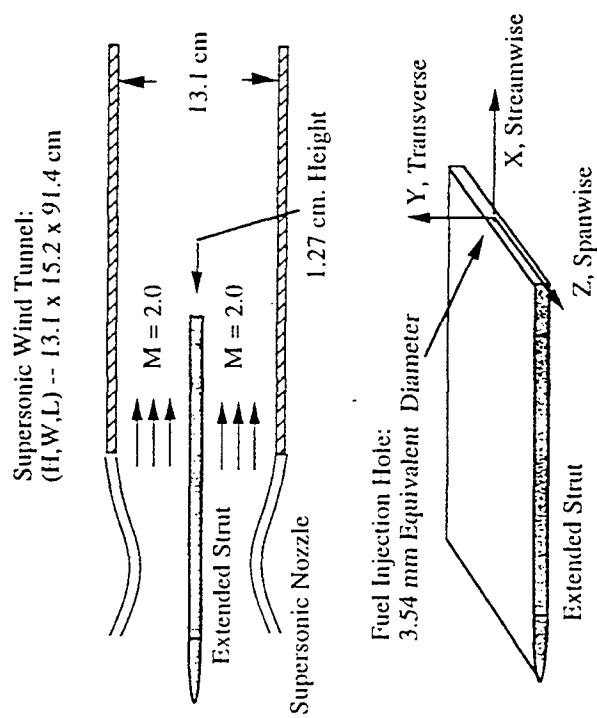


Figure 1: Schematic of extended strut in tunnel and reference coordinate system.

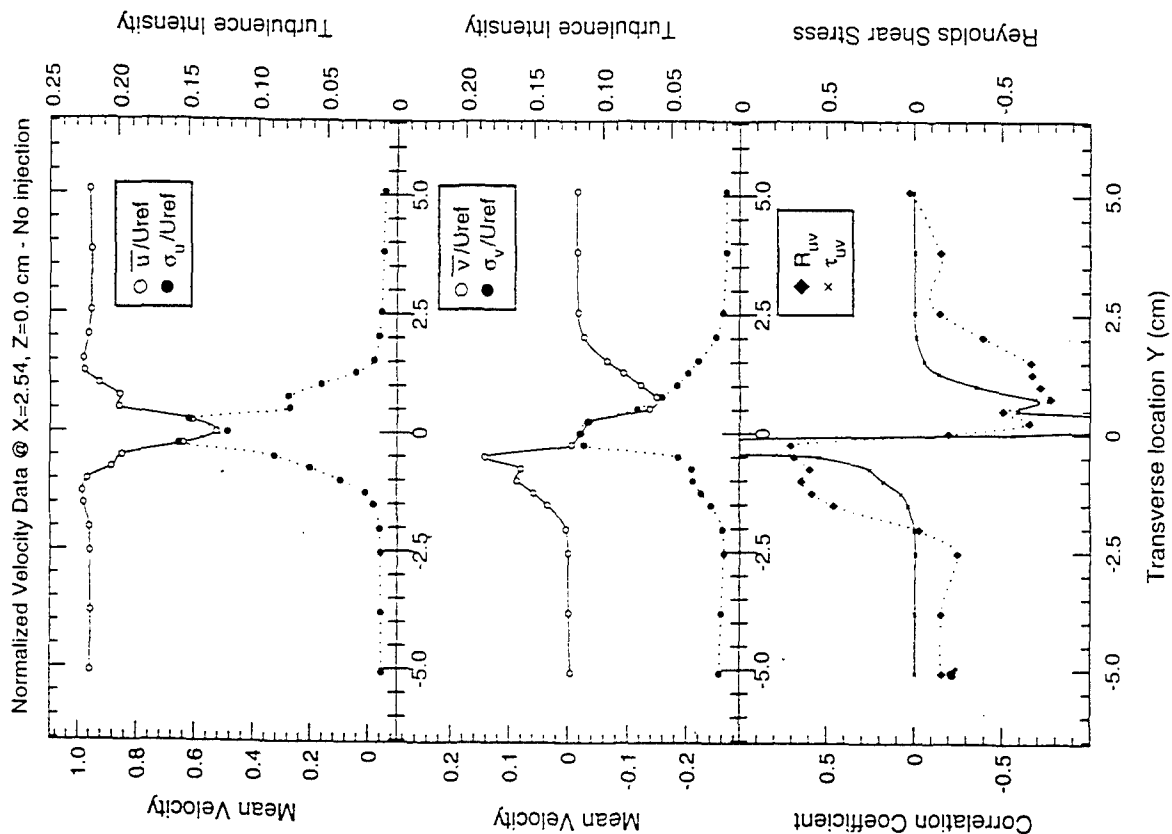


Figure 2: LDV transverse velocity profile and related statistical parameters for the no injection case at x = 2.54 cm, z = 0.

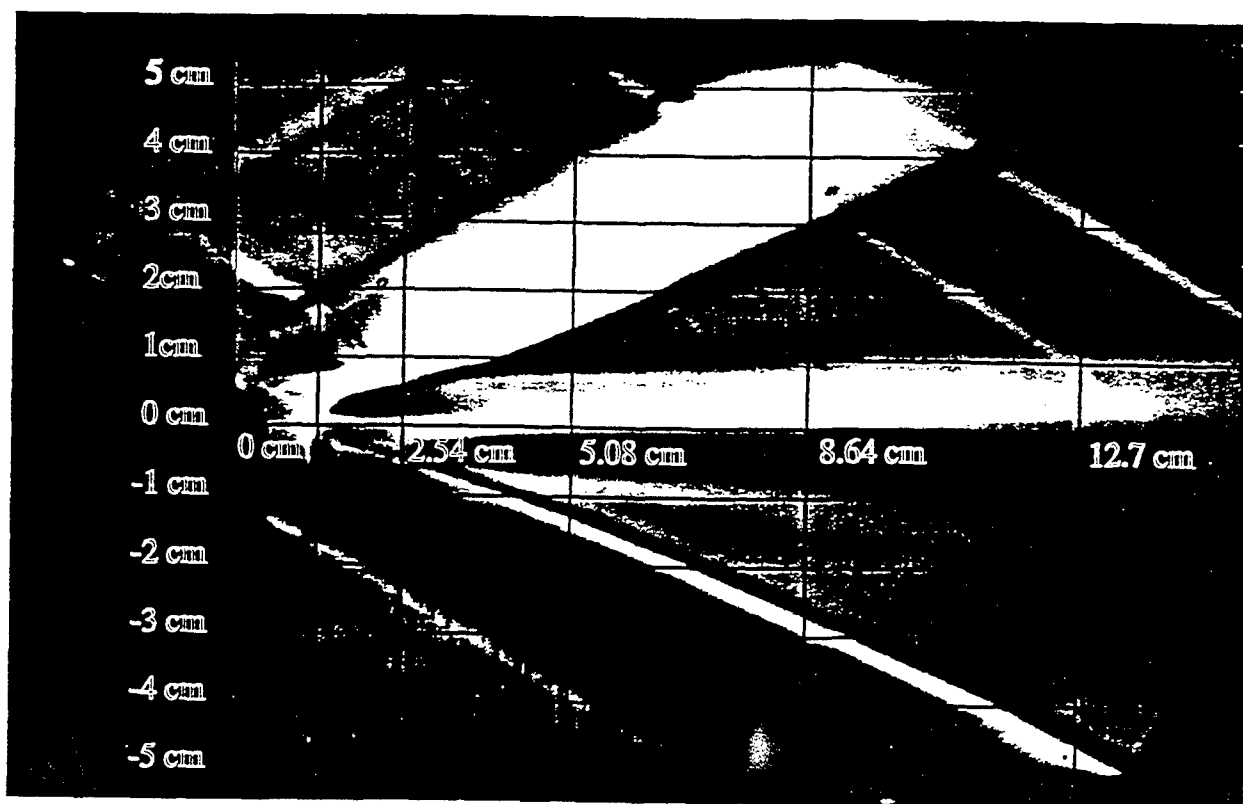


Figure 6: Schlieren photography for streamwise plane of view. No injection.

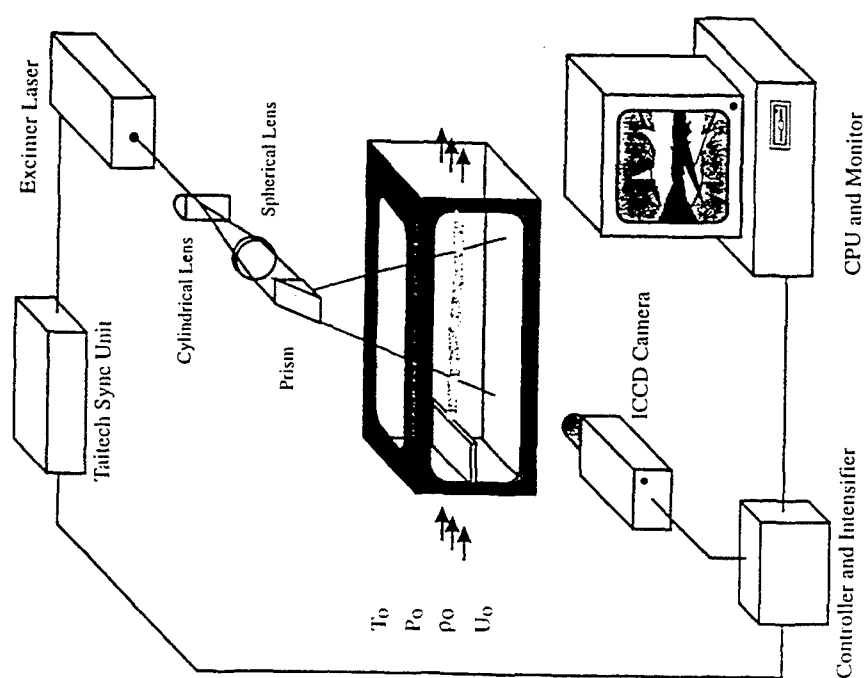


Figure 5: Schematic of Rayleigh/Mie scattering system for the streamwise plane of view.

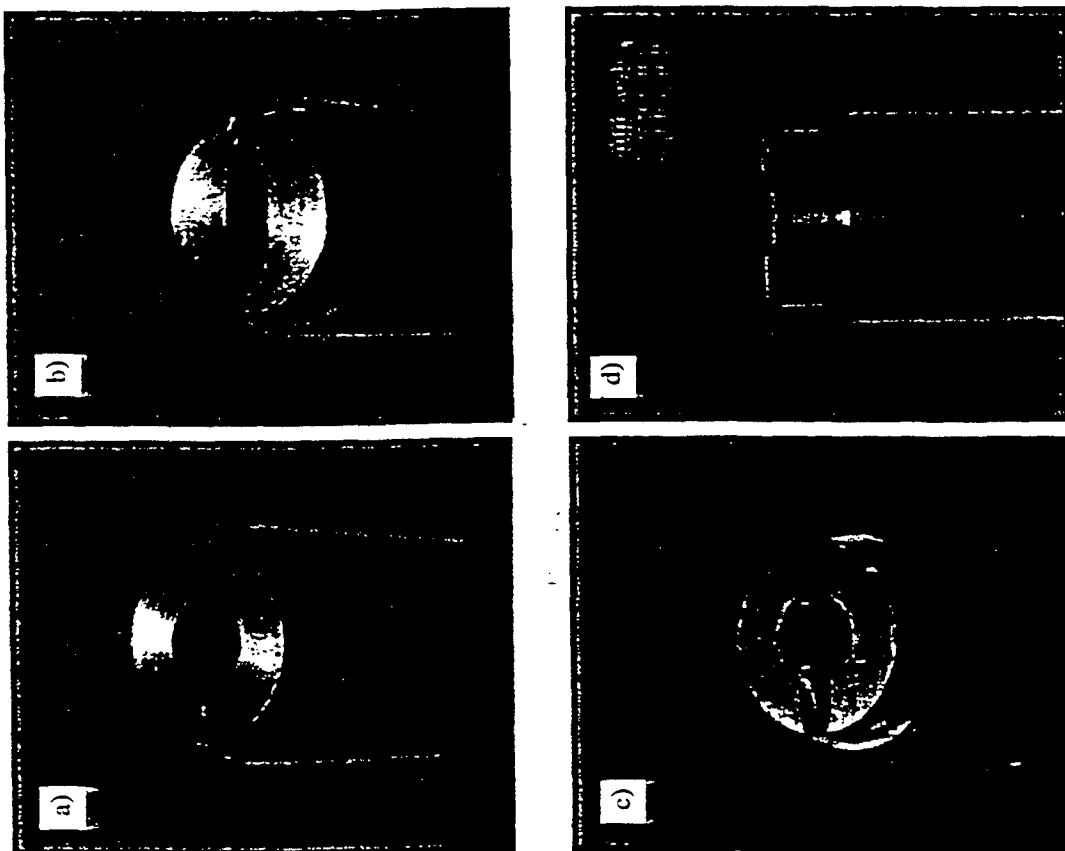


Figure 3: Photographs of the tips of nozzles a) circular, b) elliptical, and c) & d) circular-with-tabs.

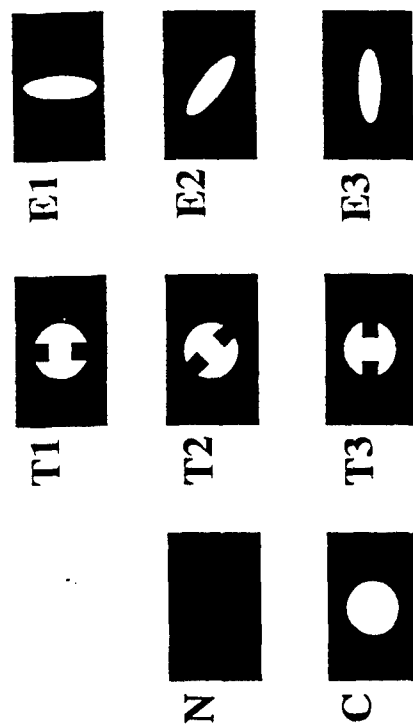


Figure 4: Schematic of nozzle orientations with nozzles mounted in the base of an extended strut. No injection (N), and helium injection: circular (C), circular-with-tabs (T1, T2, T3), and elliptic (E1, E2, E3).

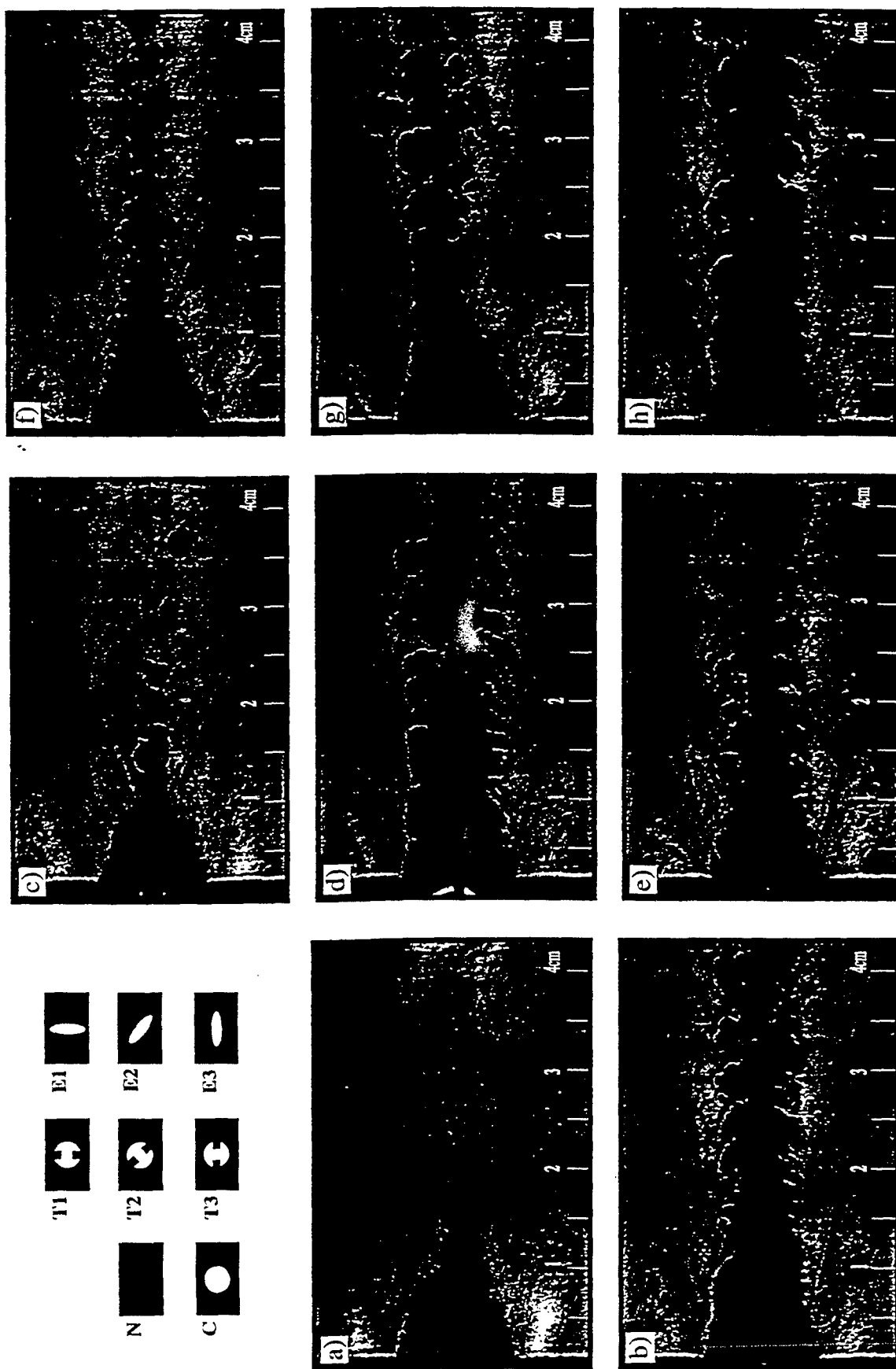
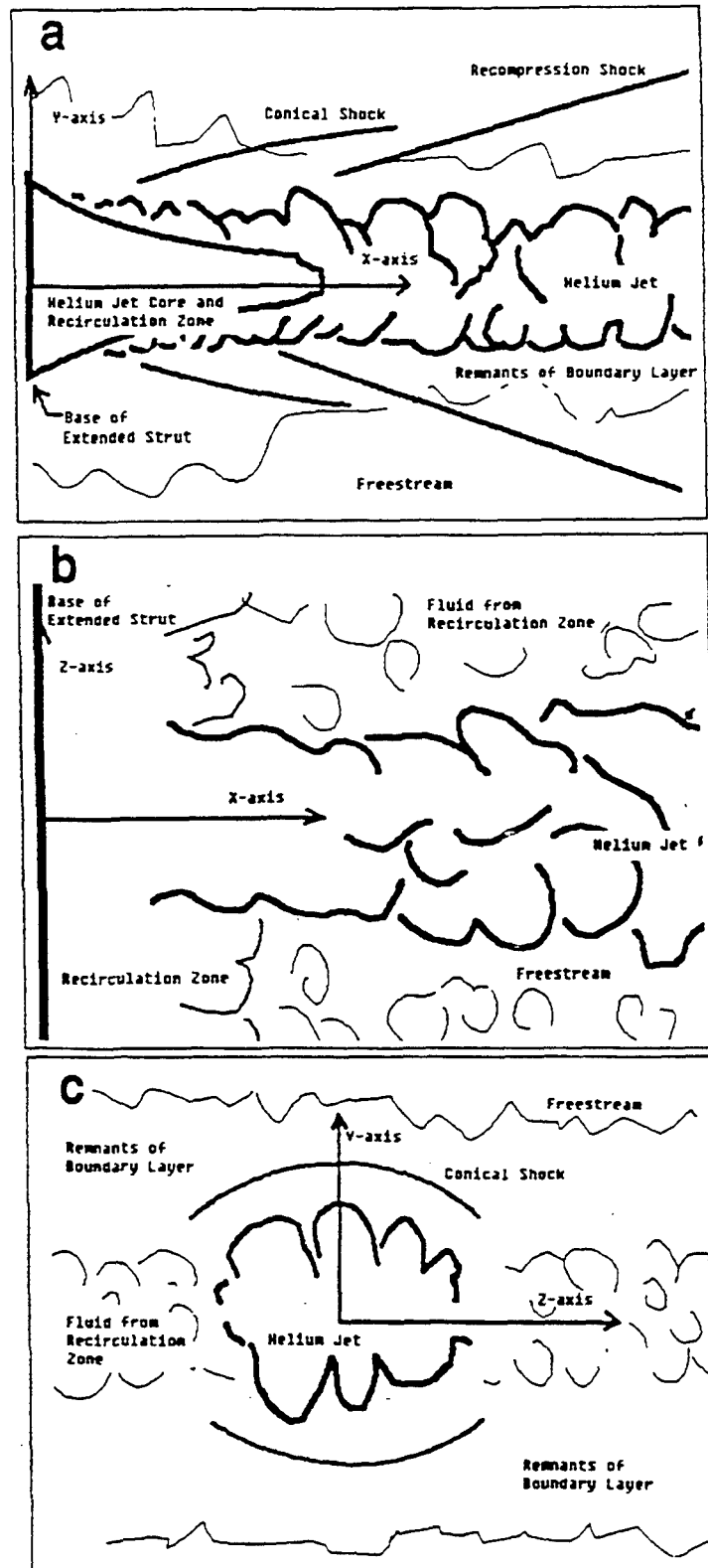


Figure 7: Instantaneous Rayleigh/Mie images of streamwise plane of view located on centerline of tunnel ( $z = 0$ ) for no injection: a) N, and helium injection cases: b) C, c) T1, d) T2, e) T3, f) E1, g) E2, h) E3.





**Figure 8:** Schematic of instantaneous Rayleigh/Mie scattering images a) streamwise, b) plan, and c) face-on views.

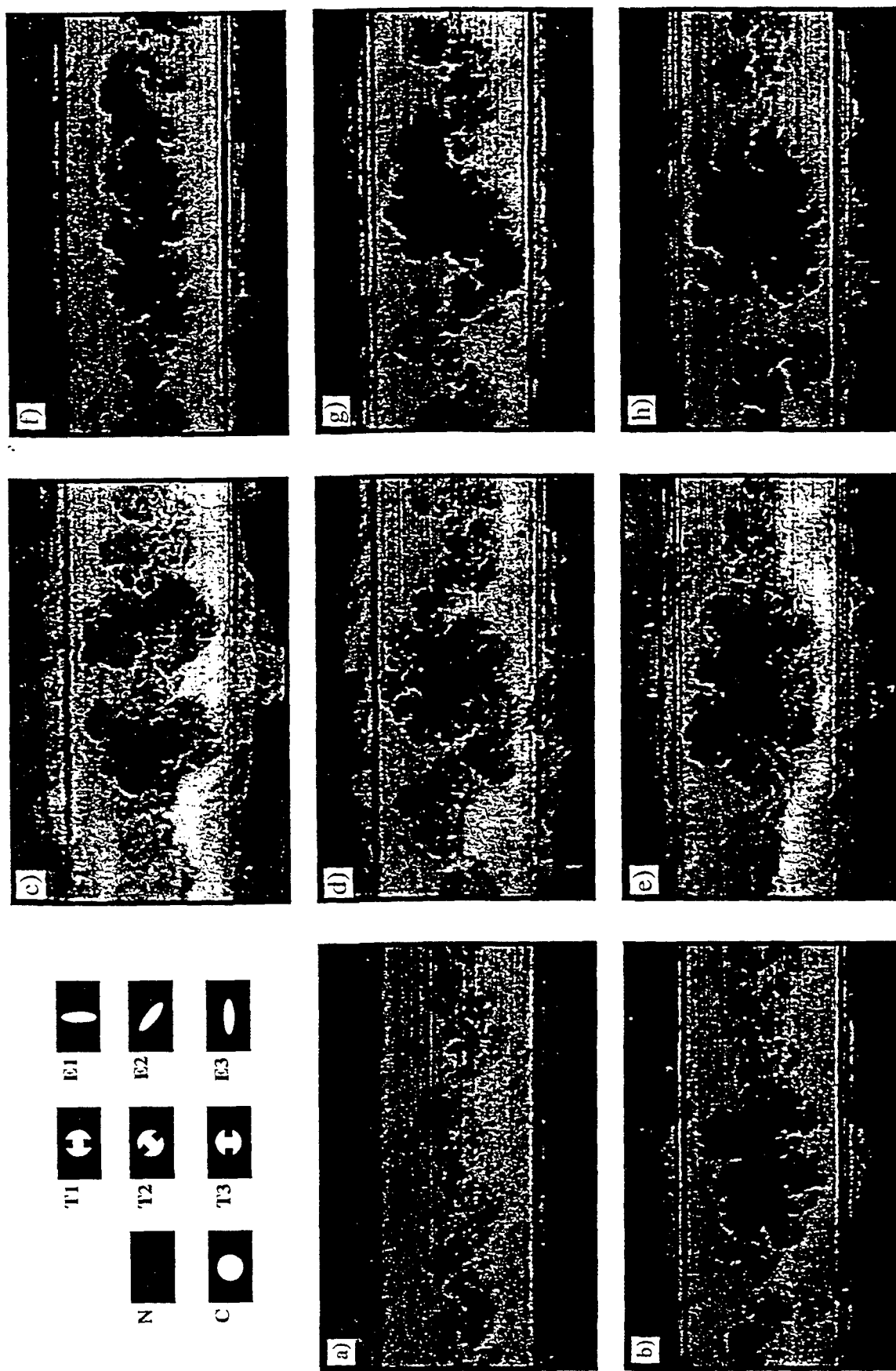


Figure 9: Instantaneous Rayleigh/Mie images of face-on plane of view located at  $x = 2.54$  cm for no injection: a)  $N_1$  and helium injection cases: b) C, c) T1, d) T2, e) T3, f) E1, g) E2, h) E3.

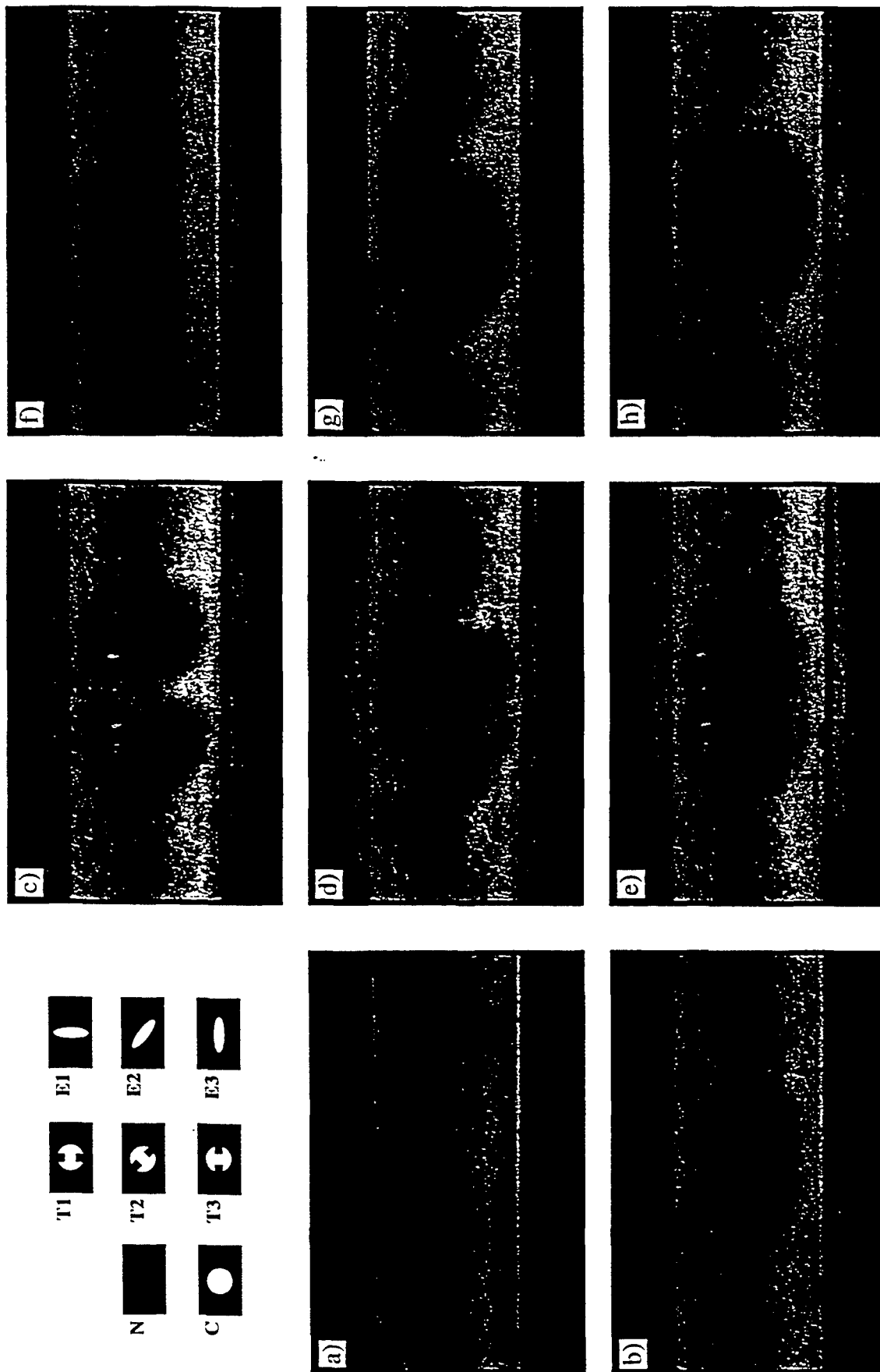


Figure 10: Average Rayleigh-Mie images of face-on plane of view located at  $x = 2.54$  cm for no injection: a) N, and helium injection cases: b) C, c) T1, d) T2, e) T3, f) E1, g) E2, h) E3.

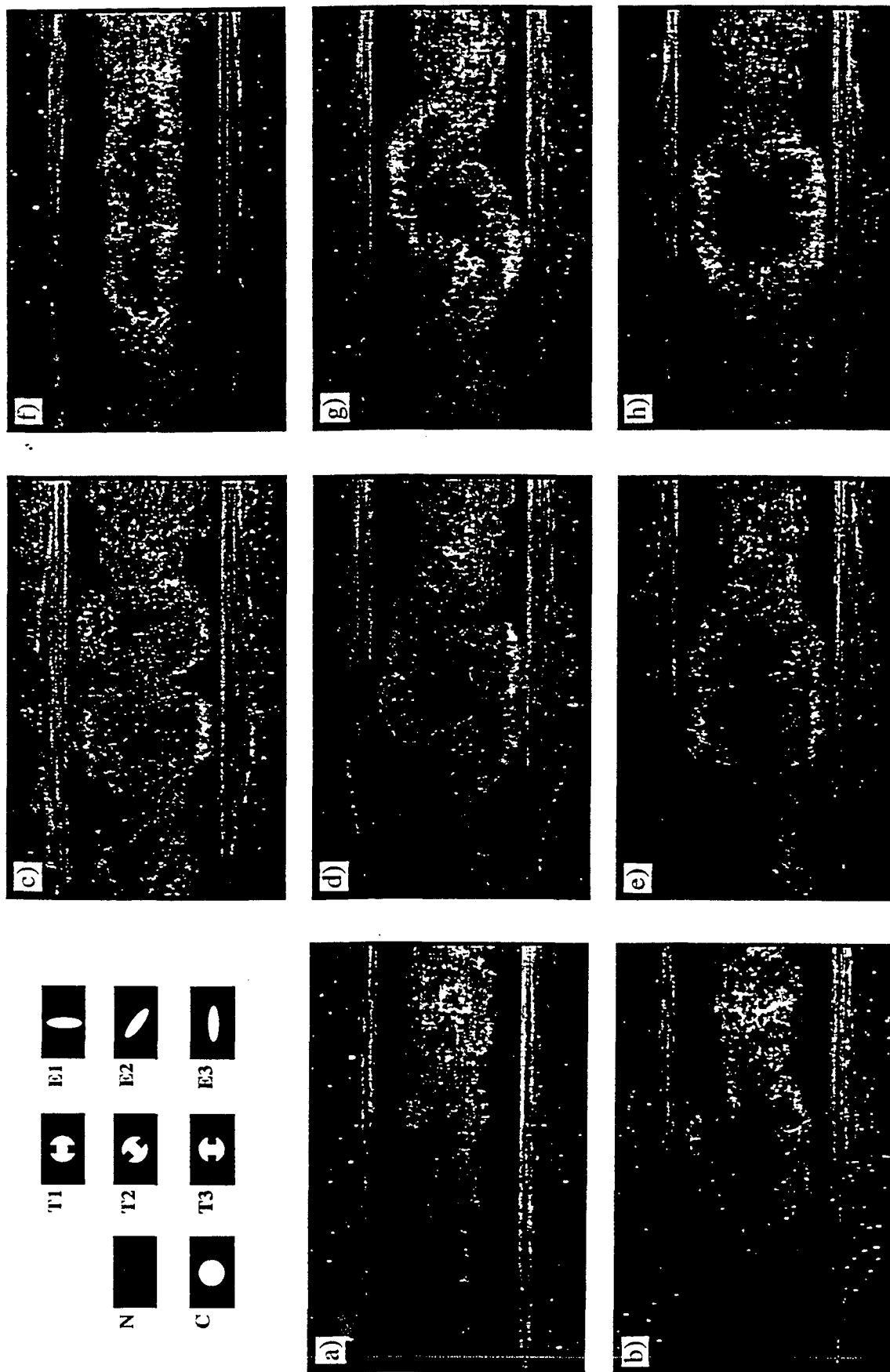
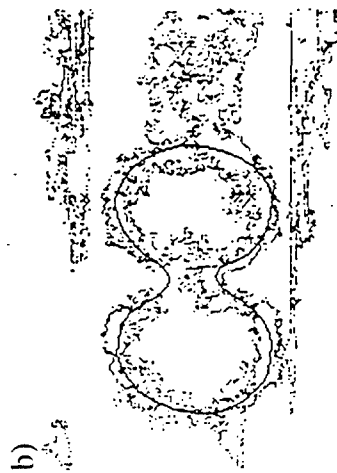
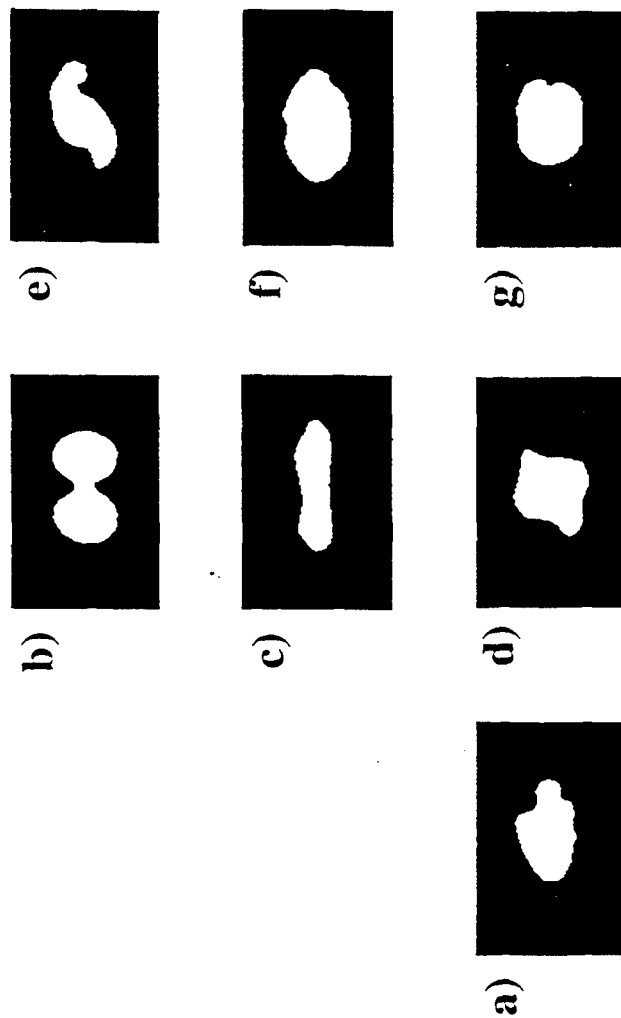


Figure 11: RMS Rayleigh/Mie images of face-on plane of view located at  $x = 2.54$  cm for no injection: a) N, and helium injection cases: b) C, c) T1, d) T2, e) T3, f) E1, g) E2, h) E3.



**Figure 12:** a) RMS Rayleigh/Mie image and b) Schematic of high RMS contour with superimposed visual approximation of T1 jet perimeter for the face-on plane of view located at  $x = 2.54$  cm.



**Figure 13:** Perimeters of jet determined from high RMS contours of face-on plane of view at  $x = 2.54$  cm for helium injection cases a) C, b) T1, c) T2, d) T3, e) E1, f) E2, and g) E3.

E1 T2 E2 T3

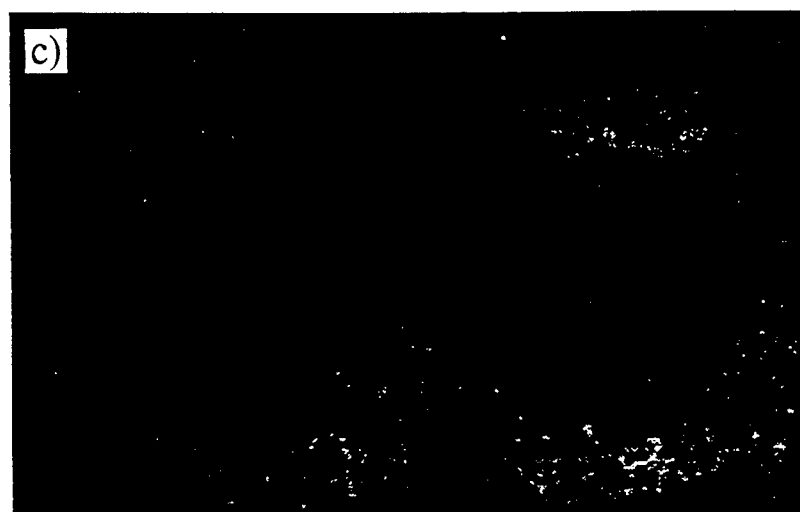
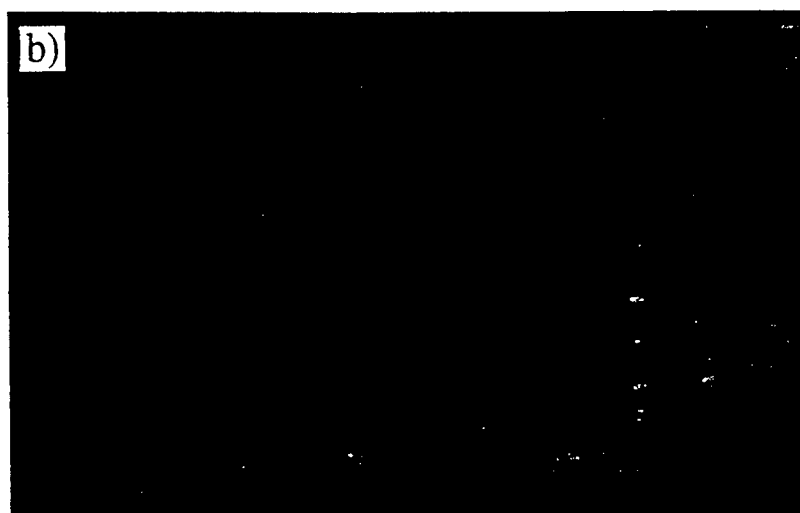
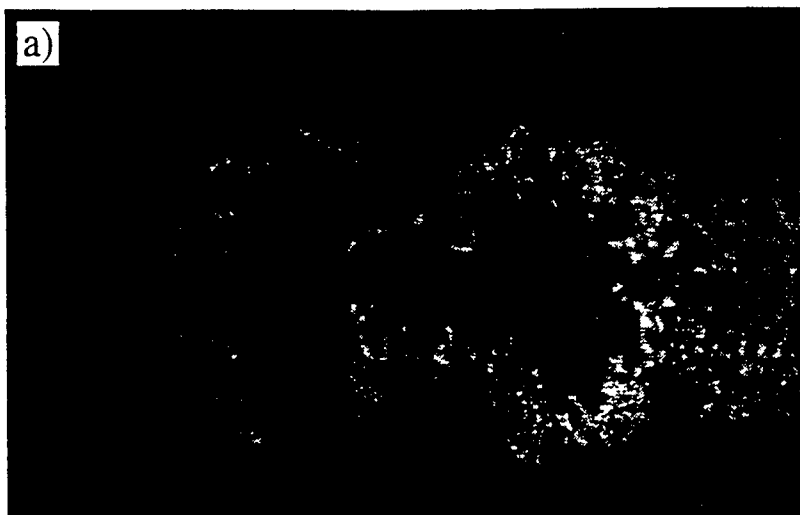


**Figure 16:** Mixedness images for helium injection case T1. Face-on plane of view located at  $x =$  a) 1.27, b) 2.54, and c) 5.08 cm.

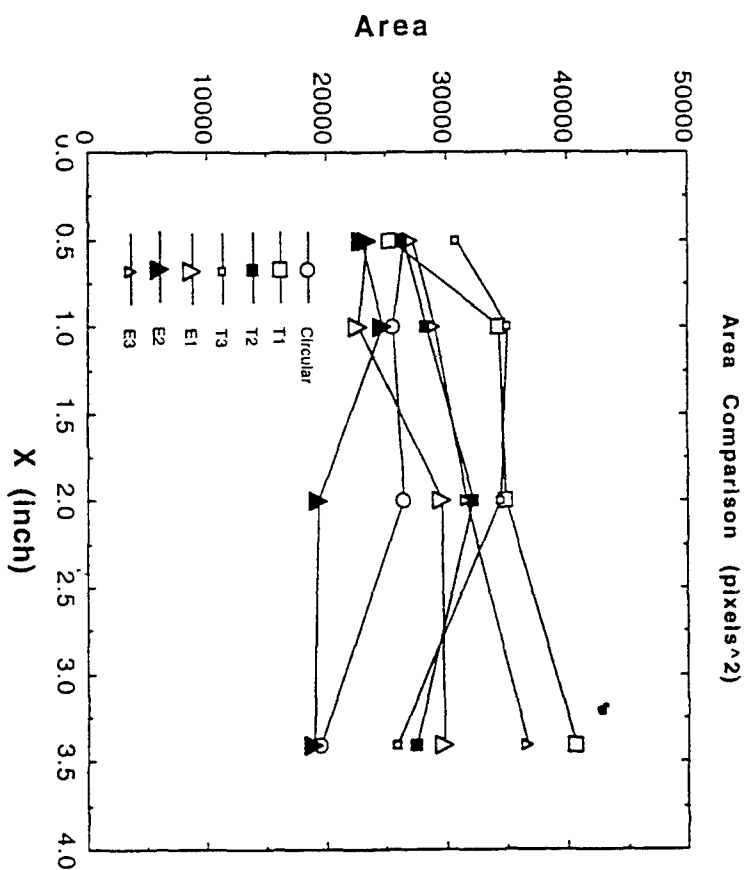


Figure 14: Plot of area values determined from approximated jet perimeters.

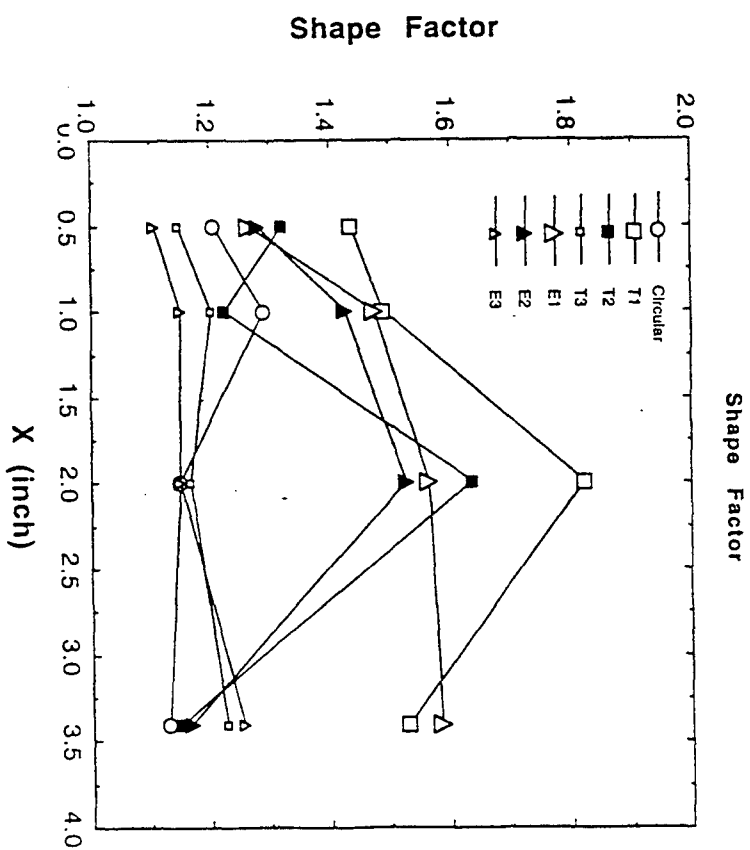


Figure 15: Plot of shape factor determined from approximate jet perimeters and calculated areas.



**AIAA 95-2150**

**Circular and Elliptical Transverse Injection  
into a Supersonic Crossflow--  
The Role of Large-Scale Structures**

M.R. Gruber and A.S. Nejad  
Wright Laboratory, WL/POPT  
1950 Fifth Street  
Wright-Patterson AFB, OH 45433-6563

J.C. Dutton  
Dept. of Mechanical and Industrial Engineering  
University of Illinois at Urbana-Champaign  
Urbana, IL 61801

**26th Fluid Dynamics Conference**  
**June 19-22, 1995 / San Diego, CA**



THIS PAGE LEFT BLANK INTENTIONALLY.

# CIRCULAR AND ELLIPTICAL TRANSVERSE INJECTION INTO A SUPERSONIC CROSSFLOW--THE ROLE OF LARGE-SCALE STRUCTURES

M.R. Gruber\* and A.S. Nejad†

Advanced Propulsion Division, Experimental Research Branch  
Wright-Patterson AFB, Ohio

J.C. Dutton§

Department of Mechanical and Industrial Engineering  
University of Illinois at Urbana-Champaign  
Urbana, Illinois

## Abstract

An examination of the large-scale structure of the flowfields associated with sonic transverse injection through circular and elliptical nozzles into a Mach 2 crossflow is reported. Instantaneous shadowgraph photos provide documentation of the flowfields. Planar Rayleigh scattering images of near-field flow planes produce substantial information about the jet/crossflow interaction. Instantaneous images allow examination of the structural details, while ensemble-averaged images provide transverse penetration and lateral spread data for each injector. Standard deviation images produce information regarding the large-scale mixing and document the development of mixing zones associated with these flows. Results show a highly three-dimensional interaction dominated in the near-field by two types of large-scale vortical motions: shear layer eddies and a counter-rotating vortex pair. Substantial differences in the shear layer structure occur when using air or helium as the injectant gas. Penetration results show that the elliptical jet spreads more quickly in the lateral direction than the circular jet, confirming that some axis-switching phenomenon is present. Near-field transverse penetration data collapse well with low speed scaling conventions, and the power law curve fits obtained are in good agreement with previous results. Finally, analysis of mixing potential from the standard deviation images indicates that the helium and air injection flowfields show significant differences that suggest air injection yields better large-scale mixing potential than helium injection.

## Nomenclature

a	semi-major axis of an ellipse, speed of sound
A	area
b	semi-minor axis of an ellipse
$d_p$	particle diameter
$d_{eff}$	effective injector diameter = $(4A_{xs} / \pi)^{1/2}$
I	intensity
$\bar{I}$	mean intensity
J	jet-to-freestream momentum flux ratio
Kn	Knudsen number

$\ell$	mean free path
M	Mach number
N	number of images
p	static pressure
P	perimeter
$r_o$	effective radius = $(A_G / \pi)^{1/2}$
R	area ratio = $A_G / A_{xs}$ or $A_G / A_x$ , gas constant
S	large-scale shape parameter = $P / 2\pi r_o$
$t_p$	particle response time
$t_\delta$	large-eddy rollover time
u	velocity
x	streamwise coordinate
y	transverse coordinate
z	spanwise coordinate
$\delta$	boundary layer thickness
$\Delta U$	velocity difference
$\epsilon$	eccentricity
$\gamma$	specific heat ratio
$\mu$	dynamic viscosity
$\rho$	density
$\sigma$	standard deviation

## Subscripts

cl	injector centerline
e	exit
f	freestream
j	jet
p	particle
x	streamwise coordinate
xs	jet cross section
$\sigma$	standard deviation

## Introduction

Efficient injection, mixing, and reaction processes that occur inside a supersonic combustion chamber will be fundamental to the success of air breathing hypersonic vehicles. These processes must take place in a supersonic stream due to undesirable effects associated with decelerating a supersonic flow ( $M = 6-8$ ) to appropriate speeds for subsonic combustion. Residence times within

\* Aerospace Engineer, Member AIAA.

† Senior Research Engineer.

§ Professor, Associate Fellow AIAA.

This paper is declared a work of the U.S. Government and is not subject to copyright protection in the United States.

such combustors will necessarily be short, thus requiring the mixing and combustion to occur rapidly. The present work is an experimental investigation of the flowfields created by gaseous jets injected transversely into supersonic crossflows, which is one possible arrangement for fuel injection in supersonic combustors.

Schematics of the transverse jet injected into a supersonic crossflow appear in Fig. 1. Figure 1a shows the qualitative features of the flowfield in a plane through the spanwise jet centerline. A three-dimensional bow shock forms ahead of the injectant stream and interacts with the approaching boundary layer, resulting in a separation bubble. A barrel shock also occurs as the underexpanded jet accelerates into the crossflow. Acceleration of the jet core flow continues until a normal shock, or Mach disk, forms. Directly downstream of the jet plume another separated zone develops in the region between the jet exit and the boundary layer reattachment point. Figure 1b is a perspective view of the three-dimensional flowfield. This schematic shows the pair of counter-rotating vortices generated within the jet fluid. A horseshoe-vortex region also forms near the jet exit and wraps around the injector as illustrated in the schematic.

Fric and Roshko<sup>1,2</sup> conducted an experimental study using smoke-wire visualization in an attempt to examine the development of large-scale structures in the flowfield created by a jet injected into a low speed stream. Their photos illustrate the emergence of four types of vortical structures near the injector exit: the shear layer vortices, the counter-rotating pair, the horseshoe vortices in the near-wall region, and the vortex system formed in the wake region. The shear layer vortices developed from vorticity contained in the jet boundary layer, and oriented themselves in such a way as to roll up into the freestream fluid. This indicated that the injectant fluid moved with a higher velocity tangent to the interface than the freestream fluid in the injector near-field. The counter-rotating structures, which also formed from vorticity present in the jet boundary layer,<sup>1,3</sup> appeared two-dimensional and were oriented in the streamwise direction.<sup>4</sup> These vortices persisted far downstream, although their strengths decreased due to viscous dissipation.<sup>5</sup> Other authors have presented evidence of the dominance of these counter-rotating vortices formed within the injectant for the case of low speed crossflows.<sup>6,7</sup> Horseshoe vortices form in the near-wall region from vorticity within the crossflow boundary layer and vorticity generated due to the wall pressure gradient resulting from the jet/freestream interaction. These structures bend around the jet orifice before proceeding downstream. The most interesting findings of Fric and Roshko<sup>1,2</sup> were the vortices observed in the wake region downstream of the injector. McMahon, et al.<sup>8</sup> obtained vortex shedding measurements from the wake region thereby acknowledging the presence of such structures, but the dynamics of their formation and their characteristic motions were unknown. By tagging different regions with smoke, Fric and Roshko<sup>1,2</sup> found that the jet's

vorticity did not contribute to the formation of wake vortices; rather, these structures formed from vorticity present in the crossflow boundary layer. They also showed a dramatically different wake structure compared to that formed behind a solid protrusion in the crossflow.

Fundamental investigations of the vortex structure of wall injection into a supersonic flow are less common than for the low speed case. Heister and Karagozian<sup>9</sup> proposed a model of the flow based on the dominant counter-rotating vortex pair formed within the jet. Other experimental<sup>10-14</sup> and numerical<sup>15-17</sup> studies of basic and complex injection flowfields consistently document the presence of these characteristic vortices. However, the shock structures within the freestream and the underexpanded jet, along with the time-averaged features of the flow, received more attention than the role of this important vortex pair in the near-field region. Recently, instantaneous planar laser-induced fluorescence (PLIF) of nitric oxide<sup>18</sup> and acetone<sup>19</sup> and Mie scattering<sup>14,19,20</sup> images have revealed large-scale vortices present within the shear layer at the jet/freestream interface. These vortices, similar to those observed by Fric and Roshko<sup>1</sup> in that their orientation suggests faster injectant fluid tangent to the interface near the injector, appeared to contribute significantly to near-field entrainment. Surface flow visualization studies<sup>10,17,19</sup> clearly illustrate the region where horseshoe vortices wrap around the injector orifice. No evidence of the wake vortices observed in the low speed flow case is available for supersonic injection. However, since these structures arise from vorticity contained in the crossflow boundary layer, they are likely to also exist in the supersonic flow case unless the bow shock acts in some way to inhibit this vorticity from entering the wake.

Circular and non-circular nozzles produce jets exhibiting very different structural characteristics in the presence of both quiescent and co-flowing environments.<sup>21-25</sup> Studies of a small aspect ratio elliptical jet showed that the boundary layer momentum thickness varied around the circumference of the jet orifice.<sup>21</sup> Ho and Gutmark<sup>22</sup> found that the instability in the elliptic jet arose from the maximum vorticity associated with the smallest momentum thickness. This asymmetric instability led to the development of asymmetric vortices around the nozzle exit. An important result of this asymmetry was that the spreading characteristics in the major- and minor-axis planes became very different as the flow developed in the streamwise direction. At some point downstream, depending on the aspect ratio of the nozzle, the widths of the jet in the two planes were equal. However, downstream of this point an axis-switch occurred as the spreading of the minor-axis plane overtook that of the major-axis.<sup>23,24</sup> Thus, the rate of spread in the minor-axis plane was larger than the rate of spread in the major-axis plane. This minor-axis spreading was significantly greater than the spread associated with a circular jet, where symmetric vortices form at the nozzle exit. The expansion ratio of the jet also affected the

structure; underexpanded elliptical jets spread much faster than perfectly expanded or subsonic elliptical jets.<sup>23</sup> The shock structure within the underexpanded jet contributed strongly to this result through acoustic feedback between sound waves and the large structures of the shear layer.<sup>26</sup> Similar feedback effects occurred in circular underexpanded jets. These effects manifested themselves in vortical mode changes within the jet structure and alterations of the near-field pressure fluctuations rather than in spreading enhancement.<sup>25</sup>

The objective of the current work is to obtain a more thorough understanding of the dominant features that govern the near-field mixing in flowfields created by transverse injection into supersonic streams. As suggested by the results presented above, large-scale motions dominate the near-field mixing processes in these flows. By using a planar imaging technique in the near-field, more insight into the fundamental fluid mechanics of these flows is obtained. Relevant data include transverse and lateral penetrations, as well as statistics concerning the streamwise vortex pair, large-scale shear layer structures, and near-field mixing.

### Experimental Facility

The experiments documented herein were performed in the supersonic combustion research facility located at Wright-Patterson Air Force Base. The various components of this facility have been discussed in detail elsewhere;<sup>27</sup> only a summary of the important features is included here.

### Flow Facility

The wind tunnel used in this investigation is shown schematically in Fig. 2. A series of compressors capable of producing a continuous 34-lb<sub>m</sub>/s flow of air at about 750-psig and ambient temperature supplied the facility. Additionally, an exhaust system evacuated the test section to approximately 3-psia before starting the tests.

A rearward-facing perforated cone, along with an array of mesh screens and a section of honeycomb, conditioned the air within the settling chamber. The cone spread the flow uniformly within the chamber while the screens and honeycomb reduced large-scale turbulence and straightened the flow before acceleration by the supersonic nozzle. Tunnel stagnation conditions were monitored by a general purpose data acquisition system.

A nozzle designed with a method of characteristics code<sup>28</sup> produced a Mach 2 freestream. Recent results indicated that the flow is uniform and two-dimensional within the test section at a Mach number of about 1.98.<sup>27</sup> The nominal cross sectional dimensions of the constant area test section used in these studies were 5" by 6". A pair of side windows and a top window provided optical access to the flow.

For the present study, injector geometries were incorporated into the removable test inserts housed within the bottom wall of the test section. Both injector geometries were placed at the same streamwise location to

ensure that the boundary layer thickness approaching the injector would be the same for each case. At the chosen injector location, the boundary layer thickness-to-effective jet diameter ratio is approximately  $\delta/d_{\text{eff}} = 1$ .

### Injectors

The two transverse injector geometries designed for these experiments included circular and elliptical nozzles. To ensure a proper comparison between the two injectors, each had a cross sectional area of 0.049-in<sup>2</sup>. The orifice diameter of the circular injector was, therefore, 0.25". The resulting elliptical aspect ratio was 3.8:1. Table 1 presents the geometries of the injectors, where  $a$  and  $b$  are the semi-major and semi-minor axes, respectively, and  $\epsilon$  is eccentricity. Figure 3 illustrates the cross sectional and plan views of the injector geometries. The resulting injectors have the same effective diameter ( $d_{\text{eff}} = 0.25"$ ).

Each injector was equipped with a pressure tap near its exit, as shown in Fig. 3, for static pressure measurements. A pressure transducer was connected to this port and its output was documented using a general purpose data acquisition system composed of a 486 PC, a bank of Preston amplifiers, and a National Instruments A/D converter. In addition to this, the jet stagnation temperature was measured just upstream of the entrance to each injector using a thermocouple that was monitored by the same system. Both readings allowed the operating conditions of the injectant flow to be accurately set.

Dry air and helium served as injectant gases in these studies. Tube trailers containing large volumes of high pressure (2000-psig) air or helium were available outside the test cell. A high-pressure regulator fed a 2" supply line from the trailer. This line led to a manifold in the test cell, where a 1" line supplied the injector. A dome regulator placed in the line controlled the injectant pressure. A small amount of gas from the supply line loaded the regulator dome allowing very repeatable pressure conditions at the jet exit to be set. Two solenoid valves were installed between the dome supply and the regulator to conserve the injectant gas. Another solenoid valve allowed fast on/off cycling.

### Shadowgraph System

Shadowgraph photography resulted in instantaneous visualizations of the flowfield of interest. A Xenon nanopulser with a pulse duration of approximately 10-ns provided the light source. The light from this lamp was collimated by a 4" lens and then focused using another 4" lens. Photographs were taken with a large format 4" x 5" back plane camera using Polaroid ASA 3000 film. A schematic of the system appears in Fig. 4.

### Imaging System

For the present experiments, two optical arrangements provided the means by which the flowfield is interrogated. Figures 5a and b present schematics of the configurations used for single-shot images, where a Spectra Physics

Quanta-Ray DCR-4 Nd:YAG laser provided the laser beam. The output of the laser passed through a second harmonic generator to produce a beam of light at 532-nm (approximately 400-mJ/pulse). A turning prism directed this beam to the traversable optical table mounted beneath the test section where a combination of mirrors, prisms, and lenses (-150-mm cylindrical and 500-mm biconvex) produced the collimated laser sheet used for illuminating the flowfield. For end view images, the sheet entered the test section through one side window, while in the side view images, the sheet entered through the top window. The laser sheet had a width of approximately 50-mm and a thickness (measured using a photodiode and an oscilloscope) of roughly 200- $\mu$ m at the long focal waist.

A Princeton Instruments ICCD camera (384 x 576 pixel array) and image acquisition system (controller model ST-130) obtained the flowfield images. The camera was water cooled and purged with nitrogen to reduce dark current noise. A Nikon UV-Nikkor 105-mm f/4.5 telephoto lens placed in front of the pixel array improved the resolution associated with the pixel area. A Princeton Instruments pulse generator (PG-10) synchronized the laser flash lamp and the camera so that only a single laser pulse was imaged, and a 486 PC running the CSMA image acquisition software collected the images. Further image analysis was done using the 486 PC and a Macintosh.

### Seeding Issues and Technique

Particle response characteristics are very important in scattering experiments; seed particles must follow the fluctuations within the turbulent flowfield so that the collected images may be accurately interpreted. Samimy and Lele<sup>29</sup> found that accurate particle response for Mie scattering images required a Stokes number, defined as the ratio of the particle response time scale to the characteristic fluid dynamic time scale, of less than about 0.5. The particle response time is modeled using a Stokesian drag law<sup>30</sup> given by

$$t_p = (1 + 2.76 \cdot Kn) \frac{\rho_p d_p^2}{18\mu}, \quad (1)$$

and the characteristic fluid dynamic time used is the large-eddy rollover time that takes the form

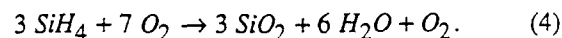
$$t_\delta = \frac{\delta}{\Delta U}, \quad (2)$$

where  $\delta$  is the shear layer vorticity thickness, and  $\Delta U$  is the velocity difference across the shear layer. Thus, both particle size and density play major roles in the ability of a seed medium to adequately follow the turbulent fluctuations within compressible flows. Maxwell's relation, given by

$$\ell \equiv 1.5 \frac{\mu}{\rho a}, \quad (3)$$

allows estimation of the mean free path and thus calculation of the Knudsen number assuming a nominal particle diameter is available.

In the present study, silane ( $\text{SiH}_4$ ) combustion produced the seed that marked freestream fluid. Silane is a pyrophoric gas that, when exposed to oxygen, burns to form primarily solid silicone dioxide ( $\text{SiO}_2$ ), water, and hydrogen. In their study of the silane/oxygen reaction, Hartman, et al.<sup>31</sup> found that the stoichiometry for reactions with less than 30% silane in oxygen took the form



No chemically detrimental byproducts are created in this reaction; however, silane presents some handling difficulties since it is pyrophoric. In another study, Rogers, et al.<sup>32</sup> used an electron microscope to characterize the silicone dioxide particle sizes. The authors found that a nominal particle diameter of 0.2- $\mu$ m results from this reaction. The specific gravity of silicone dioxide is roughly 2.2 making the Stokes number, found using the expected operating conditions, approximately 0.1. Thus, these particles are small enough to allow accurate interpretation of the scattering images. Additionally, the particles are truly passive participants in the fluid dynamic mixing processes encountered in the jet/freestream interaction. Therefore, large-scale mixing information may be directly obtained from the images. That is, the images may be used to interpret injectant concentration on the scale of the imaging pixels. Molecular mixing information cannot be directly inferred from the images obtained here since the relative resolution of the probe volume size to the diffusion scale of the flow is large because of the high Reynolds numbers encountered.

During initial hot-flow experiments with this technique, acquired signal-to-background levels were found to be too low for acceptable data quality. Thus, the  $\text{SiO}_2$  seeding technique was supplemented by operating the facility at ambient temperatures so that the particles provided nucleation sites for condensation of naturally occurring water vapor in the freestream air. This technique provided adequate signal-to-background levels; however, the completely passive nature of the  $\text{SiO}_2$  particles was sacrificed. A separate examination of particle size using polarization effects indicated that the combined seeding technique produced particles that reside in the Rayleigh scattering regime. Intrusive probe measurements aimed at determining the accuracy of the concentration measurements made using the pseudo-passive scalar imaging technique are presently in progress.

A schematic of the silane injection system appears in Fig. 6. This figure shows key components of the system including a cross purge assembly, check valves, regulators, shutoff valves, and remotely activated solenoid valves. Nitrogen provides the flush gas for the system. A regulator sets the outlet pressure of the nitrogen bottle and a solenoid valve opens while the silane is idle to allow flushing. A vacuum pump connects to another leg of the cross so that the entire system can be evacuated. Finally, the supply leg of the system consists of a shutoff valve followed by a

regulator, a pair of check valves, and a solenoid valve. Check valves straddle the solenoid valve so that the silane reaction is delayed until just prior to entering the tunnel.

### Results and Discussion

Flow conditions for the present investigation appear in Table 2. The key parameter that remains constant throughout the experiments is the jet-to-freestream momentum flux ratio ( $J$ ) defined as

$$J = \frac{(\rho u^2)_j}{(\rho u^2)_f} = \frac{(\gamma p M^2)_j}{(\gamma p M^2)_f} \quad (5)$$

This has been identified in the past as the principal parameter controlling the jet's penetration into the crossflow.<sup>33,34</sup>

The following sections present the various results obtained in this investigation. Shadowgraph photos appear first, followed by end view and side view imaging results.

#### Shadowgraph Photos

Instantaneous flow visualizations for each of the four cases appear in Figs. 7a-d. The scale of the photographs is approximately twice the actual scale of the injection flowfield. Clearly present in each photo is the freestream shock structure created by the presence of the jet. Both the bow shock and the separation shock formed ahead of the injector orifice are captured. It is interesting to note that the inclination of the bow shock changes with the injector geometry. Figures 7a and b illustrate the flowfield created by the circular jet. Compared to the bow shocks created in the elliptical cases (Figs. 7c and d), those in the circular cases appear stronger. Another feature in these photos worth some attention is the separation zone ahead of the injector orifice. The shadowgraphs suggest that the elliptical injector produces a smaller region of separation than the circular orifice, while each jet has the same effective diameter and operates at the same value of  $J$ .

In addition to the freestream shock structure, the characteristics of the jet also appear in these photographs. In the cases where the injectant is air (Figs. 7a and c), the jet shock structure is observed. The barrel shock created in the elliptical case appears to be oriented at a shallower angle above the bottom wall than that associated with the circular orifice. Also apparent in each case is the Mach disk at the downstream end of the barrel shock. Beyond the shock structure in these two figures, the large-scale eddies formed at the interface between the jet and freestream fluids are apparent. These structures form immediately as the jet exits into the freestream. The shadowgraphs also indicate that the structures roll into the freestream as observed in previous work.<sup>14,19,20</sup> The photos of the helium injection cases (Figs. 7b and d) appear quite different in comparison. Here, the jet's shock structure does not appear. However, the interface between the jet and freestream is clarified and the structures that reside there appear rather amorphous compared to those

that form in the air cases. Nonetheless, large-scale behavior is clearly visible. Other features that appear in the helium photos that are absent from those taken with air injection are curved shock waves in the region above the jet. These waves are most probably shocklets generated by the large-scale eddies. Some of these waves are relatively strong as indicated by the curvature change induced in the bow shock at their point of intersection.

#### End View Images

Results of the end view imaging experiments are discussed in the following sections. Instantaneous images are presented first followed by statistical results. Both ensemble-averaged and standard deviation analyses are discussed. The instantaneous shots provide a great deal of information regarding the structure of the flowfield and the characteristics of the jet. Ensemble-averaged images reveal transverse and lateral jet penetrations. Finally, analyses of standard deviations provide substantial information concerning the fluctuations in this highly turbulent, three-dimensional flowfield. From these images it will be shown that descriptions of the flowfield in the time-mean sense are not enough to gain an understanding of where the mixing regions form and how enhancement of that mixing can be accomplished.

Each end view image displayed covers approximately 6.4 effective diameters in the spanwise direction and 5.5 effective diameters in the transverse direction. The flow direction in all of the images is out of the paper. The color palette has been reversed so that pure seeded fluid appears black while pure unseeded fluid appears white. This highlights the features within the jet fluid.

#### Instantaneous Results

Figures 8-11 show select instantaneous images of the four cases studied in this investigation. Four streamwise image planes are represented for each case. Images taken with the laser sheet positioned at the jet centerline (i.e.,  $x/d_{\text{eff}} = 0$ ) clearly show the shape of the bow shock. These images illustrate the three-dimensional nature of the flow by showing the intersection of the bow shock with the separation shock. This intersection region can perhaps be most clearly discerned in the first image of Fig. 9. The curved bow shock suddenly changes shape at the outer edges of the image where the separation shock has wrapped around the injector orifice. Figure 1b provides some illustration of this phenomenon. Also very prominent in the images from this location are the large-scale eddies that form in the interfacial region between the jet and freestream fluids. Obviously, these structures form at the earliest stages of the flowfield's development. Another notable feature observed in the images obtained at  $x/d_{\text{eff}} = 0$  is that the elliptical jet spreads laterally as much as the circular jet with half the span.

As the image plane moves downstream, the vortical structure of the jet fluid becomes quite dramatic. Each case studied here shows significant large-scale behavior at

$x/d_{eff} = 4$ . Counter-rotating vortices emerge as the jets elevate off the floor of the tunnel. The edges of the jet fluid appear highly convoluted and dominated by small-scale vortices. By  $x/d_{eff} = 8$ , the jet fluid in the air injection cases has begun to break up considerably, while the helium cases appear to remain more coherent. Also detectable here are eddy shocklets that form as the large-scale eddies protrude into the supersonic crossflow. Finally, the images at  $x/d_{eff} = 10$  continue to show the spatial development of the jet along with relative intensity decreases that are indicative of mixing between the two streams. Large- and small-scale eddies remain very prominent and shocklets are again observed.

#### Ensemble-Averaged Results

Figure 12 presents the averaged results obtained from the flowfield generated by helium injection through the circular nozzle. Depending on the image plane location, either 20 or 100 images were used to compute the average images shown (20 shots at  $x/d_{eff} = 0$  and 8, 100 shots at  $x/d_{eff} = 4$  and 10). The larger ensembles were taken to provide better averages for comparison to the probe-based concentration studies that are currently underway.

The first image shows the uniform freestream above the curved cross section of the bow shock. The jet fluid appears white in the image and extends from approximately  $z/d_{eff} = -1$  to 1. Some mixing between the two streams is indicated at the upper edge of the jet fluid by the intermediate gray scales found there. This is the region where large-scale eddies first appear as shown in the instantaneous images presented earlier. The sharp gradients along the sides of the jet fluid suggest that the small-scale eddies that form there do not provide significant mixing potential as the jet exits the orifice and interacts with the freestream fluid. Moving downstream to  $x/d_{eff} = 4$ , the counter-rotating vortex pair formed within the jet fluid appears. These two structures create a void region within the central core of the jet allowing fluid from the freestream to be engulfed. Peripheral mixing between the two streams appears to have increased by this station as suggested by the marked increase in gray levels. The two average images computed for  $x/d_{eff} = 8$  and 10 illustrate similar characteristics. By the final image plane location, the amount of mixed fluid appears to have substantially increased over that shown in the image from  $x/d_{eff} = 4$ .

The results of analyzing the averaged images for jet penetration appear in Figs. 13 and 14. Here, both transverse and lateral penetrations are shown, where the maximum jet penetration is defined as the location of 90% of the average freestream intensity behind the bow shock. The transverse results in Fig. 13 indicate that the jets have all reached their maximum extent into the crossflow by roughly  $x/d_{eff} = 8$ . In fact, downstream of  $x/d_{eff} = 4$ , only slight changes occur. Further, all four cases demonstrate comparable values providing more evidence that the jet-to-freestream momentum flux ratio is a correlating parameter

for transverse jet penetration. Figure 14 presents the lateral penetration results. All four cases start with about the same spread at  $x/d_{eff} = 4$ . From here, the spreading trends are not completely clear, though all cases eventually indicate some lateral contraction occurring. This observation is consistent with previous data obtained farther upstream<sup>14</sup> and is thought to be indicative of the jet diffusing into the crossflow (i.e., that the jet fluid is mixing with the crossflow fluid yielding smaller regions containing high concentrations of injectant). Helium cases appear to decay at a slower rate than those for air. The elliptical jets consistently spread as much or more than the circular jets on the average. This implies that the injectant fluid spreads laterally at least two times faster in the elliptical cases than in the circular since the span of the elliptical jet is initially half that of the circular. It also indicates that the axis-switching phenomenon observed in other elliptical injection studies is preserved here.<sup>23,24</sup> Further work to quantify and understand these trends is presently underway.

#### Standard Deviation Results

Beyond the time-averaged data, it is important to understand the fluctuations found in turbulent, compressible mixing flowfields. By examining the image standard deviation given by

$$\sigma = \sqrt{\frac{(I - \bar{I})^2}{N - 1}}, \quad (6)$$

more insight into the location, formation, and development of regions of fluctuating fluid can be better understood. For example, the interface region between the jet and freestream fluids may be examined in more detail. Also, the lifetime of the unfluctuating jet core can be identified in terms of streamwise position.

Standard deviation images appear in Fig. 15 for the injection of helium through the circular nozzle. As with the averaged images presented above, either 20 or 100 images were used to compute the standard deviation images shown (20 shots at  $x/d_{eff} = 0$  and 8, 100 shots at  $x/d_{eff} = 4$  and 10). At the first measurement station, several details are worth noting. First, the bow shock appears to fluctuate slightly. Examining the ensemble of instantaneous shots from this location reveals that the bow shock is influenced by the large-scale eddies that form intermittently at the jet's upper edge. Second, the shearing region around the periphery of the jet is observed. As suggested by the ensemble-averaged image in Fig. 12, the sides of the jet at this measurement plane are characterized by thin regions of fluctuating fluid as compared to the top of the jet. Thus, most of the freestream entrainment that occurs at this location does so due to the large-scale eddies evolving at the upper edge of the jet. Third, the jet core and the crossflow are essentially undisturbed.

Moving downstream to  $x/d_{eff} = 4$ , the development of the mixing region around the periphery of the jet can be examined in closer detail. Here, the region of fluctuating

fluid has grown substantially on both the sides and the top of the jet. Note the region between the two counter-rotating vortices near the bottom wall where significant entrainment appears. Also note that the central cores of the two counter-rotating vortices remain relatively devoid of fluctuating fluid compared to the region surrounding them. Thus some regions of "unmixed" fluid (in terms of the turbulent fluctuations) still exist. Continuing downstream, similar characteristics are observed, although the extent of the fluctuating fluid continues to increase. By  $x/d_{eff} = 10$ , no undisturbed cores remain.

In an attempt to quantify the large-scale mixing characteristics of the four cases studied here, further analysis of the standard deviation images was undertaken. Each image was normalized by an average fluctuation level from the freestream. Then, an arbitrary contour (here 70%) was chosen that gave an accurate representation of the region containing fluctuating fluid. This region can be thought of as an active large-scale mixing zone. In no way is this contour attempting to quantify *how much* freestream fluid has been entrained. Within this region, the large eddies actively entrain fluid from the crossflow thereby giving the two fluids the *potential* to become molecularly mixed. The contours corresponding to the images of Fig. 15 appear in Fig. 16. Once these contours were obtained, the area enclosed within them and their perimeters were computed. A shape parameter ( $S$ ), defined by

$$S = \frac{P}{2\pi r_o} \text{ where } r_o = \sqrt{\frac{A_\sigma}{\pi}}, \quad (7)$$

is used to indicate the amount of large-scale mixing occurring between the two streams. The shape parameter has been used in a recent investigation of parallel injection into a supersonic stream with good success.<sup>35</sup> This parameter attempts to describe the relationship between the perimeter and area of a given contour and compares them to a perfectly circular contour. If the contour of interest was a perfect circle, the value of  $S$  produced would be unity. This is also the geometry that leads to a minimum value of the shape parameter defined above. Thus, contours that lead to shape parameters greater than unity are considered to have greater mixing potential than those having values of  $S$  near unity by virtue of increased mixing area and the presence of large-scale structure.

Plots of the area and shape parameter appear in Figs. 17-18, respectively. Some very discernible trends appear in these data. First, Fig. 17 shows the area ratio resulting from the computations. This ratio is defined as the area inside the standard deviation contour,  $A_\sigma$ , divided by the cross sectional area of the injector,  $A_{xs}$ . All four cases appear in the figure and two distinct pairs of lines result. The fluctuation areas in the air injection flowfields grow until  $x/d_{eff} = 4$  and then fall off or plateau toward  $x/d_{eff} = 8$  before increasing again. The drop-off seems to result from the cores of the jet located within the counter-rotating vortex pair remaining more unmixed over this region. In contrast, the helium injection cases grow monotonically

across the entire region of investigation. It is therefore inferred that the helium flowfields result in faster decay of the jet cores and, therefore larger regions of fluid characterized by turbulent fluctuations.

Figure 18 illustrates the shape parameter data for each case. All four curves have similar characteristics in that a sharp decay is experienced in the far-field (between  $x/d_{eff} = 8$  and 10). The plateau region occurs at or above a value of  $\sim 3$  in the near-field region. This suggests that the contours are highly convoluted when compared to a perfect circle. The sharp decay indicates that the contours are tending to become more circular (or at least more toward the tunnel shape parameter of 1.13) in the far-field mixing region. Thus, large-scale mixing appears more prominent in the near-fields of these injectors. Glawe, et al.<sup>35</sup> indicate that the combination of a large shape parameter and a large area are desired for favorable mixing characteristics. On the basis of this observation and the data presented in Figs. 17-18, the helium flowfields appear to result in better mixing characteristics downstream of about 4 effective diameters than the air cases since they produce larger values  $A_\sigma$  while the values of  $S$  remain relatively constant. Also, the air cases appear to "catch up" to the helium cases in the far-field as the area ratio sharply increases toward the helium values.

There is some inconsistency observed when analyzing the areas using the method discussed above. Both instantaneous and ensemble-averaged results indicate that the helium injection cases remain more unmixed than the air cases. That is, the data suggest that the air cases mix better than the helium cases in a large-scale sense. In these flowfields, the jet-to-freestream momentum flux ratio remained constant, but the mass flow rate of air was different from the mass flow rate of helium. For this reason, it is thought that another area should perhaps be used to normalize the data presented in Fig. 17. If the jet fluid is assumed to remain entirely unmixed as it interacts with the freestream, then the cross sectional area of the jet at any streamwise plane,  $x$ , can be computed as

$$A_x = \frac{(\rho_j u_j A_{xs})_e}{(\rho_j u_j)_x} \quad (8)$$

Further assuming that: (1) the static pressure field has equilibrated, (2) the static temperature field has equilibrated, and (3) the velocity field at the desired streamwise location has become uniform allows calculation of the unmixed area occupied by the jet fluid. Recent laser Doppler velocimetry data show that by  $x/d_{eff} = 4$ , the streamwise velocity and mean Mach number fields have become relatively uniform.<sup>36</sup> Then, Eq. 8 may be simplified for  $x/d_{eff} = 4$  as follows:

$$A_4 = \left( \frac{A_{xs} \cdot p_{ej}}{M_f \cdot p_f} \right) \left( \frac{\gamma_j R_j T_f}{\gamma_f R_f T_{ej}} \right)^{1/2} \quad (9)$$

For helium and air, the two resulting values of  $A_4$  are 0.60 and 0.23 in<sup>2</sup>, respectively. Using these values to normalize



the areas inside the standard deviation contours results in the data shown in Fig. 19. Here, two distinct pairs of curves appear. The data from the air cases fall much higher on the plot than those from the helium cases. Thus, this analysis, coupled with the shape factor data of Fig. 18, suggests that helium does remain more unmixed over the range of study and that air injection results in more mixing potential than helium injection.

### Side View Images

Results of the side view imaging experiments are discussed below. Instantaneous images appear first, followed by ensemble-averaged results, and then standard deviations. The instantaneous shots provide a great deal of information regarding the structure of the flowfield and the characteristics of the jet, with particular emphasis on the large-scale eddies that form between the jet and freestream fluids. Ensemble-averaged images produce transverse jet penetrations. Finally, standard deviation images provide further information concerning the growth of the mixing region at the upper edge of the jet and the effects of the turbulent fluctuations.

Each side view image displayed (laser sheet placed at the spanwise jet centerline) covers approximately 5.6 effective diameters in the streamwise direction and 5.3 effective diameters in the transverse direction. The flow direction in all of the side view data is left to right. The color palette has again been reversed so that pure seeded fluid appears black while pure unseeded fluid appears white. Two image planes (100 images each) separated by 0.4 effective diameters in the streamwise direction were examined for each case.

### Instantaneous Results

Figures 20-23 show select instantaneous images of the four cases studied here. The first image of each pair illustrates the formation of the bow and separation shocks ahead of the jet exit. These shots also demonstrate the large-scale behavior at the jet/crossflow interface. Significant differences in structure size and shape occur between the air and helium injection cases. The eddies in the air cases are predominantly long, well pronounced roll-ups into the freestream fluid. Discernible "braiding" regions form between pairs of large structures. These regions highlight the role of large-scale eddies in the engulfment process. The large structures strain the interface between them and then wrap freestream fluid into their cores. The structures in the helium cases are much flatter and more amorphous than those found in air injection. Also, the braiding regions are not nearly as well pronounced suggesting that less freestream engulfment occurs in the helium injection cases. Small-scale eddies appear more common here. The contrast between the two injectant gases resembles the effects of compressibility seen in two-dimensional shear layers.<sup>37,38</sup> In an earlier study using carbon dioxide and helium, similar structural characteristics were observed.<sup>14</sup>

As the image plane moves downstream, the jet structure changes dramatically. The jet breaks up quickly in the air cases, while more coherency remains in the helium cases. In Fig. 20, two large-scale eddies located at  $x/d_{eff} = 7$  and 9.6 appear to have diffused significantly as they have convected downstream. Some evidence of vortex structure within the wake region also appears in these images, although it is inconclusive at this point whether or not a system of wake vortices similar to that documented in incompressible injection studies<sup>2</sup> is established here.

### Ensemble-Averaged Results

Figure 24 illustrates the results of analyzing the averaged side view images for jet penetration. The intensity of the jet boundary presented corresponds to 90% of the average freestream intensity behind the bow shock (i.e., outer edge of the jet). Each of the plots compares the performance of an individual injector configuration. Keffer and Baines<sup>39</sup> found that the penetration profile data obtained from a subsonic jet in crossflow collapsed to a single curve in the *near injector* region when the coordinate axes were scaled by  $J^{-1}$ . The same convention has been applied here. Power law curve fits applied to the data result in the following correlations for circular and elliptical injection, respectively:

$$\frac{y}{d_{eff} \cdot J} = 1.20 \left( \frac{x - x_{cl}}{d_{eff} \cdot J} \right)^{0.344} \quad (10)$$

$$\text{and} \quad \frac{y}{d_{eff} \cdot J} = 1.10 \left( \frac{x - x_{cl}}{d_{eff} \cdot J} \right)^{0.344} \quad (11)$$

From these results it appears that the elliptical injector (Fig. 24b) actually suffers a slight reduction in transverse penetration compared to the circular case shown in Fig. 24a. The forms of the present correlations are the same as that used previously to describe the behavior of circular jets at several values of  $J$ .<sup>14</sup>

### Standard Deviation Results

A pair of side view standard deviation images from air injection through the circular injector appears in Fig. 25. The left image illustrates the slight fluctuation in the bow shock position. As in the end view images from  $x/d_{eff} = 0$ , the intermittent large-scale eddies formed at the upper edge of the jet boundary were found to influence the shock's position. The most prominent feature observed in this image is the mixing layer that grows from the upstream edge of the injector orifice. This mixing region grows very rapidly. Other features visible in the left image include the unfluctuating freestream and jet core regions. The jet core viewed at the spanwise jet centerline exists until approximately  $x/d_{eff} = 5$  where the fluctuations of the mixing layer above and wake below coalesce. Downstream of this location, the entire jet region contains fluctuations.

Future work on the standard deviation results will include documentation of the growth of the upper mixing layer, determination of the coalescence point between the mixing layer and wake, and identification of where the majority of the upper edge fluctuations occur--above or below the mean penetration contour. Also, a covariance analysis will be used to examine size and orientation of the large-scale structures.

### Summary and Conclusions

This study of the interaction of sonic jets injected transversely into a supersonic crossflow through circular and elliptical nozzles produced shadowgraph photos and two-dimensional images of the large-scale structures that dominate the mixing process in the near-field. Shadowgraph photos reveal stark differences among the four cases examined. The freestream shock structure formed in the elliptical case suggests that the elongated geometry produces a smaller separated region upstream of the jet orifice than the relatively blunt circular case. Also, the bow shock produced appears weaker in the elliptical case. The photos distinctly reveal large-scale structures at the interface between the jet and freestream. These structures appear to be influenced by the characteristics of the injectant gas, with helium giving rise to "clumpier" eddies compared to the more distinct roll-ups visible in the air cases. The shock structure within the jet appears clearly in air injection cases while relatively strong eddy shocklets were found in helium injection.

Instantaneous end view images of the jet/crossflow interaction demonstrate the highly three-dimensional nature of the flowfield. These shots illustrate large-scale eddies emerging at the outer edge of the jet (shear layer eddies) as well as within the jet (counter-rotating vortices). They also suggest that air injection leads to more rapid break-up of the jet than helium injection. Ensemble-averaged end view images produce detailed information regarding the transverse and lateral spreading of the jet. These data show that jets from elliptical nozzles spread faster in the lateral direction than jets from circular nozzles. Additionally, these data indicate that large-scale mixing in helium flowfields is slower than in air injection. Future work will be aimed at obtaining injectant concentration profiles from these images. Standard deviation images are used to examine the active large-scale mixing zone around the periphery of the jet. Analyses of standard deviation contours produce area and shape factor information that suggest air injection yields better mixing potential than helium in both circular and elliptical injector cases. These images also illustrate the dramatic variation in mixing zone thickness around the jet periphery.

Instantaneous side view images taken at the spanwise jet centerline dramatically illustrate the structure of the jet as it penetrates into the crossflow. As suggested by the shadowgraph images, substantial differences occur between the air and helium injection flowfields. Air injection gives rise to long, well pronounced eddies that

roll up into the freestream. These eddies strain the interface between them and serve the engulfment process well. Structures at the interface of the helium jet appear more amorphous. These images also illustrate the rapid break-up of the jet in the far-field (downstream of about  $x/d_{\text{eff}} = 6$ ). Also, some evidence for the presence of wake vortices exists. Ensemble-averaged images yield transverse penetration data for all cases. Using low speed scaling techniques to collapse the near-field data produces two correlations describing the circular and elliptical penetrations. Both correlations compare well to previous results. Standard deviation images illustrate the rapid growth of the mixing layer at the upper edge of the jet and the rapid decay of the jet core. These images also show the growth of the wake region downstream of the jet orifice and its coalescence with the upper edge mixing layer.

### Acknowledgments

The authors would like to acknowledge the contributions of Messrs. D. Schommer and C. Smith for painstaking assistance during the experiments. Useful discussions with and advice from Mr. J. Donbar, Ms. D. Glawe, and Drs. C. Carter, T. Chen, A. Creese, and P. Wu were greatly appreciated. This work was supported by the Air Force Office of Scientific Research.

### References

- <sup>1</sup>Fric, T.F., and Roshko, A., "Structure in the Near Field of the Transverse Jet," *Seventh International Symposium on Turbulent Shear Flows*, Stanford University, 1989, pp. 225-237.
- <sup>2</sup>Fric, T.F., and Roshko, A., "Vortical Structure in the Wake of a Transverse Jet," *Journal of Fluid Mechanics*, Vol. 279, 1994, pp. 1-47.
- <sup>3</sup>Andreopoulos, J., and Rodi, W., "Experimental Investigation of Jets in a Crossflow," *Journal of Fluid Mechanics*, Vol. 138, 1984, pp. 93-127.
- <sup>4</sup>Karagozian, A.R., "An Analytical Model for the Vorticity Associated with a Transverse Jet," *AIAA Journal*, Vol. 24, No. 3, 1986, pp. 429-436.
- <sup>5</sup>Durando, N.A., "Vortices Induced in a Jet by a Subsonic Cross Flow," *AIAA Journal*, Vol. 9, No. 2, 1971, pp. 325-327.
- <sup>6</sup>Kamotani, Y., and Greber, I., "Experiments on a Turbulent Jet in a Cross Flow," *AIAA Journal*, Vol. 10, No. 11, 1972, pp. 1425-1429.
- <sup>7</sup>Fearn, R., and Weston, R.P., "Vorticity Associated with a Jet in a Cross Flow," *AIAA Journal*, Vol. 12, No. 12, 1974, pp. 1666-1671.
- <sup>8</sup>McMahon, H.M., Hester, D.D., and Palfrey, J.G., "Vortex Shedding from a Turbulent Jet in a Cross-Wind," *Journal of Fluid Mechanics*, Vol. 48, 1971, pp. 73-80.
- <sup>9</sup>Heister, S.D., and Karagozian, A.R., "Gaseous Jet in Supersonic Crossflow," *AIAA Journal*, Vol. 28, No. 5, 1990, pp. 819-827.

- <sup>10</sup>Torrence, M.G., "Concentration Measurements of an Injected Gas in a Supersonic Stream," NASA, TN D-3860, 1967.
- <sup>11</sup>Lee, M.P., McMillin, B.K., Palmer, J.L., and Hanson, R.K., "Planar Fluorescence Imaging of a Transverse Jet in a Supersonic Crossflow," *Journal of Propulsion and Power*, Vol. 8, No. 4, 1992, pp. 729-735.
- <sup>12</sup>Hartfield, R.J., Hollo, S.D., and McDaniel, J.C., "Experimental Investigation of a Supersonic Swept Ramp Injector Using Laser-Induced Iodine Fluorescence," *Journal of Propulsion and Power*, Vol. 10, No. 1, 1994, pp. 129-135.
- <sup>13</sup>Hollo, S.D., McDaniel, J.C., and Hartfield, R.J., "Quantitative Investigation of Compressible Mixing: Staged Transverse Injection into Mach 2 Flow," *AIAA Journal*, Vol. 32, No. 3, 1994, pp. 528-534.
- <sup>14</sup>Gruber, M.R., Nejad, A.S., Chen, T.H., and Dutton, J.C., "Mixing and Penetration Studies of Sonic Jets in a Mach 2 Freestream," *Journal of Propulsion and Power*, Vol. 11, No. 2, 1995, pp. 315-323.
- <sup>15</sup>Fujimori, T., Kawai, M., Ikeda, H., Ando, Y., Ohmori, Y., Aso, S., and Fukuda, M., "Numerical Predictions of Two and Three Dimensional Sonic Gas Transverse Injections into Supersonic Crossflow," AIAA Paper 91-0415, January 1991.
- <sup>16</sup>Waitz, I.A., Marble, F.E., and Zukoski, E.E., "Investigation of a Contoured Wall Injector for Hypervelocity Mixing Augmentation," *AIAA Journal*, Vol. 31, No. 6, 1993, pp. 1014-1021.
- <sup>17</sup>Aso, S., Tannou, M., Maekawa, S., Okuyama, S., Ando, Y., Yamane, Y., and Fukuda, M., "A Study on Mixing Phenomena in Three-Dimensional Supersonic Flow with Circular Injection," AIAA Paper 94-0707, January 1994.
- <sup>18</sup>McMillin, B.K., Palmer, J.L., Seitzman, J.M., and Hanson, R.K., "Two-Line Instantaneous Temperature Imaging of NO in a SCRAMJET Model Flowfield," AIAA Paper 93-0044, January 1993.
- <sup>19</sup>VanLerberghe, W.M., Dutton, J.C., Lucht, R.P., and Yuen, L.S., "Penetration and Mixing Studies of a Sonic Transverse Jet Injected into a Mach 1.6 Crossflow," AIAA Paper 94-2246, June 1994.
- <sup>20</sup>Hermanson, J.C., and Winter, M., "Mie Scattering Imaging of a Transverse, Sonic Jet in Supersonic Flow," *AIAA Journal*, Vol. 31, No. 1, 1993, pp. 129-132.
- <sup>21</sup>Schadow, K.C., Wilson, K.J., and Lee, M.J., "Enhancement of Mixing in Reacting Fuel-Rich Plumes Issued from Elliptical Nozzles," *Journal of Propulsion and Power*, Vol. 3, No. 2, 1987, pp. 145-149.
- <sup>22</sup>Ho, C., and Gutmark, E., "Vortex Induction and Mass Entrainment in a Small-Aspect-Ratio Elliptic Jet," *Journal of Fluid Mechanics*, Vol. 179, 1987, pp. 383-405.
- <sup>23</sup>Gutmark, E., Schadow, K.C., and Wilson, K.J., "Noncircular Jet Dynamics in Supersonic Combustion," AIAA Paper 87-1878, June 1987.
- <sup>24</sup>Schadow, K.C., Gutmark, E., Koshigoe, S., and Wilson, K.J., "Combustion-Related Shear-Flow Dynamics in Elliptic Supersonic Jets," *AIAA Journal*, Vol. 27, No. 10, 1989, pp. 1347-1353.
- <sup>25</sup>Gutmark, E., Schadow, K.C., and Bicker, C.J., "Mode Switching in Supersonic Circular Jets," *Physics of Fluids A*, Vol. 1, No. 5, 1989, pp. 868-873.
- <sup>26</sup>Glass, D.R., "Effects of Acoustic Feedback on the Spread and Decay of Supersonic Jets," *AIAA Journal*, Vol. 6, No. 10, 1968, pp. 1890-1897.
- <sup>27</sup>Gruber, M.R., and Nejad, A.S., "A New Supersonic Combustion Research Facility," *Journal of Propulsion and Power*, (to be published).
- <sup>28</sup>Carroll, B.F., Dutton, J.C., and Addy, A.L., "NOZCS2: A Computer Program for the Design of Continuous Slope Supersonic Nozzles," University of Illinois at Urbana-Champaign, UILU ENG 86-4007, 1986.
- <sup>29</sup>Samimy, M., and Lele, S.K., "Motion of Particles with Inertia in a Compressible Free Shear Layer," *Physics of Fluids A*, Vol. 3, No. 8, 1991, pp. 1915-1923.
- <sup>30</sup>Melling, A., "Seeding Gas Flows for Laser Anemometry," *AGARD Advanced Instrumentation for Aero Engine Components*, Philadelphia, 1986, pp. 8.1-8.11.
- <sup>31</sup>Hartman, J.R., Famil-Ghiriha, J., Ring, M.A., and O'Neal, H.E., "Stoichiometry and Possible Mechanism of SiH<sub>4</sub>-O<sub>2</sub> Explosions," *Combustion and Flame*, Vol. 68, 1987, pp. 43-56.
- <sup>32</sup>Rogers, R.C., Weidner, E.H., and Bittner, R.D., "Quantification of Scramjet Mixing in the Hypervelocity Flow of a Pulse Facility," AIAA Paper 94-2518, June 1994.
- <sup>33</sup>Schetz, J.A., and Billig, F.S., "Penetration of Gaseous Jets Injected into a Supersonic Stream," *Journal of Spacecraft and Rockets*, Vol. 3, No. 11, 1966, pp. 1658-1665.
- <sup>34</sup>Papamoschou, D., and Hubbard, D.G., "Visual Observations of Supersonic Transverse Jets," *Experiments in Fluids*, Vol. 14, 1993, pp. 468-476.
- <sup>35</sup>Glawe, D.D., Samimy, M., Nejad, A.S., and Chen, T.H., "Effects of Nozzle Geometry on Parallel Injection from Base of an Extended Strut into a Supersonic Flow," AIAA Paper 95-0522, January 1995.
- <sup>36</sup>Santiago, J.G., and Dutton, J.C., "Velocity Measurements for a Sonic Underexpanded Transverse Jet Injected into a Supersonic Flow," AIAA Paper 95-0525, January 1995.
- <sup>37</sup>Clemens, N.T., and Mungal, M.G., "Two- and Three-Dimensional Effects in the Supersonic Mixing Layer," *AIAA Journal*, Vol. 30, No. 4, 1992, pp. 973-981.
- <sup>38</sup>Messersmith, N.L., and Dutton, J.C., "Measurements of Scalar Mixing in Compressible Free Shear Layers," *Sixth International Symposium on Laser Techniques and Applications in Fluid Mechanics*, Lisbon, 1992, pp. 415-432.
- <sup>39</sup>Keffer, J.F., and Baines, W.D., "The Round Turbulent Jet in a Cross-Wind," *Journal of Fluid Mechanics*, Vol. 15, 1963, pp. 481-496.

**Table 1** Injector Geometries

Injector	a (in.)	b (in.)	A <sub>xs</sub> (in <sup>2</sup> )	ε
Circular	0.125	0.125	0.049	0
Elliptical	0.246	0.064	0.049	0.97

**Table 2** Experimental Flow Conditions

Case	J	M <sub>f</sub>	M <sub>j</sub>	P <sub>f</sub> (psia)	P <sub>j</sub> (psia)	γ <sub>j</sub>
1C	2.9	2.0	1.0	6.0	69.0	1.40
2E	2.9	2.0	1.0	6.0	69.0	1.40
3C	2.9	2.0	1.0	6.0	58.0	1.67
4E	2.9	2.0	1.0	6.0	58.0	1.67

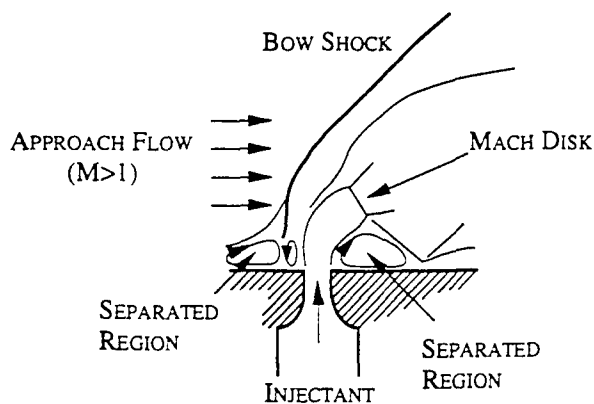


Figure 1a Transverse Injection Flowfield Schematic

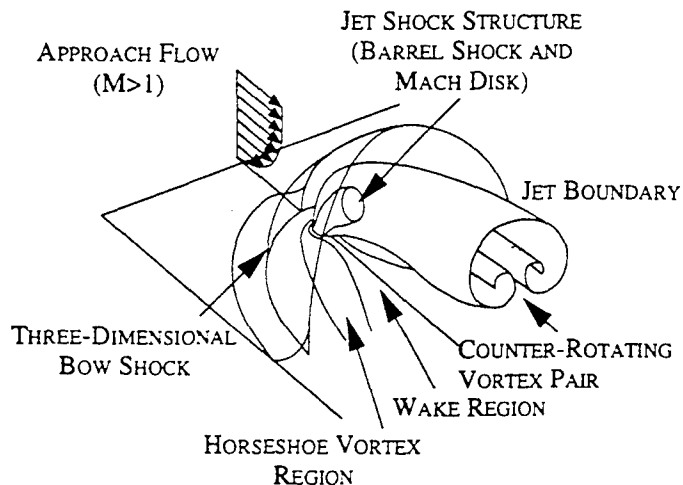


Figure 1b Perspective View of Transverse Injection Flowfield

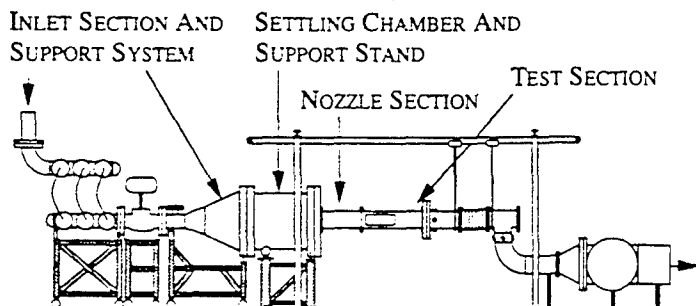


Figure 2 Schematic of Supersonic Combustion Tunnel

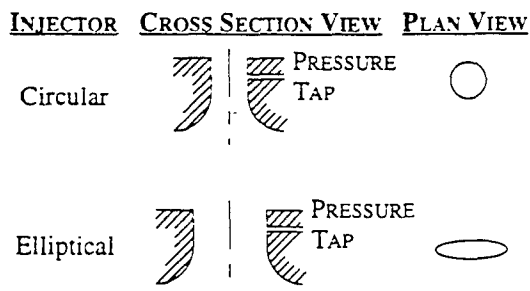


Figure 3 Illustration of Injector Configurations

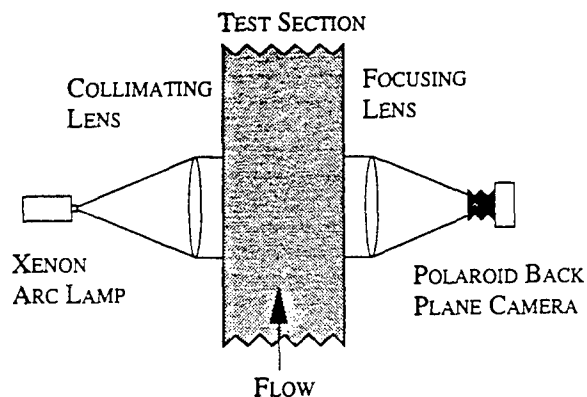


Figure 4 Schematic of Pulsed Shadowgraph System

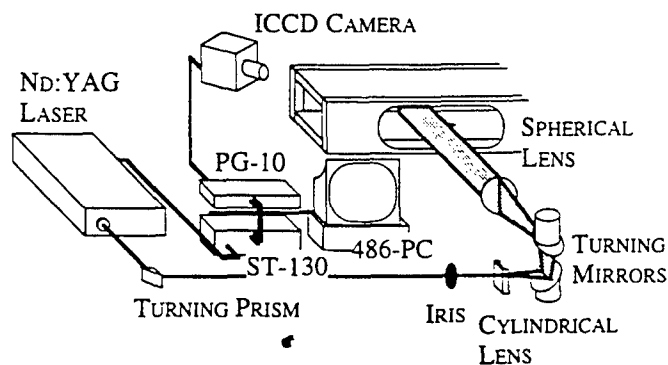


Figure 5a End View Optical Arrangement

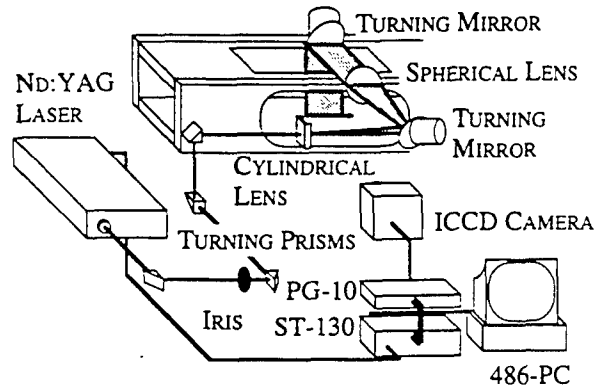


Figure 5b Side View Optical Arrangement

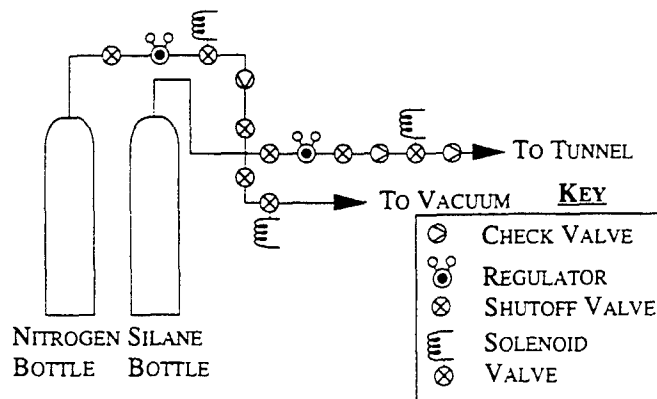


Figure 6 Schematic of Silane Seeding System

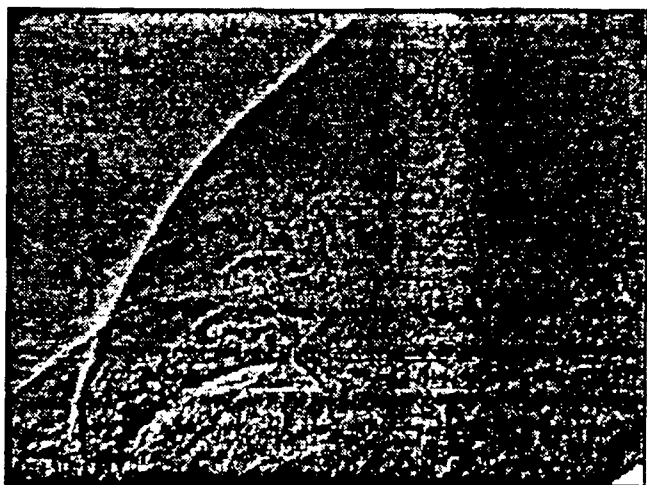


Figure 7a Shadowgraph-Circular Injection of Air

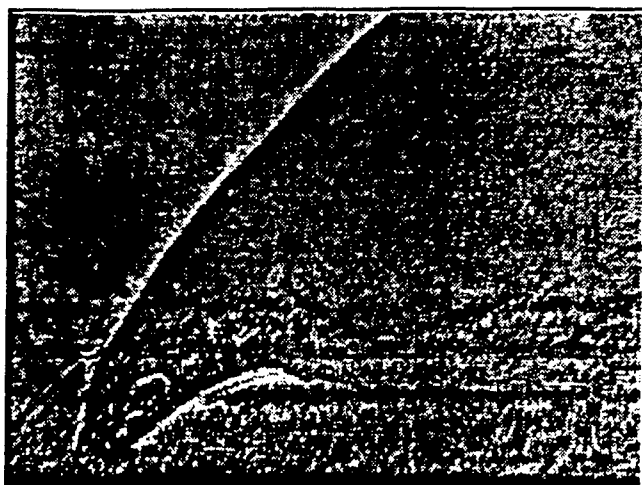


Figure 7c Shadowgraph-Elliptical Injection of Air

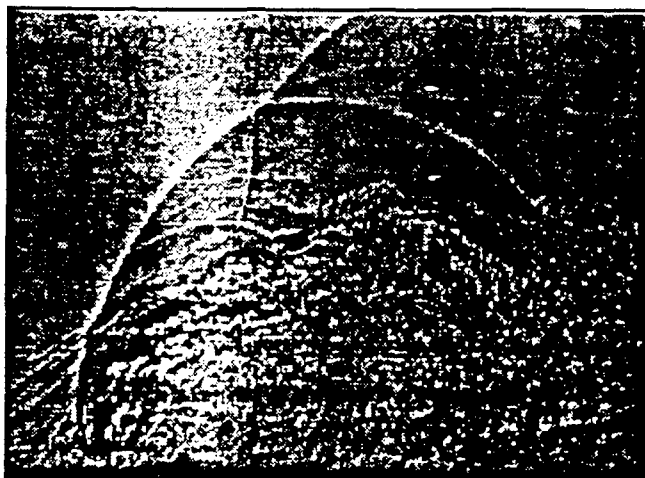


Figure 7b Shadowgraph-Circular Injection of Helium



Figure 7d Shadowgraph-Elliptical Injection of Helium

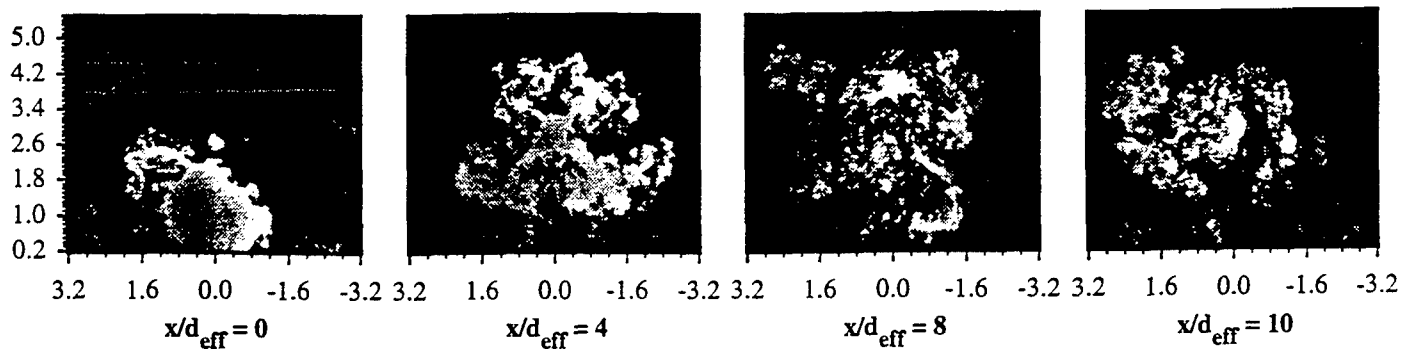


Figure 8 Instantaneous End View Images of Circular Injection Using Air

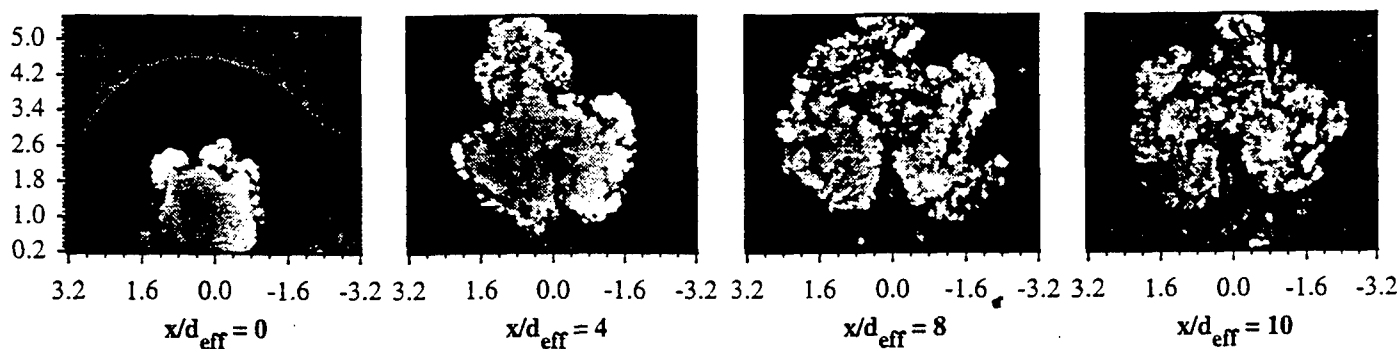


Figure 9 Instantaneous End View Images of Circular Injection Using Helium

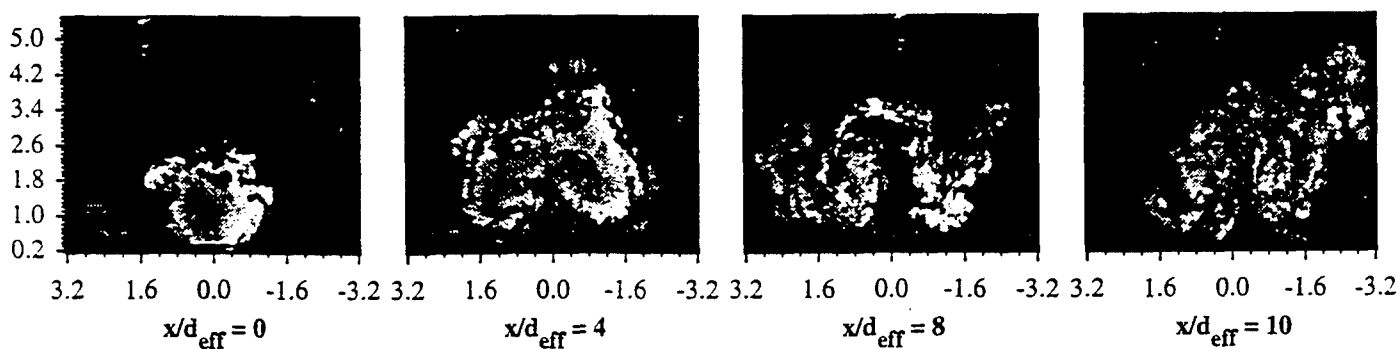


Figure 10 Instantaneous End View Images of Elliptical Injection Using Air

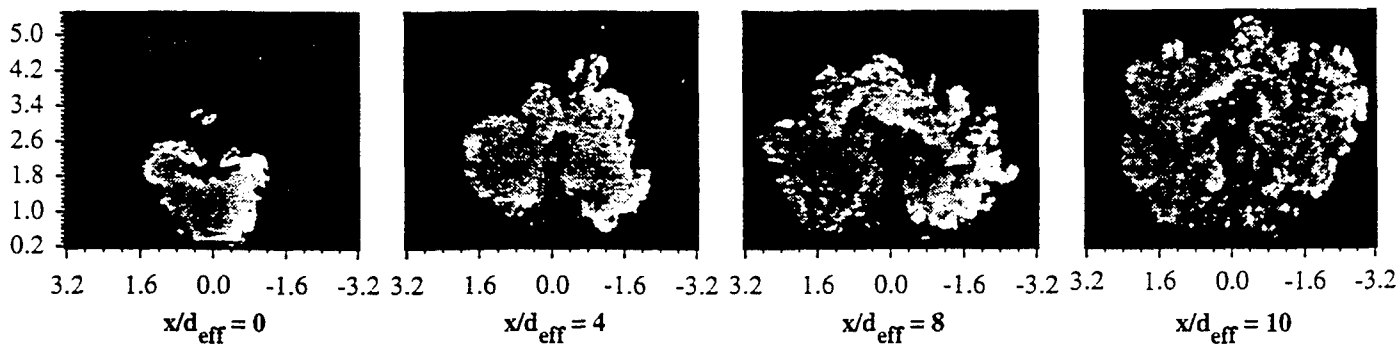


Figure 11 Instantaneous End View Images of Elliptical Injection Using Helium

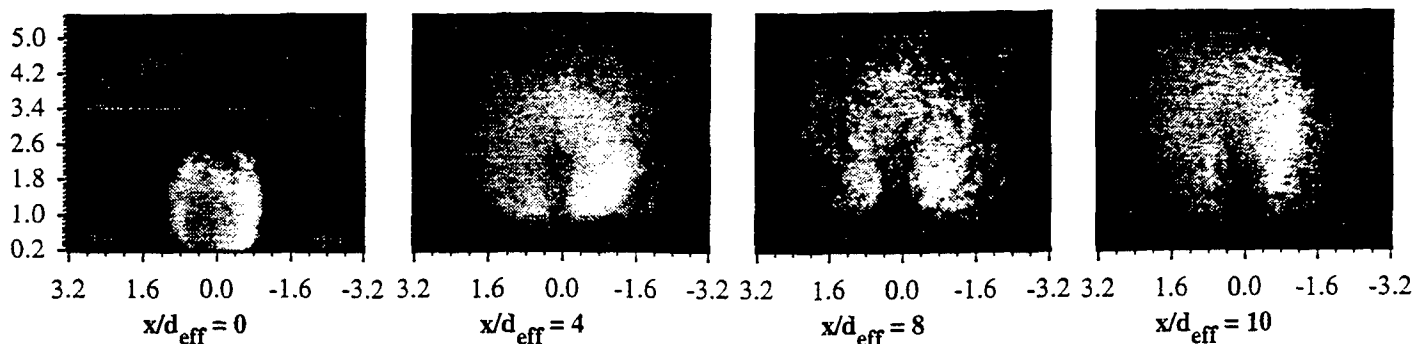


Figure 12 End View Mean Images of Circular Injection Using Helium

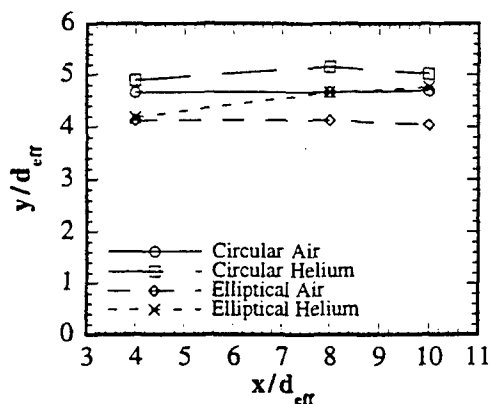


Figure 13 Transverse Penetration from Mean End View Images

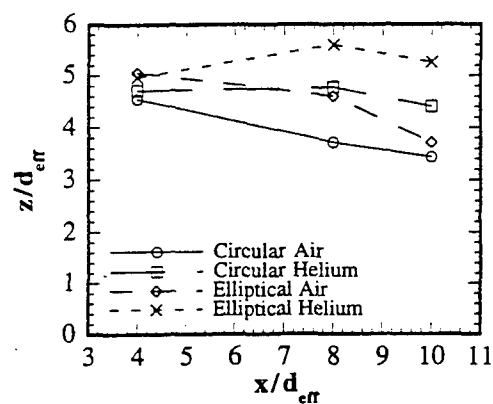


Figure 14 Lateral Spread from Mean End View Images

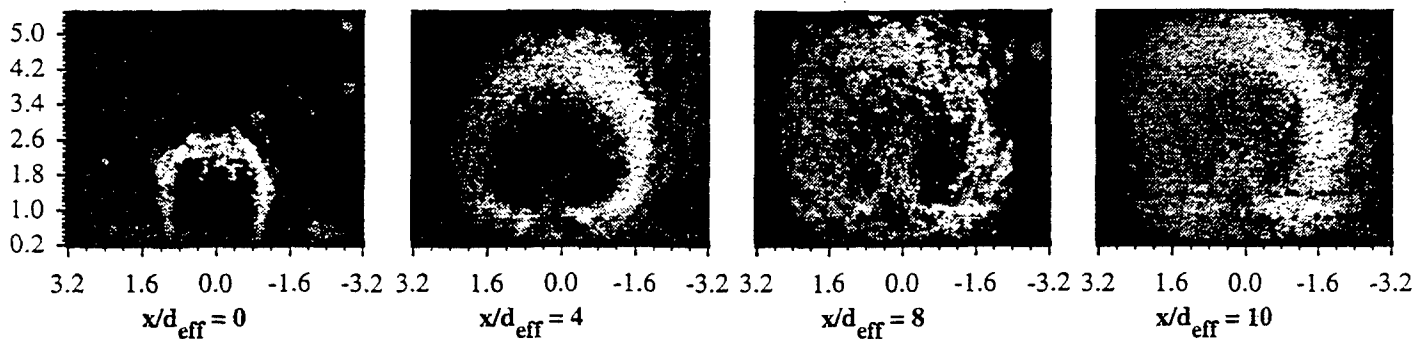


Figure 15 End View Standard Deviation Images of Circular Injection Using Helium

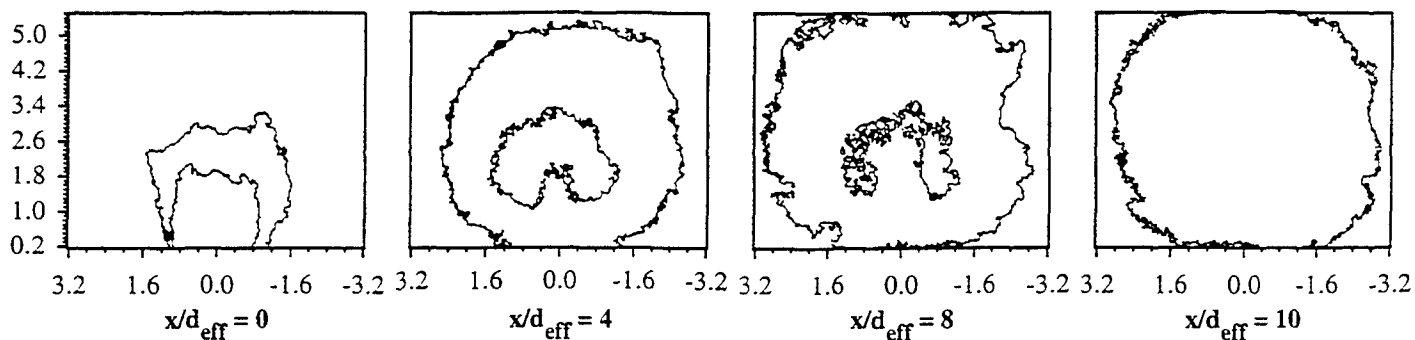


Figure 16 70% Normalized Standard Deviation Contours Corresponding to Images of Figure 15



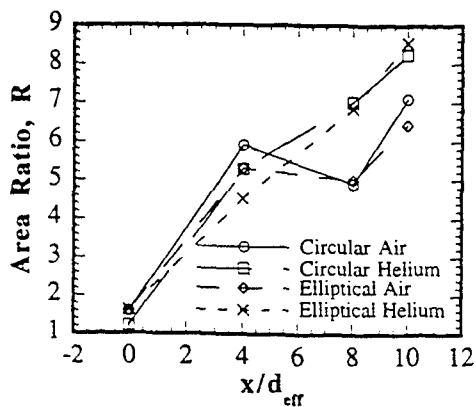


Figure 17 Area Ratio Determined from End View Standard Deviation Contours Using  $A_{x_s}$  to Normalize

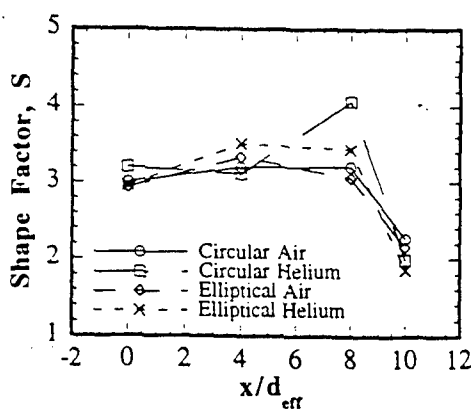


Figure 18 Shape Factor Determined from End View Standard Deviation Contours

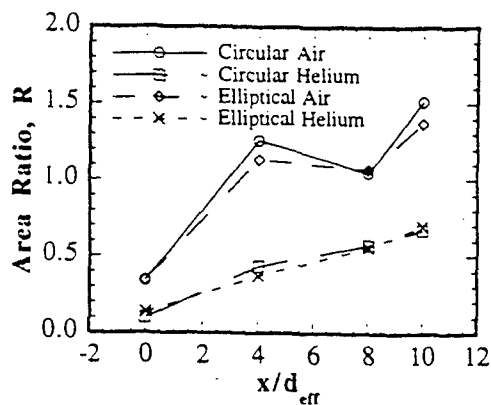


Figure 19 Area Ratio Determined from End View Standard Deviation Contours Using  $A_4$  to Normalize

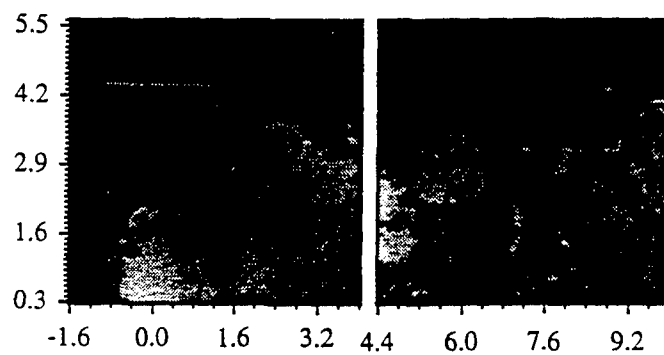


Figure 20 Instantaneous Side View Images of Circular Injection Using Air

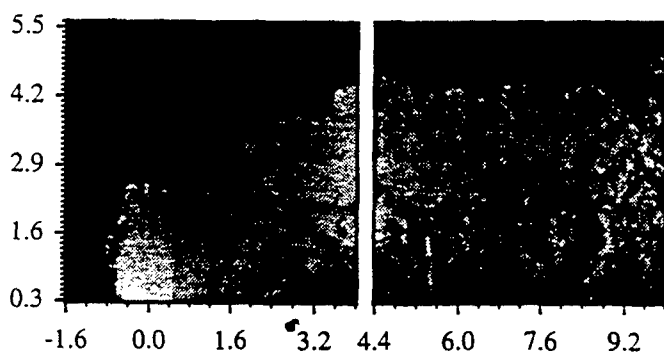


Figure 21 Instantaneous Side View Images of Circular Injection Using Helium

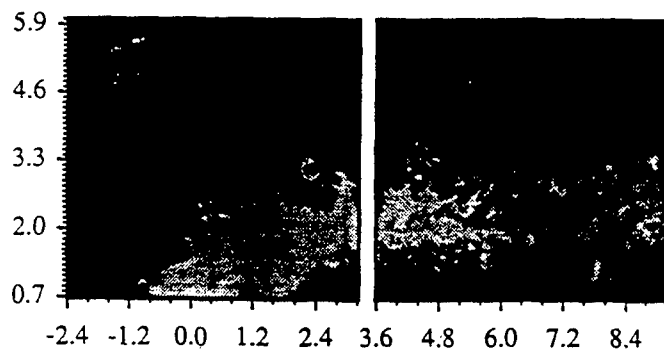


Figure 22 Instantaneous Side View Images of Elliptical Injection Using Air

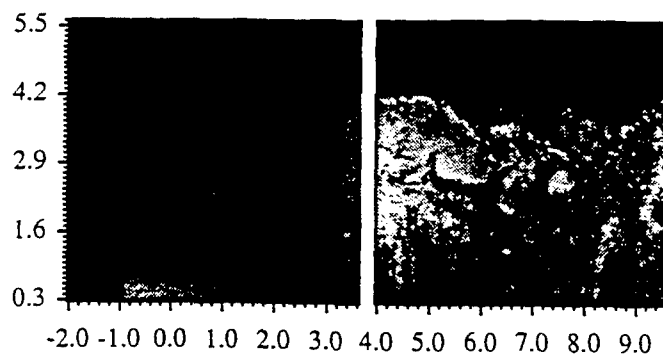


Figure 23 Instantaneous Side View Images of Elliptical Injection Using Helium

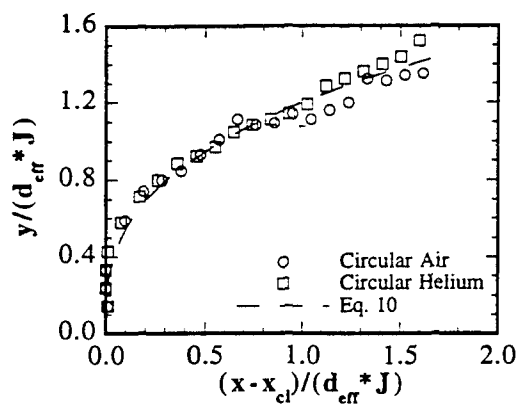


Figure 24a Transverse Penetration of Circular Injector

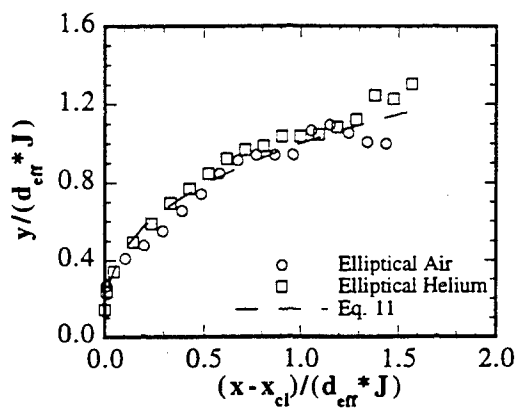


Figure 24b Transverse Penetration of Elliptical Injector

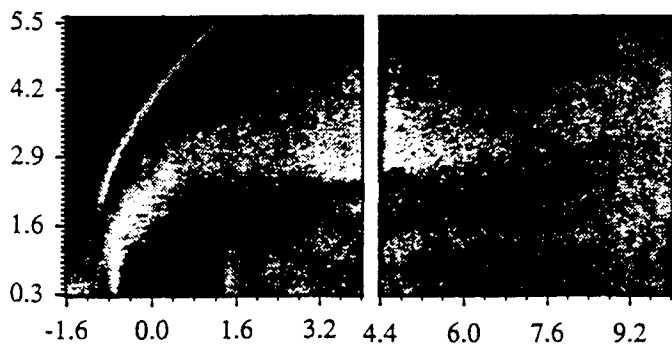


Figure 25 Side View Standard Deviation Image of Circular Injection Using Air

THIS PAGE LEFT INTENTIONALLY BLANK

## **Compressibility effects in supersonic transverse injection flowfields**

M. R. Gruber and A. S. Nejad

Wright Laboratory, WL/POPT, Wright-Patterson AFB, Ohio 45433

T. H. Chen

Taitech, Inc., Beavercreek, Ohio 45440

J. C. Dutton

University of Illinois at Urbana-Champaign, Urbana, Illinois 61801

The flowfields created by transverse injection of sonic gaseous jets through a circular nozzle into a supersonic crossflow have been experimentally investigated using planar Rayleigh/Mie scattering from silicon dioxide particles seeded into the crossflow stream. Helium and air were used as injectant gases allowing an examination of the effects of compressibility on the large-scale structural development and near-field mixing characteristics present within the flowfield. Instantaneous images from end and side view image planes show a highly three-dimensional interaction dominated by both large- and small-scale vortices. Analyses of these image ensembles provide jet spreading and penetration characteristics, standard deviation statistics, large-scale mixing information, and two-dimensional spatial correlation fields. Results indicate that injectant molecular weight does not strongly affect the jet's transverse penetration into the crossflow, although it leads to substantially different compressibility levels that dramatically influence the characteristics of the large-scale structures formed in the shear layer and the entrainment and mixing occurring between the injectant and crossflow fluids. The large-scale eddies tend to rapidly break-up in the low compressibility injection case while those in the high compressibility case remain coherent over a longer spatial range. Mixing layer fluctuations present in the low compressibility case intrude deeply into the jet fluid as compared to the high compressibility case, where these fluctuations are confined near the jet edge.

## I INTRODUCTION

Transverse injection into a supersonic stream is of fundamental interest to the supersonic propulsion community since it represents a potential fuel injection scheme for use in supersonic combustion ramjet (scramjet) engines. Candidate fuels for these engines include hydrogen and various hydrocarbons. The dramatic molecular weight difference associated with these fuels leads to a wide variation in the level of compressibility of the mixing layer that develops between the injectant and crossflow streams. Several studies of two-stream compressible shear layers have provided strong evidence that increasing compressibility affects the mixing layer growth rate,<sup>1</sup> stability,<sup>2,3</sup> turbulence levels,<sup>4,5</sup> and turbulent structures.<sup>6-8</sup> The level of compressibility is described in terms of the convective Mach number ( $M_c$ ). This parameter, given by either

$$M_{c,1} = (U_1 - U_c)/a_1 \text{ or } M_{c,2} = (U_c - U_2)/a_2, \quad (1)$$

characterizes the convective velocity of the large-scale structures ( $U_c$ ) relative to either the high speed stream ( $U_1$ ) or the low speed stream ( $U_2$ ).<sup>9</sup> Compressibility effects in transverse injection are important to quantify for a more complete understanding of the potential performance differences associated with the range of fuels under consideration for scramjets.

Figure 1 presents a schematic of the transverse injection concept, where a sonic gaseous fuel jet exhausts perpendicularly into a supersonic crossflow. The disturbance to the crossflow results in the creation of a bow shock wave that interacts with the approaching turbulent boundary layer producing a region of separated flow upstream of the injector exit and a separation shock wave. The bow shock strength varies from essentially a normal shock near the injector wall to a Mach wave far above the injector wall. In the three-dimensional injection case, the bow shock curves quickly around the injectant plume, and a pair of horseshoe vortices forms near the wall and sweeps around the injector exit. The underexpanded jet accelerates out of the nozzle and rapidly bends toward the downstream direction. A system of shock waves, consisting of a barrel shock and a Mach disk, is generated in the injectant plume. Several types of vortices also develop in the injectant fluid. First, a system of vortices forms around the periphery of the

jet plume. These eddies, hereafter referred to as shear layer vortices, begin to develop immediately as the jet fluid exits the nozzle.<sup>10</sup> They contribute to the mixing that occurs between the jet and crossflow as they actively entrain freestream fluid and enhance the interfacial strain until length scales reach the Kolmogorov scale ( $\lambda_K$ ) given by<sup>11</sup>

$$\lambda_K = \delta_\omega / Re_\delta^{3/4}, \quad (2)$$

where  $\delta_\omega$  is the shear layer vorticity thickness and  $Re_\delta$  is the local Reynolds number based on  $\delta_\omega$  and the velocity difference across the shear layer. The mixing layer compressibility level has already been found to significantly affect the convection characteristics of these vortices in the near-field.<sup>12</sup> The second dominant vortex structure that develops in the jet fluid is the counter-rotating streamwise-oriented vortex pair. Similar to those observed in incompressible jets in crossflow,<sup>13,14</sup> these eddies contribute to the engulfment of freestream fluid into the jet. A third vortex motion in the transverse injection flowfield, the wake vortex system, was first identified in a study of an incompressible case.<sup>13</sup> These vortices have been observed in compressible injection flowfields, though their roles in the mixing process remain uncertain.<sup>15-17</sup>

The objective of the present paper is to study the effects of compressibility on the near-field development in the flowfield created by sonic transverse injection through a circular nozzle into a supersonic crossflow. Cases that use air and helium as the injectant gas are studied; these choices allow a wide compressibility range to be investigated. The focus of this work is on the large-scale turbulent structures, along with the mixing and spreading characteristics of these two injection cases. A model of the near-field region is presented whereby an estimate of the mixing layer compressibility level is made. Ensembles of instantaneous two-dimensional images obtained using planar Rayleigh/Mie scattering are extensively analyzed resulting in transverse penetration and lateral spreading characteristics, standard deviation statistics, large-scale mixing information, and spatial correlation fields. The penetration and spreading data give quantitative representations of the ensemble-averaged flowfield. Standard deviation statistics indicate regions of large-scale fluctuation and reveal the developmental characteristics of these mixing

zones. Analyses of these statistical results yield important inferences regarding the freestream entrainment occurring in the two injection cases. Finally, spatial correlation maps provide detailed examinations of the large-scale vortex development within the shear layer.

## II EXPERIMENTAL FACILITY AND DIAGNOSTIC TECHNIQUE

The experiments documented herein were conducted in a supersonic research facility located at Wright-Patterson Air Force Base, Ohio. A continuous source of up to 15.4 kg/s of air at a maximum pressure of 5.27 MPa and a maximum temperature of 922 K is available. This air flows through a large settling chamber (fitted with pressure and temperature sensors for measurements of freestream stagnation conditions) into a planar, two-dimensional, variable Mach number nozzle section. For the present study, this section housed a pair of nozzle blocks designed to produce a nominal freestream Mach number of 2. The 131 mm by 152 mm constant area test section holds two side wall windows and one top wall window for optical access to the flowfield. The circular injector mounts directly into the bottom wall of the test section. This nozzle has an exit diameter of 6.35 mm and exhausts normal to the crossflow. A pressure tap placed at the injector nozzle exit and a thermocouple placed in the injectant supply line provide measurements of the jet flow conditions. Finally, the turbulent boundary layer approaching the injector nozzle is approximately one jet diameter thick at the injection location (determined using a boundary layer rake).<sup>18</sup> Figure 2 illustrates the experimental facility; a more detailed description of the supersonic tunnel, its calibration, and its supporting equipment may be found elsewhere.<sup>18</sup>

Mie or Rayleigh scattering imaging techniques rely on the collection of light scattered by particles and/or molecules suspended in the flowfield of interest. A thin laser sheet, with a pulse duration short enough to freeze the flow, illuminates the particle-laden flowfield. The pixel array of an intensified charge coupled device (ICCD) camera obtains a digital image of the flowfield by collecting the scattered light. The resulting image contains intensity information where high intensities correspond to particle-containing regions. This information is directly related to

seeded fluid concentration if the particles used for scattering are passive participants in the mixing process. Non-passive seed can also produce concentration information if the local thermodynamic conditions are accurately modeled. However, in either case, the mixing information obtained is only spatially resolvable down to the scale of the imaging pixels. Due to the finite thickness of the laser sheet, the pixel array yields an averaged intensity over a pixel volume defined by the pixel area and the sheet thickness. When compared to the Kolmogorov scale (Eq. 2) of the high Reynolds number flowfields encountered in supersonic mixing investigations, the probe volume is quite large, making it impossible to determine whether fluid is molecularly mixed or simply macroscopically stirred. Thus, mixing interpretations are limited to those involving large-scale stirring of the fluids.<sup>11,19</sup>

Two optical arrangements provided the means by which the flowfield was interrogated. Schematics of the equipment appear in Fig. 3. A frequency doubled Spectra Physics Quanta-Ray DCR-4 Nd:YAG laser provided the laser energy (~400 mJ/pulse at 532 nm). A combination of mirrors, prisms, and lenses produced the collimated laser sheet used for illuminating the injection flowfield. For end view images, the sheet entered the test section through one side window, while in the side view images the sheet entered through the top window. The laser sheet had a thickness of roughly 200  $\mu\text{m}$  at the long focal waist and a width of approximately 50 mm. A Princeton Instruments image acquisition system and ICCD camera (water cooled and nitrogen purged, 384 x 576 pixel array), fitted with a Nikon UV-Nikkor 105 mm f/4.5 telephoto lens, captured the flowfield images. The laser flash lamp and the camera were synchronized using a Princeton Instruments pulse generator, and a 486-based computer running the CSMA image acquisition software collected the images. Image processing and analysis were done using the acquisition computer and a Power Macintosh.

Accurate interpretations of the digital images depend directly on the ability of the seed particles to rapidly adjust to the turbulent fluctuations encountered in the flowfield. For accurate Mie scattering images, Samimy and Lele<sup>20</sup> found that particle response must be characterized by a Stokes number (defined as the ratio of the particle response time scale to the characteristic fluid



dynamic time scale) of less than 0.5. Melling's<sup>21</sup> drag law provides the particle response time scale while the large-eddy rollover time gives an estimate of the fluid dynamic time scale. Seeding for the present experiments was accomplished by injecting silane ( $\text{SiH}_4$ ) into the freestream air resulting in a reaction whereby silicon dioxide ( $\text{SiO}_2$ ) particles were formed. In lean reactions silane burns with oxygen to form primarily solid silicon dioxide and water.<sup>22</sup> The silicon dioxide particles were characterized as being  $\sim 0.2 \mu\text{m}$  in diameter.<sup>23</sup> The physical properties of  $\text{SiO}_2$  and the tunnel operating conditions yield a Stokes number of approximately 0.09. Seeding with  $\text{SiO}_2$  alone did not produce acceptable data quality in all of the images; thus, the facility was operated at ambient temperatures such that the  $\text{SiO}_2$  particles acted as nucleation sites for the naturally occurring water vapor in the freestream air. Rotating the polarization of the incident laser light showed that the  $\text{SiO}_2/\text{ice}$  particles were in the Rayleigh scattering regime and had a maximum Stokes number of 0.38.<sup>12,16</sup> Comparing these results to Samimy and Lele's<sup>20</sup> Stokes number criterion indicates that the  $\text{SiO}_2/\text{ice}$  particles accurately follow the large-scale turbulent fluctuations encountered within this flowfield. It is important to note that, due to the presence of water vapor and the varying thermodynamic conditions throughout the jet interaction, this study yields no direct measurements of injectant concentration.

### III RESULTS AND DISCUSSION

Flow conditions for the two cases studied in this investigation appear in Table I. These are denoted CA and CH for injection of air and helium through the circular nozzle, respectively. Included in this table are pertinent freestream and jet exit flow conditions including the jet-to-freestream momentum flux ratio ( $J$ ), which is the main parameter governing the jet's transverse penetration into the crossflow.<sup>24</sup> This parameter is given by the following expression:

$$J = \left( \rho U^2 \right)_{\text{jet}} / \left( \rho U^2 \right)_{\text{freestream}} = \left( \gamma p M^2 \right)_{\text{jet}} / \left( \gamma p M^2 \right)_{\text{freestream}} \quad (3)$$

Also included in the table are the parameters characteristic of the mixing layer formed between the two streams, including the velocity ratio ( $r$ ), density ratio ( $s$ ), local Reynolds number ( $\text{Re}_\delta$ ),

and convective Mach number. The following subsection details the calculations used for estimating these parameters at a single point within the mixing layer. It is worth noting here that the two cases have essentially the same momentum flux ratio while the mixing layer convective Mach number of case CH is approximately three times that of case CA. Thus, based on previous jet penetration studies,<sup>24</sup> the two jets examined here should have comparable transverse penetrations into the crossflow. However, the large-scale vortices and mixing characteristics are expected to be influenced by the stark difference in compressibility level of the peripheral mixing layer. The other tabulated mixing layer parameters likely play roles in its development, although, as mentioned in section I, the effects of compressibility are expected to be the dominant influences on the stability and structural characteristics of the mixing layer formed in the transverse injection flowfield. Following the presentation of the convective Mach number model, the planar imaging results are presented and discussed. These are broken into two main subsections corresponding to end and side view results. Within each subsection, the instantaneous images are presented along with the various statistical results obtained.

#### A. Convective Mach number model

Compressibility is an important issue to address, as this property has been shown to strongly affect the behavior of turbulent shear layers. In the classic constant pressure shear layer formed between two parallel uniform freestreams, compressibility effects are often correlated using the convective Mach number (Eq. 1). Several fluid dynamic features serve to complicate the determination of this parameter in the present flowfield. Unlike the simple two-dimensional shear layer, the transverse injection flowfield is highly three-dimensional. The bow shock upstream of the injector alters the properties of the crossflow fluid so that uniform conditions no longer exist around the mixing layer. Injectant fluid expands to unknown supersonic velocities as it enters the crossflow and rapidly decelerates across the Mach disk. Due to this combination of accelerating and/or decelerating constituent fluids and variable thermodynamic properties,  $M_c$

is difficult to predict and, presumably, not constant as the mixing layer develops. The following analysis attempts to quantify the compressibility level at a single point in the mixing layer.

Figure 4 presents an idealized schematic of the injection flowfield at the spanwise centerline. The point labeled A is the location at which the convective Mach number is to be found. As shown in the sketch, the two streams that form the mixing layer have velocities  $U_1$  (injectant fluid) and  $U_2$  (freestream fluid). The eddies in the mixing layer at point A are assumed to convect with a velocity  $U_c$  at an angle parallel to the two constituent streams. Neither  $U_1$  nor  $U_2$  is known explicitly; thus, additional assumptions are required to allow determination of the properties of the freestream fluid above and injectant fluid below point A.

For the injectant fluid, knowledge of the Mach number just upstream of the Mach disk ( $M_1$ ) is required. Knowing the value of  $M_1$  immediately before the Mach disk permits the use of the normal shock and isentropic relations to determine the pressure downstream of the Mach disk ( $p_1$ ). Combining these relations produces

$$p_1 = \left( \frac{2\gamma_j M_1^2 - (\gamma_j - 1)}{\gamma_j + 1} \right) \frac{p_{o,j}}{\left( 1 + \frac{1}{2}(\gamma_j - 1)M_1^2 \right)^{\gamma_j/\gamma_j - 1}} \quad (4)$$

and, for given freestream conditions (i.e.,  $p_{o,\infty}$  and  $M_\infty$ ), the pressure ratio  $p_1/p_\infty$  is found using

$$\frac{p_1}{p_\infty} = \left( \frac{2\gamma_j M_1^2 - (\gamma_j - 1)}{\gamma_j + 1} \right) \frac{\left( 1 + \frac{1}{2}(\gamma_\infty - 1)M_\infty^2 \right)^{\gamma_\infty/\gamma_\infty - 1}}{\left( 1 + \frac{1}{2}(\gamma_j - 1)M_1^2 \right)^{\gamma_j/\gamma_j - 1}} \frac{p_{o,j}}{p_{o,\infty}} \quad (5)$$

Clearly, a prescribed value for this pressure ratio combined with known injectant and freestream stagnation conditions and the freestream Mach number leads to the calculation of the Mach number upstream of the Mach disk using Eq. 5. The value of  $M_1$  then permits calculation of the pertinent properties in the injectant fluid near point A using the isentropic relations. Thus, given the injectant and freestream stagnation conditions and the freestream Mach number, the properties of the injectant fluid below point A are fully prescribed by assuming a value for

$p_1/p_\infty$ . In another study of circular injection into a supersonic crossflow, the Mach number just upstream of the Mach disk was measured.<sup>25</sup> For the conditions of that experiment, (i.e.,  $\gamma_\infty = \gamma_j = 1.4$ ,  $M_1 = 2.66$ ,  $p_{0,j} = 476$  kPa,  $M_\infty = 1.6$ , and  $p_{0,\infty} = 241$  kPa), Eq. 5 yields a pressure ratio  $p_1/p_\infty = 3.1$ . Since the freestream and injectant conditions of the current investigation are significantly different than those of Santiago's,<sup>25</sup> there is no reason to expect that this ratio should hold in the present cases. However, for these calculations, a range of pressure ratios was used to determine the sensitivity of  $p_1/p_\infty$  on  $M_c$ .

For the freestream fluid above point A, the oblique shock relations may be used to determine the flow turning angle and fluid dynamic properties downstream of the bow shock at a prescribed shock angle. Thus, the shock angle was allowed to vary between  $90^\circ$  (i.e., a normal shock) and the Mach angle. The question as to which shock angle yields the appropriate freestream velocity remains. The double-pulsed imaging experiments of Gruber, et al.<sup>12</sup> guide this choice, since they provide the inclination angle with which the large-scale structures convect ( $\phi$ ). It was assumed earlier that the upper and lower freestream velocity vectors are parallel to the large-scale convection velocity near point A. Thus, the bow shock angle that results in a turning angle equal to  $\phi$  was used to determine the freestream fluid properties above point A.

Having determined the velocities and all the relevant properties of the constituent streams near point A, the large-scale convection velocity must be calculated to determine  $M_c$ . In the convective reference frame (Fig. 4), there is a saddle point between two consecutive structures. This point is a stagnation point for both constituent streams so that the total pressures of the streams at this point must be equal.<sup>1</sup> Assuming that the static pressures of the streams are locally equal, the following expression must then hold:

$$\left[ 1 + \frac{\gamma_1 - 1}{2} \left( \frac{U_1 - U_c}{a_1} \right)^2 \right]^{\gamma_1/(\gamma_1 - 1)} = \left[ 1 + \frac{\gamma_2 - 1}{2} \left( \frac{U_c - U_2}{a_2} \right)^2 \right]^{\gamma_2/(\gamma_2 - 1)} \quad (6)$$

Using Eq. 6 to compute  $U_c$  then permits solving Eq. 1 for either  $M_{c1}$  or  $M_{c2}$  at point A.

Results obtained using this procedure are presented in Fig. 5. The point of interest was chosen at a streamwise position of roughly  $x/d = 1.5$ . Figure 5a contains the variation in the maximum Mach number upstream of the Mach disk, as a function of the pressure ratio  $p_1/p_\infty$ , for cases CA and CH. This plot indicates, as expected, a moderate dependence of  $M_1$  on this pressure ratio. However, the convective Mach number data shown in Fig. 5b indicate a comparatively weak dependence on the assumed pressure ratio. Despite the slight variation over the selected pressure range, the clear observation from Fig. 5b is that *a significant difference exists in the compressibility level associated with the two mixing layers in the air and helium injection flowfields*. In fact, the convective Mach number of the mixing layer formed in case CH is roughly three times that of case CA at the selected point. Thus, the structural and stability characteristics associated with the shear layers for the two cases are expected to be quite different. To determine the accuracy of the above analysis, the computed convection velocities were compared to experimental results from a separate study.<sup>12</sup> Good agreement was observed in each case (generally within 10-20%). Note that the mixing layer parameters listed in Table I are found using  $p_1/p_\infty = 3.0$ .

## B. End view imaging results

Visualizing the jet/freestream interaction from the end provides a cross-sectional look at the flow such as that illustrated in Fig. 1. Moving the image plane in the direction of the freestream flow makes it possible to build an understanding of the near-field development. In these images, pixel dimensions were  $(\Delta x, \Delta y, \Delta z) = (200 \mu\text{m}, 90.7 \mu\text{m}, 90.7 \mu\text{m})$ . Each end view image displayed in this section covers about 6.4 diameters (40.6 mm) in the spanwise (z) direction and 5.4 diameters (34.3 mm) in the transverse (y) direction. The flow direction in all the images is out of the paper. The image gray scales were reversed to highlight the jet/freestream interface yielding images where pure seeded crossflow fluid appears black while pure unseeded jet fluid appears white. These images have been stretched in the spanwise direction to preserve the aspect ratio of the pixel array.

Instantaneous images provide a great deal of information regarding the structure of the flowfield and the characteristics of the jet. Ensemble-averaged results obtained from statistically analyzing the instantaneous images include the lateral jet spread and the plume area. Finally, analyses of standard deviations provide substantial information concerning the fluctuations in this flowfield. These images offer an understanding of where the large-scale mixing regions form and the differences encountered between the two compressibility cases examined. Shock reflections off of the wind tunnel walls were not observed in the region upstream of approximately  $x/d = 20$  in this flowfield; it is therefore expected that the penetration and mixing characteristics observed throughout the jet/freestream interaction are free from such effects.

### 1. Instantaneous images

Instantaneous end view images of case CA obtained from streamwise locations at  $x/d = 0$ , 4, and 8 appear in Fig. 6a. The first image in the figure clearly shows the bow shock and illustrates the three-dimensional nature of the flow by showing the intersection of the bow shock with the separation shock at the left side of the image. The change in signal level across the bow shock is due to the increased density across the sharp discontinuity. Greater changes in signal level from the level in the approaching freestream occur for increasing shock strength. Prominent features in this image are the large-scale eddies that form in the interfacial region between the jet and freestream. The larger eddies reside at the upper edge of the jet while the sides contain predominantly smaller structures. As the image plane moves downstream, the vortical structure of the jet becomes quite apparent. Large- and small-scale vortices appear regularly throughout the image at  $x/d = 4$ . Evidence of the counter-rotating vortex pair emerges now as the jet elevates entirely above the test section bottom wall (ensemble-averaged images illustrate these vortex structures more clearly but were not included due to space limitations). Large extrusions from the jet fluid into the freestream are captured; these features increase the interfacial surface area and perimeter of the jet fluid thereby increasing the potential for diffusion of freestream fluid across the strained interface. Farther downstream, the jet becomes severely

broken and highly convoluted. Increased intermediate gray levels observed at  $x/d = 8$  indicate mixing between the jet and freestream fluids, although some areas of nearly pure jet fluid remain near the jet core.

The circular injector fueled with helium (case CH) produces a flowfield with some interesting differences compared to case CA. Figure 6b presents instantaneous images for this case taken from each of the aforementioned streamwise image planes. Features found at  $x/d = 0$  are similar to those shown in Fig. 6a for case CA. In particular, the large-scale structures at the upper edge of the interaction remain prominent with smaller eddies located at the sides of the jet. However, as the image plane moves downstream, the helium jet appears to remain more coherent than the air jet. Figure 6b shows the image from the second streamwise position (i.e.,  $x/d = 4$ ) where the counter-rotating vortex pair becomes clear as freestream fluid fills the void created between the vortices. The interfacial structure in this image is less broken than in case CA and small-scale eddies are more frequent than large-scale extrusions. Thus, the increased compressibility level of the helium jet seems to strongly affect its structural characteristics. Farther downstream, these observations prevail as the imaged region contains sharper gradients between the jet and freestream fluids than were found in case CA (the gradients were computed by normalizing the images by an average signal level from the freestream and analyzing them using an image processing software package). The interface appears highly broken and populated with small-scale mushroom-shaped eddies.

From this examination of the instantaneous images of the two injection cases, it appears that the compressibility level strongly affects the large-scale shear layer vortices that form around the periphery of the injectant plume. It is also apparent that the entrainment characteristics of the two cases are somewhat different since the jet in case CH appears to remain more coherent over the same spatial development length as the jet in case CA.

## 2. Ensemble-averaged results

The ensembles of instantaneous images (20 images at  $x/d = 0$  and 8, 100 images at  $x/d = 4$  and 10) were corrected for background reflections and nonuniformities in both the laser sheet and camera response using the technique outlined by Long.<sup>26</sup> The corrected images were then ensemble-averaged. The edge of the injectant plume was identified using an arbitrary intensity value as a threshold corresponding to 90% of the intensity in the freestream fluid just downstream of the bow shock. Similar to the velocity thickness commonly used in studies of mixing layers, this definition has been shown to accurately identify the edge of the jet.<sup>27</sup> Applying this definition to the ensemble-averaged images yields an average jet boundary. The lateral extent (i.e., spanwise) of this boundary, defined as the lateral spread of the jet plume, and the area enclosed within this boundary are used in the following analysis.

Figure 7a presents the lateral spreading results where the data are normalized by the injector diameter. Both cases have about the same absolute spanwise spread at  $x/d = 0$  and 4. Beyond this location, the spreading trends indicate some lateral contraction occurring. Case CH contracts at a slower rate on average than case CA, implying that the two injectant gases mix with the freestream air differently. These results suggest that mixing in the helium injection flowfields (high  $M_c$ ) is slower than mixing in the air injection cases (low  $M_c$ ). Presumably, contours obtained farther downstream would show sharp contraction trends in the helium injection cases as well. More description of this contraction phenomenon will be given below.

The areas enclosed by the 90% intensity contours give further indications regarding the large-scale mixing present. This enclosed area should be thought of as an effective area of unmixed fluid rather than the physical extent of the jet itself. Physically, the area enclosed by the 90% contour becomes smaller as the number of scattering particles (i.e., the amount of freestream fluid) in the jet region increases since pure injectant fluid has a scattering intensity value of zero while pure freestream fluid has a value of unity. Figure 7b presents results for the areas enclosed by the jet boundary ( $A_{90}$ ) normalized by the injector exit area at each streamwise position. The data in the plot indicate two separate trends. Case CA shows increasing areas up



to approximately  $x/d = 4$ . After this position, the area ratio decreases monotonically. The trend for helium injection is quite different in that the area ratio data continue increasing until  $x/d = 8$ . The sharp reduction in area observed for air injection beyond  $x/d = 4$  suggests the increased presence of freestream fluid in the jet region. On the other hand, the fact that the helium contour does not experience the same decreasing trend in area within the present measurement domain suggests that freestream fluid is not as prominent within the jet region for that case. Based on the observations from the instantaneous images and the trends produced from the lateral spread and area ratio analyses, the low  $M_c$  case (air) seems to result in better large-scale entrainment than does the high  $M_c$  case (helium).

### 3. Standard deviation analysis

By examining the image standard deviation, more insight can be gained into the location, formation, and development of regions of fluctuating fluid. These regions are important to examine in turbulent, compressible flowfields since they govern how effectively and rapidly the two fluids mix. The images shown here have been rescaled and normalized using

$$\sigma_{norm,i,j} = |1 - \sigma_{i,j} / \bar{\sigma}_{\infty}| \quad (7)$$

such that the intensity values range from  $\sigma_{norm} = 0$  in the freestream and jet core regions to values approaching  $\sigma_{norm} = 1$  in the intensely fluctuating shear layers. Note that in Eq. 7,  $\sigma_{i,j}$  is the standard deviation at a given pixel location and  $\bar{\sigma}_{\infty}$  is the average standard deviation in the freestream fluid. As with the ensemble-averaged results presented above, either 20 or 100 images were used in the calculation of the standard deviation.

The normalized standard deviation images from case CA appear in Fig. 8a. At  $x/d = 0$ , several details are worth noting. First, the bow shock fluctuates slightly in response to the large-scale shear layer vortices. Second, the shear layer around the periphery of the jet is clearly observed. Third, the jet core and the crossflow are black indicating essentially undisturbed fluid. Moving downstream to  $x/d = 4$ , the region of fluctuating fluid grows substantially on both the

sides and the top of the jet. Note the region between the two counter-rotating vortices near the bottom wall where significant fluctuations appear. Also note that the central cores of the two counter-rotating vortices remain relatively devoid of fluctuating fluid compared to the region surrounding them. Thus, some regions of "unmixed" fluid (in terms of turbulent fluctuations) still exist within the jet core. Continuing downstream to  $x/d = 8$ , similar characteristics are observed, although the spatial extent of the fluctuating fluid continues to increase.

Normalized standard deviation images from case CH appear in Fig. 8b. The image computed for  $x/d = 0$  contains several features common to the corresponding image from case CA, including the slight fluctuation in the bow shock position and the essentially unfluctuating nature of the freestream and jet core. In contrast, however, the fluctuations in the position of the bow shock are not as large and the peripheral mixing region is thinner. The spanwise extent of this region also appears reduced compared to that shown in Fig. 8a. At  $x/d = 4$ , the region of highest fluctuations around the periphery of the jet again appears thinner than its counterpart in case CA. This is due to the higher convective Mach number (and higher compressibility level) in case CH. This image also suggests that the jet core occupies a larger area in the central region of the jet as compared to case CA. Features in the image at  $x/d = 8$  appear qualitatively similar to those at  $x/d = 4$  although the jet core disintegrates with increasing streamwise distance.

An arbitrary intensity contour (here  $\sigma_{\text{norm}} = 0.30$ ) was selected in the normalized images in order to give an accurate representation of the region containing fluctuating fluid. This region can be thought of as an active mixing zone. Within this contour either large- or small-scale mixing of the two fluids occurs. Large-scale mixing involves the active entrainment of fluid from the crossflow, thereby initiating the turbulent energy cascade and giving the two fluids the potential to become molecularly mixed. Small-scale mixing, on the other hand, involves the diffusion of the fluids into one another at scales smaller than the discernible pixel resolution. Thus, the contours obtained from this analysis can be used to describe the "mixing potential" of a particular injection scheme, since they essentially enclose the entire mixing region.

Figure 9a shows the area ratio  $R_\sigma$ , defined as the area enclosed within the  $\sigma_{\text{norm}} = 0.30$  contour ( $A_\sigma$ ) divided by the area inside the 90% contour computed from the ensemble-averaged images ( $A_{90}$ ). Values of  $R_\sigma$  near unity indicate that the mixing zone area is of the same size as the area enclosed by the penetration contour at a given streamwise position, while values greater than unity indicate that the mixing zone has grown beyond the bounds of the penetration contour. The curves in Fig. 9a show both cases with approximately the same value of  $R_\sigma$  at  $x/d = 0$ . Downstream of this location, the curves separate with case CA increasing to values of approximately  $R_\sigma = 1.5$  by  $x/d = 4$  while case CH reaches values near  $R_\sigma = 1.2$ . Beyond this streamwise position, the two curves depart from each other more dramatically, with the air injection results continually above those for helium injection. Eventually, by  $x/d = 10$ , the area ratio from case CA reaches a level of roughly  $R_\sigma = 3.0$  while case CH achieves  $R_\sigma = 2.0$ . These data provide further indications that the low compressibility air injection case has better entrainment characteristics than case CH for which  $M_c$  is significantly larger.

To further quantify the mixing potential of the two cases studied here, another geometric analysis of the 30% contours was undertaken. Large-scale eddies that form in the shear layer entrain freestream fluid and enhance the volume of fluid within the mixing zone, along with both the interfacial surface area and perimeter between the two streams. The mixing zone cross-sectional area ( $A_\sigma$ ) and perimeter ( $P$ ) computed from the  $\sigma_{\text{norm}} = 0.30$  contours permit an analysis involving a shape parameter ( $S$ ), defined by<sup>28</sup>

$$S = P / (2\pi r_o) \quad \text{where } r_o = \sqrt{A_\sigma / \pi}. \quad (8)$$

This parameter describes the relationship between the perimeter of the mixing zone and that of a perfectly circular contour of radius  $r_o$  whose area is  $A_\sigma$ . If the contour of interest were a circle, the value of  $S$  produced would therefore be unity. The perfectly circular contour also leads to a minimum value of the shape parameter defined above. Thus, contours yielding shape parameters greater than unity have greater large-scale mixing potential than those having values of  $S$  near unity by virtue of an increased mixing area and the presence of large-scale structures that

enhance the perimeter of the mixing zone. Small-scale mixing does occur inside these contours along with large-scale entrainment. However, as small-scale effects increase, the fluctuations diffuse and become more uniform causing the values of  $S$  to tend toward unity.

Figure 9b illustrates the shape parameter data for each case. The two curves have similar characteristics in that a sharp decay is experienced in the far-field (between  $x/d = 8$  and 10). The plateau region occurs at or above a value of approximately  $S = 3.0$  in the near-field region, suggesting that the near-field contours are highly convoluted when compared to a perfect circle. The sharp decay downstream of  $x/d = 8$  indicates that the contours tend to become more circular in the far-field mixing region. Thus, large-scale entrainment appears more prominent in the near-field regions of these injection flowfields. Glawe, et al.<sup>28</sup> indicate that the combination of a large shape parameter and a large mixing zone area is desired for favorable large-scale mixing characteristics. On the basis of this observation and the data presented in Fig. 9, the air injection flowfield results in better large-scale mixing characteristics over the range of study than the helium case by virtue of its larger area ratio. This analysis suggests that increasing compressibility adversely affects the mixing potential and entrainment in transverse injection flowfields upstream of ten injector diameters.

### C. Side view imaging results

Side view images were also obtained for the two injection flowfields. The pixel dimensions in these images were  $(\Delta x, \Delta y, \Delta z) = (87.6 \mu\text{m}, 87.6 \mu\text{m}, 200 \mu\text{m})$ , and each side view image displayed covers roughly 5.6 diameters (35.6 mm) in the streamwise ( $x$ ) direction and 5.3 diameters (33.7 mm) in the transverse ( $y$ ) direction. Ensembles of temporally uncorrelated images were acquired from two adjacent streamwise imaging planes (100 images each) positioned at the spanwise centerline of the jet (i.e.,  $z/d = 0$ ) so that a wide field of view could be examined. The flow direction in all the images is from left to right, and the gray scale palette shows pure seeded fluid (crossflow) as black and pure unseeded fluid (injectant) as white.

Instantaneous images provide information about the flowfield structure, with particular emphasis on the large-scale eddies that form at the interface between the jet and crossflow. The transverse penetration of the jets results from examining the ensemble-averaged images, while a standard deviation analysis provides information concerning the turbulent fluctuations. These images reveal further details about the behavior of the wake and upper edge mixing layer, as well as the spatial extent of the undisturbed jet core. Finally, two-dimensional spatial correlations of the intensity fluctuations were computed at various positions within the images, providing quantitative measures of the large structure size, shape, and orientation.

### 1. Instantaneous images

Figure 10a shows select instantaneous images of case CA. Several observations can be made from them. First, the upstream image captures the bow and separation shocks ahead of the jet exit. Secondly, the jet/freestream interface demands attention since it is inundated with vortex structures that form rapidly as the jet fluid enters the freestream. As the jet bends downstream due to the momentum of the crossflow, these eddies grow, interact with each other, and apparently entrain large quantities of freestream fluid. Discernible braiding regions form between consecutive pairs of large-scale structures. These regions, which appear in slightly different forms in classic planar shear layers, highlight the role of large-scale eddies in the engulfment process where the large, well-pronounced structures strain the interface between them and then wrap freestream fluid into their cores. Such interfacial strain leads to locally steep concentration gradients and molecular diffusion across the interface. As other investigations of transverse injection into low speed and supersonic crossflows have suggested,<sup>15,27,29</sup> the predominant roll-up direction of the eddies in these images is into the freestream fluid (i.e., counter-clockwise). This implies that the jet fluid tangent to the interface moves with a higher velocity than the adjacent freestream fluid. Santiago<sup>25</sup> confirmed this observation with an extensive study of the velocity field around a transverse sonic jet injected into a supersonic crossflow using laser Doppler velocimetry. The large-scale vortex motions appear highly

diffused in the downstream portions of the flowfield. Downstream of  $x/d = 5$ , the jet core region breaks up resulting in increased gray areas, and some evidence of wake vortex structures appear.

Case CH produces significantly different structure sizes and shapes compared to case CA. The instantaneous images shown in Fig. 10b provide evidence of the influence of compressibility on the large-scale vortices. The structures in case CH are flatter and more amorphous than those of case CA. Also, the braid regions are not nearly as well pronounced suggesting less freestream engulfment in case CH as compared to case CA. Small-scale eddies appear to be more common along the interface as they ride with the larger motions that predominantly roll-up into the freestream fluid. Consistent with the end views (Fig. 6), the eddies in case CH diffuse more slowly in the downstream regions compared to case CA. White regions, indicating relatively pure jet fluid, persist even at the farthest downstream location in Fig. 10b. Structures present between the wall and the jet suggest the presence of wake vortices in this flowfield.

## 2. Ensemble-averaged results

The results of analyzing the corrected, averaged side view images for jet penetration appear in Fig. 11a. An ensemble of 100 images was used for this analysis. The intensity of the jet boundary presented corresponds to 90% of the average freestream intensity behind the bow shock. Keffer and Baines<sup>30</sup> found that the penetration data obtained from a low speed jet in crossflow collapsed to a single curve in the near-field region when the coordinate axes were scaled by  $J^{-1}$  for several values of the jet-to-freestream momentum flux ratio. Results of a recent study examining helium injection into a supersonic crossflow at various values of  $J$  confirmed these results in the region near the injector orifice.<sup>27</sup> The data in Fig. 11a reflect this scaling.

The transverse penetration data from cases CA and CH collapse very well in the near-field region when the inverse  $J$  scaling is used. In Fig. 11a, circular symbols show the average upper boundary for case CA while square symbols indicate the average upper boundary for case CH. A power law curve fit resulted in the following correlation:

$$y/(d \cdot J) = 1.20[(x + r)/(d \cdot J)]^{0.344}. \quad (9)$$

In this correlation, the origin of the penetration boundary is shifted to the upstream edge of the injector orifice using the radius ( $r$ ) of the circular nozzle. This expression fits the experimental data with a correlation coefficient of approximately 98%. Clearly, this equation can only be applied in the near-field region since it predicts the transverse penetration tending toward infinite levels as the streamwise position moves far downstream. Comparisons of three recent correlations for the transverse penetration of jet injected into a supersonic crossflow appear in Fig. 11b. McDaniel and Graves<sup>31</sup> used planar laser-induced iodine fluorescence to obtain their penetration curve, while Rothstein<sup>32</sup> relied on planar laser-induced fluorescence of OH in a reacting flowfield. Clearly, the results of the present investigation fall well within the bounds of the other experimental data shown.

### 3. Standard deviation analysis

The utility of standard deviation statistics was demonstrated in the end view analysis presented earlier. In a similar way, the intensity standard deviations from the side view images provide more insight into the location, formation, and development of regions of fluctuating fluid. The interfacial region between the jet and freestream fluids may be examined in more detail. The shear layer formed in this region can fluctuate intensely and has been shown in the preceding material to be a prime contributor to the freestream entrainment process. The extent of the undisturbed jet core can be identified in terms of streamwise position, and the fluctuations within the wake region downstream of the injector can also be examined. The images and profiles shown here were normalized in an identical manner as those from the end views (i.e.,  $\sigma_{\text{norm}} = 0$  in the freestream and jet core regions and  $\sigma_{\text{norm}} = 1$  in the fluctuating shear layers).

The standard deviation images from case CA appear in Fig. 12a. As with the ensemble-averaged results presented above, 100 instantaneous images were used to compute the standard deviations shown. The upstream image in Fig. 12a illustrates the fluctuation in the bow shock position. As in the end view image from  $x/d = 0$  (Fig. 8a), the intermittent large-scale eddies

formed at the upper edge of the jet boundary influence the shock's position.<sup>10</sup> More intense fluctuations of the bow shock position are localized near the mixing layer where the large-scale eddies form. Farther out in the freestream, the shock fluctuations diminish in intensity. The most prominent feature observed in this image is the mixing layer that develops from the upstream edge of the injector orifice. This mixing region grows rapidly as the jet bends due to the oncoming crossflow. Other features visible in the left image include the freestream and jet core regions which contain relatively low intensity fluctuation levels. The jet core exists until approximately  $x/d = 6$ , where the fluctuations of the mixing layer and wake coalesce. Beyond this position, the entire jet region contains fluctuating fluid. This is consistent with the end view images which show the jet core becoming indistinct between  $x/d = 4$  and 8.

Transverse intensity profiles taken from the normalized standard deviation images allow closer inspection of the mixing layer, core, and wake in terms of the relative levels of fluctuations present. Figure 12b illustrates several of these profiles obtained from case CA. Dotted lines in the plot indicate locations where the normalized standard deviations reach values of unity as indicated by the scale shown on the plot's upper axis. Also included in the plot is a dashed line that represents the penetration correlation given above in Eq. 9. Downstream of about  $x/d = 1$ , the bow shock fluctuations, indicated by the peak in the fluctuations at large  $y/d$ , no longer appear in the profiles, leaving only the fluctuating shear layer, the jet core, and the growing wake region near the bottom wall. Downstream of about  $x/d = 6$ , the influence of the jet core disappears, leaving only a slight depression in the profiles that are otherwise dominated by the mixing layer and wake. It should also be noted that the normalized fluctuation levels within the upper edge shear layer decrease with streamwise position downstream of  $x/d = 5$ . However, the mixing layer continues to grow up to the final position shown at  $x/d = 8$ . Interestingly, the peak values of normalized standard deviation generally fall well below the average penetration boundary of the jet. This indicates that the regions of high fluctuations in the upper shear layer occur near the jet core and that freestream fluid is entrained well into the jet region for case CA.



The two normalized standard deviation images computed for case CH appear in Fig. 13a. Three main features demonstrate appreciable fluctuations in these images: the bow shock, the upper edge mixing layer, and the wake region developing near the injector wall. The images from case CH contain several noticeable differences when compared to the results shown in Fig. 12a for case CA. First, the fluctuation of the bow shock in the helium injection case appears less intense than in case CA, as suggested by its darker color. As noted in the instantaneous visualizations from these two cases, the air injection flowfield (low compressibility) fostered the development of long, well-defined large-scale structures in the upper edge mixing layer that were separated by wide braid regions. On the other hand, the helium injection flowfield (high compressibility) contained relatively flat eddies and narrow braid regions. Thus, the bow shock in case CA had more oscillatory disturbances acting on it than in case CH, leading to the observed differences in shock fluctuation levels. Secondly, the upper edge mixing layer developing in case CH is somewhat thinner than the corresponding feature in Fig. 13a. Because of its apparently slower growth, the upper edge shear layer in case CH remains more distinct in the downstream regions of the image than in case CA. The wake region that develops downstream of the injector orifice in case CH, however, grows in a manner similar to that in Fig. 12a. As a result, the jet core remains preserved for a longer streamwise distance in case CH.

Normalized intensity profiles from case CH, shown in Fig. 13b, provide clearer evidence of these observations. The widths of the upper edge mixing layer indicated near the injector exit are significantly narrower than in case CA. The low intensity region between the mixing layer and wake indicates the persistent core of the jet. Clearly, the core remains distinct as far downstream as  $x/d = 8$ . This profile shows the peak-to-peak distance between the fluctuation intensities in the mixing layer and the wake to be about 2.8 jet diameters, while the same distance in the downstream profile of Fig. 12b is about 1.8 jet diameters. In addition to the wider separation between the mixing layer and wake in case CH, the normalized intensities found within this region are appreciably lower than in case CA, indicating slower turbulent diffusion into the jet core. This effect is primarily due to the slower growth of the upper edge shear layer

in the helium injection case. Also, the peak normalized intensity values within the mixing layer of case CH occur at higher transverse positions relative to the mean penetration curve than in case CA. This phenomenon contributes to the persistence of the jet core since the strongest turbulent fluctuations in the shear layer remain well outside the central jet region. Thus, the large-scale entrainment characteristics appear significantly suppressed in the high  $M_c$  case as compared to those of the low  $M_c$  case.

#### 4. Spatial correlation results

A wide variety of structure sizes and orientations appears in the instantaneous side view images. To this point, the mixing layer thickness, as inferred from the standard deviation results, has provided a comparative measure of the large-scale structure size in the two cases examined. Another result that provides information about the behavior of the large eddies formed in the mixing layer is the two-dimensional spatial correlation field. This property has been used to examine the large structures in a variety of flowfields.<sup>6,33,34</sup> The form used here is given by

$$C(\Delta x, \Delta y) = \frac{1}{N} \sum_{n=1}^N I'(x, y) \cdot I'(x + \Delta x, y + \Delta y), \quad (10)$$

where the point  $(x, y)$  is the reference location about which the features are correlated. Correlations are computed using the intensity fluctuations ( $I'$ ) and the two lag parameters ( $\Delta x$  and  $\Delta y$ ). For the present calculations, the correlation domain is 256 pixels wide by 256 pixels high corresponding to a box just over 3.5 diameters (22.2 mm) on a side. Each pixel location is used as a reference location in the calculation to avoid subjectivity. The center of the domain is placed at one location in each instantaneous upstream and downstream image obtained from the cases studied. For the upstream images, the center of the computational domain corresponds to a location on the theoretical near-field penetration curve (Eq. 9). In the downstream images, the center of the domain is placed roughly in the center of the upper edge mixing layer at a given streamwise position. Finally, the results from the instantaneous images are averaged together

over the entire ensemble producing an averaged correlation map of the given spatial region. Note that the two-dimensional spatial correlation used in this way sheds no light on a structure's three-dimensionality. However, the spatial correlation in the side view plane does provide a measure of the average geometric features of the large-scale eddies that can be used for comparison between the cases studied here. Table II summarizes the spatial correlation results.

The ensemble-averaged correlation maps for case CA are presented in Fig. 14a. Here the upstream and downstream contour maps are shown where the contour levels vary in increments of 0.125 from 0.125 to unity. The 50% contour (representative of a large structure) in the left plot has a normalized major axis of  $2a/d = 0.44$ . The eccentricity of the elliptical contour is  $\epsilon = 0.75$  (circular contour has an  $\epsilon = 0$ ), and the inclination angle with respect to the freestream flow direction is about  $\alpha = 24^\circ$ . Moving downstream, the inclination angle increases to  $\alpha = 45^\circ$ . The normalized major axis becomes shorter ( $2a/d = 0.33$ ) and the 50% contour becomes more circular ( $\epsilon = 0.65$ ). Thus, the structure loses some of its coherency and rotates significantly into the freestream as it convects downstream due to the mixing between the injectant and crossflow.

Ensemble-averaged results from case CH (Fig. 14b) are somewhat different. The 50% contour in the left plot in Fig. 14b has a major axis 0.43 jet diameters long and an eccentricity of about  $\epsilon = 0.67$ . These values suggest that the average eddy in the helium case at this streamwise position is essentially the same size as in case CA and has a somewhat more circular shape. It is also more inclined to the freestream flow with an inclination angle of about  $\alpha = 29^\circ$ . Moving downstream, the normalized structure size increases to about  $2a/d = 0.54$ . The average structure in the downstream position increases in eccentricity ( $\epsilon = 0.73$ ) and in inclination angle ( $\alpha = 64^\circ$ ). Thus, in the high compressibility injection case, the large-scale structures rotate more as they move downstream compared to case CA, and they grow in size. Thus, helium (i.e., high compressibility) injection consistently provides evidence of slower diffusion and break-up of the large-scale eddies as they move downstream than does air injection. The results of the correlation analysis substantiate this further by showing growth of the average eddy in case CH as it convects downstream, while the average eddy in case CA shrinks. Increasing

compressibility diminishes the entrainment effectiveness of the large-scale shear layer eddies leading to slower large-scale break-up.

#### IV SUMMARY AND CONCLUSIONS

An experimental investigation of compressibility effects in transverse injection into a supersonic crossflow has been presented. The following conclusions are drawn:

(1) A model of the near-field of the transverse injection flowfield was used to predict the convective Mach number of the developing mixing layer at one spatial location. It was shown that the convective Mach number is relatively insensitive to the value of  $p_1/p_\infty$  selected over a range from  $2 < p_1/p_\infty < 4$ . Based on this model, the convective Mach number for helium injection in these experiments is approximately three times that of air injection.

(2) The large-scale vortices that develop at the jet/freestream interface generally roll into the freestream indicating that the injectant fluid below the mixing layer moves faster than does the crossflow fluid directly above it.

(3) Compressibility effects manifest themselves in the rate of contraction of the average jet penetration contours. These contours, obtained by applying the 90% penetration definition to the ensemble-averaged end view images, indicate slower injectant plume contraction in the high compressibility case compared to the low compressibility case. Since a larger penetration contour implies less freestream entrainment at a given streamwise location, the results suggest that injection at low  $M_c$  provides better entrainment characteristics than injection at high  $M_c$ .

(4) When the streamwise and transverse positions are scaled using the jet-to-freestream momentum flux ratio, the transverse penetration data from the ensemble-averaged side view images collapse very well in the near-field region. Mixing layer compressibility does not strongly affect the transverse penetration of the jet. The power law form of the penetration correlation found in this investigation compares closely to those of other studies using different diagnostics, lending credence to the present jet boundary definition in the near-field.

(5) Geometric analyses of the mixing zone contours derived from the end view standard deviation images using an area ratio and a shape factor definition provide comparisons of the mixing potential. The area ratio results indicate that case CA (low compressibility) contained a larger mixing zone than case CH (high compressibility). Results of the shape factor analysis suggest that the large-scale eddies, which dominate the near-field, become less influential downstream of  $x/d = 8$  for both cases, yielding to small-scale turbulence. These results indicate that the mixing potential afforded by injection at low  $M_c$  is larger than that at high  $M_c$ .

(6) Normalized standard deviation profiles from the side view images indicate that the peak fluctuations occurring in the upper edge mixing layer intrude deeper into the jet core region in the low compressibility injection case than in the high compressibility injection case. Thus, increased compressibility acts to localize the upper edge turbulent fluctuations to regions nearer the jet boundary. This leads to poorer freestream entrainment and a more prominent jet core in the high compressibility case. Normalized standard deviation results from both views show thinner mixing layers developing in the high compressibility case. These results also show that the upper edge mixing layer is significantly thicker than those developing on the sides of the jet fluid irrespective of the compressibility level. Further, these results suggest that, as the jet develops in the streamwise direction, the turbulent fluctuations located at the edges of the jet fluid diffuse into the unfluctuating core region more rapidly in the low compressibility case.

(7) Two-dimensional spatial correlations computed from the side view images provide information regarding the sizes and orientations of the large-scale eddies that form in the upper edge mixing layer. Ensemble-averaged correlation maps show compressibility strongly affecting the development of these vortices. In low  $M_c$  injection, the eddies become less organized, more inclined to the freestream, and more circular as they propagate downstream. High  $M_c$  injection leads to structures that grow as they convect downstream, becoming more coherent. These eddies become more inclined to the freestream and more elliptical as they move downstream.

## ACKNOWLEDGMENTS

The contributions of Messrs. J. Donbar, D. Schommer, C. Smith, Drs. C. Carter, D. Glawe, and the support of the Air Force Office of Scientific Research are appreciated.

- <sup>1</sup>D. Papamoschou and A. Roshko, "The compressible turbulent shear layer: An experimental study," *J. Fluid Mech.* **197**, 453 (1988).
- <sup>2</sup>N. D. Sandham and W. C. Reynolds, "Compressible mixing layer: Linear theory and direct simulation," *AIAA J.* **38**, 618 (1990).
- <sup>3</sup>L. J. Leep, J. C. Dutton, and R. F. Burr, "Three-dimensional simulations of compressible mixing layers: Visualizations and statistical analysis," *AIAA J.* **31**, 2039 (1993).
- <sup>4</sup>M. Samimy and G. S. Elliott, "Effects of compressibility on the characteristics of free shear layers," *AIAA J.* **28**, 439 (1990).
- <sup>5</sup>S. G. Goebel and J. C. Dutton, "Experimental study of compressible turbulent mixing layers," *AIAA J.* **29**, 538 (1991).
- <sup>6</sup>N. L. Messersmith and J. C. Dutton, "Characteristic Features of Large Structures in Compressible Mixing Layers," *AIAA J.* **34**, 1814 (1996).
- <sup>7</sup>N. T. Clemens and M. G. Mungal, "Two- and three-dimensional effects in the supersonic mixing layer," *AIAA J.* **30**, 973 (1992).
- <sup>8</sup>N. L. Messersmith and J. C. Dutton, "Laser induced fluorescence measurements of scalar transport in compressible mixing layers," *AIAA Paper No. 92-3547*, 1992.
- <sup>9</sup>D. W. Bogdanoff, "Compressibility effects in turbulent shear layers," *AIAA J.* **21**, 926 (1983).
- <sup>10</sup>M. R. Gruber, A. S. Nejad, T. H. Chen, and J. C. Dutton, "Observations of the bow shock-jet interaction in compressible transverse injection flowfields," *AIAA J.* (to appear).
- <sup>11</sup>J. E. Broadwell and M. G. Mungal, "Large-scale structures and molecular mixing," *Phys. Fluids A* **3**, 1193 (1991).
- <sup>12</sup>M. R. Gruber, A. S. Nejad, T. H. Chen, and J. C. Dutton, "Large structure convection velocity measurements in compressible transverse injection flowfields," *Exp. Fluids* (to appear).

- <sup>13</sup>T. F. Fric and A. Roshko, "Vortical structure in the wake of a transverse jet," *J. Fluid Mech.* **279**, 1 (1994).
- <sup>14</sup>Y. Kamotani and I. Greber, "Experiments on a turbulent jet in a cross flow," *AIAA J.* **10**, 1425 (1972).
- <sup>15</sup>M. R. Gruber, A. S. Nejad, and J. C. Dutton, "Circular and elliptical transverse injection into a supersonic crossflow--The role of large-scale structures," *AIAA Paper No. 95-2150*, 1995.
- <sup>16</sup>M. R. Gruber, "An experimental investigation of transverse injection from circular and elliptical nozzles into a supersonic crossflow," Ph.D. thesis, University of Illinois at Urbana-Champaign, Urbana, IL, 1996.
- <sup>17</sup>W. M. VanLerberghe, "Large-scale structure and mixing in a sonic transverse jet injected into a supersonic crossflow," Ph.D. thesis, University of Illinois at Urbana-Champaign, Urbana, IL, 1995.
- <sup>18</sup>M. P. Gruber and A. S. Nejad, "New supersonic combustion research facility," *J. Prop. Power* **11**, 1080 (1995).
- <sup>19</sup>H. Aref and S. W. Jones, "Enhanced separation of diffusing particles by chaotic advection," *Phys. Fluids A* **1**, 470 (1989).
- <sup>20</sup>M. Samimy and S. K. Lele, "Motion of particles with inertia in a compressible free shear layer," *Phys. Fluids A* **3**, 1915 (1991).
- <sup>21</sup>A. Melling, "Seeding gas flows for laser anemometry," *AGARD Advanced Instrumentation for Aero Engine Components*, (Philadelphia, 1986), pp. 8.1-8.11.
- <sup>22</sup>J. R. Hartman, J. Famil-Ghiriha, M. A. Ring, and H. E. O'Neal, "Stoichiometry and possible mechanism of  $\text{SiH}_4\text{-O}_2$  explosions," *Comb. Flame* **68**, 43 (1987).
- <sup>23</sup>R. C. Rogers, E. H. Weidner, and R. D. Bittner, "Quantification of scramjet mixing in the hypervelocity flow of a pulse facility," *AIAA Paper No. 94-2518*, 1994.
- <sup>24</sup>D. Papamoschou and D. G. Hubbard, "Visual observations of supersonic transverse jets," *Exp. Fluids* **14**, 468 (1993).

- <sup>25</sup>J. S. Santiago, "An experimental study of the velocity field of a transverse jet injected into a supersonic crossflow," Ph.D. thesis, University of Illinois at Urbana-Champaign, Urbana, IL, 1995.
- <sup>26</sup>M. B. Long, "Multidimensional imaging in combustions flows by Lorentz-Mie, Rayleigh and Raman scattering," in *Instrumentation for Flows with Combustion*, edited by A.M.K.P. Taylor (Academic Press, San Diego, 1993).
- <sup>27</sup>M. R. Gruber, A. S. Nejad, T. H. Chen, and J. C. Dutton, "Mixing and penetration studies of sonic jets in a Mach 2 freestream," *J. Prop. Power* **11**, 315 (1995).
- <sup>28</sup>D. D. Glawe, M. Samimy, A. S. Nejad, and T. H. Chen, "Effects of nozzle geometry on parallel injection from base of an extended strut into a supersonic flow," AIAA Paper No. 95-0522, 1995.
- <sup>29</sup>J. C. Hermanson and M. Winter, "Mie scattering imaging of a transverse, sonic jet in supersonic flow," *AIAA J.* **31**, 129 (1993).
- <sup>30</sup>J. F. Keffer and W. D. Baines, "The round turbulent jet in a cross-wind," *J. Fluid Mech.* **15**, 481 (1963).
- <sup>31</sup>J. C. McDaniel and J. Graves, "Laser-induced fluorescence visualization of transverse gaseous injection in a nonreacting supersonic combustor," *J. Prop. Power* **4**, 591 (1988).
- <sup>32</sup>A. D. Rothstein, "A study of normal injection of hydrogen into a heated supersonic flow using planar laser-induced fluorescence," Los Alamos National Laboratory, LA-12287-T, 1992.
- <sup>33</sup>S. A. Arnette, M. Samimy, and G. S. Elliott, "The effect of expansion on large scale structure evolution in a compressible turbulent boundary layer," AIAA Paper No. 94-2228, 1994.
- <sup>34</sup>K. M. Smith and J. C. Dutton, "Large-scale structures in supersonic reattaching shear flows," AIAA Paper No. 95-2251, 1995.



TABLE I. Summary of experimental conditions.

	Case CA	Case CH
$\gamma_j$	1.40	1.67
$M_j$	1.0	1.0
$p_j$ (kPa)	476	405
$U_j$ (m/s)	317	882
$\rho_j$ (kg/m <sup>3</sup> )	6.64	0.867
$Re_j = (\rho_j \cdot U_j \cdot d_j) / \mu_j$	$8.36 \times 10^5$	$3.00 \times 10^5$
$\gamma_\infty$	1.40	1.40
$M_\infty$	1.98	1.98
$p_\infty$ (kPa)	41.8	41.8
$U_\infty$ (m/s)	516	515
$\rho_\infty$ (kg/m <sup>3</sup> )	0.860	0.866
$Re_\infty = (\rho_\infty \cdot U_\infty) / \mu_\infty$ (m <sup>-1</sup> )	$3.87 \times 10^7$	$3.91 \times 10^7$
$J$	2.90	2.93
Mixing Layer Parameters at a Single Point (see Fig. 4)		
$r = U_2/U_1$	0.522	0.212
$s = \rho_2/\rho_1$	5.39	29.0
$Re_\delta = (\bar{\rho} \cdot \Delta U \cdot \delta) / \bar{\mu}$	$1.50 \times 10^5$	$4.30 \times 10^5$
$M_c$	0.66	1.92

TABLE II. Ensemble-averaged spatial correlation results.

Case	Center Position	2a/d	2b/d	$\epsilon$	$\alpha$
CA	x/d = 1.8, y/d = 2.9	0.44	0.29	0.75	24°
	x/d = 7.0, y/d = 3.5	0.33	0.25	0.65	45°
CH	x/d = 1.8, y/d = 2.9	0.43	0.32	0.67	29°
	x/d = 7.0, y/d = 3.5	0.54	0.37	0.73	64°

## FIGURE CAPTIONS

FIG. 1. Perspective view of the mean transverse injection flowfield.

FIG. 2. Schematic of supersonic combustion tunnel.

FIG. 3. Schematics of Rayleigh/Mie scattering optical arrangements: (a) end view; (b) side view.

FIG. 4. Region of interest for convective Mach number calculations.

FIG. 5. Results of convective Mach number calculations using a range of pressure ratios: (a) maximum Mach number ( $M_1$ ) variation; (b) convective Mach number ( $M_{cl}$ ) variation.

FIG. 6. Instantaneous end view images: (a) case CA; (b) case CH.

FIG. 7. End view ensemble-averaged results: (a) normalized lateral spread; (b) area ratio.

FIG. 8. End view standard deviation images: (a) case CA; (b) case CH.

FIG. 9. Results of a geometric analysis of end view standard deviation images: (a) area ratio; (b) shape factor.

FIG. 10. Instantaneous side view images: (a) case CA; (b) case CH.

FIG. 11. Transverse penetration data: (a) present cases; (b) comparison with other correlations at  $J = 2.9$ .

FIG. 12. Side view standard deviation results from case CA: (a) images; (b) profiles.

FIG. 13. Side view standard deviation results from case CH: (a) images; (b) profiles.

FIG. 14. Ensemble-averaged two-dimensional spatial correlation contours: (a) case CA; (b) case CH.

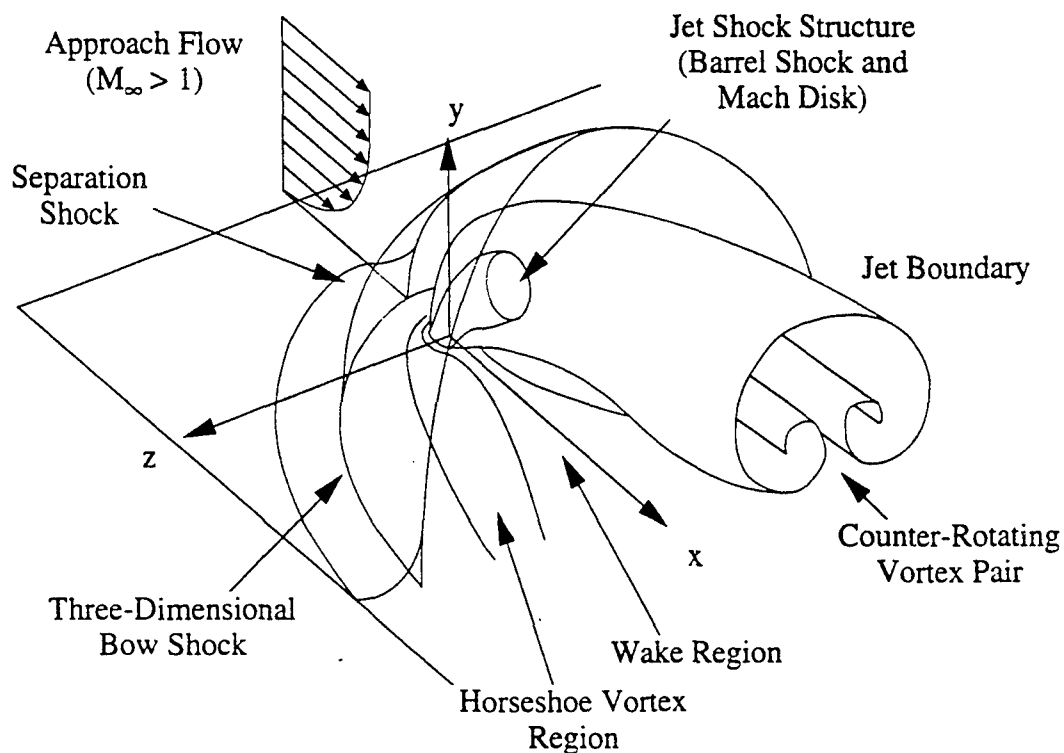


FIG. 1. Perspective view of the mean transverse injection flowfield.

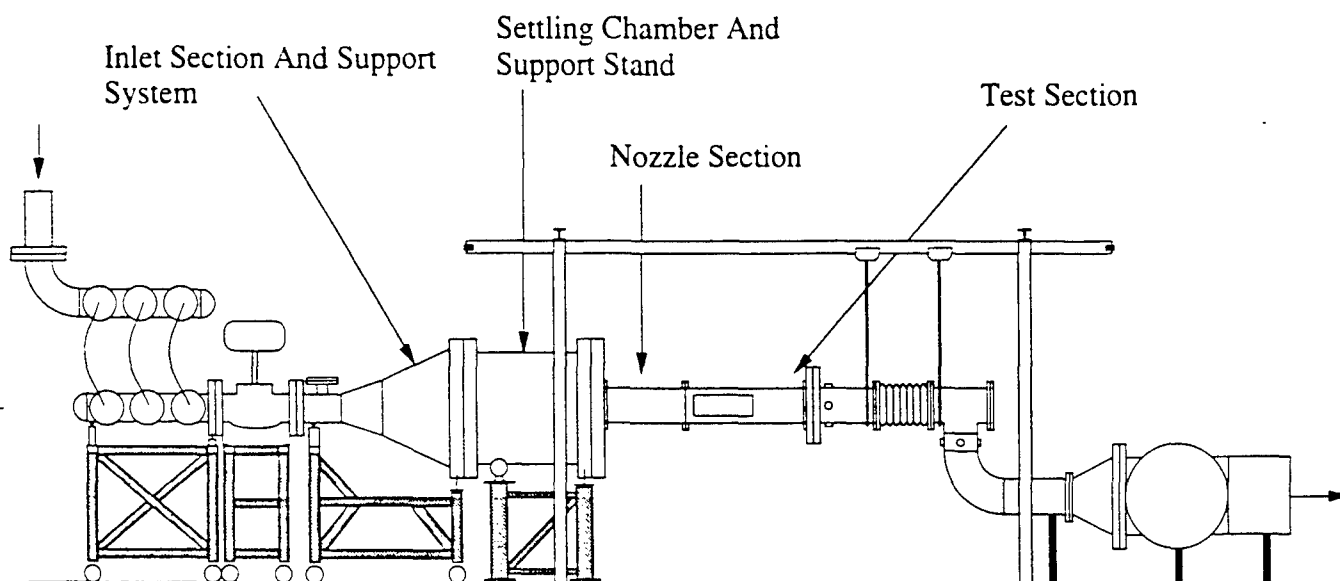


FIG. 2. Schematic of supersonic combustion tunnel.

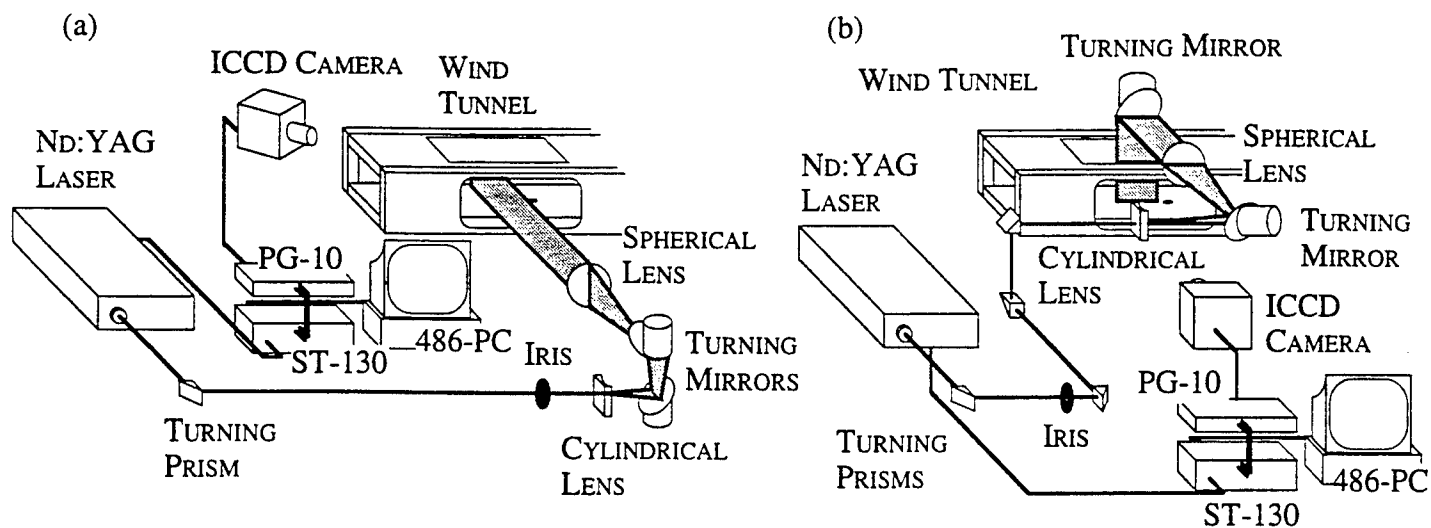


FIG. 3. Schematics of Rayleigh/Mie scattering optical arrangements: (a) end view; (b) side view.

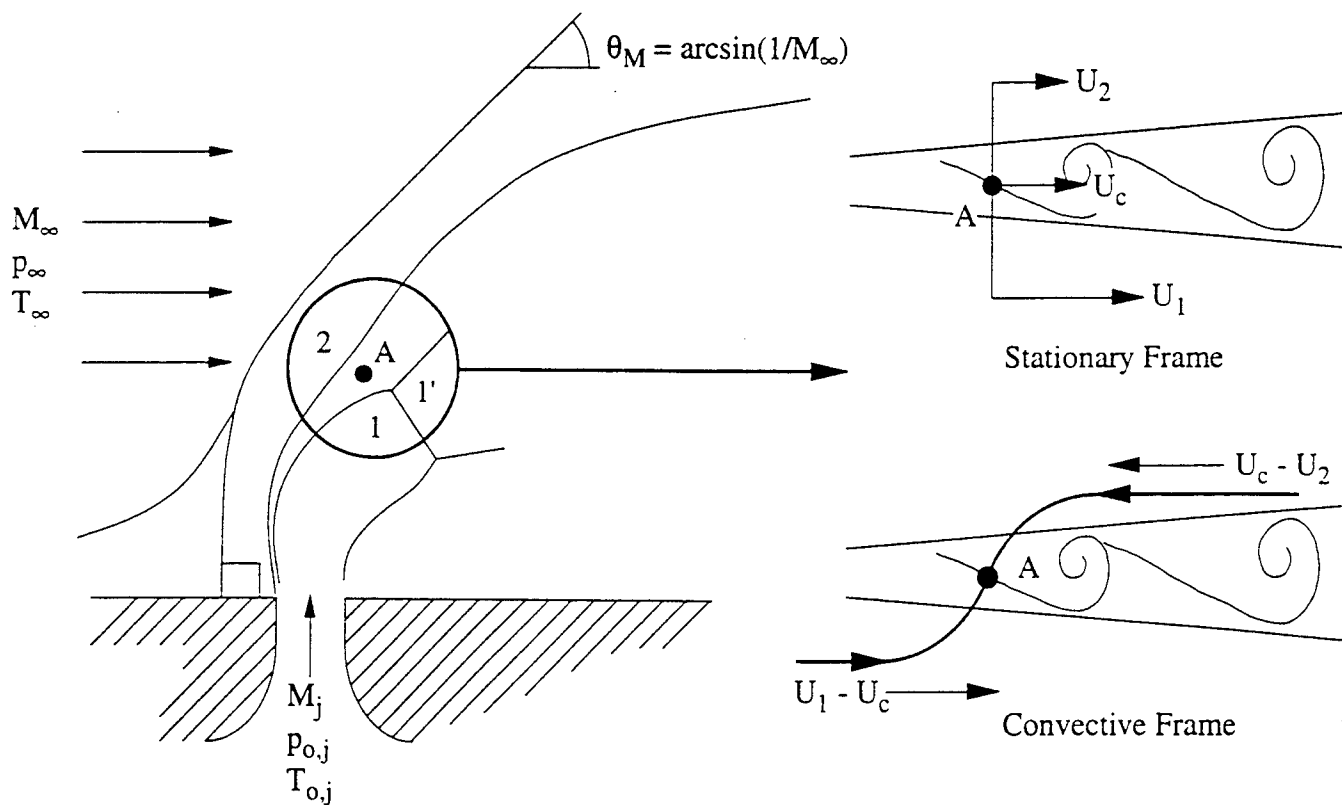


FIG. 4. Region of interest for convective Mach number calculations.

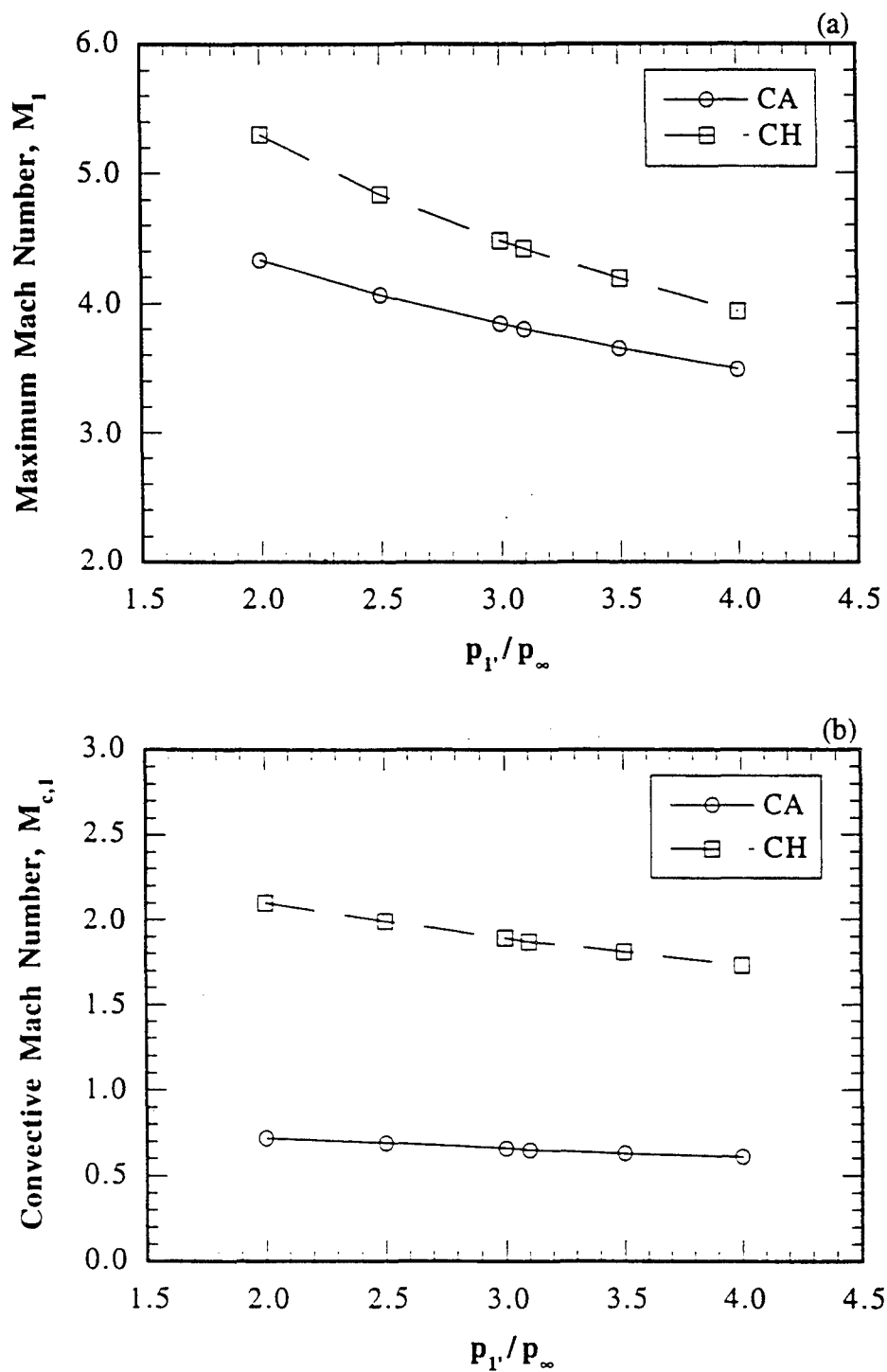


FIG. 5. Results of convective Mach number calculations using a range of pressure ratios: (a) maximum Mach number ( $M_1$ ) variation; (b) convective Mach number ( $M_{c1}$ ) variation.

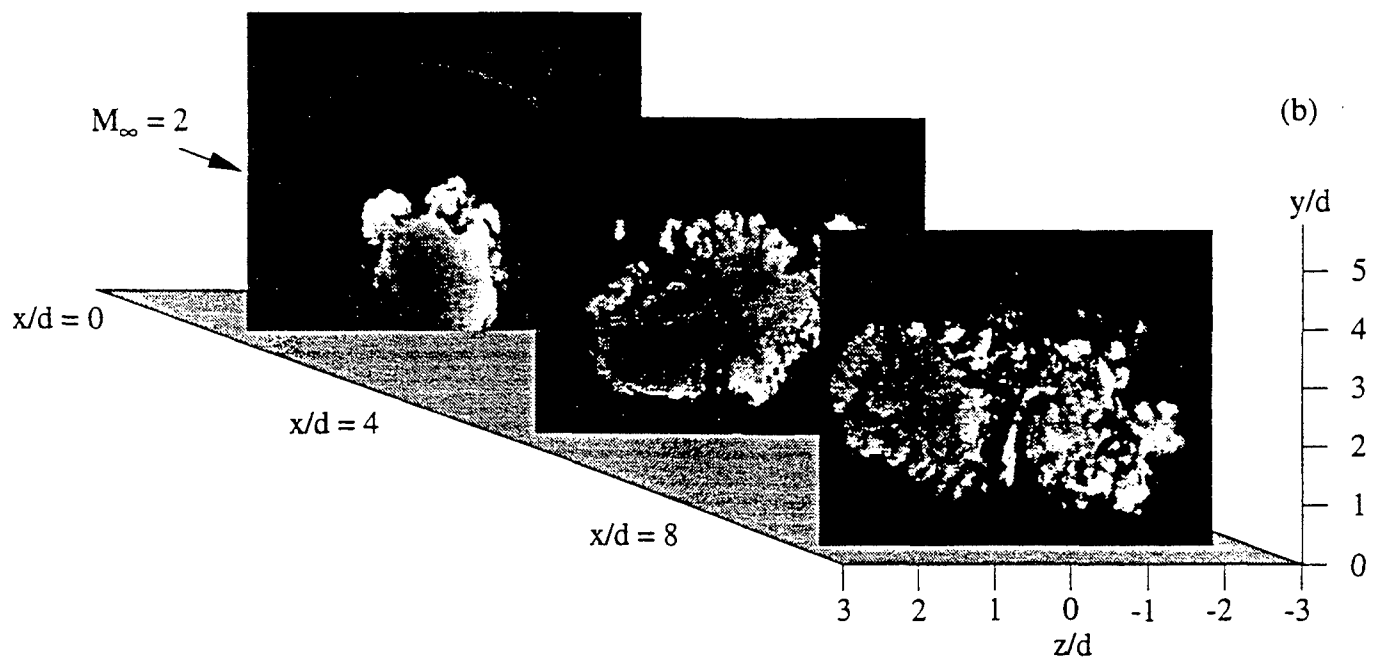
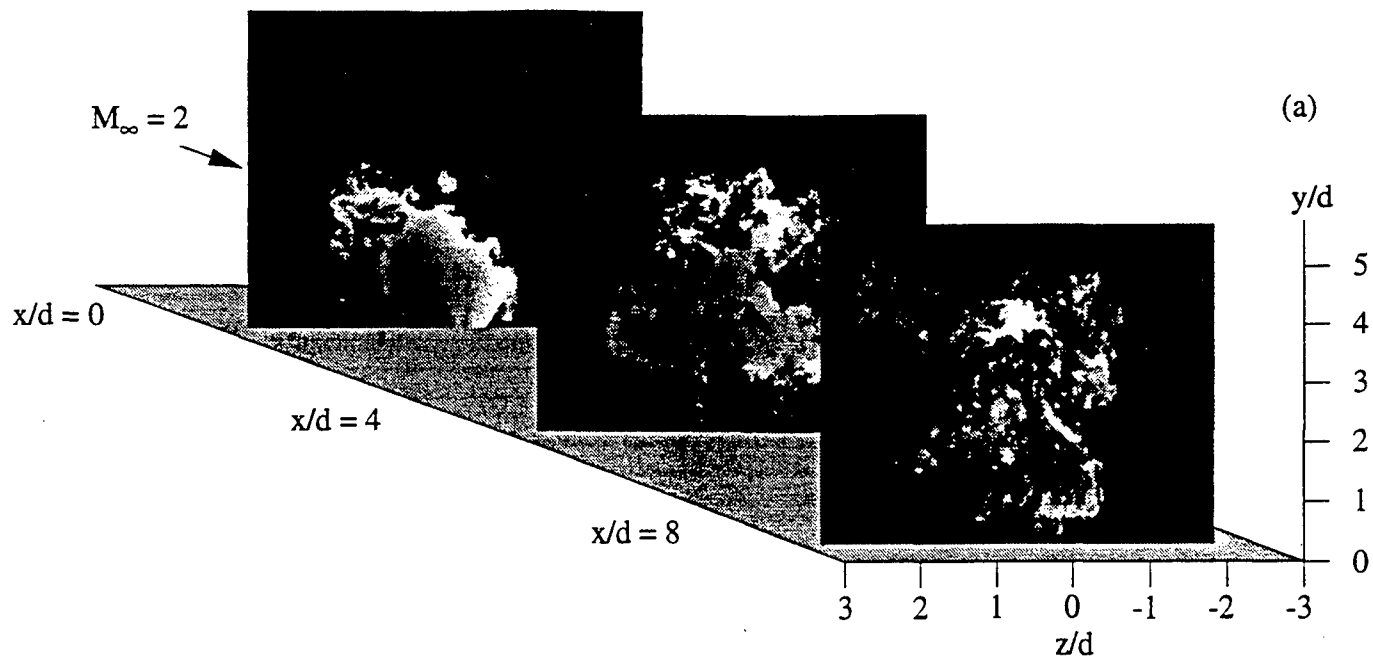


FIG. 6. Instantaneous end view images: (a) case CA; (b) case CH.

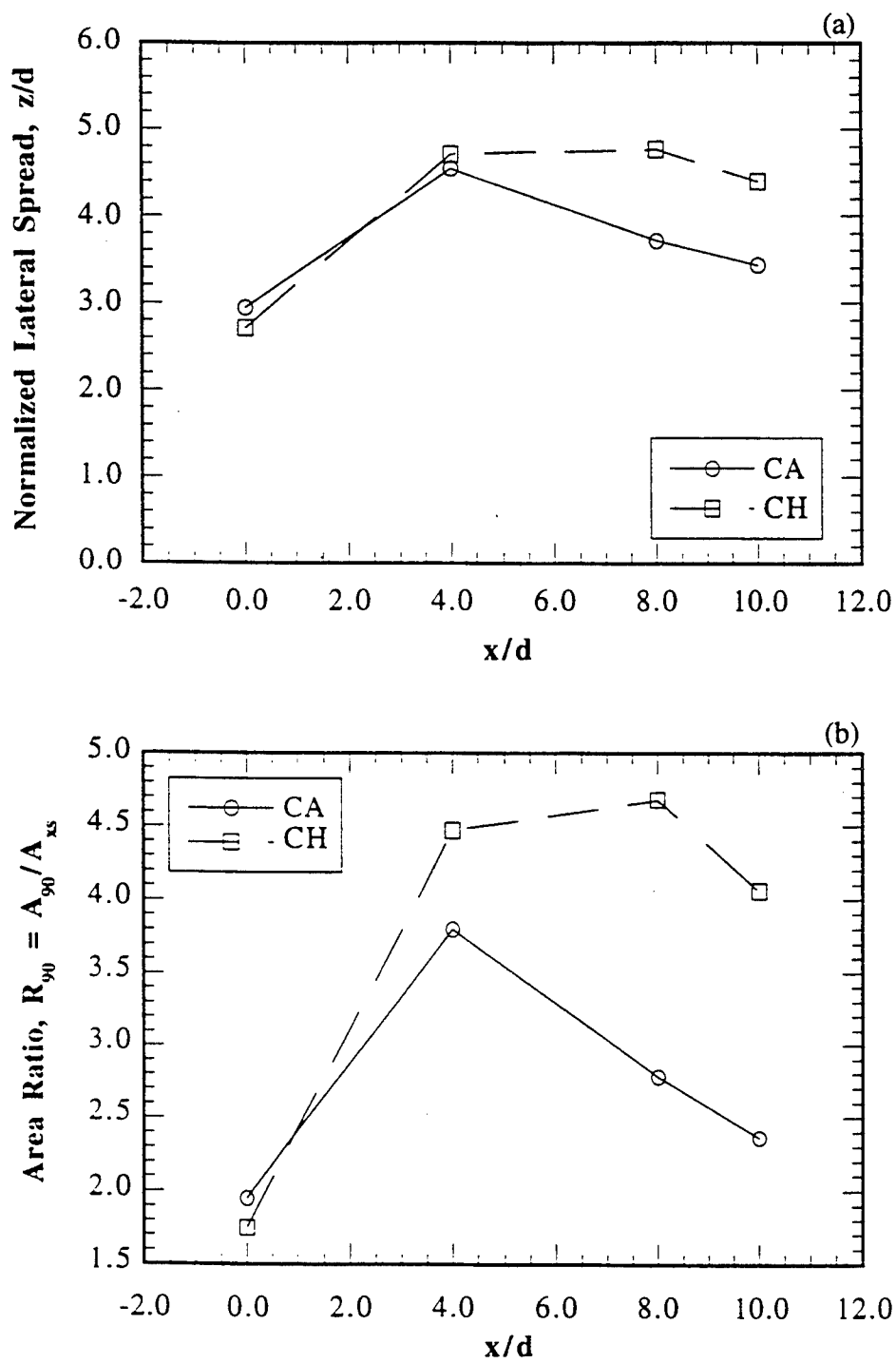


FIG. 7. End view ensemble-averaged results: (a) normalized lateral spread; (b) area ratio.

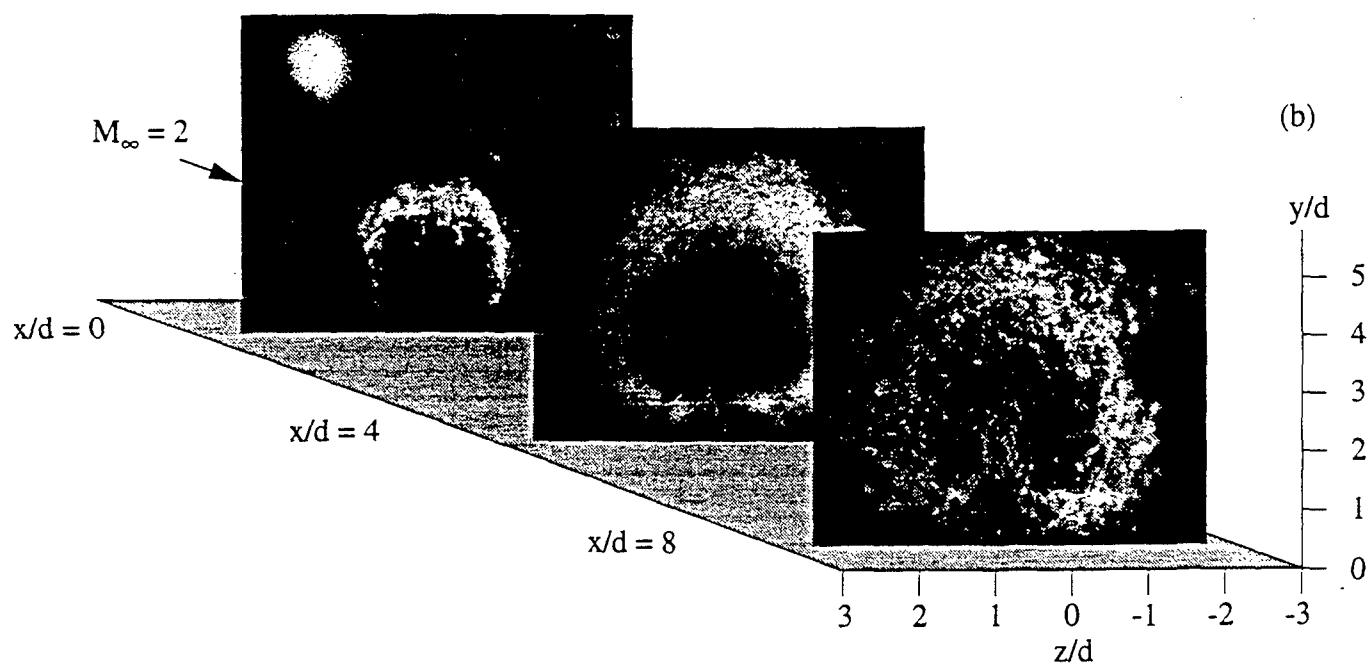
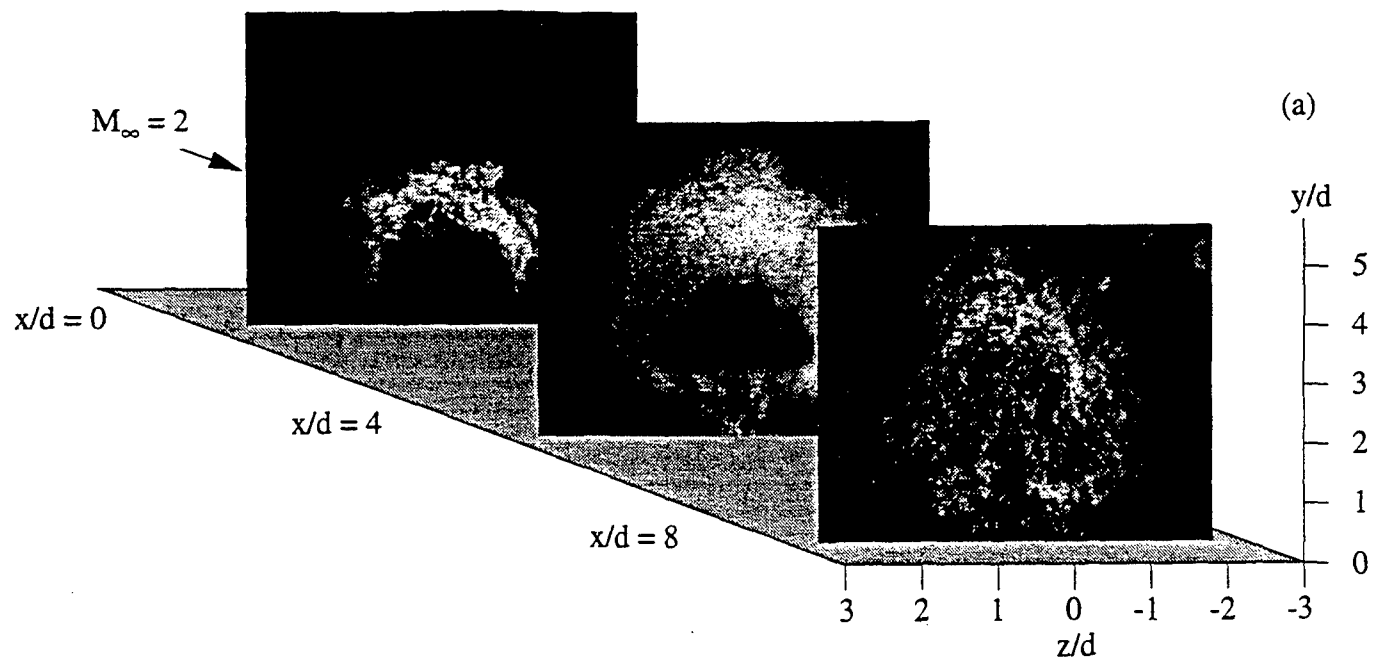


FIG. 8. End view standard deviation images: (a) case CA; (b) case CH.



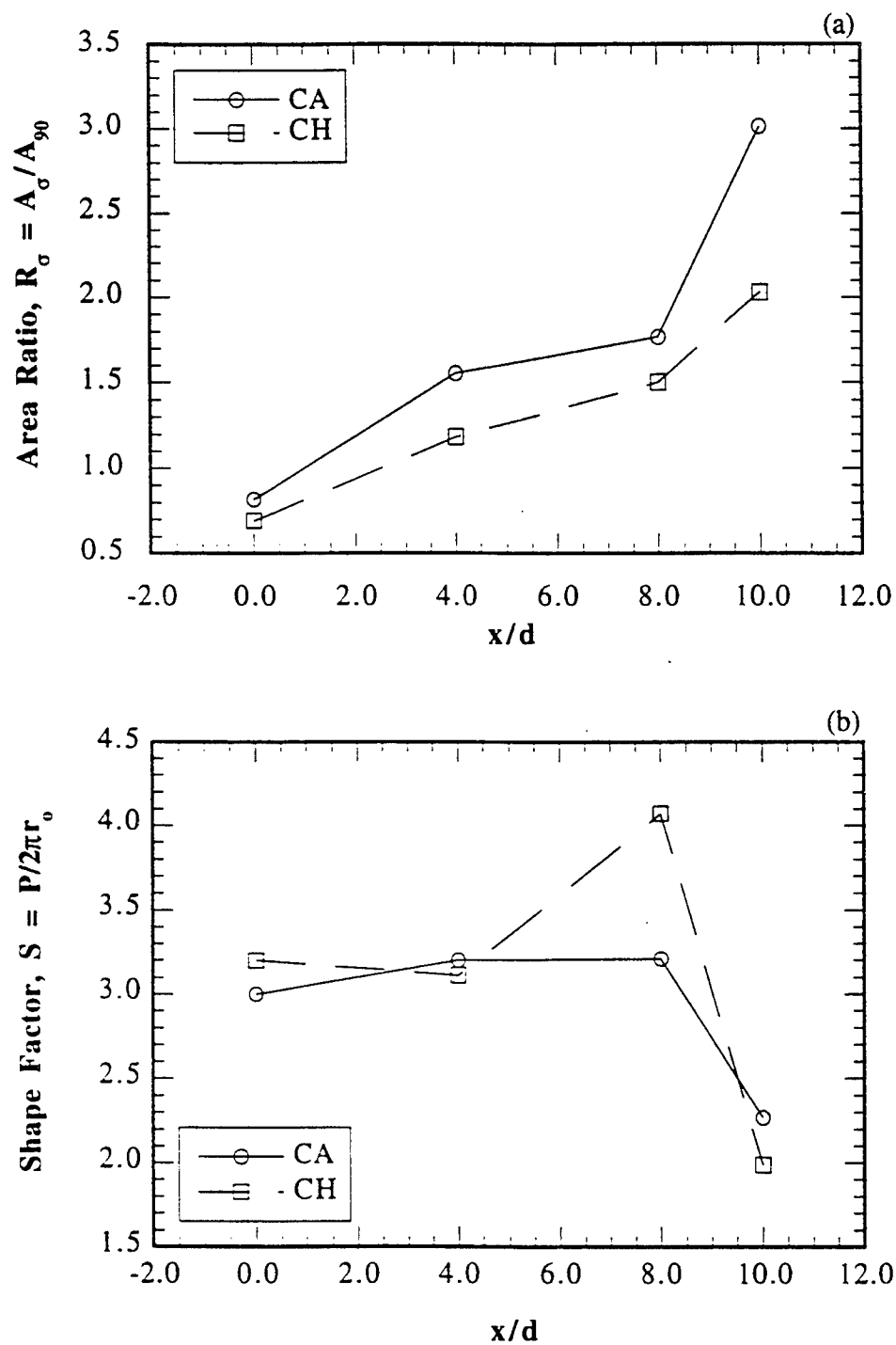


FIG. 9. Results of a geometric analysis of end view standard deviation images: (a) area ratio; (b) shape factor.

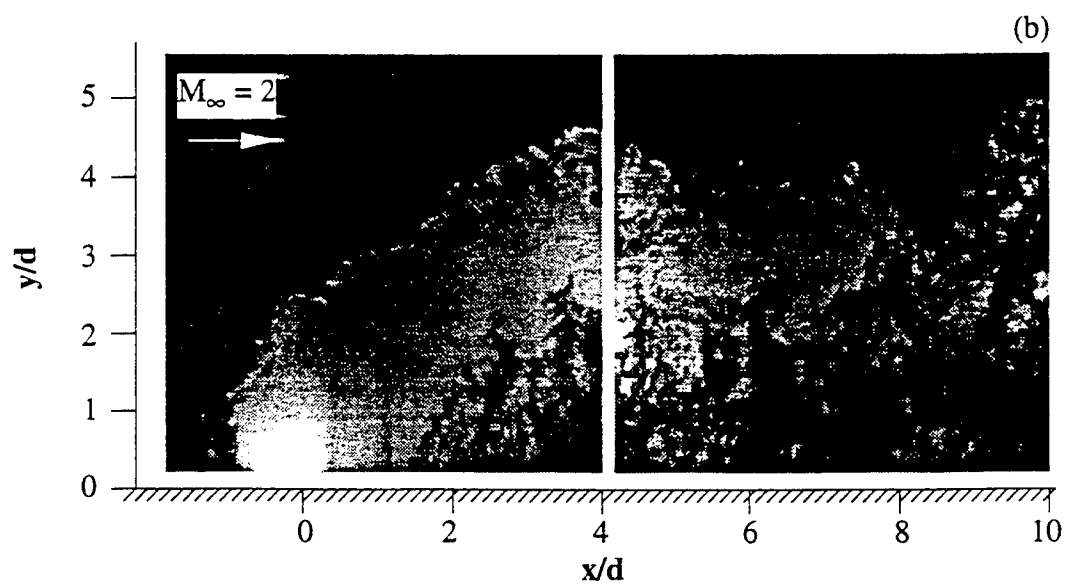
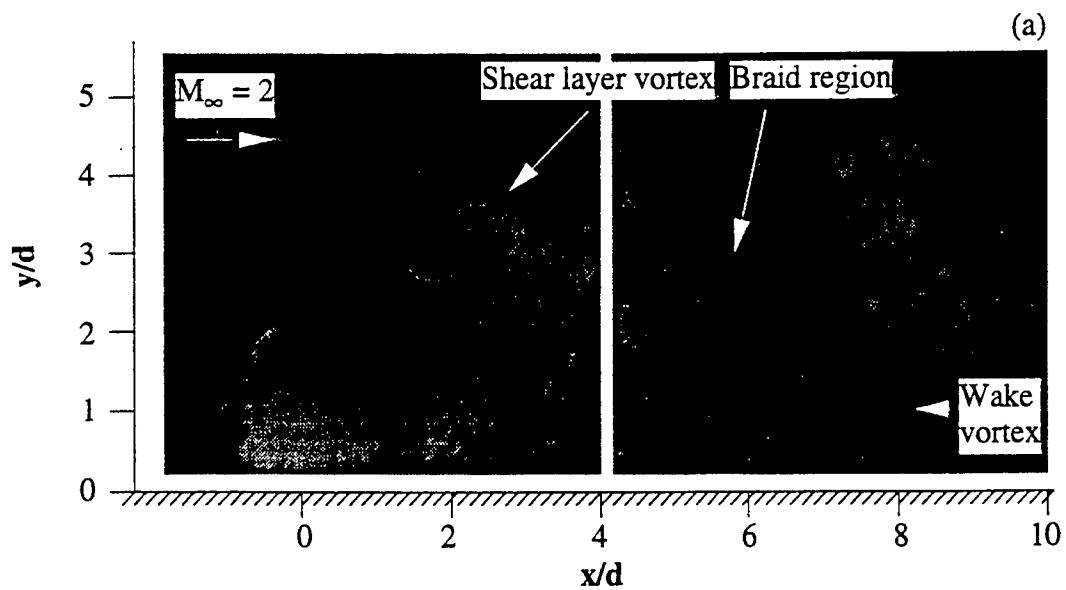


FIG. 10. Instantaneous side view images: (a) case CA; (b) case CH.

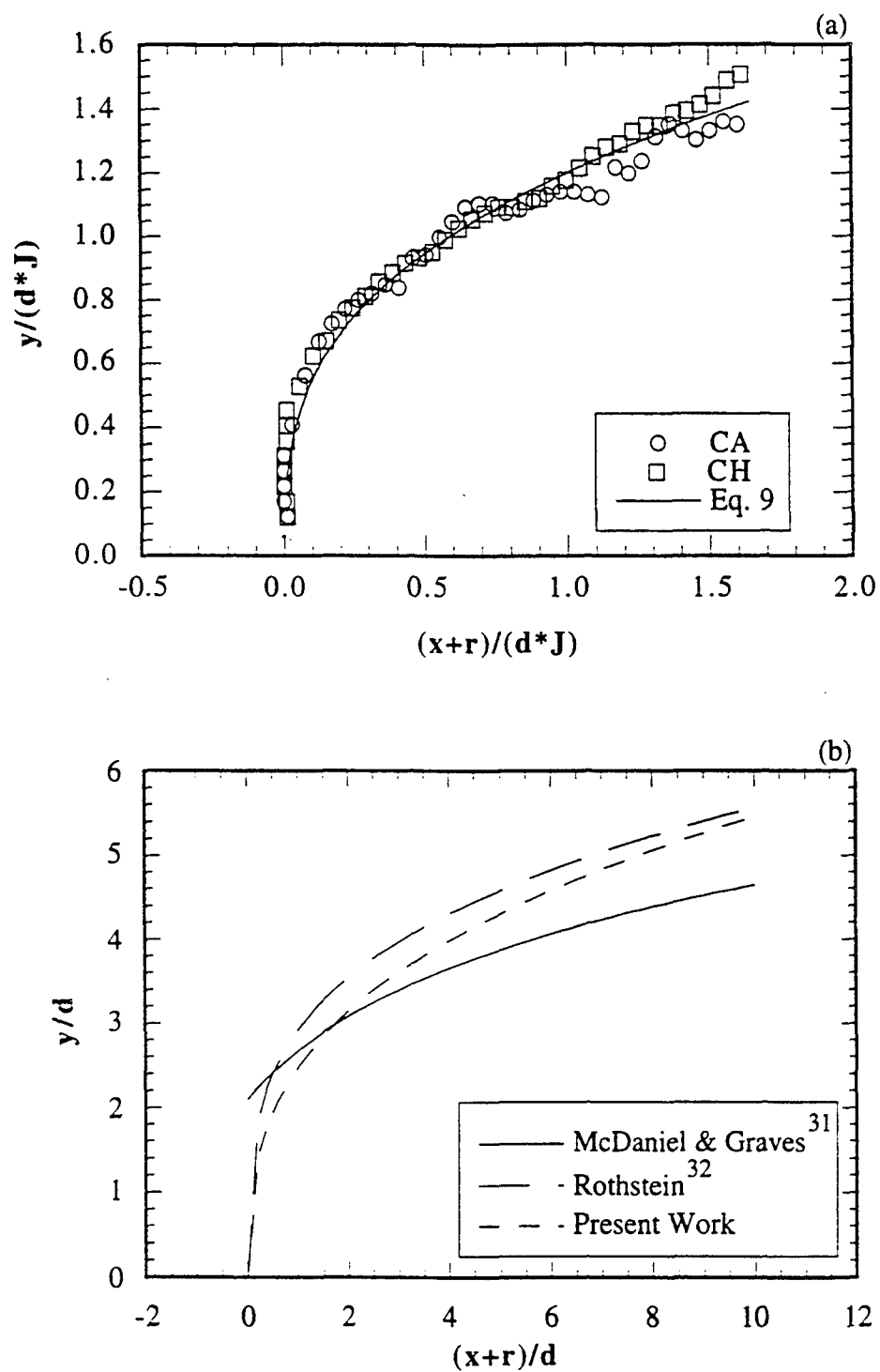


FIG. 11. Transverse penetration data: (a) present cases; (b) comparison with other correlations at  $J = 2.9$ .

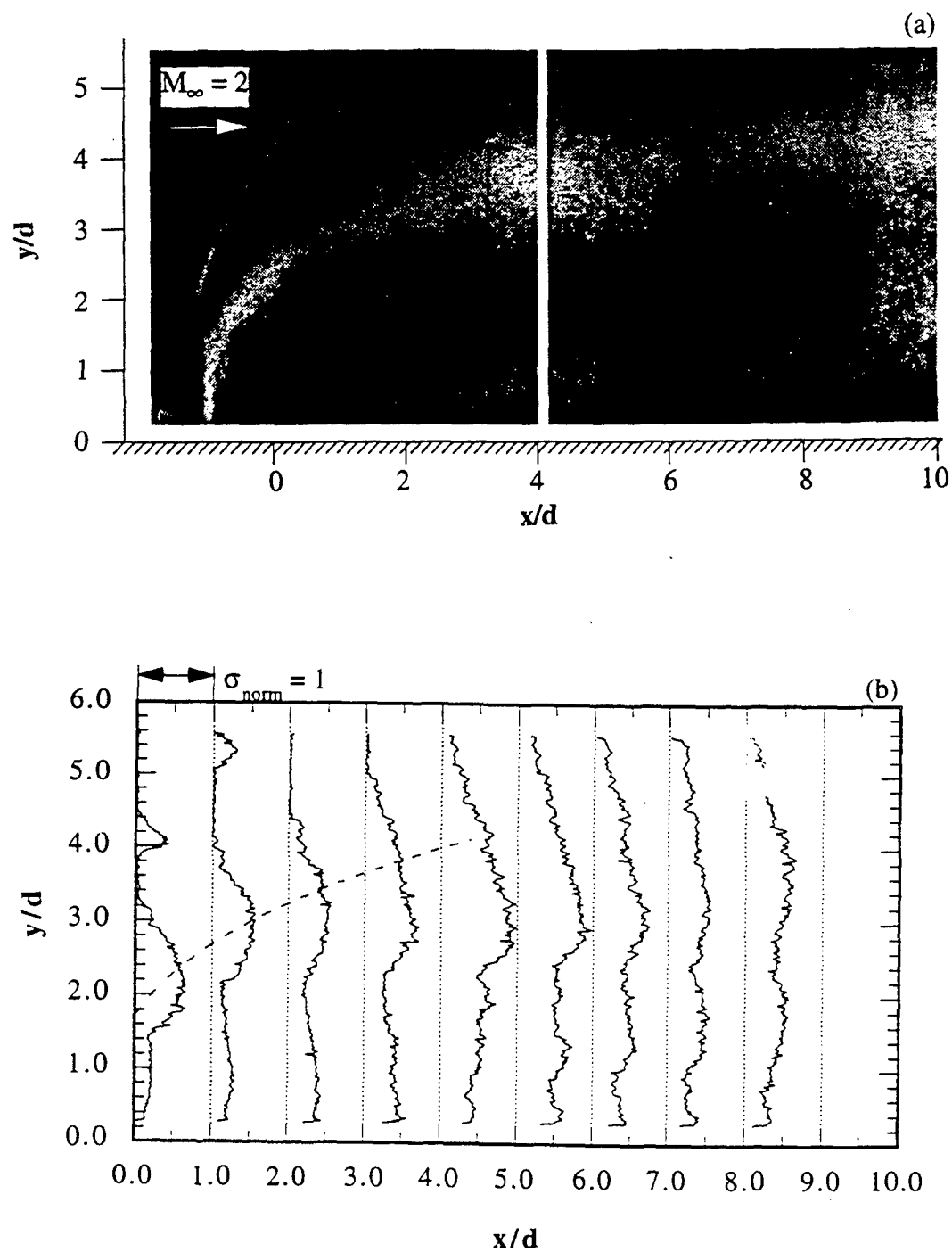


FIG. 12. Side view standard deviation results from case CA: (a) images; (b) profiles.

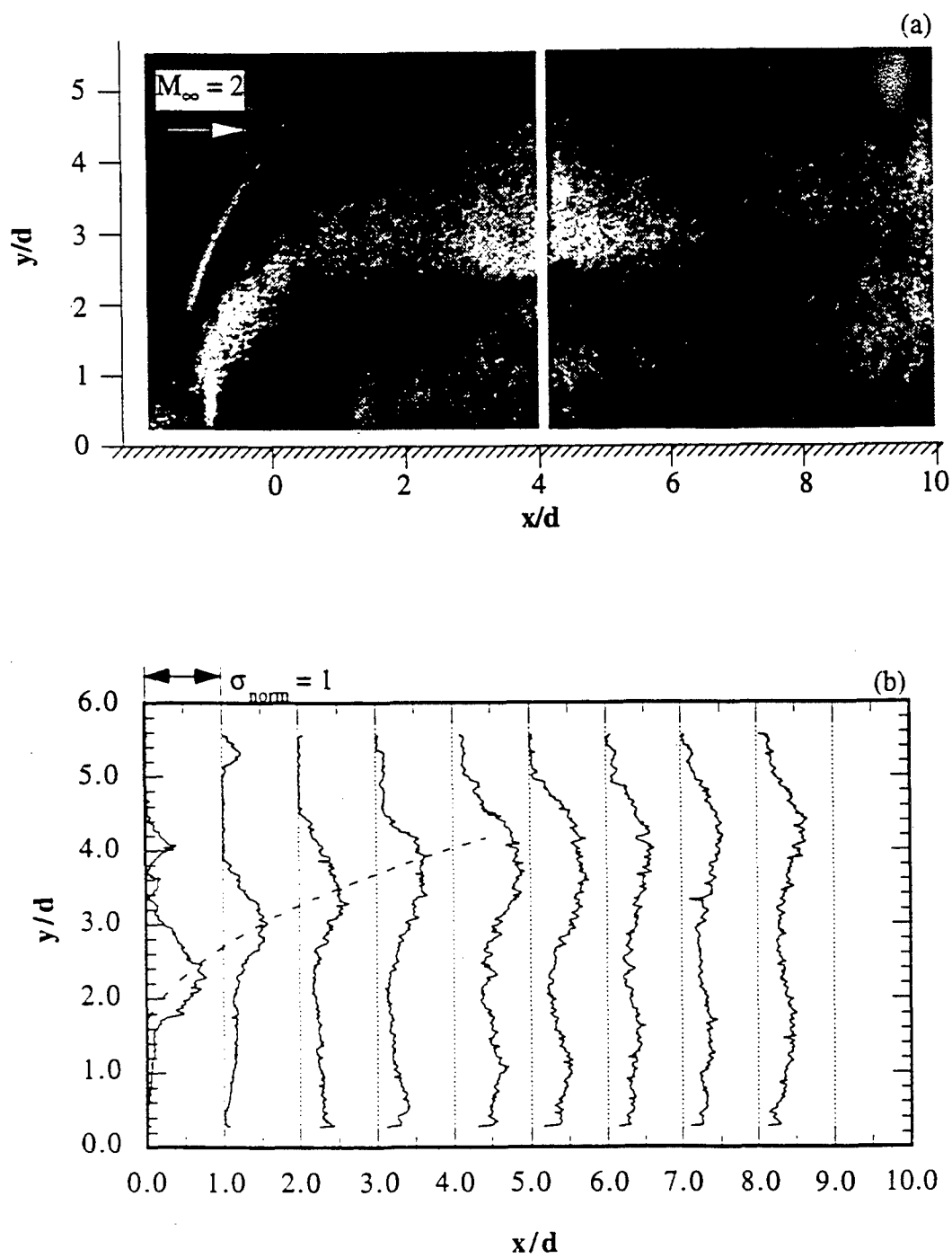


FIG. 13. Side view standard deviation results from case CH: (a) images; (b) profiles.

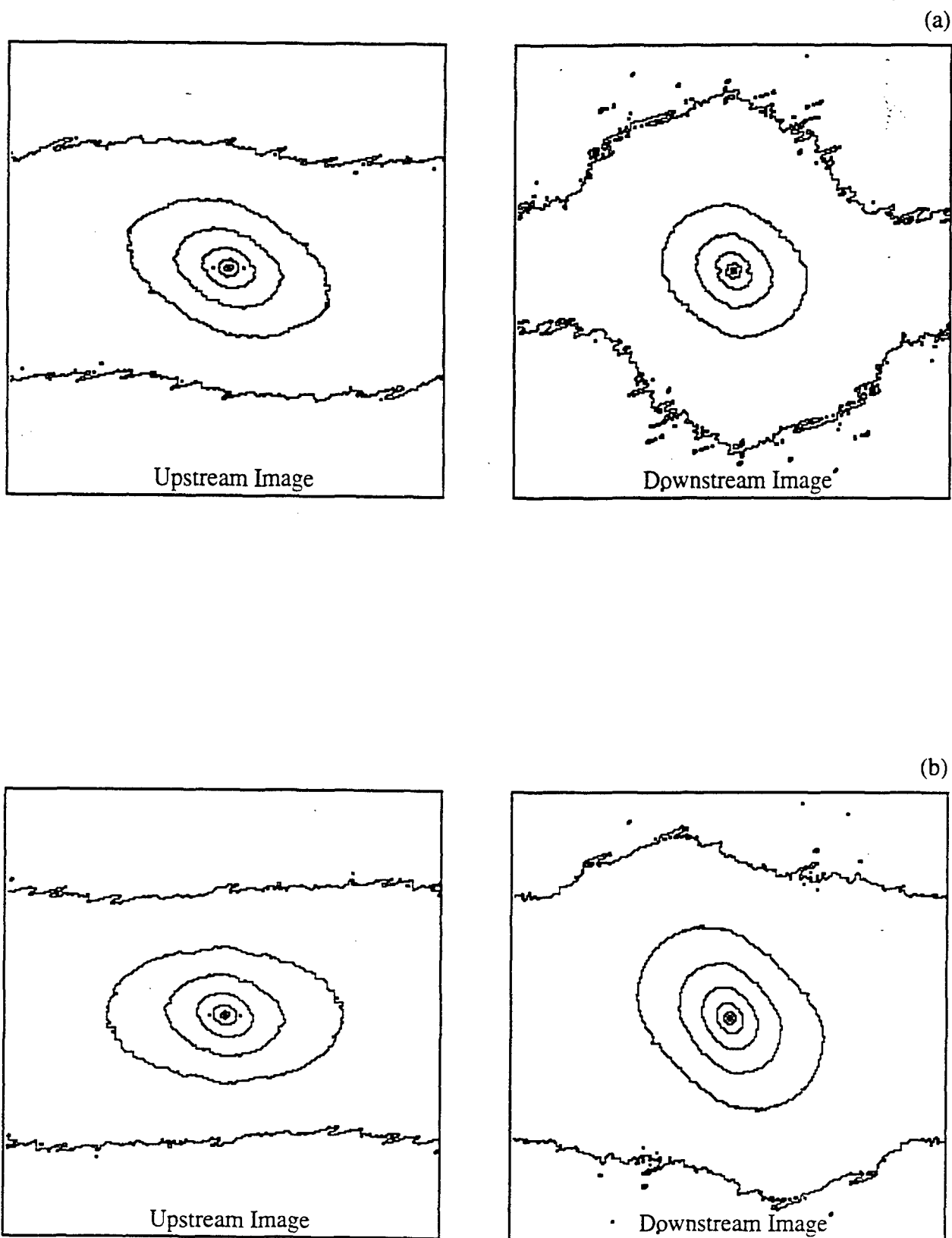


FIG. 14. Ensemble-averaged two-dimensional spatial correlation contours: (a) case CA;  
(b) case CH.

THIS PAGE LEFT INTENTIONALLY BLANK



**AIAA 96-0203**

**Large Structure Convection Velocity  
Measurements in Compressible Transverse  
Injection Flowfields**

M.R. Gruber and A.S. Nejad  
Wright Laboratory, WL/POPT  
1950 Fifth Street  
Wright-Patterson AFB, Ohio 45433

T.H. Chen  
Taitech Inc.  
3675 Harmeling Drive  
Beavercreek, OH 45440

J.C. Dutton  
Dept. of Mechanical and Industrial Engineering  
University of Illinois at Urbana-Champaign  
Urbana, IL 61801

**34th Aerospace Sciences  
Meeting & Exhibit**  
January 15-18, 1996 / Reno, NV



THIS PAGE LEFT INTENTIONALLY BLANK

# LARGE STRUCTURE CONVECTION VELOCITY MEASUREMENTS IN COMPRESSIBLE TRANSVERSE INJECTION FLOWFIELDS

M.R. Gruber\*  
Wright Laboratory, WL/POPT  
Wright-Patterson AFB, Ohio 45433

A.S. Nejad\*\*  
Wright Laboratory, WL/POPT  
Wright-Patterson AFB, Ohio 45433

T.H. Chen†  
Taitech, Inc.  
Beavercreek, Ohio 45440

J.C. Dutton§  
Department of Mechanical and Industrial Engineering  
University of Illinois at Urbana-Champaign  
Urbana, Illinois 61801

## Abstract

An examination of the convection characteristics of the large-scale structures developing in flowfields created by sonic transverse injection through circular and elliptical nozzles into a Mach 1.98 crossflow is reported. Temporally correlated Rayleigh/Mie scattering images taken at the spanwise centerline of the jet/freestream interaction illustrate the characteristics of the highly intermittent structures residing at the interface and allow determination of both the structure convection velocity and structure convection angle. Results indicate that, for a given jet-to-freestream momentum flux ratio, both injector geometry and compressibility play significant roles in influencing the convection characteristics of the large eddies. High compressibility injection cases have dramatically larger near-field convection velocities than their low compressibility counterparts. Farther downstream, as the jet plume bends due to the oncoming freestream flow, the large-scale vortices tend to travel at velocities nearer the freestream velocity. Injector geometry primarily affects the near-field behavior with the elliptical nozzle producing shallower convection angles and convection velocities that are skewed toward the velocity of the freestream. Apparently, the axis-switching phenomenon and the weaker bow shock associated with the elliptical nozzle geometry influence the structural development, resulting in the documented trends.

## Nomenclature

$a$	semi-major axis of an ellipse, speed of sound
$A_{xs}$	cross-sectional area
$b$	semi-minor axis of an ellipse
$d$	diameter
$d_{eff}$	effective injector diameter = $(4A_{xs}/\pi)^{1/2}$
$J$	jet-to-freestream momentum flux ratio
$Kn$	Knudsen number
$\ell$	mean free path
$M$	Mach number
$M_c$	convective Mach number
$p$	static pressure

$p_0$	stagnation pressure
$Re$	local Reynolds number
$t_p$	particle response time
$t_{\delta\omega}$	large-eddy rollover time
$T_0$	stagnation temperature
$u$	velocity
$U_c$	structure convection velocity
$x, y, z$	Cartesian coordinates
$\delta$	boundary layer thickness
$\delta_\omega$	shear layer vorticity thickness
$\Delta r$	structural displacement
$\Delta t$	laser sheet time separation
$\Delta U$	velocity difference
$\Delta x$	streamwise pixel dimension
$\Delta y$	transverse pixel dimension
$\Delta z$	spanwise pixel dimension
$\epsilon$	eccentricity
$\phi$	structure convection angle
$\gamma$	specific heat ratio
$\lambda_K$	Kolmogorov length scale
$\mu$	dynamic viscosity
$\rho$	density

## Subscripts

$e$	exit
$j$	jet
$p$	particle
$\infty$	freestream
1, 2	image #1, image #2

## Introduction

Mixing in compressible, turbulent shear flows is an important issue in the areas of supersonic combustion and jet noise. A prospective fuel injection scheme for hypersonic air-breathing propulsion systems involves the injection of a gaseous fuel jet transversely into a supersonic crossflow. A schematic of the time-averaged transverse injection flowfield appears in Fig. 1. This illustration shows the qualitative features of the flowfield in a plane through the spanwise jet centerline including the three-dimensional

\* Aerospace Engineer, Member AIAA.

\*\* Senior Research Engineer.

† Senior Research Scientist, Senior Member AIAA.

§ Professor, Associate Fellow AIAA.

bow shock, the separation shock, the jet shock structure, and the upstream and downstream separation zones. The large-scale vortices that are the subject of the present investigation reside at the upper jet boundary. Key participants in the mixing processes that occur in this flow are these large-scale eddies that initiate the turbulent energy cascade which proceeds down to the molecular scales. These large-scale motions are considered important because they actively entrain large quantities of one fluid into another. They also enhance the interfacial strain until the length scales of the motions reach the Kolmogorov scale<sup>1</sup> given by

$$\lambda_K \approx \frac{\delta_w}{Re^{3/4}} \quad (1)$$

where the local Reynolds number is computed using

$$Re = \frac{\delta_w \cdot \Delta U \cdot \rho}{\mu} \quad (2)$$

Most planar visualization techniques only examine the instantaneous vortex structure of the flowfield. Knowledge of the temporal development of the eddies produces important information about the evolution of these features including their convection characteristics.

Fric and Roshko<sup>2</sup> conducted an experimental study using the smoke-wire visualization technique to examine the development of large-scale structures in the flowfield created by a jet injected into a low speed crossflow. Their photos illustrate the emergence of four types of vortical structures near the injector including vortices that form in the upper edge shear layer. These eddies oriented themselves in such a way as to roll up into the freestream fluid indicating that, in the region near the injector exit, the injectant fluid moved with a higher velocity tangent to the interface than the freestream fluid. However, to date the convective characteristics of these features have not been reported.

Fundamental investigations of the structure of transverse injection into a supersonic flow are less common than for the low speed case. Recently, instantaneous planar images<sup>3-8</sup> have revealed large-scale vortices present within the shear layer at the jet/freestream interface. These vortices, similar to those observed by Fric and Roshko<sup>2</sup> in that their orientation suggests faster injectant fluid tangent to the interface in the near-jet region, appeared to contribute significantly to the near-field mixing. Again, no special examination of the convection characteristics of these vortices has been undertaken to date.

Jets developing from circular and non-circular nozzles exhibit very different structural characteristics in both quiescent and co-flowing environments.<sup>9-13</sup> The momentum thickness variation around the circumference of a small aspect ratio elliptical nozzle produces an asymmetric instability leading to the development of asymmetric vortices.<sup>9,10</sup> The resulting spreading characteristics associated with the major- and minor-axis planes develop quite differently and at some point an axis-switch is realized.<sup>11,12</sup> That is, the spread in the minor-axis plane overtakes the spread in the major-axis plane. Previous work

has shown that the axis-switch phenomenon persists in the transverse injection flowfield.<sup>7,8</sup> It is therefore expected that some structural differences between the circular and elliptical jet plumes are present in the transverse injection cases of this study.

The large-scale eddies in a planar turbulent shear layer have been studied recently by Bunyajitradulya and Papamoschou<sup>14,15</sup> using a two laser/single camera technique. The authors used planar laser-induced fluorescence (PLIF) of acetone to discern the mixing layer structure. The temporal characteristics of the structures were captured by placing two laser sheets side by side in the flow direction and imaging the fluorescence from both sheets onto a single detector. Measurements of convective velocity were obtained and compared to theoretical predictions. Results from several cases showed significant deviations from theory with the measured convective velocity tending toward the velocity of one of the freestreams. The main problem with this technique is the relatively long time delay (~35-65  $\mu$ s) between the two laser sheet pulses. This long delay allows the structures to change shape enough that measurements of displacement can be somewhat arbitrary.

Large-scale convection velocities have been measured using Mie scattering in studies of important compressible flows.<sup>16,17</sup> In their studies of large-scale structures in expanded compressible turbulent boundary layers, Arnette, et al.<sup>16</sup> used a single laser/two camera imaging technique. Here, time delays of 15-50  $\mu$ s between laser pulses were used. Less structure break-up was encountered for these smaller delays and correlation analyses made the measurement of displacement less arbitrary. Elliott, et al.<sup>17</sup> used similar imaging and analysis techniques to measure convection velocities in compressible mixing layers. Their results indicated a variation in  $U_c$  across the mixing layer where eddies on the high and low speed sides traveled faster and slower than the theoretical convective velocity, respectively. Measured values of  $U_c$  at the center of the mixing layer agreed well with theory.

The objective of the present work is to gain a better understanding of the temporal characteristics of the large-scale eddies that exist along the jet/freestream interface in the flowfields created by sonic transverse jets injected into a supersonic crossflow. Temporally correlated image pairs are obtained by illuminating the seeded flowfield with two coincident laser sheets and collecting the scattered light onto two intensified charge coupled device (ICCD) cameras, each synchronized to and gated around one of the sheets. The laser sheets are separated by a fixed time difference so that obtaining the structural displacement from one image to the other leads directly to a measurement of the velocity with which the structure convects. Four cases are investigated using two injector geometries (circular and elliptical) fueled by helium and air. These two injectant gases allow the examination of the effects of compressibility on the convection of the large-scale interfacial structures.

### Experimental Facility

The transverse injection experiments discussed below were performed in the supersonic research facility located at Wright-Patterson Air Force Base. The details of the facility design appear elsewhere;<sup>18,19</sup> the major highlights appear in the following section.

### Flow Facility

Figure 2 provides a schematic of the supersonic research facility. A continuous supply of pressurized air enters the inlet section of the test apparatus and flows into the settling chamber. This section houses the appropriate flow conditioning devices including a rearward-facing perforated cone that acts as a flow spreader, an array of mesh screens, and a section of honeycomb. The air is then accelerated in the two-dimensional nozzle section by a pair of nozzle blocks producing a uniform Mach 1.98 freestream. This supersonic flow then enters the constant area test section (cross section dimensions of 131 mm by 152 mm). Several fused silica windows placed in the test section walls allow for non-intrusive investigations of the flowfield.

For the present study, two separate injector geometries were incorporated into the removable test inserts housed within the bottom wall of the test section. The details of the injector designs appear elsewhere;<sup>7,8,20</sup> Table 1 summarizes the important geometric features of each injector including the eccentricities ( $\epsilon$ ), and the semi-major ( $a$ ) and semi-minor ( $b$ ) axes. Also, Fig. 3 provides a schematic of the two configurations, where the freestream flow direction is from left to right. Each injector was placed at the same streamwise location to ensure that the approaching turbulent boundary layer would be of the same thickness for each case. At the chosen injector location, the ratio of boundary layer thickness-to-effective jet diameter is  $\delta/d_{\text{eff}} \approx 1$ .

### Imaging System

Figure 4 illustrates the double-pulsed imaging system used in these experiments. Two Spectra Physics Nd:YAG lasers (a DCR-4 and a GCR-170) provided the two pulsed laser beams required. The output of these lasers passed through second harmonic generators to produce vertically polarized beams of light at 532 nm (approximately 400 mJ/pulse). This allowed both beams to be combined on a 50% beam splitter optic so that a single optical train could be used to produce the two coincident laser sheets required. A combination of mirrors, prisms, and lenses (-150 mm cylindrical and 500 mm biconvex) produced the collimated laser sheets used for illuminating the transverse injection flowfield. The sheets entered through the top window of the test section (see Fig. 4). Each laser sheet was roughly 50 mm wide and about 200  $\mu\text{m}$  thick at the long focal waist (measured using a photodiode and an oscilloscope).

Two independent camera systems were placed on opposite sides of the test section to collect the scattered light. Each imaging system was composed of a single Princeton Instruments ICCD camera (384 x 576 pixel array) and image acquisition system (controller model ST-130).

The cameras were water-cooled and purged with nitrogen to reduce dark current noise. A Nikon UV-Nikkor 105 mm f/4.5 telephoto lens placed in front of each pixel array improved the resolution associated with the pixel area. Careful adjustments of the cameras using a common transparent target led to identical imaging areas with identical resolutions. Each camera was gated around a single laser pulse so that two temporally correlated images of the injector flowfield could be obtained. The time delay between the arrival of the first and second laser sheets was set using a custom built delay controller coupled with a pulse generator. Two 486-based computers running the CSMA image acquisition software collected the images. Further analysis of the images was performed on a Power Macintosh and is discussed below.

The two computer systems required a master/slave relationship to ensure that each system started from the same temporal reference. A computer code written for the CSMA acquisition software gave the two computers the ability to communicate with each other through their printer ports. Once the master machine was cued to begin acquiring data, it was instructed by the code to wait for a ready response from the slave machine. A monostable multivibrator chip (DM74121) provided an adjustable time delay (from 2 to 20 sec) for the two systems and their individual software programs to come to equilibrium. Controlling the time delay between the laser sheets was accomplished using another DM74121 chip to open a window for firing the master laser. Since it was operated in a free-running mode, the master laser fired at 10 Hz during the time the window was opened (between 1 and 5 sec). The first electronic pulse from the lamp of the master laser traveled through a DM7408 "and" gate to the master imaging system trigger and to the delay pulse generator (Systron Donner, Model 100C). This device was used to fire the slave laser and to set the desired delay between the two laser sheets. A LeCroy 9314L digital oscilloscope received signals from each camera system and a photodiode (placed behind the 50% beam splitter) allowing the temporal separation of the laser sheets to be monitored and proper gating of each camera to be achieved. The first laser pulse from the slave laser triggered the slave imaging system resulting in the collection of two temporally correlated images separated in time by the delay set on the pulse generator. The acquisition software was allowed to loop until the desired ensemble size had been obtained. Figure 5 illustrates the delay system.

### Seeding Issues and Technique

The seed particles introduced into the flowfield must rapidly adjust to the turbulent fluctuations so that the collected images may be accurately interpreted. It has been found that accurate particle response for Mie scattering images requires a Stokes number, defined as the ratio of the particle response time scale to the characteristic fluid dynamic time scale, of less than about 0.5.<sup>21</sup> A Stokesian drag law<sup>22</sup> and the large-eddy rollover time provide

estimates of the particle response and fluid dynamic time scales, respectively. These estimates are computed using the following expressions:

$$t_p = (1 + 2.76 \cdot Kn) \frac{\rho_p d_p^2}{18\mu} \quad (3)$$

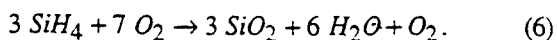
and 
$$t_{\delta\omega} = \frac{\delta\omega}{\Delta U} \quad (4)$$

Maxwell's relation, given by

$$\ell \approx 1.5 \frac{\mu}{\rho a} \quad (5)$$

allows estimation of the mean free path and thus calculation of the Knudsen number.

Combustion of silane ( $\text{SiH}_4$ ) was used to produce the particles required for obtaining images of the jet/crossflow interaction. Silane burns with oxygen to form primarily solid silicone dioxide ( $\text{SiO}_2$ ), water, and hydrogen. In lean reactions (less than 30% silane), Hartman, et al.<sup>23</sup> found that the reaction stoichiometry took the form



Rogers, et al.<sup>24</sup> characterized the silicone dioxide particle sizes using an electron microscope and found the particles to be in the 0.2  $\mu\text{m}$  diameter range. Using the specific gravity of silicone dioxide ( $\text{SG} \approx 2.2$ ) along with the expected operating conditions of the jet and freestream flows then yields an estimate of the Stokes number as approximately 0.09. However, this seeding technique did not provide adequate signal levels for acceptable data quality. Thus, the  $\text{SiO}_2$  seeding technique was supplemented by operating the facility at ambient temperatures so that the naturally occurring water vapor in the freestream air condensed around the  $\text{SiO}_2$  particles. A separate examination of particle size in this combined seeding arrangement using horizontally polarized laser light indicated that the particles were in the Rayleigh scattering regime. Since the incident wavelength in these experiments was 532 nm, an upper bound on the particle diameter resulting from the combined seeding technique is  $\sim 0.5 \mu\text{m}$  yielding a Stokes number of  $\sim 0.38$ . This suggests that even particles with this upper bound diameter accurately follow the turbulent fluctuations.

### Results and Discussion

The conditions of the approaching freestream air were documented as follows:  $M_\infty = 1.98$ ,  $p_{0,\infty} = 317 \text{ kPa}$ , and  $T_{0,\infty} = 300\text{--}302 \text{ K}$ . Injectant flow conditions for the four injection cases studied in this investigation appear in Table 2. Labeling of the cases is done as follows: air and helium injection through the circular nozzle are cases C1A and C2H, respectively, while air and helium injection through the elliptical nozzle are cases E1A and E2H, respectively. The key parameters in Table 2 are the jet-to-freestream momentum flux ratio ( $J$ ) given by

$$J = \frac{(\rho u^2)_j}{(\rho u^2)_\infty} = \frac{(\gamma p M^2)_j}{(\gamma p M^2)_\infty} \quad (7)$$

the jet exit velocity ( $u_{e,j}$ ) and density ( $\rho_{e,j}$ ), and the convective Mach number of the upper edge shear layer ( $M_c$ ). Each case operates at essentially identical values of jet-to-freestream momentum flux ratio, which is the dominant parameter controlling the jet's penetration into the crossflow.<sup>7,8,20,25</sup> The tabulated values of convective Mach number were computed for a single point within the upper edge mixing layer of the circular jet plumes. The computations are based on a simple model of the transverse injection flowfield<sup>20</sup> and the laser Doppler velocimetry data of Santiago.<sup>26</sup> The values shown in Table 2 indicate significant compressibility differences between the air and helium injection flowfields.

The various results obtained in this investigation are presented in the sections to follow. First, the temporally correlated image pairs are presented. Following this is a brief description of the analysis technique used to compute the convection characteristics of the large-scale eddies. Then, the resulting convection velocities and angles are presented and discussed.

### Temporally Correlated Image Pairs

To obtain these results, the optical and electronic arrangements shown in Figs. 4-5 were used to capture two images of the same region within the flowfield at fixed temporal separations. Pixel dimensions in the images were roughly  $(\Delta x, \Delta y, \Delta z) = (66.8 \mu\text{m}, 66.8 \mu\text{m}, 200 \mu\text{m})$ . Each image displayed in this section covers roughly 5.2 effective diameters (33.0 mm) in the streamwise direction and 4.0 effective diameters (25.4 mm) in the transverse direction. The freestream flow direction is from left to right while the injectant flow enters the field of view from the lower left edge of the picture. Gray levels in these images were assigned so that the jet fluid appears dark while seeded freestream fluid appears light. Ensembles of 20 image pairs were acquired for all four cases (C1A, C2H, E1A, and E2H) with the laser sheets positioned at the spanwise centerline of the jet (i.e.,  $z/d_{\text{eff}} = 0$ ).

Selected instantaneous image pairs from the four cases studied here appear in Figs. 6-9. A grid has been superimposed on the individual images so that structural movement from the first image to the second image is more easily identified. Clearly, the two cameras produced images with significantly different signal-to-noise ratios. The right hand images exhibit relatively poor definition in the very near-field of the injector exit, though structures in the downstream portion of these images are clearer. This problem presents a real difficulty in the analysis of the image pairs; the analysis technique is discussed in the next section. Nonetheless, interfacial structural activity is captured by each camera and the movements of the individual eddies can be visually tracked. Figure 6 shows an image pair from case C1A, where a time delay of 2  $\mu\text{s}$  was used. Three structures present in the first image are visible in the second image. These eddies are located near  $x/d_{\text{eff}} = 1.75, 2.5$ , and  $3.0$  in the first image. Notice that the structure positioned near  $x/d_{\text{eff}} = 3.0$  has moved

downstream and rotated somewhat even after only 2  $\mu$ s. The interfacial structure in the images of case C2H, shown in Fig. 7, is somewhat clearer than that of case C1A. In this case, a time delay of 1  $\mu$ s was used. The eddies that dominate the interface are all easily tracked from one image to the next allowing several convection velocity measurements to be made from one image pair.

Image pairs obtained from the elliptical nozzle appear in Figs. 8 and 9. The first figure shows two images from case E1A with a laser sheet time delay of 2  $\mu$ s. These images have three well-defined large-scale eddies positioned at the jet interface. Again, distinct movement of the structures can be observed so that the temporal displacement can be easily computed. Finally, images from case E2H appear in Fig. 9. Here, a time delay of 1.2  $\mu$ s was used and the resulting images again clearly show both interfacial structure and displacement.

### Analysis Technique

As noted above, the two cameras used in this experimental arrangement produced images with significantly different signal-to-noise ratios rendering mathematical manipulation of the data using a cross-correlation technique entirely inconclusive. Thus, these images were analyzed manually such that individual structures were tracked from one shot to the next and their positions in the streamwise and transverse directions (i.e.,  $(x_1, y_1)$ ,  $(x_2, y_2)$  from images #1 and #2, respectively) were determined. In this tracking procedure, the position of the center of a particular feature was identified in each image. Once known, these positions yield the structure's displacement between images from

$$\Delta r = \sqrt{(x_2 - x_1)^2 + (y_2 - y_1)^2}, \quad (8)$$

and, for a known laser sheet time separation  $\Delta t$ , the large-scale convection velocity is determined using

$$U_c = \frac{\Delta r}{\Delta t}. \quad (9)$$

Note that Eqs. 8 and 9 assume that the eddy moves only in the plane of the laser sheet for a given temporal separation. The convection angle  $\phi$  associated with this velocity magnitude may be computed from the following trigonometric relation.

$$\phi = \arctan\left(\frac{y_2 - y_1}{x_2 - x_1}\right) \quad (10)$$

Figure 10 provides a schematic that illustrates these quantities and the general method for obtaining them from the images. Analyzing the images in this way produces some subjectivity concerning the pixel location of a given structure in the two images. It is estimated that the error involved in measuring the structural displacements in the two coordinate directions was  $\pm 1$  pixel. This leads to potential errors in the reported values of  $U_c$  and  $\phi$ . All of the results presented below that were computed from the images are qualified with error bars that represent this

measurement uncertainty. The following section presents the results of the convection velocity analysis.

### Convection Characteristics

The ensembles of image pairs have been analyzed using the methodology and expressions discussed above and shown in Fig. 10. This procedure resulted in measurements of large-scale convection velocity ( $U_c$ ) and structure convection angle ( $\phi$ ) for approximately 30 instantaneous eddies in each case. It should be emphasized that these measurements are instantaneous in nature (i.e., not ensemble-averaged); thus, scatter in the data is expected, although general trends may be observed. Both of the measured quantities are functions of the streamwise and transverse positions of the individual structure; however, the results that follow are only plotted against the streamwise coordinate. This gives some indication of the behavior of the interfacial eddies as the jet is turned downstream.

Figure 11 presents the results of analyzing the image pairs of case C1A. Large-scale convection velocities appear in Fig. 11a. This plot contains two velocity reference lines that indicate both the crossflow air velocity ( $u_\infty = 516$  m/s) and the velocity of the sonic air jet at its exit ( $u_{ej} = 317$  m/s). Also note that error bars are included on all of the measured values of  $U_c$ . In this case, the  $\pm 1$  pixel uncertainty in the structure's position translates into a convection velocity measurement uncertainty of  $\pm 47$  m/s. Initially, near the jet exit (i.e.,  $x/d_{eff} = 0$ ), the eddies that form at the jet/freestream interface convect with velocities that are larger than the exit velocity of the jet. This phenomenon results from the fact that the jet is underexpanded and, as it expands out of the nozzle, the velocity of the jet fluid increases. As the jet turns toward the downstream direction, the convection velocities of the structures generally increase toward the freestream velocity. Several eddies, however, move with velocities close to the jet exit velocity downstream of  $x/d_{eff} = 1$ . The results of applying Eq. 10 for the convection angle to the eddy position measurements are presented in Fig. 11b. In this plot, the crossflow direction is represented using a solid line at  $\phi = 0^\circ$ . The circles that indicate the actual measured convection angles are bounded by error bars that correspond to the  $\pm 1$  pixel accuracy of the measurements. As the air jet exits the circular nozzle, the structural convection angle is relatively high as evidenced by the values plotted near  $x/d_{eff} = 0$ . This is expected since the jet's momentum is originally perpendicular to the flow direction of the approaching freestream. With increasing streamwise position, the eddies begin to move at shallower angles to the crossflow direction. At the farthest downstream measurement station, however, the structure convection angles generally remain greater than zero suggesting that the transverse penetration of the jet fluid is still increasing.

Injection of helium from a circular nozzle (case C2H) results in significantly different trends regarding the convection velocities of the large-scale vortices. Figure 12a presents the convection velocity measurements from within

this flowfield. Note the two reference lines on the plot that are the crossflow air velocity ( $u_\infty = 515$  m/s) and the jet exit velocity ( $u_{e,j} = 882$  m/s). In this case, the jet exit velocity is larger than the approaching freestream velocity as opposed to case C1A where the opposite was true. The error bars in this plot are twice as wide ( $\pm 95$  m/s) as in Fig. 11a since the temporal separation of the laser sheet is only  $1.0 \mu\text{s}$ . Clearly, as the helium jet exits the circular nozzle, the large-scale eddies formed in the upper edge shear layer move markedly faster than the jet exit velocity. Again, this is due to the underexpanded condition of the jet. Comparing the performance of the two injectant gases in the very near-field of the jet/crossflow interaction (i.e.,  $x/d_{\text{eff}} \leq 2$ ) shows that the eddies in case C2H move roughly three times faster than those from case C1A. This observation provides further evidence of the effects of the large value of convective Mach number ( $M_c = 1.9$ ) for case C2H. The data in Fig. 12a suggest a local maximum in  $U_c$  occurring near  $x/d_{\text{eff}} = 1.0$ , downstream of which the convection velocity rapidly relaxes toward the freestream velocity. The structure convection angles in Fig. 12b for case C2H closely resemble those in Fig. 11b for case C1A in that the data show relatively large angles as the jet enters the freestream fluid, and these angles rapidly decrease in the streamwise direction becoming more parallel to the crossflow.

Figure 13 illustrates the results obtained from analyzing the image pairs from case E1A. The convection velocity data presented in Fig. 13a show the eddies rapidly reaching the crossflow velocity. Compared to Fig. 11a for case C1A, the near-field results in Fig. 13a suggest a quicker acceleration up to the freestream velocity. However, as the flow develops farther downstream, the two cases behave very similarly in that each produces large-scale convection velocity magnitudes that hover around the velocity of the freestream. Examining the structure convection angles presented in Fig. 13b shows that the large-scale eddies move at shallower angles with respect to the freestream fluid in the near-injector region than in case C1A (see Fig. 11b). The angles plotted in Fig. 13b decay as expected toward the freestream flow direction ( $\phi = 0^\circ$ ) with increasing streamwise distance from the injector exit. It is suspected that the axis-switching phenomenon present in the elliptical injector flowfield causes the observed differences in the behavior of  $U_c$  and  $\phi$  in the near-field regions of cases C1A and E1A. This phenomenon, caused by the asymmetric distribution of momentum thickness around the elliptical nozzle exit,<sup>9</sup> results in faster spreading in the minor-axis plane than in the major-axis plane. Another potential contributor to the observed differences in behavior of the convection velocity and convection angle results for the circular and elliptical injectors is the weaker bow shock present in the elliptical injector flowfield. The bow shock strength directly affects the velocity distribution of the freestream fluid behind it. In addition, this fluid is one of the streams involved in the formation of the mixing layer at the upper edge of the jet fluid. Since the convection characteristics of the large-scale eddies that form within the

mixing layer are highly sensitive to the velocities of either stream involved in its development,<sup>15,27</sup> the differences in shock strength could result in the observed differences in  $U_c$  and  $\phi$  between circular and elliptical injection.

Results from case E2H appear in Figs. 14a and 14b. The very near-field of this injection case contains eddies that convect with velocities between the jet exit velocity and the freestream velocity as in case E1A. As the eddies move downstream, their convection velocities begin to taper off toward the freestream velocity, though several of the instantaneous structures analyzed have measured values of  $U_c$  both higher and lower than  $u_\infty$ . The near-field behavior in this case is substantially different from that observed in case C2H (Fig. 12a) where the shear layer vortices moved much faster than the jet exit velocity. This difference is again thought to be caused by the axis-switching phenomenon associated with the elliptical nozzle geometry. Apparently, the momentum thickness asymmetry that leads to axis-switching also affects the development of the vortices in the mixing layer that forms at the jet/freestream interface. It is also possible that the weaker bow shock formed in the elliptical injection flowfield plays a role in the significantly different near-field convection velocity characteristics of the large-scale eddies. The structure convection angles presented in Fig. 14b appear very similar to those from case E1A that were shown in Fig. 13b. The near-injector region contains relatively shallow convection angles compared to case C2H while the angles gradually tend toward the freestream flow direction as expected. The non-zero angles found by four effective diameters downstream of the injector exit are consistent with the other double-pulsed data and with the results of both ensemble-averaged end view and side view images<sup>8,20</sup> that indicate increasing transverse penetration at this streamwise position.

### Summary and Conclusions

Large-scale convection velocity measurements have been made in the flowfields generated by transverse injection from circular and elliptical nozzles into a supersonic crossflow. Convection characteristics obtained from temporally correlated image pairs show a strong dependence on both mixing layer compressibility level and injector geometry. For a given injector geometry, the near-field convection velocities are larger for the high compressibility cases (helium injection) than for the low compressibility cases (air injection). In the far-field, after the jet plume has been bent downstream, the eddies tend to convect with velocities that are closer to the velocity of the freestream, and convection angles rapidly decay toward the freestream flow direction. Injector geometry principally affects the near-field behavior. Convection angles are shallower for elliptical injection than they are for circular injection, and the near-field convection velocities from the elliptical injection cases are skewed toward the freestream velocity. It is thought that the axis-switching phenomenon affects the development of the large-scale eddies in the near-field of the elliptical injector, resulting in the observed

trends. Also, the weaker bow shock generated in the elliptical injection flowfield may contribute to the observed differences in convection characteristics.

### Acknowledgments

The authors would like to acknowledge Messrs. D. Schommer and C. Smith for their operation of the facility. Useful discussions with Mr. J. Donbar, Dr. C. Carter, and Dr. D. Glawe were greatly appreciated. This work was supported by the Air Force Office of Scientific Research.

### References

- <sup>1</sup>Broadwell, J.E., and Mungal, M.G., "Large-Scale Structures and Molecular Mixing," *Physics of Fluids A*, Vol. 3, No. 5, 1991, pp. 1193-1206.
- <sup>2</sup>Fric, T.F., and Roshko, A., "Structure in the Near Field of the Transverse Jet," *Seventh International Symposium on Turbulent Shear Flows*, Stanford University, 1989, pp. 225-237.
- <sup>3</sup>McMillin, B.K., Palmer, J.L., Seitzman, J.M., and Hanson, R.K., "Two-Line Instantaneous Temperature Imaging of NO in a SCRAMJET Model Flowfield," AIAA Paper 93-0044, January 1993.
- <sup>4</sup>VanLerberghe, W.M., "Large-Scale Structure and Mixing in a Sonic Transverse Jet Injected into a Supersonic Crossflow," Ph.D. Thesis, Department of Mechanical and Industrial Engineering, University of Illinois at Urbana-Champaign, Urbana, IL, 1995.
- <sup>5</sup>Hermanson, J.C., and Winter, M., "Mie Scattering Imaging of a Transverse, Sonic Jet in Supersonic Flow," *AIAA Journal*, Vol. 31, No. 1, 1993, pp. 129-132.
- <sup>6</sup>VanLerberghe, W.M., Dutton, J.C., Lucht, R.P., and Yuen, L.S., "Penetration and Mixing Studies of a Sonic Transverse Jet Injected into a Mach 1.6 Crossflow," AIAA Paper 94-2246, June 1994.
- <sup>7</sup>Gruber, M.R., Nejad, A.S., Chen, T.H., and Dutton, J.C., "Mixing and Penetration Studies of Sonic Jets in a Mach 2 Freestream," *Journal of Propulsion and Power*, Vol. 11, No. 2, 1995, pp. 315-323.
- <sup>8</sup>Gruber, M.R., Nejad, A.S., and Dutton, J.C., "Circular and Elliptical Transverse Injection into a Supersonic Crossflow--The Role of Large-Scale Structures," AIAA Paper 95-2150, June 1995.
- <sup>9</sup>Schadow, K.C., Wilson, K.J., and Lee, M.J., "Enhancement of Mixing in Reacting Fuel-Rich Plumes Issued from Elliptical Nozzles," *Journal of Propulsion and Power*, Vol. 3, No. 2, 1987, pp. 145-149.
- <sup>10</sup>Ho, C., and Gutmark, E., "Vortex Induction and Mass Entrainment in a Small-Aspect-Ratio Elliptic Jet," *Journal of Fluid Mechanics*, Vol. 179, 1987, pp. 383-405.
- <sup>11</sup>Gutmark, E., Schadow, K.C., and Wilson, K.J., "Noncircular Jet Dynamics in Supersonic Combustion," AIAA Paper 87-1878, June 1987.
- <sup>12</sup>Schadow, K.C., Gutmark, E., Koshigoe, S., and Wilson, K.J., "Combustion-Related Shear-Flow Dynamics in Elliptic Supersonic Jets," *AIAA Journal*, Vol. 27, No. 10, 1989, pp. 1347-1353.
- <sup>13</sup>Gutmark, E., Schadow, K.C., and Bicker, C.J., "Mode Switching in Supersonic Circular Jets," *Physics of Fluids A*, Vol. 1, No. 5, 1989, pp. 868-873.
- <sup>14</sup>Bunyajitradulya, A., and Papamoschou, D., "Acetone PLIF Imaging of Turbulent Shear-Layer Structures at High Convective Mach Numbers," AIAA Paper 94-0617, January 1994.
- <sup>15</sup>Papamoschou, D., and Bunyajitradulya, A., "Double-Exposure PLIF Imaging of Compressible Shear Layers," AIAA Paper 95-0513, January 1995.
- <sup>16</sup>Arnette, S.A., Samimy, M., and Elliott, G.S., "The Effect of Expansion on Large Scale Structure Evolution in a Compressible Turbulent Boundary Layer," AIAA Paper 94-2228, June 1994.
- <sup>17</sup>Elliott, G.S., Samimy, M., and Arnette, S.A., "The Characteristics and Evolution of Large-Scale Structures in Compressible Mixing Layers," *Physics of Fluids*, Vol. 7, No. 4, 1995, pp. 864-876.
- <sup>18</sup>Gruber, M.R., and Nejad, A.S., "Development of a Large-Scale Supersonic Combustion Research Facility," AIAA Paper 94-0544, January 1994.
- <sup>19</sup>Gruber, M.R., and Nejad, A.S., "New Supersonic Combustion Research Facility," *Journal of Propulsion and Power*, Vol. 11, No. 5, 1995, pp. 1080-1083.
- <sup>20</sup>Gruber, M.R., "An Experimental Investigation of Transverse Injection from Circular and Elliptical Nozzles into a Supersonic Crossflow," Ph.D. Thesis, Department of Mechanical and Industrial Engineering, University of Illinois at Urbana-Champaign, Urbana, IL, 1996.
- <sup>21</sup>Samimy, M., and Lele, S.K., "Motion of Particles with Inertia in a Compressible Free Shear Layer," *Physics of Fluids A*, Vol. 3, No. 8, 1991, pp. 1915-1923.
- <sup>22</sup>Melling, A., "Seeding Gas Flows for Laser Anemometry," *AGARD Advanced Instrumentation for Aero Engine Components*, Philadelphia, 1986, pp. 8.1-8.11.
- <sup>23</sup>Hartman, J.R., Famil-Ghiriha, J., Ring, M.A., and O'Neal, H.E., "Stoichiometry and Possible Mechanism of SiH<sub>4</sub>-O<sub>2</sub> Explosions," *Combustion and Flame*, Vol. 68, 1987, pp. 43-56.
- <sup>24</sup>Rogers, R.C., Weidner, E.H., and Bittner, R.D., "Quantification of Scramjet Mixing in the Hypervelocity Flow of a Pulse Facility," AIAA Paper 94-2518, June 1994.
- <sup>25</sup>Papamoschou, D., and Hubbard, D.G., "Visual Observations of Supersonic Transverse Jets," *Experiments in Fluids*, Vol. 14, 1993, pp. 468-476.
- <sup>26</sup>Santiago, J.S., "An Experimental Study of the Velocity Field of a Transverse Jet Injected into a Supersonic Crossflow," Ph.D. Thesis, Department of Mechanical and Industrial Engineering, University of Illinois at Urbana-Champaign, Urbana, IL, 1995.
- <sup>27</sup>Papamoschou, D., "Structure of the Compressible Turbulent Shear Layer," AIAA Paper 89-0126, January 1989.



Table 1 Injector Geometries

Injector	a (mm)	b (mm)	$d_{eff}$ (mm)	$\epsilon$
Circular	3.18	3.18	6.35	0
Elliptical	6.25	1.63	6.35	0.97

Table 2 Injectant Flow Conditions

Case	$\gamma_j$	$P_{ej}$ (kPa)	$u_{ej}$ (m/s)	$\rho_{ej}$ (kg/m <sup>3</sup> )	J	$M_c$
C1A	1.40	476	317	6.64	2.90	0.66
C2H	1.67	405	882	0.867	2.93	1.92
E1A	1.40	476	317	6.64	2.90	-
E2H	1.67	405	882	0.867	2.93	-

INJECTOR CROSS SECTION VIEW PLAN VIEW

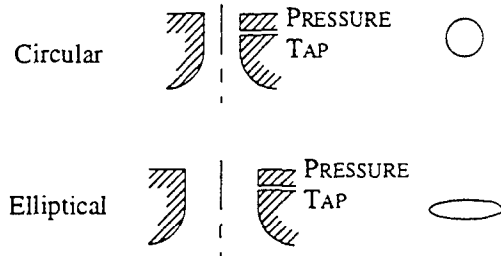


Figure 3 Illustration of Injector Configurations

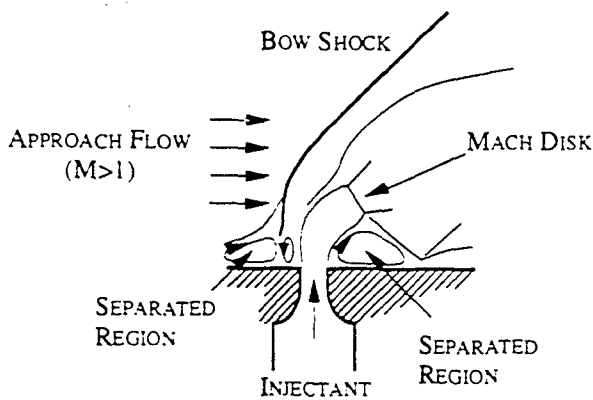


Figure 1 Transverse Injection Flowfield Schematic

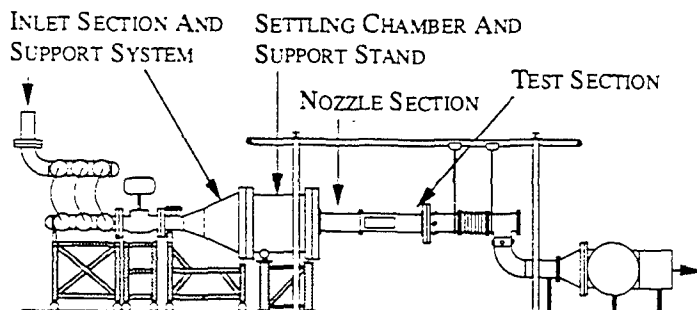


Figure 2 Schematic of Supersonic Combustion Tunnel

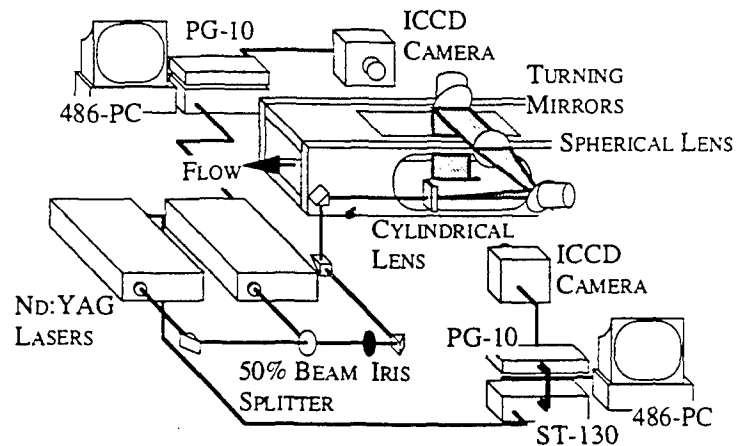


Figure 4 Schematic of Double-Pulsed Rayleigh/Mie Scattering Optical Arrangement

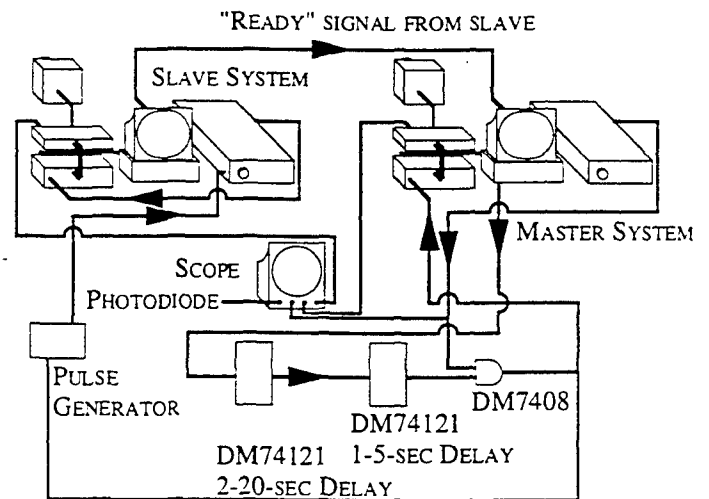
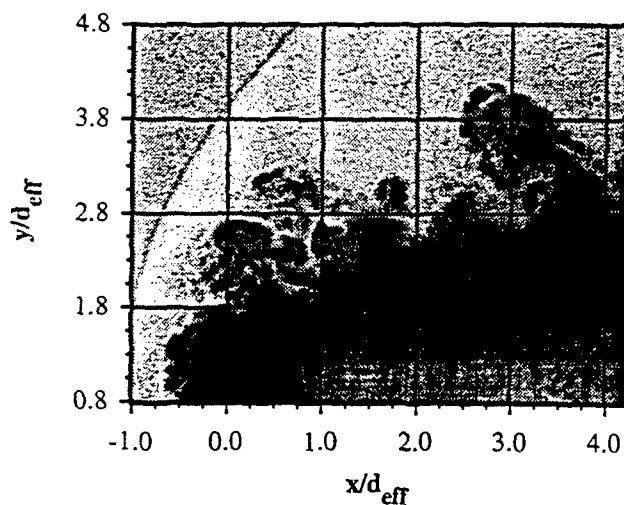
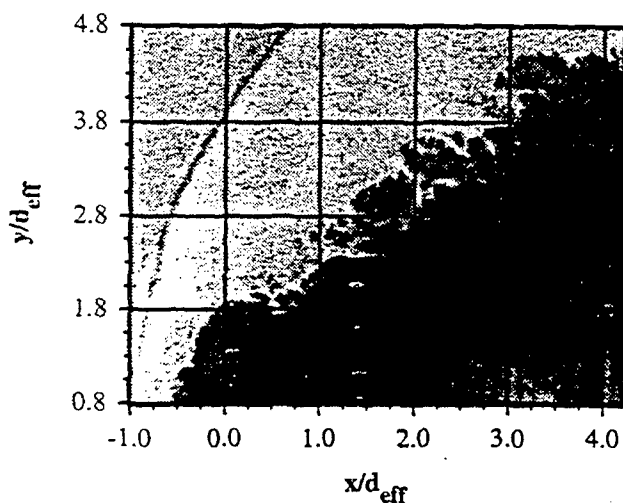
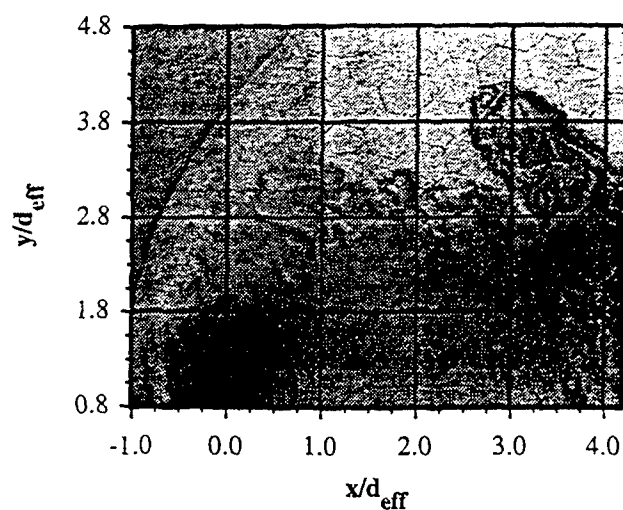


Figure 5 Delay System Electrical Schematic



**Figure 6** Instantaneous Double-Pulsed Image Pair from Circular Injection Using Air (Case C1A) with Laser Pulse Delay of  $\Delta t = 2 \mu s$



**Figure 7** Instantaneous Double-Pulsed Image Pair from Circular Injection Using Helium (Case C2H) with Laser Pulse Delay of  $\Delta t = 1 \mu s$

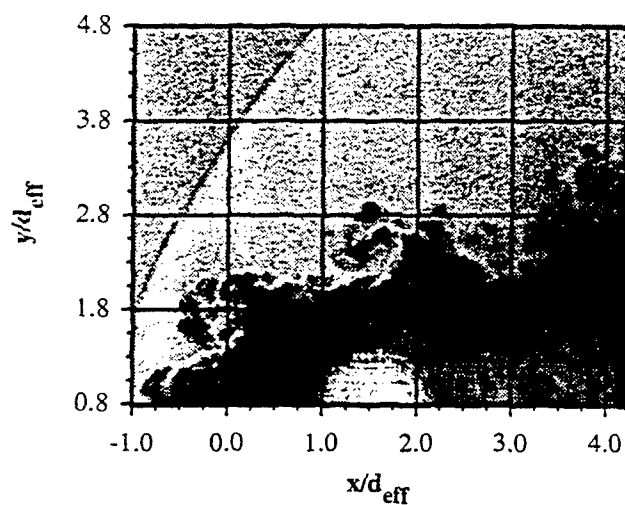
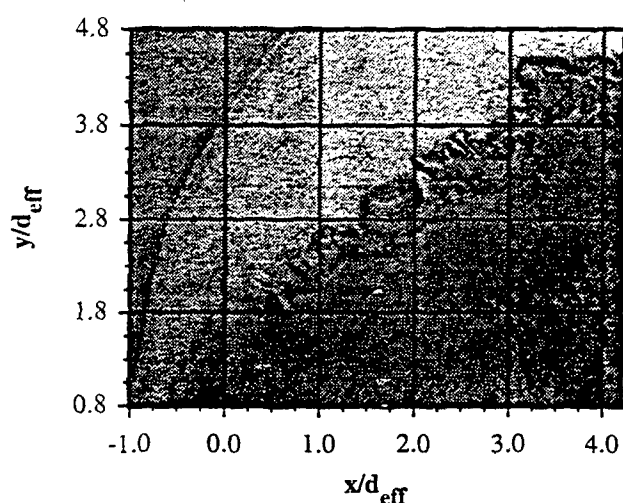


**Figure 8** Instantaneous Double-Pulsed Image Pair from Elliptical Injection Using Air (Case E1A) with Laser Pulse Delay of  $\Delta t = 2 \mu s$

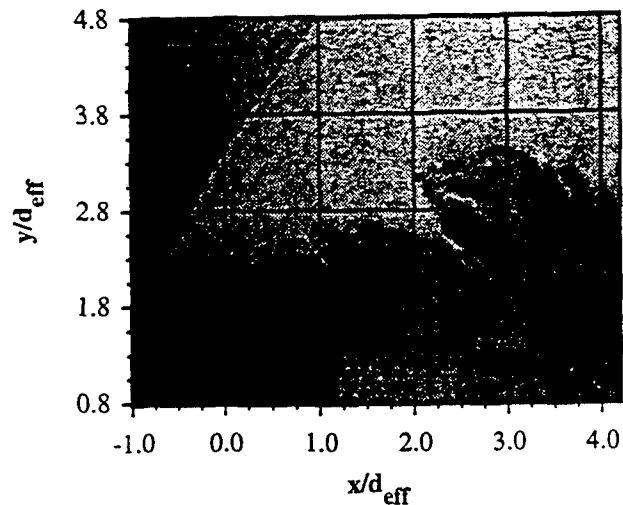
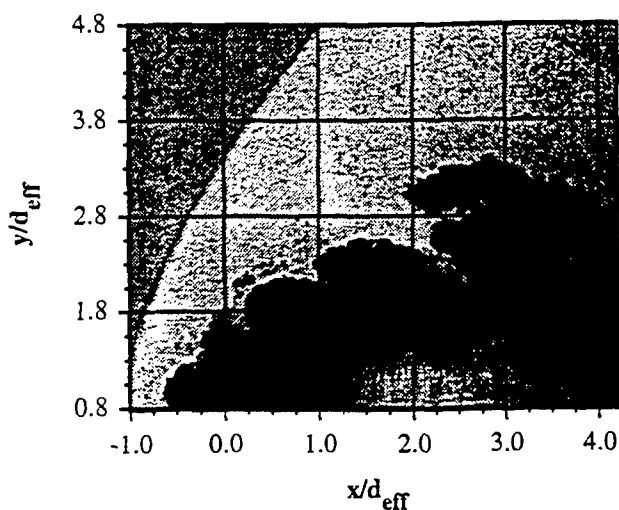
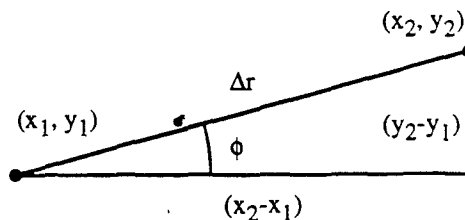
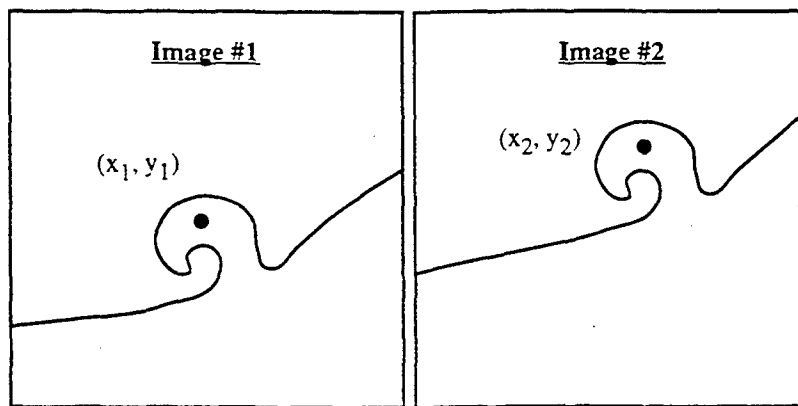


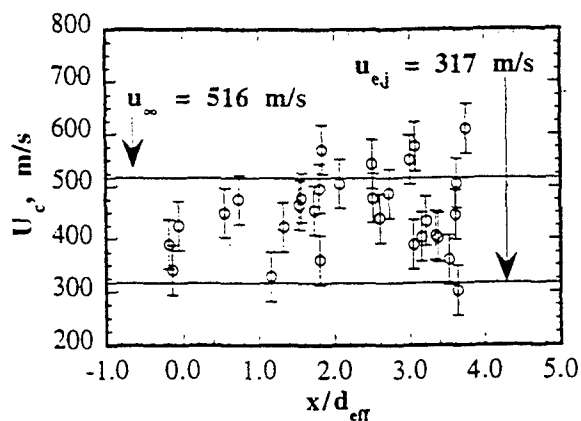
Figure 9 Instantaneous Double-Pulsed Image Pair from Elliptical Injection Using Helium (Case E2H) with Laser Pulse Delay of  $\Delta t = 1.2 \mu s$



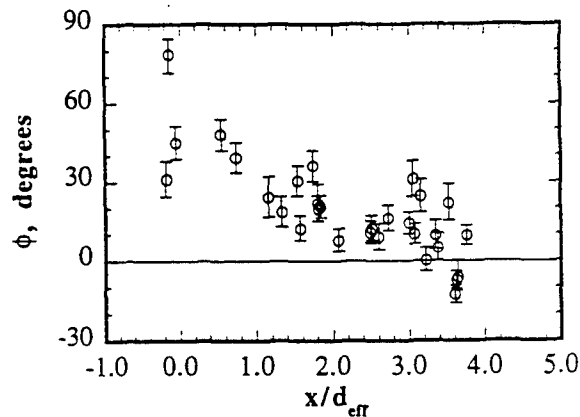
$$U_c = \frac{\Delta r}{\Delta t} = \frac{\sqrt{(x_2 - x_1)^2 + (y_2 - y_1)^2}}{\Delta t}$$

$$\phi = \arctan[(y_2 - y_1)/(x_2 - x_1)]$$

Figure 10 Large-Scale Convection Velocity and Structure Convection Angle Determination

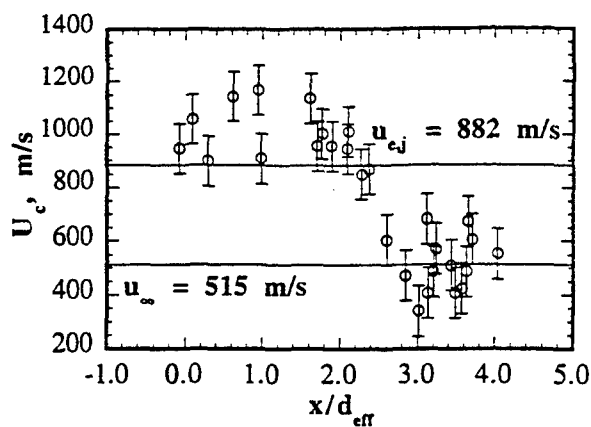


a) Convection Velocity Distribution

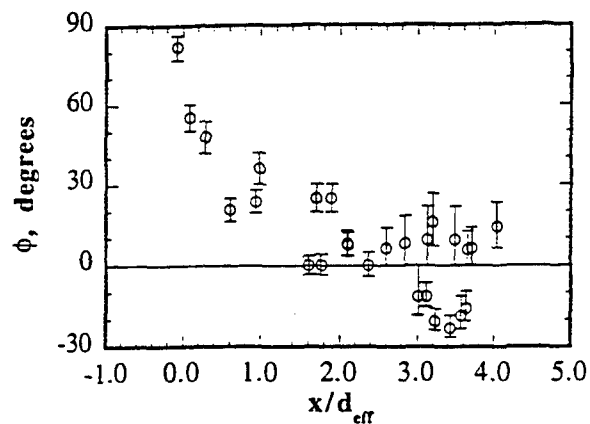


b) Convection Angle Distribution

Figure 11 Results for Circular Injection Using Air (Case C1A) a) Convection Velocity Distribution and b) Convection Angle Distribution

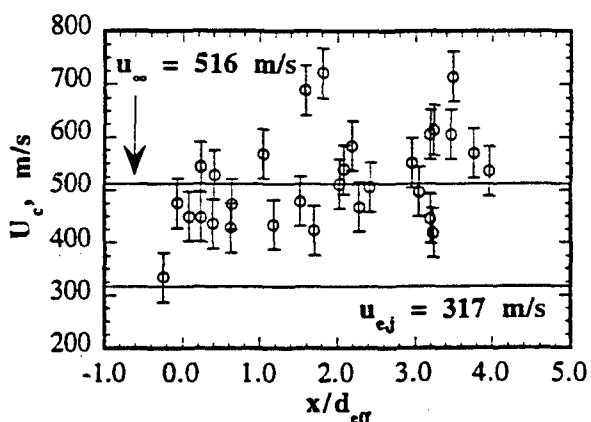


a) Convection Velocity Distribution

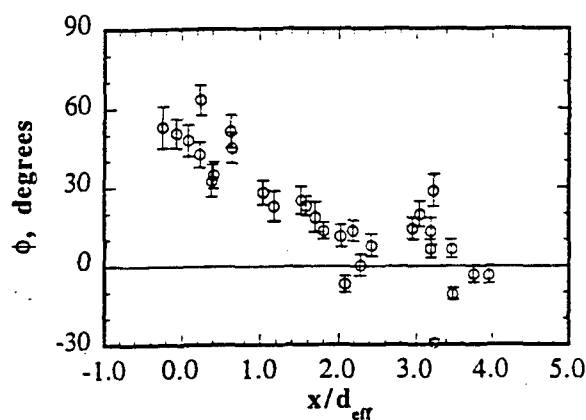


b) Convection Angle Distribution

**Figure 12** Results for Circular Injection Using Helium (Case C2H) a) Convection Velocity Distribution and b) Convection Angle Distribution

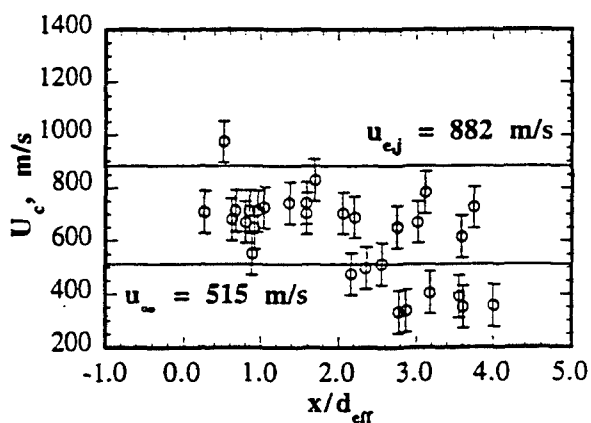


a) Convection Velocity Distribution

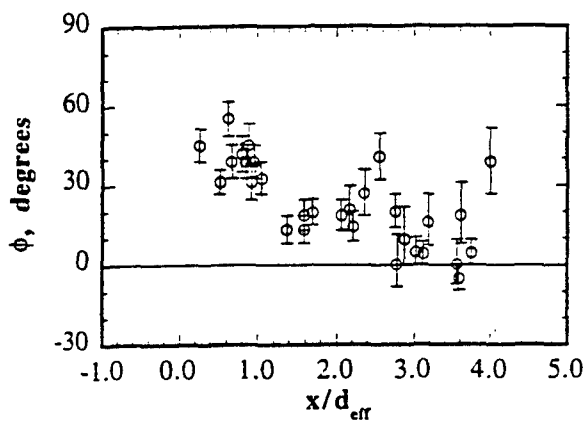


b) Convection Angle Distribution

**Figure 13** Results for Elliptical Injection Using Air (Case E1A) a) Convection Velocity Distribution and b) Convection Angle Distribution



a) Convection Velocity Distribution



b) Convection Angle Distribution

**Figure 14** Results for Elliptical Injection Using Helium (Case E2H) a) Convection Velocity Distribution and b) Convection Angle Distribution

# Mixing and Penetration Studies of Sonic Jets in a Mach 2 Freestream

M. R. Gruber\* and A. S. Nejad†

*U.S. Air Force Wright Laboratory, Wright–Patterson Air Force Base, Ohio 45433*

T. H. Chen‡

*Taitech Group, WL/POPT, Wright–Patterson Air Force Base, Ohio 45433*

and

J. C. Dutton§

*University of Illinois at Urbana–Champaign, Urbana, Illinois 61801*

A comparison of the penetration and mixing characteristics of three transverse/oblique injector configurations is presented. The three geometries studied include circular transverse, circular oblique, and elliptical transverse injectors, and the crossflow is at Mach 2. Planar Mie scattering images of three near-field flow planes produced substantial information about the flowfield created by each injector. In addition to global flowfield characteristics, the Mie scattering images provided transverse and lateral penetrations for each injector. Instantaneous and time-averaged information concerning the structural organization of the flowfields was obtained. Results demonstrate increasing jet penetration in the transverse direction with increasing jet-to-freestream momentum flux ratio. Penetration of the oblique jet is appreciably less in the near-field compared to the two transverse jets due to the reduced component of momentum in the transverse direction. The transverse elliptic jet appears to spread more quickly in the lateral direction than the other two jets, suggesting that some type of axis-switching phenomenon occurs. Large-scale structures at the interface between the jet and freestream fluids are shown for the two transversely oriented jets, while small-scale eddies are prominent in the oblique jet flowfield. Near-field mixing appears dominated by these eddies and the counter-rotating structures that develop in the streamwise direction.

## Nomenclature

$A$	= area
$a$	= semimajor axis of an ellipse
$b$	= semiminor axis of an ellipse
$d_{eff}$	= effective injector diam. $(4A_{in}/\pi)^{1/2}$
$d_p$	= particle diameter
$J$	= jet-to-freestream momentum flux ratio
$Kn$	= Knudsen number (ratio of mean free path to particle diameter)
$M$	= Mach number
$p$	= static pressure
$T_0$	= total temperature
$t_p$	= particle response time
$t_A$	= large eddy rollover time
$u$	= velocity
$x$	= streamwise coordinate
$y$	= transverse coordinate
$z$	= spanwise coordinate
$\gamma$	= specific heat ratio
$\delta$	= boundary layer thickness, shear layer vorticity thickness
$\epsilon$	= eccentricity
$\mu$	= dynamic viscosity
$\rho$	= density

## Subscripts

ex	= exit
f	= freestream
j	= jet
p	= particle
xs	= cross section

## Introduction

FUNDAMENTAL to the success of hypersonic air-breathing propulsion systems are the efficient injection, mixing, and combustion processes that occur inside the combustion chamber. These processes will take place in a supersonic stream, and thus, must occur quickly because residence times within such combustors will necessarily be short, even when fuel dispersion is aided by such intrusive features as struts or ramps. The transverse jet injected into a supersonic crossflow represents a possible configuration for fuel delivery in such engines.

Many early investigations of the transverse gaseous jet in supersonic crossflow revolved around qualitative examinations of the underexpanded injection flowfield and analytical descriptions of the injectant penetration depth as a function of various flow parameters.<sup>1,2</sup> Schlieren photographs of the injection flowfield revealed the presence of a bow shock wave upstream of the injector exit, rapid turning of the injectant gas, a Mach disk, and regions of recirculating flow immediately upstream and downstream of the jet orifice. Figure 1 is a schematic representation of the flowfield.

One analytical model developed for the prediction of jet penetration assumed that the sonic jet issues into a stream with no boundary layer and that no mixing occurs between the injectant and freestream fluids near the injector orifice.<sup>1</sup> A momentum balance applied to a prescribed plume geometry resulted in a functional form for the penetration depth that accurately predicted the jet penetration determined from the

Received Dec. 20, 1993; presented as Paper 94-0709 at the AIAA 32nd Aerospace Sciences Meeting, Reno, NV, Jan. 10–13, 1994; revision received July 13, 1994; accepted for publication Aug. 9, 1994. This paper is declared a work of the U.S. Government and is not subject to copyright protection in the United States.

\*Aerospace Engineer, Advanced Propulsion Division, Experimental Research Branch, Member AIAA.

†Senior Research Engineer, Advanced Propulsion Division, Experimental Research Branch.

‡Senior Research Scientist, Senior Member AIAA.

§Professor, Department of Mechanical and Industrial Engineering, Associate Fellow AIAA.

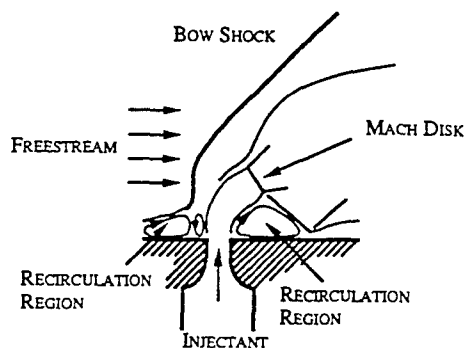


Fig. 1 Transverse injection flowfield schematic.

measured maximum injectant concentration profile. A similar model developed in another study<sup>2</sup> resulted in an expression for the penetration that suggested that the jet-to-freestream momentum flux ratio (or dynamic pressure ratio), given by

$$J = \frac{(\rho u^2)_j}{(\rho u^2)_f} = \frac{(\gamma p M^2)_j}{(\gamma p M^2)_f} \quad (1)$$

was the principal controlling parameter. Another concept introduced in this study was that of the "effective back pressure" seen by the jet. This pressure, analogous to the back pressure in the flowfield formed by a jet issuing into a quiescent environment, is the average pressure in the near-jet region. The complex nature of the pressure field surrounding the injector orifice in this flow makes it difficult to determine an accurate effective back pressure when using conventional methods. Schetz and Billig<sup>2</sup> suggested that injection at a pressure-matched condition (i.e., where the static pressure of the jet is equal to the effective back pressure) produced a more optimum penetration than simply overpressurizing the jet, due to reduced shock losses.

Recent studies investigated the issue of penetration more fully.<sup>3,4</sup> Papamoschou and Hubbard<sup>3</sup> examined the effects of freestream and jet Mach numbers, static pressure and density ratios, and momentum flux ratio on penetration using schlieren photography. Results indicated that the jet's penetration into the supersonic crossflow was principally dependent on the momentum flux ratio defined in Eq. (1). They found little or no effect due to the freestream or jet Mach numbers, while evidence of an optimum penetration at a certain pressure ratio provided support for the matched pressure condition cited above.<sup>2</sup> Rothstein<sup>4</sup> used planar laser-induced fluorescence (PLIF) to study transverse injection of hydrogen into a Mach 1.5 oxygen crossflow. A power law fit to the penetration data was proposed. The constants in the power law expression have been determined by numerous authors and are found to vary widely between studies.

In addition to the extent of jet penetration, the issue of jet/freestream mixing is of critical importance for hypersonic propulsion applications. This issue has been addressed by using a concentration probe and PLIF of iodine.<sup>1,5</sup> The results of the former study suggested that streamwise vortices generated at either side of the jet play an important role in the near-field mixing process. Time-averaged mole fraction images obtained from a complex staged injector flowfield<sup>5</sup> demonstrated rapid mixing in the region between the two injectors, while the mixing just downstream of the second injector appeared strongly influenced by streamwise vorticity. These vortices, which arise from vorticity in the boundary layer of the injectant fluid,<sup>6</sup> appear very prominently in incompressible transverse injection flowfields,<sup>7</sup> where both the temperature and velocity fields are significantly affected by their presence.

Structural organization within a flow can have direct implications on its mixing characteristics, as in the fully developed compressible shear layer.<sup>8,9</sup> Recent transverse jet studies made note of the large-scale structures that formed at the

interface between the freestream and injectant fluids.<sup>10,11</sup> These structures persisted until far downstream and appeared to occur on a somewhat regular basis. Two-dimensional acetone PLIF images taken of a subsonic jet injected into a subsonic crossflow revealed similar large-scale behavior.<sup>12</sup>

One drawback to transverse injection is the stagnation pressure loss due to the relatively strong bow shock present just ahead of the injector. This issue was addressed in two studies where the effects of injection at low transverse angles to the freestream were examined.<sup>13,14</sup> Reduced total pressure losses resulted due to the weaker bow shock produced. Results from Fuller et al.<sup>14</sup> indicate that for low angle injection ( $\theta = 30^\circ$  and  $\theta = 15^\circ$ ), an increase in injection angle (combined with fixed jet pressure-to-effective back pressure ratio) produces a faster mixing rate in the near field due to the increased disturbance felt by the freestream. However, in the far field, the peak injection concentrations of the two cases are nearly equal. Transverse and oblique mixing data have been compiled by Schetz et al.<sup>15</sup> and the results presented demonstrate similar conclusions, i.e., that increases in injection angle of oblique jets produce faster mixing in the near-field, larger total pressure losses due to increased disturbance effects, and no mixing advantage in the far field over the lower angle counterparts.

Studies of a small aspect ratio elliptical jet showed that the boundary-layer momentum thickness varied around the nozzle circumference leading to the development of asymmetric vortices at the exit plane.<sup>16,17</sup> In quiescent and coflowing environments, spreading rates in the minor-axis plane of the elliptical jet were faster than those associated with the major-axis plane. This eventually led to the minor-axis spread being larger than the major-axis spread (a phenomenon termed axis-switching). Further spreading enhancement occurs in under-expanded elliptical jets compared to those operated perfectly expanded (sonic) or subsonic.<sup>18</sup>

This investigation is a comparison of the near-field mixing and penetration characteristics of three basic injector geometries. Planar Mie scattering is used to study the flowfields created by jets issuing from circular transverse, circular oblique, and elliptical transverse injectors into a Mach 2 crossflow. Of specific interest are the transverse and lateral spread of the jet from each injector, and the instantaneous and time-averaged structural behavior of the jet/freestream interface. Examination of the jet's penetration, both transversely and laterally into the freestream, allows conclusions to be drawn concerning the effectiveness of the injection process and the effects of both injector geometry and orientation. Investigation of the jet/freestream interfacial structure will lead to qualitative interpretations of the mixing characteristics of each injector by revealing the large- and small-scale motions characteristic of each. Finally, this work will be used as a baseline for future, more exhaustive studies of the three injection flowfields.

## Experimental Facility

The experiments documented herein were performed in a newly constructed supersonic combustion research facility located at Wright-Patterson Air Force Base. The various components of this facility, as well as quantitative flow quality measurements, have been discussed in great detail elsewhere<sup>19</sup>; only a summary of the important features is included here.

### Flow Facility

The wind tunnel used in this investigation is shown schematically in Fig. 2. A series of compressors capable of producing a continuous 34-lbm/s flow of air at about 750 psig and ambient temperature supplied the facility. Additionally, an exhaust system evacuated the test section to approximately 3 psia before starting the tests.

A rearward-facing perforated cone, along with an array of mesh screens and a section of honeycomb, conditioned the

Table 1 Injector geometries

Injector	a, in.	b, in.	$A_{in}$ , in. <sup>2</sup>	$A_{ex}$ , in. <sup>2</sup>	$\epsilon$
1	0.125	0.125	0.049	0.049	0
2	0.483	0.125	0.049	0.190	0.97
3	0.246	0.064	0.049	0.049	0.97

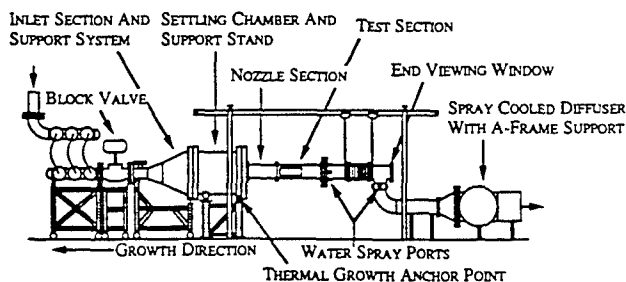


Fig. 2 Schematic of supersonic combustion tunnel.

air within the settling chamber. The cone spread the flow uniformly within the chamber while the screens and honeycomb served to reduce large-scale turbulence and straighten the flow before acceleration by the supersonic nozzle. Tunnel stagnation conditions were monitored by a Johnson-Yokogawa control system used for feedback and control of the various valves in the system.

The present investigation used a nozzle section designed with a method of characteristics code<sup>20</sup> to produce a nominally Mach 2 freestream. Results of a recent effort to characterize the tunnel indicated that the flow is uniform and two dimensional within the test section at a Mach number of about 1.98.<sup>19</sup> The cross-sectional dimensions of the constant area test section used in these studies were 5 in. by 6 in. A number of fused quartz windows, including a pair of side windows, a top window, and an end window, provided optical access to the flow. The resulting access to the flow allowed direct imaging of three orthogonal flow planes.

For the present study, injector geometries were incorporated into the removable test inserts housed within the bottom wall of the test section. Five streamwise positions were available for injector placement. For this study, all injectors were placed at the same streamwise location to ensure that the boundary-layer thickness approaching the injector would be the same for each case. At the chosen injector location, the boundary-layer thickness-to-effective jet diameter ratio is approximately  $\delta/d_{eff} = 1$ .

### Injectors

The three injector geometries designed for these experiments included 1) a circular jet issuing transversely,  $\theta = 90$  deg, 2) a circular jet issuing obliquely,  $\theta = 15$  deg, and 3) an elliptical jet issuing transversely,  $\theta = 90$  deg. To ensure a proper comparison among the three injectors, each had a cross-sectional area (i.e., area perpendicular to the jet axis) of 0.049 in.<sup>2</sup>. The orifice diameter of injector 1 was, therefore, 0.25 in. An additional constraint on injectors 2 and 3 was that the elliptical geometries at the nozzle exits be similar. Equating the eccentricities of the ellipses and the cross-sectional areas of the supply tubes allowed this constraint to be met. Table 1 presents the geometries of the injectors, where the eccentricity  $\epsilon$  is

$$\epsilon = \sqrt{1 - (b^2/a^2)} \quad (2)$$

and  $a$  and  $b$  are the semimajor and semiminor axes, respectively. Figure 3 illustrates the cross-sectional and plan views of the injector geometries. The resulting injectors have the same effective diameter ( $d_{eff} = 0.25$  in.), whereas the exit

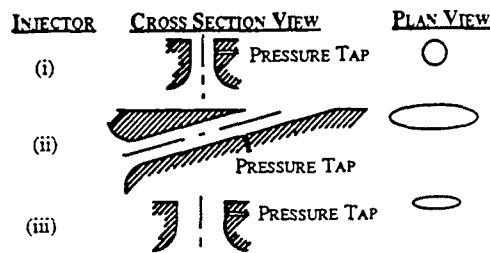


Fig. 3 Illustration of injector configurations used in the present study.

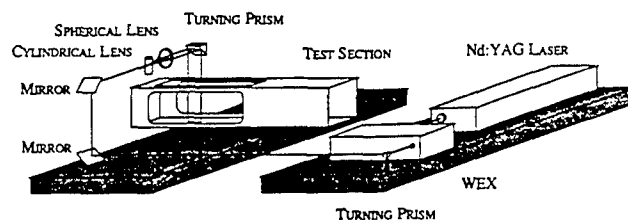


Fig. 4 Mie scattering optical arrangement.

area of the circular oblique injector differs from that of the other two.

Each injector was equipped with a pressure tap near the exit, as shown in Fig. 3, for static pressure measurements. A bank of Pressure Systems Incorporated pressure transducers controlled by a 386-PC acquired pressure data from the injectors. In addition to this, the jet stagnation temperature was measured just upstream of the entrance to each injector using a thermocouple that was monitored visually. Both readings allowed the operating conditions of the injectant flow to be set.

Dry carbon dioxide and helium served as injectant gases in these studies. The CO<sub>2</sub> was supplied to the injector using a manifold system of five bottles. A high mass flow hand regulator was used to set injectant pressures, and a 50-gal hot water bath and resistive heat tape heated the copper supply line. The energy supplied by the heaters maintained the jet stagnation temperature at roughly 540°R. Helium was supplied through a separate line using a 66,000-ft<sup>3</sup> trailer pressurized to 2000 psig. Helium pressures and temperatures were regulated with the same systems as for the carbon dioxide.

### Imaging System

A Spectra Physics Quanta-Ray DCR-4 Nd:YAG laser with an 8-ns pulse duration provided the laser beam used in these experiments. The laser pulsed at 10 Hz and a second harmonic generator frequency doubled the 1064-nm beam to 532 nm. This beam was again frequency doubled by a WEX system to produce UV light at 266 nm (approximately 90 mJ/pulse). A prism directed the beam from the laser table to the traversing table positioned beneath the test section. A pair of coated mirrors reflected the beam up and toward the test section at the desired elevation. Finally, a cylindrical/spherical lens system produced the thin laser sheet used for illuminating the desired flow plane. Figure 4 provides a schematic illustration of the laser system used in these experiments.

The unintensified CCD camera and image acquisition system used here were manufactured by Princeton Instruments. The camera was water cooled and purged with dry nitrogen to reduce dark count noise. A Nikon UV-Nikkor 105-mm f/4.5 telephoto lens was used for imaging the 266-nm Mie scattering from naturally occurring ice crystals in the free-stream, which provided a "scalar transport" seeding arrangement.<sup>8, 21</sup> Studies of condensation inside supersonic nozzles have shown that the ice crystals formed were nearly monodisperse with diameters between 0.003–0.014  $\mu$ m, depending on the humidity of the inlet air.<sup>22, 23</sup> Accurate particle response

Table 2 Image acquisition details

View	$J$	Injector	Injectant	Image plane location
Side	1, 2, 3	1, 2, 3	He, CO <sub>2</sub>	$z/d_{eff} = 0$
Top	3	1, 2, 3	He, CO <sub>2</sub>	$y/d_{eff} = 2$
End	3	1, 2, 3	He, CO <sub>2</sub>	$x/d_{eff} = 2.5$

for Mie scattering images requires a Stokes number, defined by

$$\text{Stokes number} = \frac{t_p}{t_\delta} = \frac{\text{particle response time}}{\text{large eddy rollover time}} \quad (3)$$

of less than about 0.5 (Ref. 24). The two time scales involved in determining the Stokes number are

$$t_p = (1 + 2.76 \cdot Kn) \frac{\rho_p d_p^2}{18\mu} \quad \text{and} \quad t_\delta = \frac{\delta}{\Delta U} \quad (4)$$

Using a conservative ice crystal diameter of  $0.02 \mu\text{m}$  and an average velocity difference between the jet and freestream fluids of  $400 \text{ m/s}$  yields a Stokes number of  $0.003$  for the present operating conditions, thereby indicating that the crystals easily follow the turbulent fluctuations within this flow-field. The resulting images were characterized by high intensity values in pure freestream regions and low intensities in regions of pure injectant. A Princeton Instruments pulse generator provided synchronization between the flash lamp of the laser and the camera, and the camera was gated to visualize one entire laser pulse. The  $384 \times 576$  pixel density of the CCD array, combined with the optical arrangement described, produced spatial resolutions of  $125 \mu\text{m}/\text{pixel}$  in the side view images,  $65 \mu\text{m}/\text{pixel}$  in the top view images, and  $460 \mu\text{m}/\text{pixel}$  in the end view images. Each 14-bit image was sent to a 486-PC for preliminary analysis, display, and storage. Side view images were collected at  $J = 1, 2$ , and  $3$  for each injector and both injectant gases. Top and end view images were collected for each injector and both gases at  $J = 3$ . Table 2 contains details concerning the various image plane locations used here.

Further analysis of the images was performed on the 486-PC and a Macintosh Quadra. Normalized averages were computed and corrected for reflections and nonuniformities in both the CCD array and laser sheet for each of the three image planes. To carry out the correction procedure, 10 background images (taken with no flow) for each case were averaged and the average was subtracted from each of 10 laser sheet profiles (taken with freestream flow only) and 10 instantaneous jet images. These corrected beam profiles and jet images were then averaged. The average beam profile was divided out of the average jet image and the resulting corrected jet image was then normalized by the maximum intensity within the image. This procedure was carried out for each flow condition. Other image processing was completed and is discussed below.

## Results and Discussion

Experimental conditions for the present study are listed in Table 3. Notice that the static pressure within the test section was held constant while jet operating conditions were adjusted to provide the desired jet-to-freestream momentum flux ratio. Global flowfield characteristics were visualized using the Mie scattering technique. Intensity contours defined in the various averaged images were used to provide quantitative information about the transverse and lateral penetration of the three injector geometries. In addition, analysis of the instantaneous images gave information about the structural behavior of the jet/freestream interface region and qualitative characteristics

Table 3 Experimental flow conditions ( $T_{0,f} = 560\text{--}580^\circ\text{R}$ )

$J$	Injectant	$M_j$	$M_f$	$p_f$ , psia	$p_j$ , -psia	$\gamma_j$
1	CO <sub>2</sub>	2.0	1.0	5.3	23.0	1.29
1	He	2.0	1.0	5.3	17.8	1.67
2	CO <sub>2</sub>	2.0	1.0	5.3	46.0	1.29
2	He	2.0	1.0	5.3	35.5	1.67
3	CO <sub>2</sub>	2.0	1.0	5.3	69.0	1.29
3	He	2.0	1.0	5.3	53.3	1.67

Fig. 5 Instantaneous side view image; elliptical, 90-deg injector, CO<sub>2</sub>.

of the near-field mixing. These results are addressed individually below.

### Global Flowfield Characteristics

Planar imaging techniques, such as the Mie scattering used here, result in two-dimensional images containing intensity information. Figure 5 shows a typical instantaneous side view image of a CO<sub>2</sub> jet formed using the elliptical transverse injector. The location of the injector appears at the bottom of the image. Freestream fluid, characterized by high signal (white), contained the ice crystals used for scattering. The jet fluid appears black/gray except within the barrel shock region. This apparent anomaly will be discussed below. The three-dimensional bow shock upstream of the injector is clearly visible in the figure. From shot-to-shot, the bow shock appeared to be stationary with no large fluctuations in position.

The interface between the jet and the freestream is especially interesting. The presence of large-scale structures is immediately apparent. The orientation of these structures, i.e., rolling up into the freestream fluid, implies that the jet fluid at the boundary moves with a higher velocity tangent to the interface than the freestream fluid. This tendency is clearly evident in studies of planar shear layers.<sup>8,9</sup> A final feature of the image in the figure is the appearance of the barrel shock and Mach disk within the underexpanded jet. These features are not visible in the cases where helium is used, and are most prominent in CO<sub>2</sub> images at high  $J$ . Based on models of the barrel shock/Mach disk region<sup>2,25</sup> and the thermodynamic characteristics of carbon dioxide,<sup>26</sup> it is thought that as the injectant accelerates into the freestream the CO<sub>2</sub> undergoes a phase change from gas to solid due to the drop in temperature and pressure. The frozen CO<sub>2</sub> is then able to scatter laser light and thus appears as white in the image. Signal is lost downstream of the Mach disk as the frozen carbon dioxide is sublimated due to the sudden compression (and increase in both temperature and pressure).

### Transverse and Lateral Penetration

Defining the extent of jet penetration requires an objective reference to judge different cases fairly. Since the freestream fluid contained the scattering medium, an average freestream intensity value from the region downstream of the bow shock provided this reference. The averaged side and end view images allowed a clear definition of the freestream region downstream of the bow shock making intensity averages from within this zone possible. However, the top view images were ob-



tained at locations too near the bottom wall so that no free-stream fluid behind the bow shock was available for referencing. Also, due to the confusion associated with the condensation of carbon dioxide, transverse and lateral penetration data only result from the side and end view images using helium as the injectant.

#### Transverse Penetration

Figures 6a–6c illustrate the results of analyzing the averaged side view images for jet penetration. The intensity of the jet boundary presented corresponds to 90% of the average freestream intensity behind the bow shock (i.e., outer edge of the jet). Each of the plots compares the performance of an individual injector configuration with increasing jet-to-freestream momentum flux ratio, using helium as the injectant. The injector locations are illustrated in the figures by the shaded boxes beneath the horizontal axes. Figure 6a compares the penetration profiles of the circular 90-deg injector for values of  $J$  ranging from 1 to 3. The plot provides evidence for the expected trend of increasing transverse penetration with increasing  $J$ . Peak transverse penetration in the high  $J$  case for the field of view provided by the laser sheet is about  $y/d_{eff} = 4.2$  at  $x/d_{eff} = 5.0$ . Further increases in transverse penetration are expected downstream of this location since the asymptotic value of  $y/d_{eff}$  for circular transverse injectors occurs near  $x/d_{eff} = 8$ .

The penetration profiles of the circular 15-deg injector are shown in Fig. 6b for values of  $J$  ranging from 1 to 3. The same trend of increasing jet penetration with increasing  $J$  is evident, although the extent of penetration is suppressed due to the smaller component of transverse momentum associated with the oblique injection geometry. A peak value of about  $y/d_{eff} = 2.4$  at  $x/d_{eff} = 5.0$  is found for  $J = 3$ . The slopes of the profiles at the downstream edge of the plot suggest, however,

that the jet has not reached its full extent of penetration. Notice that the exit geometry of this injector is such that the laser sheet only allows examination of one effective diameter downstream of the trailing edge of the exit.

Figure 6c presents the transverse penetration profiles obtained for the elliptical 90-deg injector. Again, the trend of deeper penetration into the freestream with increased  $J$  is clearly observed. A peak penetration value of  $y/d_{eff} = 4.0$  at  $x/d_{eff} = 4.5$  is observed for  $J = 3$ . This value is close to the peak penetration obtained from the circular 90-deg injector. The jet cross-sectional shape does not appear to impact the extent of transverse penetration of the two transversely oriented jets substantially under the current conditions.

Keffer and Baines<sup>27</sup> found that the penetration profile data obtained from a subsonic jet in crossflow collapsed to a single curve in the near injector region when the coordinate axes were scaled by  $J^{-1}$ . Figure 6d illustrates the results of such a scaling on the profiles obtained in the current investigation. Clearly, the profiles demonstrate a high degree of collapse. The resulting power law fit is of the form

$$(y/d_{eff} \cdot J) = 1.23(x/d_{eff} \cdot J)^{0.344} \quad (5)$$

The correlation coefficient obtained from this fit was over 98%. Figure 6e compares the results of this correlation (for a momentum flux ratio of 3) to others obtained from PLIF studies.<sup>4,28</sup> The plot demonstrates very good agreement at this value of  $J$ . Although not shown, similar agreement was found for the  $J = 2$  case while the present correlation fell below both referenced curves for  $J = 1$ . Figures 6d and 6e suggest that the present method for determining the jets' penetration profiles produces adequate results for comparison with other results found in the literature.

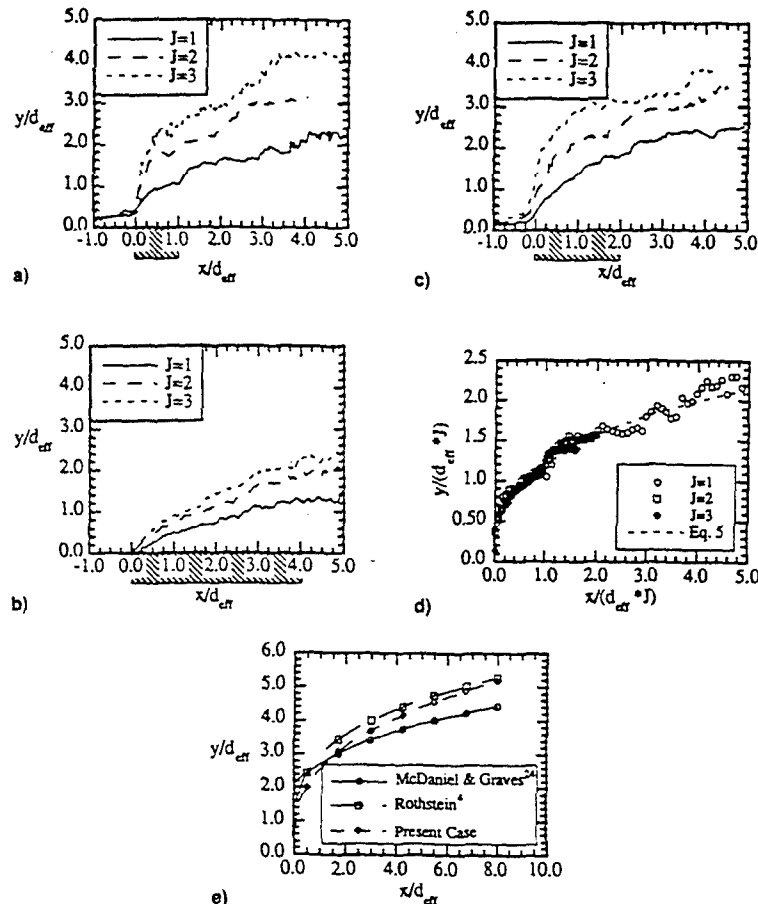


Fig. 6 Transverse jet penetration profiles: a) circular, 90-deg injector, He; b) circular, 15-deg injector, He; and c) elliptical, 90-deg injector, He. Collapse of transverse penetration profiles: d) circular, 90-deg injector, He and e) comparison of empirical correlations; circular, 90-deg injector,  $J = 3$ .

### Lateral Penetration

Contours taken from averaged end view images using helium as the injectant are presented in Figs. 7–9. As with the previously discussed side view penetration profiles, these contours correspond to intensity values equal to 90% of the averaged freestream intensity downstream of the bow shock. Shown in Fig. 7 are the two contours obtained using the circular 90-deg injector with the image planes located at  $x/d_{eff} = 2$  (Fig. 7a) and 5 (Fig. 7b). Figure 7a shows the lateral extent (i.e., extent in the  $z$  direction) covering roughly  $z/d_{eff} = 3.6$ . At the downstream location (Fig. 7b), the jet separates from the wall, and the lobes near the wall suggest the characteristic counter-rotating streamwise vortical structure present in the injectant. Further discussion of this feature is given in the following section. The lateral extent shown here is about  $z/d_{eff} = 3.4$ . Thus, the jet appears to contract laterally somewhat in the near-field region of this flowfield. The contours do exhibit transverse growth as expected.

Figures 8a and 8b illustrate the lateral and transverse spread of the obliquely oriented injector for the same streamwise image planes as Fig. 7. Again, due to the oblique geometry, transverse penetration is small for this injector compared to the previous contours for the 90-deg circular injector. Additionally, the lateral spread attributed to this injector is smaller in the near field compared to injector 1. Here, a lateral spread of about  $z/d_{eff} = 2.9$  is revealed. Figure 8b again illustrates the lobes that develop as the jet lifts from the wall, suggesting that streamwise-oriented counter-rotating structures are found in this flowfield also.

End view contours obtained for the elliptical 90-deg injector are shown in Figs. 9a and 9b. Immediately visible in the first plot is the fuller nature of the penetration contour than any of those previously discussed. Lateral penetration is roughly  $z/d_{eff} = 4.5$ . A slightly smaller extent (roughly  $z/d_{eff} = 4.2$ ) results from Fig. 9b, indicating again that the jet appears to contract laterally somewhat in the near field. The contour in Fig. 9b also suggests the same counter-rotating nature of the eddies on either side of the injector orifice as seen for the other injectors. An interesting note on the contours presented in Fig. 9 is that the elliptical orifice of injector 3 has about half the span of the circular orifice of injector 1 (see “b” of

Table 1), while its lateral penetration is 25% larger. This indicates that the flow leaving the elliptical 90-deg injector spreads very quickly (in the lateral direction) in the near field compared to the circular 90-deg injector, suggesting that the axis-switching phenomenon discussed above<sup>17</sup> may be preserved in this flowfield.

### Structural Behavior/Mixing

Select instantaneous images of the three views are shown in Figs. 10–12. All images presented are at  $J = 3$  with carbon dioxide or helium used as the injectant as indicated. Injector

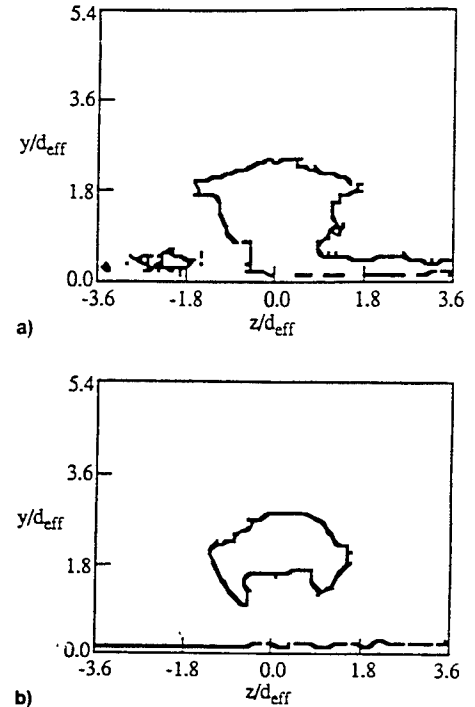


Fig. 8 Lateral penetration profiles: a) circular 15-deg injector at  $x/d_{eff} = 2$ , He at  $J = 3$  and b) circular 15-deg injector at  $x/d_{eff} = 5$ , He at  $J = 3$ .

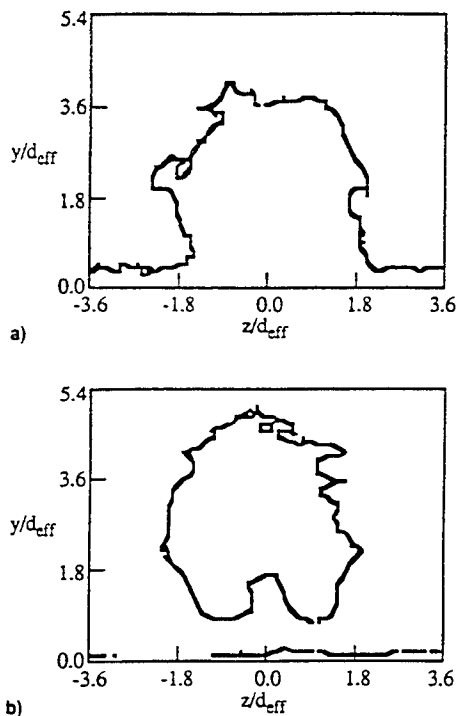


Fig. 7 Lateral penetration profiles: a) circular 90-deg injector at  $x/d_{eff} = 2$ , He at  $J = 3$  and b) circular 90-deg injector at  $x/d_{eff} = 5$ , He at  $J = 3$ .

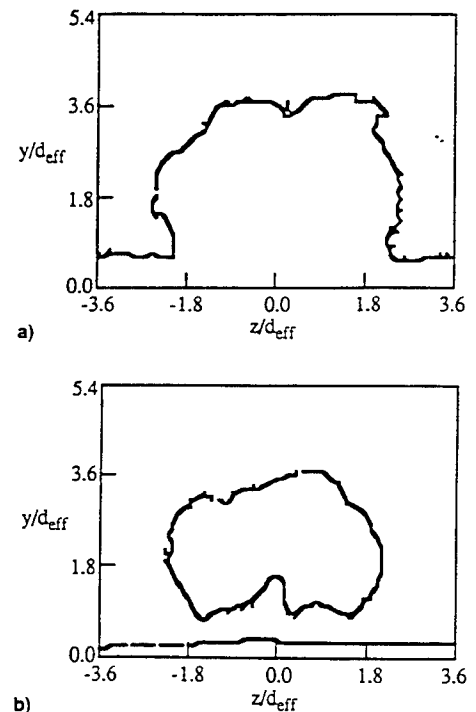


Fig. 9 Lateral penetration profiles: a) elliptical 90-deg injector at  $x/d_{eff} = 2$ , He at  $J = 3$  and b) elliptical 90-deg injector at  $x/d_{eff} = 5$ , He at  $J = 3$ .

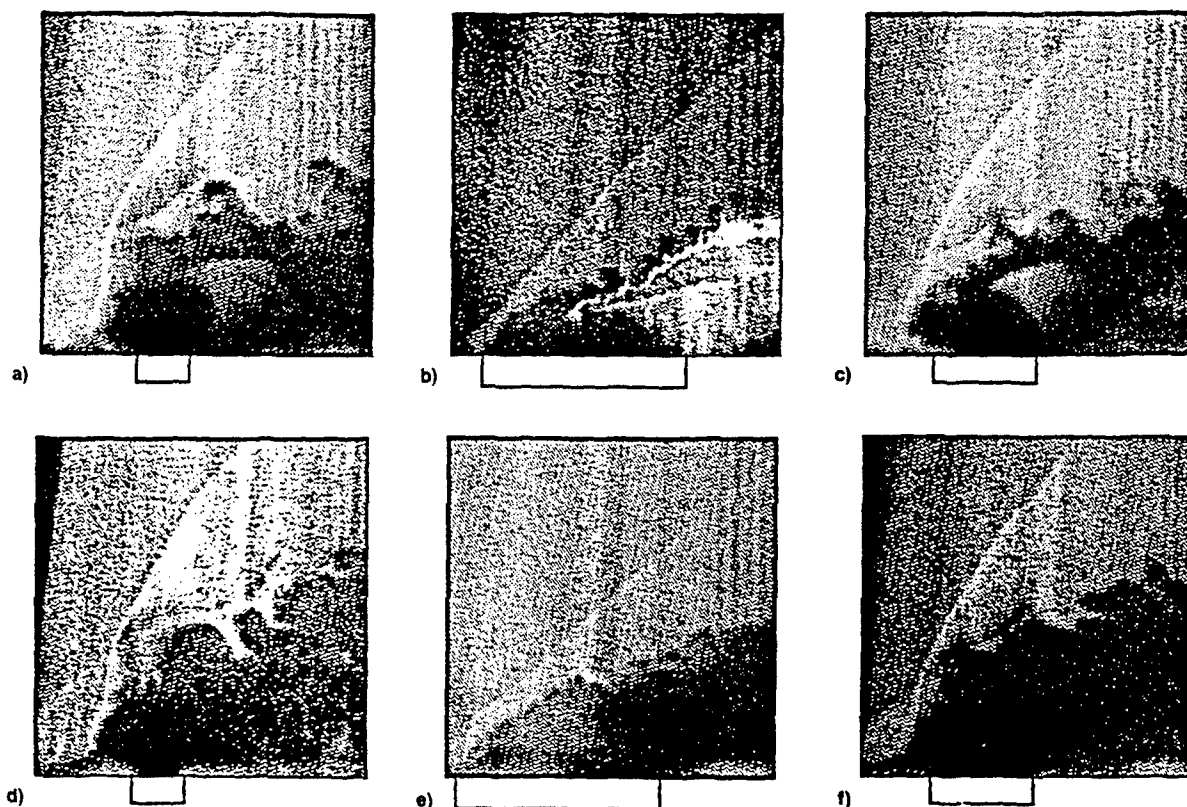


Fig. 10 Side view Mie scattering images at  $J = 3$ : a) circular 90-deg injector,  $\text{CO}_2$ ; b) circular 15-deg injector,  $\text{CO}_2$ ; c) elliptical 90-deg injector,  $\text{CO}_2$ ; d) circular 90-deg injector, He; e) circular 15-deg injector, He; and f) elliptical 90-deg injector, He.

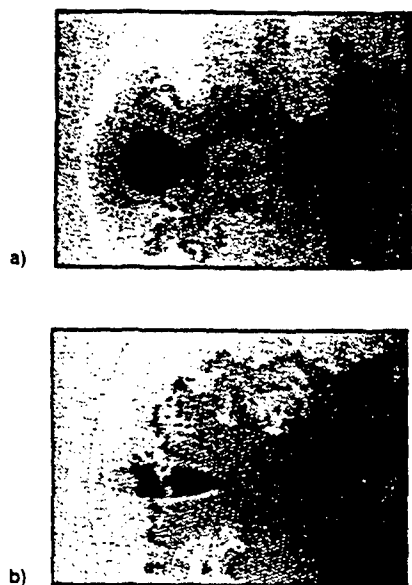


Fig. 11 Top view Mie scattering images at  $J = 3$ : a) circular 90-deg injector,  $\text{CO}_2$  and b) elliptical 90-deg injector,  $\text{CO}_2$ .

locations appear as rectangles at the bottom of each side and end view image. Flow is from left to right in Figs. 10 and 11, whereas the flow direction is out of the page in Fig. 12. As described for Fig. 5, the seeded freestream appears white while the unseeded jet appears black/gray, except where frozen carbon dioxide is present.

Side view images of the near field of the three injectant flowfields are presented in Fig. 10, where one image from the elliptical 90-deg injector is repeated from Fig. 5 for comparison. Each of the six images displays a region approximately 1.5 in. in the streamwise direction by 1.5 in. in the transverse direction. Large-scale structures appear prominently in the images of the circular 90-deg injection flowfield (Figs. 10a

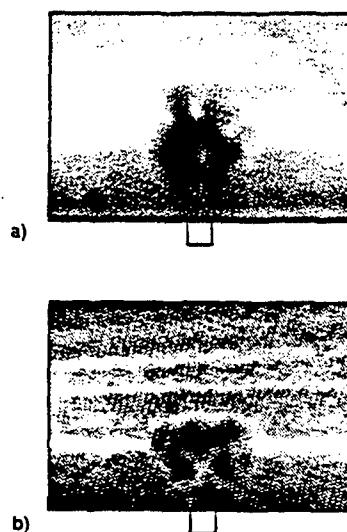


Fig. 12 End view Mie scattering images at  $J = 3$ : a) circular 90-deg injector; He at  $x/d_{inj} = 2$  and b) circular 15-deg injector; He at  $x/d_{inj} = 5$ .

and 10d). Two well-defined features are clearly present in the first image (carbon dioxide injection), and the birth of a third is suggested by the "clump" of fluid appearing just upstream of the middle structure. The vortices present in the helium injector flowfield (Fig. 10d) are nearly as well defined and appear comparable in size to those in Fig. 10a. Freestream fluid is entrained into the jet fluid in the region between the large structures as clearly evidenced in both images. In fact, the helium flowfield contains several "finger-like" intrusions of freestream fluid into the injectant. Small-scale structures are visible throughout the braid regions between the large-scale vortices. Also visible in these images is the separation shock upstream of the injector where boundary-layer separation occurs.

Figures 10b and 10e illustrate the instantaneous flowfield created by the circular 15-deg injector fed with  $\text{CO}_2$  and helium, respectively. Immediately apparent in both images is the lack of large-scale protrusions of jet fluid into the freestream as were seen for the circular, transverse injector. Small-scale eddies appear to dominate the interfacial structure in the near field, and freestream fluid does not penetrate into the jet region as dramatically as for the transverse injector. However, an interesting feature common to both of these images is the bow shock. Figures 10a and 10d display rather strong waves as suggested by the near normal shock behavior near the injector wall. In contrast, the waves found in the oblique flowfield are substantially weaker; the disturbances behave almost entirely as oblique waves. Smaller total pressure losses are therefore expected in the oblique injection flowfield than in the transverse injection flowfield, and the Mach number behind the oblique wave will be greater than that associated with the near normal wave in Figs. 10a and 10d. This may affect the mixing that occurs in the interfacial region, depending on the expansion characteristics of the oblique jet, since the mixing layer formed between the jet and freestream is strongly affected by the respective Mach numbers of each stream.<sup>8,9</sup>

The instantaneous elliptical injector flowfield, shown in Figs. 10c and 10f, has characteristics similar to Figs. 10a and 10d, in that large turbulent structures are again very prominent. Once again, freestream fluid appears to be entrained into the jet fluid at a faster rate than for the oblique case (in its near field) due to these large eddies. As in the circular 90-deg flowfield, finger-like intrusions of freestream fluid appear in the helium image, and small-scale eddies grow throughout the braiding regions between large structures in the carbon dioxide case. The bow shocks in these images also behave in a similar manner to the strong waves in Figs. 10a and 10d. A final feature of interest in Fig. 10c is the inclination of the barrel shock region with respect to the horizontal. Compared to Fig. 10a, the barrel shock for the elliptical injector is oriented at a steeper angle. This is thought to be indicative of the reduced orifice dimension in the spanwise direction of the elliptical geometry.

Figures 11a and 11b illustrate top views of the circular and elliptical transverse injectors, respectively. Each image covers approximately 1.4 in. in the streamwise direction and 1 in. in the spanwise direction. The oblique injector has been omitted since the field of view offered little information in this case. Figure 11a shows the injector location, the projection of the bow shock at the laser sheet elevation, and the cross section of the jet. The high-intensity region just downstream of the jet orifice is a cross section of the barrel shock region made visible by the frozen carbon dioxide particles present. Large protrusions of jet fluid into the freestream are clearly visible in this image, and a variety of both large- and small-scale structures appear all along the interface. Several features suggesting mushroom-shaped counter-rotating pairs of vortices are noted.

The image shown in Fig. 11b demonstrates the dramatic nature of the elliptical injector flowfield. The jet spreads very quickly in the lateral direction near the exit compared to the previous figure. This trend of rapid lateral spreading within the elliptical injector flowfield is also suggested by the averaged results presented above. Large quantities of freestream fluid are engulfed by the vortices, as evidenced by the white regions just downstream of the injector. Smaller scale mushroom-shaped structures, indicating the presence of counter-rotating vortical pairs, are also present.

Instantaneous end view images of the flowfields created by the transverse and oblique circular injectors are presented in Fig. 12. Approximate spatial dimensions of each image are 2.9 in. in the spanwise direction and 1.9 in. in the transverse direction. Figure 12a shows the streamwise plane at  $x/d_{\text{exit}} = 2$ , whereas Fig. 12b is taken at  $x/d_{\text{exit}} = 5$ . Counter-rotating

vortices oriented in the streamwise direction (out of the page) are very prominent features of each image. Additionally, Fig. 12a shows finger-like structures that burst outward into the freestream around the periphery of the jet/freestream interface. These structures are thought to be cross sections of the vortices noticed in the side view images of Fig. 10d. No such structures are apparent in Fig. 12b; this is consistent with the side view image of this flowfield in that large-scale eddies are not found. These end views give insight into the role that the streamwise vortices play in the engulfment of freestream fluid. Clearly, as the pair roll toward each other, freestream fluid fills the region in between and is essentially swallowed into the jet where the small-scale turbulence then takes over the mixing process.

### Summary and Conclusions

This investigation into the penetration and mixing associated with three injector geometries produced two-dimensional images yielding global injector flowfield characteristics, details of the transverse and lateral spread of the jets, and qualitative information concerning the structural organization and mixing. Condensed ice crystals in the freestream provided the sites for the Mie scattering technique used. This seeding arrangement, due to the small crystal sizes, provided clear identification of the jet/freestream interface in each of the three visualized flow planes. It should be emphasized that since the present seeding technique is not truly "passive" in nature (due to its dependence on the local thermodynamic conditions), no quantitative mixing interpretations can be made from these images.

A stationary three-dimensional bow shock created by the presence of the injectant fluid is clearly observed in all of the images. Also evident in the images obtained from the transverse injector flowfields using carbon dioxide as the injectant are the barrel shock region and Mach disk of the underexpanded jet. Orientations of the large-scale structures in the two transverse cases indicate that the freestream fluid is moving with a lower velocity tangent to the interface than the injectant fluid.

Increases in jet-to-freestream momentum flux ratio result in increased jet penetration into the freestream for all injectors studied. Injector exit geometry does not substantially affect the transverse penetration of the jet in the near field, while the orientation of the injector with respect to the freestream (i.e., transverse vs oblique) has dramatic effects. Averaged images show that the lateral spreading of the elliptical transverse injector is roughly 25% greater in the near field than the lateral spread associated with the circular transverse injector, indicating that the axis-switching phenomenon noted in previous studies of elliptical jets issuing into quiescent or coflowing environments may be preserved in this flowfield. Injector orientation plays an important role in the strength of the bow shock, with the shocks created by the oblique injector being substantially weaker than those created by the transverse injectors. This translates into a smaller expected total pressure loss in the oblique injector flowfield.

Instantaneous images of the three flow planes show a highly complicated, three-dimensional injection flowfield. Side views illustrate the large-scale eddies present along the jet/freestream interface in the flowfields created by the transverse injectors. These eddies result from both the interfacial strain produced as the jet is rapidly turned downstream and the vorticity present within the jet's boundary layer. They are thought to be the principal contributors to near-field mixing between the injectant and freestream fluids. Small-scale vortices develop in the braiding regions between the large eddies. In the oblique injector flowfield, no large-scale vortices develop along the interface in the near-field region. This is consistent with previous work that indicates that the oblique injector mixes slowly in the near field relative to transverse injectors. Top views of the transverse injector flowfields show

large-scale vortices extending appreciably into the freestream and aiding in mixing the freestream and injectant fluids. Finally, end views illustrate the counter-rotating streamwise vortices generated as the jet exits into the freestream. These structures contribute largely to freestream engulfment by the jet and are present in each flowfield studied. Two dominant types of large-scale motions are thus identified within the near injector regions of transverse injection flowfields: streamwise-oriented counter-rotating vortical pairs and vortices developing at the jet/freestream interface orienting themselves tangent to the interface.

### Acknowledgments

The authors would like to acknowledge the contributions of J. Donbar, D. Schommer, C. Smith, and D. Glawe. The long, odd hours required for these experiments were above and beyond the call. Also, support of the air facility personnel and machinists of Building 18 was greatly appreciated.

### References

- <sup>1</sup>Zukoski, E. E., and Spaid, F. W., "Secondary Injection of Gases into a Supersonic Flow," *AIAA Journal*, Vol. 2, No. 10, 1964, pp. 1689-1696.
- <sup>2</sup>Schetz, J. A., and Billig, F. S., "Penetration of Gaseous Jets Injected into a Supersonic Stream," *Journal of Spacecraft and Rockets*, Vol. 3, No. 11, 1966, pp. 1658-1665.
- <sup>3</sup>Papamoschou, D., and Hubbard, D. G., "Visual Observations of Supersonic Transverse Jets," *Experiments in Fluids*, Vol. 14, 1993, pp. 468-476.
- <sup>4</sup>Rothstein, A. D., "A Study of Normal Injection of Hydrogen into a Heated Supersonic Flow Using Planar Laser-Induced Fluorescence," Los Alamos National Lab., LA-12287-T, Los Alamos, NM, 1992.
- <sup>5</sup>Hollo, S. D., McDaniel, J. C., and Hartfield, R. J., "Characterization of Supersonic Mixing in a Nonreacting Mach 2 Combustor," *AIAA Paper 92-0093*, Jan. 1992.
- <sup>6</sup>Fric, T. F., and Roshko, A., "Structure in the Near Field of the Transverse Jet," *Seventh International Symposium on Turbulent Shear Flows*, Stanford Univ., Stanford, CA, 1989, pp. 225-237.
- <sup>7</sup>Kamotani, Y., and Greber, I., "Experiments on a Turbulent Jet in a Cross Flow," *AIAA Journal*, Vol. 10, No. 11, 1972, pp. 1425-1429.
- <sup>8</sup>Messersmith, N. L., and Dutton, J. C., "An Experimental Investigation of Organized Structure and Mixing in Compressible Turbulent Free Shear Layers," Univ. of Illinois at Urbana-Champaign, UILU-ENG-92-4002, Urbana, IL, 1992.
- <sup>9</sup>Clemens, N. T., and Mungal, M. G., "Two- and Three-Dimensional Effects in the Supersonic Mixing Layer," *AIAA Journal*, Vol. 30, No. 4, 1992, pp. 973-981.
- <sup>10</sup>Hermanson, J. C., and Winter, M., "Mie Scattering Imaging of a Transverse, Sonic Jet in Supersonic Flow," *AIAA Journal*, Vol. 31, No. 1, 1993, pp. 129-132.
- <sup>11</sup>Lee, M. P., McMillin, B. K., Palmer, J. L., and Hanson, R. K., "Planar Fluorescence Imaging of a Transverse Jet in a Supersonic Crossflow," *Journal of Propulsion and Power*, Vol. 8, No. 4, 1992, pp. 729-735.
- <sup>12</sup>Smith, S. H., Lozano, A., Mungal, M. G., and Hanson, R. K., "Scalar Mixing in the Subsonic Jet in Crossflow," *AGARD Computational and Experimental Assessment of Jets in Cross Flow*, Winchester, England, UK, 1993, pp. 6.1-6.13.
- <sup>13</sup>Mays, R. B., Thomas, R. H., and Schetz, J. A., "Low Angle Injection into a Supersonic Flow," *AIAA Paper 89-2461*, July 1989.
- <sup>14</sup>Fuller, E. J., Mays, R. B., Thomas, R. H., and Schetz, J. A., "Mixing Studies of Helium in Air at High Supersonic Speeds," *AIAA Journal*, Vol. 30, No. 9, 1992, pp. 2234-2243.
- <sup>15</sup>Schetz, J. A., Thomas, R. H., and Billig, F. S., "Mixing of Transverse Jets and Wall Jets in Supersonic Flow," *IUTAM Symposium on Separated Flows and Jets*, Novosibirsk, USSR, 1990, pp. 807-837.
- <sup>16</sup>Ho, C., and Gutmark, E., "Vortex Induction and Mass Entrainment in a Small-Aspect-Ratio Elliptic Jet," *Journal of Fluid Mechanics*, Vol. 179, 1987, pp. 383-405.
- <sup>17</sup>Schadow, K. C., Gutmark, E., Koshigoe, S., and Wilson, K. J., "Combustion-Related Shear-Flow Dynamics in Elliptic Supersonic Jets," *AIAA Journal*, Vol. 27, No. 10, 1989, pp. 1347-1353.
- <sup>18</sup>Gutmark, E., Schadow, K. C., and Wilson, K. J., "Noncircular Jet Dynamics in Supersonic Combustion," *AIAA Paper 87-1878*, June 1987.
- <sup>19</sup>Gruber, M. R., and Nejad, A. S., "Development of a Large-Scale Supersonic Combustion Research Facility," *AIAA Paper 94-0544*, Jan. 1994.
- <sup>20</sup>Carroll, B. F., Dutton, J. C., and Addy, A. L., "NOZCS2: A Computer Program for the Design of Continuous Slope Supersonic Nozzles," Univ. of Illinois at Urbana-Champaign, UILU ENG 86-4007, Urbana, IL, 1986.
- <sup>21</sup>Clemens, N. T., and Mungal, M. G., "A Planar Mie Scattering Technique for Visualizing Supersonic Mixing Flows," *Experiments in Fluids*, Vol. 11, 1991, pp. 175-185.
- <sup>22</sup>Wegener, P. P., and Pouring, A. A., "Experiments on Condensation of Water Vapor by Homogeneous Nucleation in Nozzles," *Physics of Fluids*, Vol. 7, No. 3, 1964, pp. 352-361.
- <sup>23</sup>Wegener, P. P., and Parlange, J. Y., "Non-Equilibrium Nozzle Flow with Condensation," *AGARD Recent Advances in Aerothermochemistry*, Oslo, Norway, 1967, pp. 607-634.
- <sup>24</sup>Samimy, M., and Lele, S. K., "Motion of Particles with Inertia in a Compressible Free Shear Layer," *Physics of Fluids A*, Vol. 3, No. 8, 1991, pp. 1915-1923.
- <sup>25</sup>Adamson, T. C., and Nicholls, J. A., "On the Structure of Jets from Highly Underexpanded Nozzles into Still Air," *Journal of the Aero/Space Sciences*, Vol. 26, 1959, pp. 16-24.
- <sup>26</sup>Reynolds, W. C., "Thermodynamic Properties in SI: Graphs, Tables, and Computational Equations for 40 Substances," Dept. of Mechanical Engineering, Stanford Univ., Stanford, CA, 1979.
- <sup>27</sup>Keffer, J. F., and Baines, W. D., "The Round Turbulent Jet in a Cross-Wind," *Journal of Fluid Mechanics*, Vol. 15, 1963, pp. 481-496.
- <sup>28</sup>McDaniel, J. C., and Graves, J., "Laser-Induced Fluorescence Visualization of Transverse Gaseous Injection in a Nonreacting Supersonic Combustor," *Journal of Propulsion and Power*, Vol. 4, No. 6, 1988, pp. 591-597.

# OBSERVATIONS OF THE BOW SHOCK-JET INTERACTION IN COMPRESSIBLE TRANSVERSE INJECTION FLOWFIELDS

M. R. Gruber\* and A. S. Nejad†  
Wright Laboratory, WL/POPT, Wright-Patterson AFB, Ohio 45433

T. H. Chen‡  
Taitech, Inc., Beavercreek, Ohio 45440

J. C. Dutton§  
University of Illinois at Urbana-Champaign, Urbana, Illinois 61801

## Introduction

Transverse injection of a gaseous fuel stream into a supersonic flow appears schematically in Fig. 1. This sketch illustrates the features of the flowfield in a plane through the spanwise jet centerline, where a three-dimensional bow shock forms ahead of the jet and interacts with the approaching turbulent boundary layer resulting in separation. Previous investigations of this flowfield have provided clear visualizations of the large-scale vortices formed at the interface between the freestream and injectant fluids.<sup>1-3</sup> These eddies influenced the position of the bow shock.<sup>2</sup> Some images also showed the region enclosed by the separation shock where the bow shock and turbulent boundary layer interact.<sup>1,2</sup> This region contains locally high wall static pressures as found in both experiments<sup>4</sup> and numerical predictions.<sup>5</sup> Numerical investigations of a reacting transverse hydrogen jet in a supersonic air stream by Takahashi and Hayashi<sup>6</sup> showed relatively high static temperatures occurring within this separated zone. Erosion of the injector wall could occur due to this local high temperature zone.

The objective of the present work is to investigate the interaction between the upstream shock structure and the interfacial eddies in the jet fluid. The influence of injector geometry on the separation shock is also of interest. Both issues are addressed using a planar laser-based visualization technique to capture instantaneous images of the interaction created by circular and elliptical injectors fueled with air. Details regarding the facility and imaging technique used are available elsewhere.<sup>7,8</sup> Table 1 shows geometric features of the two injectors studied.

---

\* Aerospace Engineer, Advanced Propulsion Division, Member AIAA.

† Senior Research Engineer, Advanced Propulsion Division.

‡ Senior Research Scientist, Senior Member AIAA.

§ Professor, Department of Mechanical and Industrial Engineering, Associate Fellow AIAA.

## Results and Discussion

The freestream conditions were set such that  $M_\infty = 1.98$ ,  $p_{o,\infty} = 317$  kPa, and  $T_{o,\infty} = 300$ -302 K. Jet flow conditions were set so that the jet-to-freestream momentum flux ratio ( $J$ ),

$$J = \left( \rho u^2 \right)_j / \left( \rho u^2 \right)_\infty = \left( \gamma p M^2 \right)_j / \left( \gamma p M^2 \right)_\infty, \quad (1)$$

was identical in each case ( $J = 2.90$ ). This parameter controls jet penetration into the crossflow.<sup>1,9</sup> Images were obtained for both circular and elliptical injection using air, cases C1A and E1A with the major-axis of the ellipse aligned with the freestream flow.

Instantaneous images from cases C1A and E1A appear in Figs. 2 and 3, respectively. Freestream fluid (light) flows from left to right and the jet fluid (dark) enters from the lower edge (jets are centered at  $x/d_{eff} = 0$ ). All of the images presented show some boundary layer fluid along the lower edge as it enters the region beneath the separation shock wave. Several other features can be easily observed including the bow shock standoff distance (i.e., the distance upstream of the injector leading edge where the bow shock intersects the lower edge of the image) and the streamwise ( $x$ ) and transverse ( $y$ ) dimensions of the upstream separation shock wave.

In Fig. 2 (Case C1A), the bow shock's behavior below the point of intersection with the separation shock appears strongly influenced by the structures formed after the jet fluid enters the crossflow. Instantaneous visualizations in which large eddies do not appear near the wall show the bow shock being essentially normal to the wall. In contrast, the second image of Fig. 2 contains an eddy at roughly  $y/d_{eff} = 1$ . In response to this feature, the bow shock curves sharply upstream increasing its distance from the injector centerline. Another interesting occurrence is shown in the third image where the shock apparently lifts higher off the wall allowing the boundary layer and jet fluids to mix subsonically upstream of the jet exit. This periodic lifting, caused when the approaching boundary layer is relatively thick and the sonic line occurs at a higher elevation off the wall, probably exacerbates the hot-spot phenomenon associated with reacting injection flowfields since fuel propagates farther upstream. Despite the dynamic nature of the bow shock's behavior below the intersection with the separation shock, a standoff distance of about  $0.5d_{eff}$  consistently occurs. Above the intersection point,

fluctuations in the bow shock's position also occur, although no dramatic curvature changes appear. In all the images obtained from case C1A, the bow shock intersected the top edge of the image,  $y/d_{\text{eff}} = 3.5$ , between  $-0.50 \leq x/d_{\text{eff}} \leq 0$ .

The region between the bow and separation shocks is an important feature in transverse injection flowfields in relation to its flame-holding capability in combustoring situations. At the spanwise centerline of the jet/crossflow interaction, two points describe the extent of the separation shock. The first point is upstream of the injector where the separation shock intersects the bottom edge of the image. The second point is the intersection of the bow and separation shocks that defines the highest transverse elevation of this region. In the ensemble of images collected for case C1A, the position of the first point falls between  $-3.0 \leq x/d_{\text{eff}} \leq -2.25$ , while the location of the second point varies from about 1.6 to 2.8 effective diameters above the bottom wall.

Figure 3 shows the instantaneous images obtained from case E1A. Large-scale eddies formed at the edge of the jet near the injector wall influence the behavior of the bow shock below the point of intersection with the separation shock in case E1A, though not to the degree that was observed in Fig. 2. The images in Fig. 3 give some evidence of the curvature changes induced by the eddies. Also, the third image shows the shock lifting phenomenon that appeared in case C1A. The bow shock standoff distance is approximately  $0.25d_{\text{eff}}$  (50% closer to the injector leading edge than for case C1A). This smaller standoff distance is explained by the asymmetric vortex development associated with the elliptical injector geometry leading to more rapid spreading in the minor-axis direction than in the major-axis direction.<sup>10</sup> Apparently, the jet fluid expands more in the spanwise direction ( $z$ ) than in the streamwise direction ( $x$ ) at the exit plane of the elliptical nozzle allowing the shock to stand closer to the jet exit and still accomplish the necessary pressure correction. In the region above the point of intersection of the bow and separation shocks, small fluctuations in the bow shock's position occur. However, the images shown in Fig. 3 indicate a weaker bow shock in case E1A than in case C1A as inferred by its slope. The ensemble of images obtained for case E1A indicates that the bow shock intersects the upper edge of the image at streamwise positions between  $-0.25 \leq x/d_{\text{eff}} \leq 0$ . Thus, in addition to being weaker than the wave in case C1A, the bow shock in case E1A fluctuates over a smaller spatial range.



The upstream extent of the separation shock in case E1A falls between  $-2.75 \leq x/d_{\text{eff}} \leq -1.75$ , while the point of intersection of the bow and separation shocks is between 1.1 and 2.1 effective diameters above the bottom wall. These values are significantly lower than those obtained from case C1A; thus the area beneath the separation shock associated with the elliptical injector is smaller than in circular injection at the spanwise centerline of the jet/crossflow interaction. Therefore, injection through the elliptical nozzle potentially reduces any hot-spot phenomenon associated with injection through a circular nozzle oriented perpendicular to the supersonic freestream.

### Conclusions

In flowfields created by transverse injection into supersonic crossflows, the bow and separation shocks formed upstream of the injectant plume are dominant features. In the present investigation, the interaction between these features and the large-scale eddies that develop at the jet/freestream interface has been examined. Results indicate that the large structures strongly influence the near-wall behavior of the bow shock, often resulting in severe curvature changes and positional fluctuations. The eddies exert a weaker influence on the bow shock further away from the wall. Lifting of the bow shock has been observed when the approaching boundary layer is relatively thick. In these instances, injectant and freestream fluid mix subsonically upstream of the injector orifice, thereby exacerbating the hot-spot phenomenon found in reacting transverse injection flowfields. Finally, the injector geometry strongly affected the upstream separation zone, the bow shock standoff distance, and the strength of the bow shock. Elliptical injection with the major-axis aligned with the freestream flow resulted in a smaller separation zone and standoff distance, and a weaker bow shock compared to circular injection.

### References

- <sup>1</sup>Gruber, M.R., Nejad, A.S., Chen, T.H., and Dutton, J.C., "Mixing and Penetration Studies of Sonic Jets in a Mach 2 Freestream," *Journal of Propulsion and Power*, Vol. 11, No. 2, 1995, pp. 315-323.
- <sup>2</sup>Gruber, M.R., Nejad, A.S., and Dutton, J.C., "Circular and Elliptical Transverse Injection into a Supersonic Crossflow--The Role of Large-Scale Structures," AIAA Paper 95-2150, June 1995.

<sup>3</sup>VanLerberghe, W.M., "Large-Scale Structure and Mixing in a Sonic Transverse Jet Injected into a Supersonic Crossflow," Ph.D. Thesis, Department of Mechanical and Industrial Engineering, University of Illinois at Urbana-Champaign, Urbana, IL, 1995.

<sup>4</sup>Everett, D.E., Dutton, J.C., and Morris, M.J., "Pressure-Sensitive Paint Measurements of the Pressure Field About a Sonic Jet Injected Transversely into a Mach 1.6 Freestream," AIAA Paper 95-0524, January 1995.

<sup>5</sup>Dhinakaran, R., and Bose, T.K., "Two-Dimensional Jet Interaction Flowfield Predictions with an Algebraic Turbulence Model," AIAA Paper 95-2242, June 1995.

<sup>6</sup>Takahashi, M., and Hayashi, A.K., "Numerical Study on Mixing and Combustion of Injecting Hydrogen Jet in a Supersonic Air Flow," AIAA Paper 91-0574, January 1991.

<sup>7</sup>Gruber, M.R., and Nejad, A.S., "New Supersonic Combustion Research Facility," *Journal of Propulsion and Power*, Vol. 11, No. 5, 1995, pp. 1080-1083.

<sup>8</sup>Gruber, M.R., "An Experimental Investigation of Transverse Injection from Circular and Elliptical Nozzles into a Supersonic Crossflow," Ph.D. Thesis, Department of Mechanical and Industrial Engineering, University of Illinois at Urbana-Champaign, Urbana, IL, 1996.

<sup>9</sup>Papamoschou, D., and Hubbard, D.G., "Visual Observations of Supersonic Transverse Jets," *Experiments in Fluids*, Vol. 14, 1993, pp. 468-476.

<sup>10</sup>Ho, C., and Gutmark, E., "Vortex Induction and Mass Entrainment in a Small-Aspect-Ratio Elliptic Jet," *Journal of Fluid Mechanics*, Vol. 179, 1987, pp. 383-405.

**Table 1** Injector Geometries

Injector	Semi-Major Axis a (mm)	Semi-Minor Axis b (mm)	Effective Diameter d <sub>eff</sub> (mm)	Eccentricity $\epsilon$
Circular (Case C1A)	3.18	3.18	6.35	0
Elliptical (Case E1A)	6.25	1.63	6.35	0.97

### Figure Captions

- Figure 1** Transverse Injection Flowfield Schematic
- Figure 2** Instantaneous Images of Circular Injection Using Air (Case C1A)
- Figure 3** Instantaneous Images of Elliptical Injection Using Air (Case E1A)

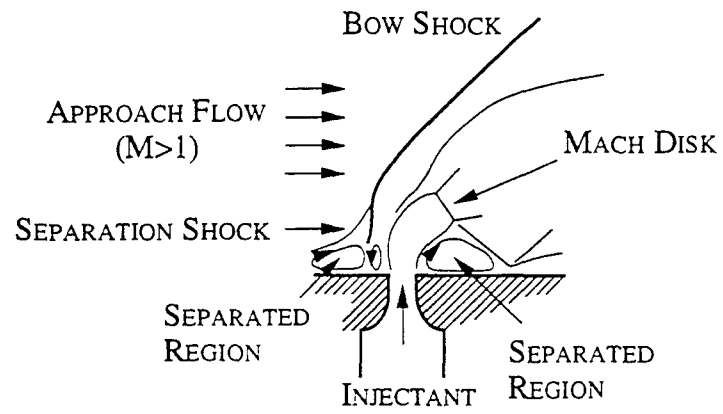


**Figure 1** Transverse Injection Flowfield Schematic

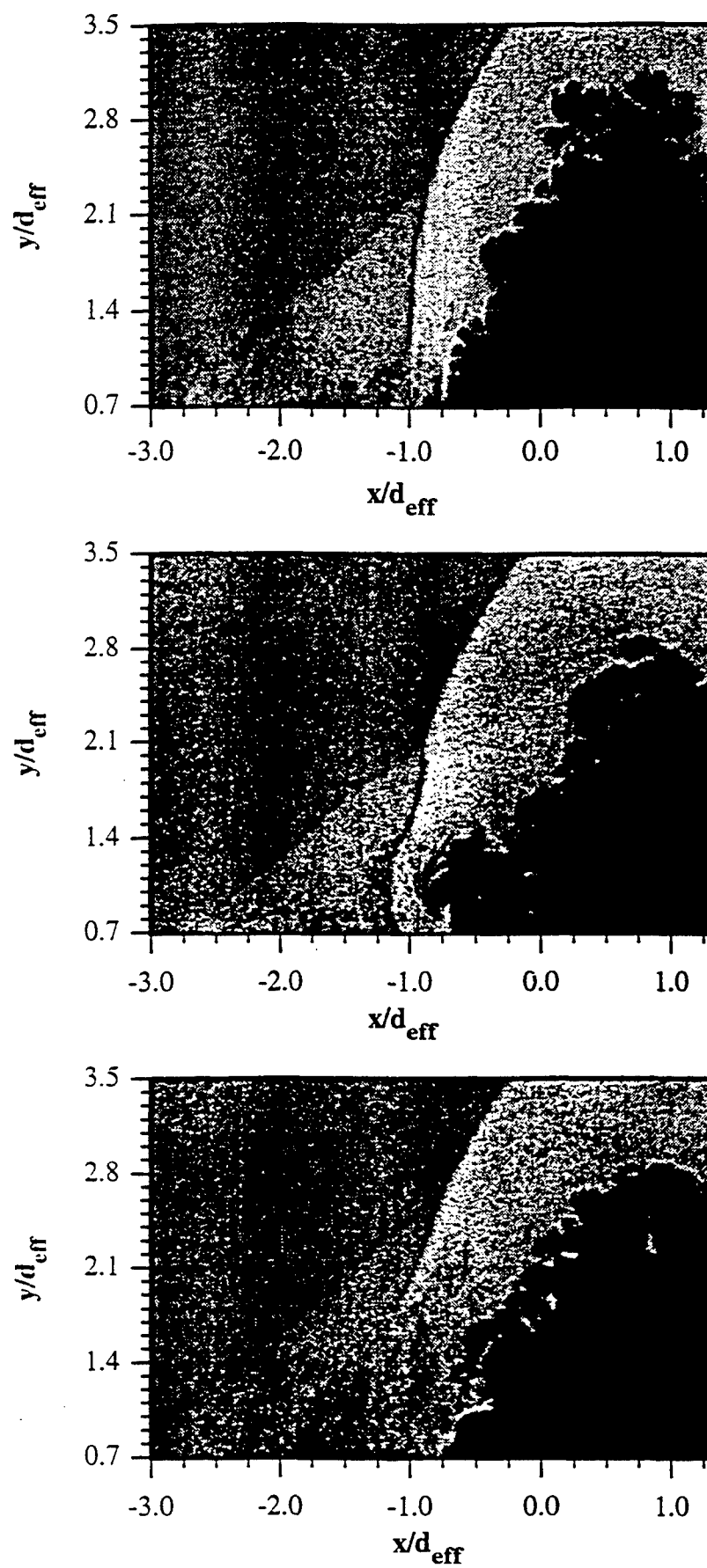
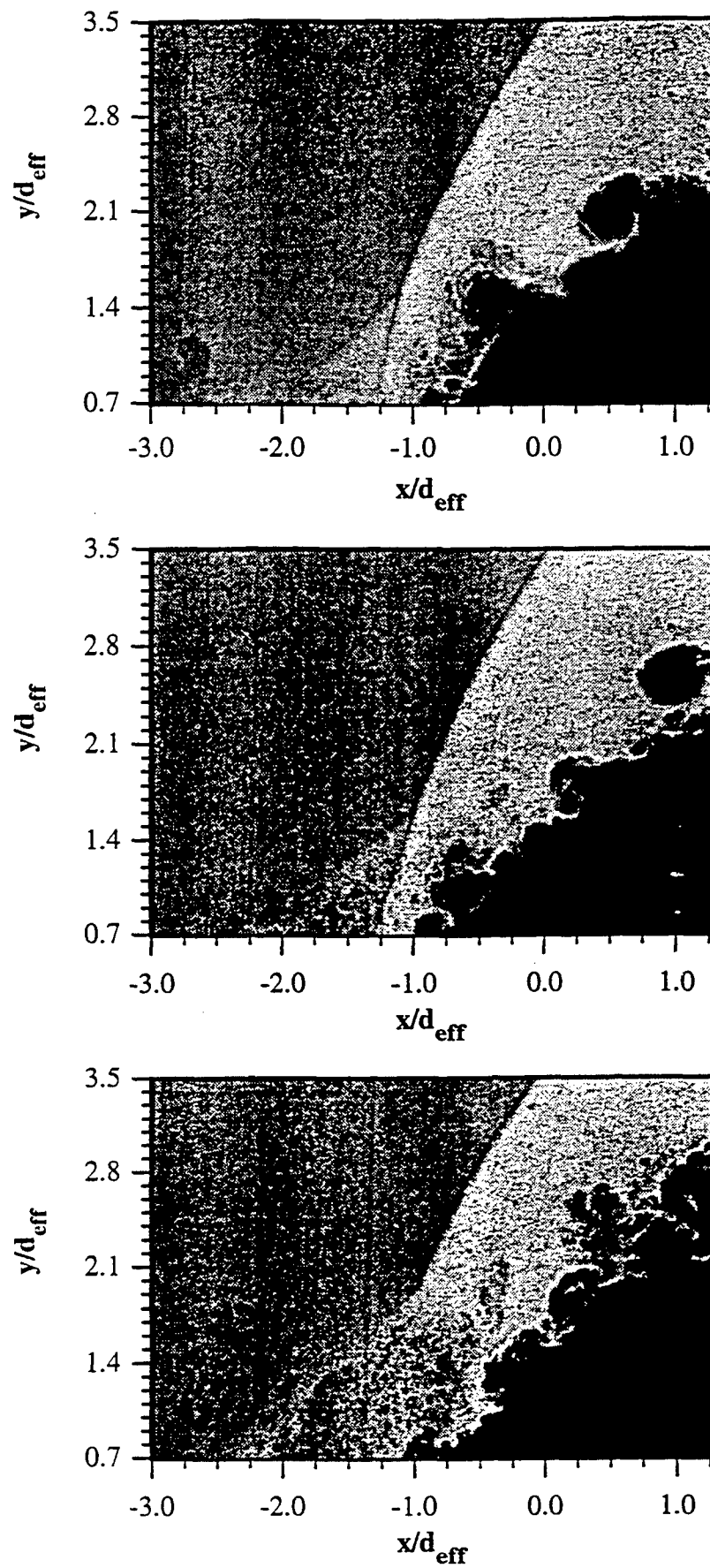


Figure 2 Instantaneous Images of Circular Injection Using Air (Case C1A)



**Figure 3** Instantaneous Images of Elliptical Injection Using Air (Case E1A)

THIS PAGE LEFT INTENTIONALLY BLANK



**AIAA 96-3024**

**Breakup Processes of Liquid Jets In  
Subsonic Crossflows**

**Pei-Kuan Wu, Kevin A. Kirkendall, Raymond P Fuller**  
Taitech, Inc.  
3675 Harmeling Drive  
Dayton, OH. 45440

**Abdollah S. Nejad**  
U.S. Air Force, Wright Laboratory/POPT  
Wright-Patterson AFB, OH. 45433

**32nd AIAA/ASME/SAE/ASEE  
Joint Propulsion Conference  
July 1-3, 1996 / Lake Buena Vista, FL**



# Breakup Processes of Liquid Jets in Subsonic Crossflows

Pei-Kuan Wu,\* Kevin A. Kirkendall,<sup>†</sup> Raymond P. Fuller<sup>‡</sup>  
Taitech, Inc., Dayton, OH. 45440

Abdollah S. Nejad<sup>§</sup>  
U.S. Air Force, Wright-Patterson AFB, OH. 45433

## ABSTRACT

The breakup processes of liquid jets injected into subsonic air crossflows were experimentally studied. Test liquids, injector diameters, and air Mach numbers were varied to provide a wide range of jet operation conditions. Results indicate that for larger injection velocity conditions liquid jets penetrate relatively far into the crossflows and exhibit surface breakup processes before the column breaks. Liquid column trajectories were correlated by liquid/air momentum flux ratios based on a force analysis of a cylindrical liquid element subjected to an aerodynamic drag force. Drag coefficients were inferred from the column trajectories and were found to exhibit a weak dependence on liquid viscosity. The heights of the column fracture points were correlated using the time required for an analogous droplet to complete an aerodynamic secondary breakup process. The success of the resulting correlation justifies the assumption that the aerodynamic forces acting on a droplet and those acting on a liquid column have similar effects. This result, combined with the trajectory correlation, leads to the conclusion that the liquid column always breaks at the same streamwise location, in agreement with the present experimental observation.

## NOMENCLATURE

a, b	constants for regression analyses
$C_x, C_y$	constants for distances to column breakup point
$C_D$	drag coefficient [= drag/(0.5 $\rho_a u_\infty^2$ )]
d	injector diameter
$M_{air}$	Mach number of air stream
$Oh_d$	Ohnesorge number [= $\mu_l/(\rho_l d \sigma)^{1/2}$ ]
$\bar{q}$	liquid/air momentum flux ratio (= $\rho_l v_j^2/\rho_a u_\infty^2$ )
$Re_{fd}$	Reynolds number (= $\rho_l d v_j/\mu_l$ )
$Re_{gd}$	Reynolds number (= $\rho_a d u_\infty/\mu_a$ )
t	time
u	velocity component in the x direction
v	velocity component in the y direction

$v_j$	liquid velocity at nozzle exit
$We_{fd}$	Weber number (= $\rho_l d v_j^2/\sigma$ )
$We_{gd}$	Weber number (= $\rho_a d u_\infty^2/\sigma$ )
x	distance in the air stream direction
y	distance in the direction transverse to the air stream
$\mu$	molecular viscosity
$\rho$	density
$\sigma$	surface tension
Subscripts	
$\infty$	air property in the free stream
b	at the point of column fracture
f	liquid-phase property
g	gas-phase property
w	property of water

## INTRODUCTION

Liquid jet atomization in an air crossflow has important applications in propulsion systems, including fuel injection in turbojet augmentor sections and ramjet and scramjet combustors.<sup>1-3</sup> In these applications, liquid fuel jets are injected from walls of combustors or bluff body flameholders into the air stream under crossflow conditions. The combustion efficiency of these combustors thus depends closely on the outcome of the jet breakup process. Additionally, current developments in spray simulation techniques require basic understanding of breakup mechanisms to construct more realistic spray atomization models. Therefore, the breakup mechanisms of liquid jets in crossflows have to be analyzed and understood. Much work has been done on the characterization of spray appearance,<sup>4-6</sup> penetration heights,<sup>7-12</sup> velocity fields,<sup>13-15</sup> and effects of liquid properties.<sup>16-18</sup> However, the understanding of breakup processes is far from complete, and additional studies of the near-field spray structures are needed to resolve the breakup mechanisms.

Previous studies of liquid injection in crossflows include analyses of liquid jets atomized in both subsonic and supersonic air streams. Kush and Schetz<sup>4</sup> demonstrated three regimes for liquid jet injection in supersonic crossflows depending on liquid/air momentum flux ratios,  $\bar{q}$ . For smaller  $\bar{q}$  (<4), waves determine the jet shape and can not be treated as simple perturbations. For  $\bar{q} = 11$ , waves grow regularly

\* Research Scientist, 3675 Harmeling Drive. Member AIAA.  
E-mail: peikuanw@possum.appl.wpafb.af.mil.

<sup>†</sup> Research Engineer, 3675 Harmeling Drive.

<sup>‡</sup> Research Scientist, 3675 Harmeling Drive. Member AIAA.

<sup>§</sup> Senior Research Scientist, Wright Laboratory/POPT.

Copyright © 1996 by Wu. Published by the American Institute of Aeronautics and Astronautics, Inc. with permission.

along the surface of the liquid column and spread droplets gradually until the point of fracture. Schetz et al.<sup>5</sup> distinguished waves as leeward and windward and related the windward waves to the liquid acceleration caused by aerodynamic drag forces. Ingebo<sup>6</sup> described the waves as capillary and acceleration-waves, and atomization was depicted as a process of forming ligaments from the crests of column waves. These studies established that liquid jets are atomized by the formation of waves caused by aerodynamic forces.

Penetration heights and spray plume trajectories have also attracted considerable attention. Schetz and Padhye<sup>7</sup> performed a momentum analysis on maximum penetration heights and found that the maximum penetration height is the distance required to redirect the liquid jet injection momentum flux to the air stream direction. The penetration height was measured at 6.25 jet diameters downstream and was correlated with  $\bar{q}$ . Ingebo<sup>8</sup> found that the maximum penetration is a function of  $(Re_{fd}/We_{gd})^{0.7}$ . Chelko<sup>9</sup> used a simple dimensional analysis to correlate jet trajectories and found that jet penetration,  $y/d$ , depends on  $v/u_\infty$ ,  $\rho/\rho_\infty$ , and  $x/d$ . Different correlations were then developed following the same methodology. Hojnacki<sup>1</sup> and Wotel et al.<sup>2</sup> developed a power law for the trajectory correlation, while Yates<sup>3</sup>, Baranovsky and Schetz<sup>10</sup>, and Inamura et al.<sup>11</sup> used a logarithmic function. These correlations, however, were all developed based on measurements at axial distances larger than 10 diameters downstream of the nozzle exit, and did not provide information about near-field structure and breakup processes.

Most recently, Chen et al.<sup>12</sup> used a Mie scattering technique to investigate jet trajectories from the nozzle exit to about 60 nozzle diameters downstream, and developed a three-parameter exponential function to account for three spray regimes: the liquid column, ligament, and droplet regimes. Droplet velocities were measured with a Particle Imaging Velocimetry (PIV) technique along the upper boundaries of 1-mm water jets.<sup>13</sup> A technique for the simultaneous velocity measurement of liquid and gas phases was also developed by Chen et al.<sup>14</sup> Inamura et al.<sup>15</sup> measured the velocity of waves on liquid columns by measuring the time interval required for a wave intersects two pulsating laser beams separated by a preset distance. Their results indicate that liquid waves are dominated by  $v_j$  when the column inclination angle from the injection direction is less than 20° and by  $u_\infty$  when the angle is larger than 40°.<sup>15</sup>

Effects of liquid properties were studied by Nejad and Schetz<sup>16,17</sup> for liquid jets in a supersonic crossflow. Surface tension was found to have negligible effects on penetration heights; on the other hand, jet

disintegration processes were faster and drop sizes were smaller for liquids with smaller surface tension. Jet penetrations were found to vary within a range of  $\pm 15\%$  when  $\mu_f$  was varied from 1 to  $60 \times 10^{-3}$  kg/m/s. Similar results were also observed by Reichenbach and Horn.<sup>18</sup> Wotel et al.<sup>2</sup> tested jet trajectories of water and JP-7 in subsonic crossflows. JP-7 has a smaller surface tension (31%) and a larger viscosity (216%) than water. Jet trajectories were found to be insensitive to liquid property variations and could be correlated using  $\bar{q}$ .

The recent development of primary and secondary breakup theories has provided a better understanding of liquid jet breakup processes. The concept of the two-stage jet breakup process has been verified by experimental evidence and the understanding of primary and secondary breakup processes has been improved dramatically.<sup>19-25</sup> When liquid/gas density ratios are large and the liquid jet has very low turbulence intensity, liquid jet breakup processes are caused by wall boundary layer vorticity along the nozzle passage; when the liquid jet is turbulent the breakup is caused by liquid turbulent eddies.<sup>21</sup> As the gas density increases, the aerodynamic secondary breakup merges with the primary breakup and drop sizes become smaller.<sup>22</sup> Aerodynamic secondary breakup processes have been found to exhibit four major breakup regimes: bag, multimode, shear, and catastrophic breakup.<sup>22-25</sup> Small droplets were stripped along the edge of parent drops and correlations were obtained by approximating the final droplet sizes with the thickness of the boundary layer along the windward side of the droplet surface.<sup>22,23</sup> Since the breakup processes of a liquid jet and a spherical droplet in an air flow are both caused by aerodynamic forces, it is reasonable to apply the general understanding of the aerodynamic secondary breakup to the present problem.

The objective of this study was to investigate the near-field structures of spray plumes to characterize liquid column properties in order to develop a better understanding of the breakup mechanisms of liquid fuel jets injected into air crossflows. Liquid column waves, trajectories, and breakup locations are the primary interest of the present study because they determine the initial locations of drop dispersion. This article begins with a description of the apparatus and instrumentation, followed by a discussion of the test conditions. Results of liquid column breakup processes are then discussed, treating liquid column wave behaviors, liquid column trajectories, and column breakup locations. The article concludes with a summary of the present findings on the breakup processes of liquid jets in subsonic crossflows.

## EXPERIMENTAL METHODS

### Apparatus and instrumentation

Liquid jets were injected vertically upward into a subsonic wind tunnel with the nozzle exit flush with the tunnel bottom wall. Detailed descriptions of the design and operation of the tunnel, along with measured air velocity fields in the test section, can be found in other studies<sup>13,26</sup> so that the following description will be brief. The wind tunnel has a rectangular test section with a cross section of 125 mm  $\times$  75 mm and a length of 406 mm. Quartz windows were installed on the top and both sides of the test section for laser diagnostics and visualization. Large vacuum pumps were connected to the end of the tunnel to maintain a constant back pressure which could be as low as 20 kPa. The air flow was provided by two large reciprocating compressors which produce a total mass flowrate of up to 2.2 kg/s at 5.1 MPa. The tunnel was operated continuously and the air Mach number was controlled by adjusting a variable-area nozzle device to obtain the correct area ratios at the choked point and at the test section.<sup>13</sup> Air pressures and temperatures were measured using strain gauges and k-type thermocouples, which were monitored by a personal computer. The uncertainties of the pressure and temperature measurements were less than 1%, while air axial turbulence intensities were about 3% at the center of the tunnel.<sup>26</sup>

The liquid injection system consisted of a large injection tank, a throttling valve, a rotary flow meter, and a nozzle unit. The injection tank has an internal volume of 0.144 m<sup>3</sup> and is rated for 3 MPa. Before the experiment, test liquids were filled into the injection tank and pressurized with high pressure air. Liquid volumetric flow rates were controlled by a throttling valve and were measured by a rotary flow meter. The rotary flow meter was calibrated to an uncertainty of less than 2%. Measured liquid volumetric flow rates were used to calculate  $v_j$  based on the nozzle exit diameter. The nozzle geometry is sketched in Fig. 1. The nozzle passage has an inlet diameter of 7.5 mm, followed by a 45° taper to the specified nozzle exit diameter, followed by a straight section with a length/diameter ratio of 4. The transition from the tapered section to the straight nozzle exit section was rounded to avoid cavitation. These nozzle passages were so designed that the liquid turbulence intensity at the exit is small. Thus, the effects of air crossflows can be studied without the presence of extraneous mechanisms.

Near-field structures and breakup properties were visualized and analyzed using a pulsed shadowgraphic technique with a frequency-doubled Nd:YAG laser as light source. The laser can produce 532 nm laser

pulses with a duration of about 10 ns, which is sufficient to freeze the motion of the liquid column and the droplets. Shadowgraphs were obtained in a darkened room with an open shutter. A 4 $\times$ 5 Speed Graphic camera, loaded with Polaroid type 52 black and white film (ASA 400) was used to record the image. Image magnification was set to be 2.5 by selecting a 250 mm object lens. The field of view was limited to 50 mm  $\times$  40 mm to maintain a good spatial resolution of the spray plume. Four shadowgraphs were obtained for each test condition. These images were digitized and analyzed to provide liquid column trajectories and the distances to the column fracture point. The distances to the column fracture point in the downstream and transverse directions were found to vary by 30% and 16% of their mean values, respectively, due to the limited sample sizes and the unsteadiness of the breakup process.

### Test conditions

Test conditions are summarized in Table 1. Liquid jets of water, ethyl alcohol, a 30% alcohol/water solution, and a 40% glycerol/water solution were used to provide a wide range of liquid properties. Mixture concentrations are volume-based. Liquid properties were measured for each test liquid before the experiment and are listed in Table 1. Liquid densities were measured using hydrometers which are accurate to 0.5 kg/m<sup>3</sup>. Cannon/Fenske viscometers were used to measure liquid viscosities with a measurement uncertainty of less than 0.2%. Liquid surface tensions in air were measured with a ring tensiometer which is accurate to 0.0005 N/m. These liquids provide: liquid densities of 781 - 1113 kg/m<sup>3</sup>, liquid viscosities of  $8.65 \times 10^{-4}$  -  $3.66 \times 10^{-3}$  kg/m/s, and surface tensions of 0.0217 - 0.0659 N/m.

Three nozzles with exit diameters of 0.5, 1.0, and 2.0 mm were manufactured and tested to demonstrate the effects of nozzle diameters. Injection velocities were varied from 8.8 to 38.5 m/s and the air Mach numbers were limited to 0.2, 0.3, and 0.4. The air static pressure was kept to be around 140 kPa. These test conditions yield jet dynamic parameters as follows:  $\bar{q}$  of 3.4 - 185,  $We_{gd}$  of 57 - 1180,  $We_{fd}$  of 760 - 20500,  $Re_{gd}$  of  $4.77 \times 10^3$  -  $3.03 \times 10^4$ ,  $Re_{fd}$  of  $3.00 \times 10^3$  -  $2.84 \times 10^4$ , and  $Oh_d$  of  $2.40 \times 10^{-3}$  -  $1.91 \times 10^{-2}$ . These ranges of test conditions cover most applications of fuel jets in propulsion systems.

## RESULTS AND DISCUSSION

Results on the near-field jet breakup processes will be discussed in terms of column wave behaviors and column trajectories and breakup locations. Liquid column waves are responsible for droplet formation,

while the liquid column trajectory and breakup location define the location of these waves. An investigation of these properties is required to understand the jet breakup mechanisms and to construct future spray atomization models.

### Column wave behaviors

#### Flow visualization

Shadowgraphs of liquid jets injected into atmospheric air environments without crossflows were taken to verify the performance of the nozzles used in the present study. A typical shadowgraph of a liquid jet injected at 30 m/s from the 0.5-mm nozzle is shown in Fig. 2; the surface of the liquid column is smooth and no droplet generation or surface protrusion is observed before 26 jet diameters. For nozzles with larger diameters, large-scale waves appear on the column surface, but no droplets are generated. These results demonstrate the near-field structures of these liquid jets without air crossflows and can be used for comparisons with the near-field structures of liquid jets in subsonic crossflows, to be discussed below.

Figure 3 shows the typical evolution of breakup processes with respect to jet diameters for water jets injected into a crossflow from nozzles with diameters of 0.5, 1.0 and 2.0 mm.  $\bar{q}$  is about the same for the three cases (roughly 9.7). For the 0.5-mm jet, the liquid column undergoes column fracture with a mechanism similar to the bag/multimode breakup of a spherical droplet.<sup>22-24</sup> Thin bag-shaped membranes can be identified at several locations, and ligaments are generated from waves with wavelengths larger than the jet diameter. Ligaments break into smaller droplets shortly after the column fracture with a shear-type secondary breakup. Drop sizes then remain relatively constant throughout the field of view. These structures demonstrate with the three previously reported breakup regimes: column, ligament, and droplet regimes.<sup>12</sup>

For the 1.0-mm water jet, the jet penetration and droplet number densities are larger than those of the 0.5-mm jet. Surface waves develop at a short distance above the nozzle exit. These waves initiate from the column periphery and extend to the leeward side; small droplets are stripped away from the end of these waves by the air stream. The liquid column then curves toward the air stream direction and large-scale waves are observed around the liquid column region. The waves on the front side of the column are called windward waves and are caused by aerodynamic acceleration along the column direction.<sup>5</sup> Waves on the leeward side of the column extend for a fairly long distance and generate both ligaments and droplets.

For 2.0-mm water jets, the jet penetration and droplet number density are even larger. The non-

uniformity of droplet spatial distributions is clearly seen in the shadowgraph. Ligaments and droplets can be grouped into lumps separated by spatial distances comparable to the wavelengths of column waves. The non-uniformity has been described by Schetz et al.,<sup>5,27</sup> and is due to the secondary breakup of the clumps of ligaments which are generated by unsteady acceleration waves. It is expected that larger diameter jets require a longer time to become fully-developed where droplets are stable and will not undergo secondary breakup.

The breakup process of the liquid column resembles the shear breakup process of a spherical droplet, except that the liquid column is traveling in the transverse direction. For the shear secondary breakup, the drop experiences deformation and then deflection of the periphery in the downstream direction. Smaller droplets are then stripped away from the periphery of these flattened parent drops.<sup>22-25</sup> These phenomena were observed, in the same order, on the liquid column at different transverse locations. The flattening of the liquid column also causes aerodynamic drag forces to increase significantly, because of the increase in the frontal projected area. This may explain why the turning of the liquid column always becomes significant when large scale waves appear on it.

Figure 4 shows shadowgraphs of water jets injected at velocities of 9.8, 19.4, and 37.9 m/s into a Mach 0.3 air stream. The liquid jet penetrates farther into the air stream as  $v_j$  increases. At  $v_j = 9.8$  m/s, the liquid column is smooth on both sides of the column immediately after injection. Then, the whole column exhibits large scale instabilities and is disintegrated by aerodynamic forces. As  $v_j$  increases, droplets are generated by waves on the leeward side of the liquid column even when the windward side exhibits a smooth surface. These waves are generally termed leeward waves,<sup>5</sup> but will be called surface breakup in this study in order to distinguish from the breakup process of the liquid column as a whole. This surface breakup process was observed especially when  $v_j$  was large (Fig. 4(c)). Drops from surface breakup are smaller than those generated by column breakup, producing a large drop size variation in the spray plume.

Effects of  $M_{air}$  on the breakup processes are demonstrated in Fig. 5 for water jets injected into air streams with  $M_{air}$  of 0.2, 0.3, and 0.4. Liquid injection velocity was 28 m/s for each case. As  $M_{air}$  increases, jet penetration decreases, because of the decrease in  $\bar{q}$ . Both surface and column breakup can be clearly identified on the shadowgraphs. The size of droplets and ligaments and the wavelength of the windward and

leeward waves decreases as  $M_{air}$  increases as a result of the increase in aerodynamic forces.

Figure 6 summarizes the jet breakup processes of three different liquids: water, the 30% alcohol/water solution, and the 40% glycerol/water solution. Liquid jets were injected at velocities from 35 to 38 m/s, resulting in a range of  $\bar{q}$  from 147 to 185. Differences between jet trajectories can be observed in these shadowgraphs. The water jet shows the straightest trajectory, while the glycerol/water solution jet curves more than the others. The column fracture point was located at the highest position for the water jet. For the 30% alcohol/water jet, the onset of surface breakup is closer to the nozzle exit and droplet sizes and ligament non-sphericities are smaller. The 40% glycerol/water jet exhibits longer threads from leeward waves and longer ligaments in the spray plume.

#### Breakup regimes

The breakup processes of liquid jets injected into air subsonic crossflows are sketched in Fig. 7. After liquid is injected, the liquid jet may firstly undergo surface breakup with droplets stripped from liquid surfaces. Acceleration waves then grow and the liquid column deforms and is flattened. The liquid column then disintegrates into ligaments and droplets. These near-field structures of the liquid column are summarized and plotted in Fig. 8, according to  $\bar{q}$  and  $We_{gd}$ . This regime map does not consider breakup mechanisms that are caused by liquid turbulence, cavitation, or effervescence.

When  $We_{gd} < 10$ , aerodynamic forces are not large as compared to liquid surface tension forces. The liquid jet is curved by aerodynamic forces, which also accelerate the breakup processes caused by capillary forces. This region is referred to as enhanced capillary breakup; examples are given by Kitamura and Takahashi.<sup>28</sup> When  $We_{gd}$  is larger than 10, aerodynamic forces dominate the breakup process. The liquid column exhibits breakup behaviors similar to those of the secondary breakup of a spherical droplet.<sup>22</sup>

<sup>24</sup> Figure 3 demonstrates a bag/multimode column breakup when  $We_{gd}$  is small, and shear column breakup when  $We_{gd}$  is large. Another interesting feature of the breakup behavior is the surface breakup process. When  $\bar{q}$  is small, the liquid jet undergoes column breakup without surface breakup. Surface breakup occurs before the liquid column instabilities when  $\bar{q}$  is large (see Figs. 3 and 4). The criterion for the existence of surface breakup is found to be a function of  $We_{gd}$  as shown in Fig. 8, with a slope of -0.81. The onset  $\bar{q}$  for surface breakup decreases as  $We_{gd}$  increases. However, the straight line plotted in

Fig. 8 is provisional and further studies are needed to identify mechanisms for this transition.

### **Column trajectories and breakup locations**

#### Liquid column trajectories

Previous measurements of spray trajectories have emphasized far downstream locations, where small droplets dominate the mixing processes.<sup>1-18</sup> To characterize breakup mechanisms, however, attention must be focused on properties of the liquid column. In order to understand the liquid column disintegration process, phenomenological analyses were employed to highlight the underlying atomization physics and to provide simple correlations without solving exact and complicated governing equations.

In this study, liquid column trajectories were analyzed by balancing liquid acceleration with aerodynamic drag forces in the air stream direction. Since the liquid column is curved in the downstream direction, the change of liquid velocities is apparently due to aerodynamic drag forces. It is assumed that the liquid column can be modeled as a cylindrical fluid element of the diameter of the nozzle exit,  $d$ , and of a length,  $\ell$ . The diameter of the fluid element is also assumed to be a constant. These assumptions neglect mass losses due to evaporation and droplet removal along the liquid column. For simplicity, the deformation and flattening of the liquid column are accounted for with an averaged drag coefficient, which will be described below. A schematic plot of the force diagram of a liquid element in a crossflow is shown in Fig. 9. The origin of the  $x$  and  $y$  coordinates is defined at the center of the nozzle exit with  $x$  pointing downstream and  $y$  pointing in the transverse direction. The force of gravity is small and negligible when compared with the aerodynamic force. It is further assumed that the transverse velocity of the liquid column remains constant to the column fracture location. By introducing an average drag coefficient,  $C_D$ , the  $x$ -momentum equation can be written as:

$$(\rho_f \pi d^2 \ell / 4) (du_f / dt) = 0.5 C_D \rho_g (u_g - u_f) [(u_g - u_f)^2 + (v_g - v_f)^2]^{1/2} \ell d, \quad (1)$$

where  $C_D$  is an average value of the drag coefficients along the entire length of the liquid column and includes the effects of liquid column deformation, flattening, droplet stripping, and disintegration. For the present test conditions,  $(v_g - v_f)^2$  is estimated to be less than 25% of  $(u_g - u_f)^2$  and is neglected in the following derivation. Additionally,  $u_f$  is estimated to be less than 16% of  $u_g$  (based on Eqs. (2) and (13), which are discussed below). Therefore, it is assumed

that the variation of  $(u_g - u_f)$  is also accounted for in  $C_D$  and can be represented by a constant,  $u_{\infty}$ . For low Mach number subsonic flows,  $\rho_g$  is assumed to have a constant value,  $\rho_{\infty}$ . Equation (1) can then be integrated with respect to time to find the velocity component,  $u_f$ , as:

$$u_f = (2C_D / \pi)[(\rho_{\infty} u_{\infty}^2) / (\rho_f d)]t. \quad (2)$$

The axial location of the liquid column can be found by integrating Eq. (2) again as  $(u_f = dx/dt)$ :

$$x = (C_D / \pi)[(\rho_{\infty} u_{\infty}^2) / (\rho_f d)]t^2. \quad (3)$$

As mentioned, the transverse velocity of the liquid column is assumed to be a constant of the value of the injection velocity,  $v_j$ . Thus, the trajectory can be obtained from Eq. (3) using  $y = v_j t$ :

$$y/d = \sqrt{(\pi / C_D)(x/d) \bar{q}}. \quad (4)$$

The column trajectory follows a parabolic curve as a result of acceleration in the  $x$  direction due to aerodynamic forces.

Liquid column trajectories were measured from the images of shadowgraphs for different liquids and jet operation conditions. The images were digitized and points on the upper surface of the liquid columns were manually located. Twenty points, roughly equidistant in the  $x$ -direction, were obtained for each image. The points from four images were then combined for trajectory analyses to obtain the best fit results for each test condition. Equation (4) was rewritten for a linear regression analysis as:

$$y / (d \bar{q}) = \sqrt{\pi / C_D} [x / (d \bar{q})]^n. \quad (5)$$

Results of the best fits of  $C_D$  and  $n$  are plotted in Fig. 10 for all the test conditions versus  $\bar{q}$ . The correlation coefficients of the regression analysis for each test condition were generally larger than 0.97, indicating a valid fitting for the present analysis. The exponents,  $n$ , varied from 0.42 to 0.56 with an average value of 0.50. The standard deviation of the exponents was 0.04 and the 95% confidence interval of the mean value was 0.01. This excellent agreement between the measured and predicted exponent values is encouraging and supports the use of the parabolic function defined above. For liquids with different viscosities, more scatter was observed in the  $C_D$  than in the exponents. Possible reasons are to be discussed below.

The current measurements also indicate that the effect of surface tension on  $C_D$  and column trajectory is not significant, suggesting that the column trajectory variation is dominated by  $\bar{q}$  and liquid viscosities. This result agrees with the findings of previous studies.<sup>16-18</sup> An averaged  $C_D$  was obtained by averaging the square root of the reciprocal of the  $C_D$ 's; the averaged value was found to be 1.696, resulting in a constant of 1.37 in Eq. (5). This value is of the same order of magnitude as the drag coefficients for flow passing a solid circular cylinder<sup>29</sup> and for the theoretical predictions of liquid injections by Adelberg<sup>30</sup> and Nguyen and Karagozian.<sup>31</sup>

Measured column trajectories are plotted with the correlation of Eq. (5) with the  $C_D$  of 1.696 and an exponent of 0.5 in Fig. 11. Measurements were grouped according to liquid type and were obtained from a wide range of test conditions. For water and alcohol, the correlation only underpredicts the results by 5% and 3% with a scatter of about  $\pm 12\%$  and  $\pm 10\%$ , respectively. However, the correlation overpredicts by about 8% and 16%, respectively, for the 30% alcohol/water solution and 40% glycerol/water solution. This agrees with the previous discussion of the viscosity dependence of column trajectories as seen in Fig. 6. The results of the 40% glycerol/water solution show a larger scatter (about  $\pm 19\%$ ) about their mean values. The larger scatter indicates a more unstable nature of the injection process for more viscous liquids.

As shown in Figs. 10 and 11, column trajectories exhibit a systematic variation with respect to  $\mu_f$ . As  $\mu_f$  increases,  $C_D$  increases and liquid jets penetrate less into the air stream. This phenomenon can be explained considering the thicker liquid boundary layer on the windward side of the jet column of the more viscous liquids. A larger portion of the liquid column is accelerated and the column therefore curves more sharply into the air stream direction and penetrates less.  $C_D$  of the different liquids was summarized and may be represented as:

$$C_D / C_{Dw} = 0.984(\mu_f / \mu_{fw})^{0.364}, \quad (6)$$

where the subscript "w" indicates the properties of water;  $C_{Dw}$  and  $\mu_{fw}$  are 1.51 and  $8.65 \times 10^{-4}$  kg/m/s, respectively. Equation (6) provides a reasonable correlation of the present data; it is of course provisional because it is based on relatively few data. The variations of  $C_D$  result in a variation of  $y$  of less than 13% because of the square root function in Eq. (4).

Measured trajectories were also tested with existing correlations developed based on results including ligament and droplet regimes. The correlations are summarized as follows: Yates<sup>3</sup> and Baranovsky and Schetz<sup>10</sup> obtained:

$$y/d = 1.15\sqrt{\bar{q}} \ln(1+6x/d). \quad (7)$$

Geery and Margetts<sup>32</sup> and Hojnacki<sup>1</sup> used:

$$y/d = 2.1\sqrt{\bar{q}}(x/d)^{0.27}. \quad (8)$$

Chen et al.<sup>12</sup> proposed a three-parameter trajectory function as:

$$y/d = 9.91\bar{q}^{0.44} [1 - \exp(-x/d / 13.1)] [1 + 1.67 \exp(-x/d / 4.77)] [1 + 1.06 \exp(-x/d / 0.86)], \quad (9)$$

while Wotel et al.<sup>2</sup> suggested:

$$y/d = 1.19\bar{q}^{0.45} (x/d)^{0.45}. \quad (10)$$

Equation (10), suggested by Wotel et al.,<sup>2</sup> has a similar functional form as Eq. (5), with a slightly different exponent. However, this correlation is empirical and was developed based on results at locations of about 5 to 140 jet diameters downstream of the nozzle exit. Ratios of the measured  $y$  values to the predicted  $y$  values from Eqs. (7)-(10) were calculated. The averaged values were found to be 0.75, 0.90, 0.75, and 1.45, with standard deviations of 0.14, 0.18, 0.11, and 0.22, respectively. Equation (5) yields a ratio of 1.00 and a deviation of 0.16 based on the same test. Equations (7)-(10) were developed with emphasis on trajectories at farther downstream locations, where ligaments and droplets dominate the mixing process. The discrepancies between the measured values and the predictions of Eqs. (7)-(10) were therefore attributed to the differences between drag coefficients and length scales for liquid/air momentum exchanges between the liquid column and the ligament/droplet regimes.

#### Column breakup locations

Column breakup locations will be discussed next in terms of the distances from the nozzle exit to the column fracture point in the  $x$  and  $y$  directions. To quantify the fracture locations, the shadowgraph images were analyzed. For low viscosity liquids, the fracture locations were identified without much difficulty by locating the mean location where the liquid column breaks into separate ligaments or

droplets. For liquids with smaller surface tensions or larger viscosities, the fracture location becomes more difficult to determine because of larger drop number densities or of the presence of longer irregularly-shaped ligaments. However, the current measurements of  $x_b$  and  $y_b$  show consistent results within reasonable uncertainties (30% and 16% respectively).

The column fracture locations were modeled using the time scale for the aerodynamic secondary breakup of a spherical droplet. This approach is plausible since the breakup mechanisms for both columns and droplets are due to aerodynamic forces. Hsiang and Faeth<sup>23</sup> found that breakup time scales were similar even in different breakup regimes. The time scale,  $t_b$ , for a droplet with negligible initial streamwise velocity can be written as:

$$t_b = 5.0d_p \sqrt{(\rho_f / \rho_\infty)} / u_\infty, \quad (11)$$

where  $d_p$  is the drop size before the breakup process.<sup>23</sup>

Time scales for the completion of the secondary breakup are applied to determine the time required for the liquid column to fracture in a crossflow condition. It is assumed that the time required for the column to fracture is a fixed portion of the time required for the completion of the breakup process. Since  $v_j$  is assumed to be constant up to the column fracture point,  $y_b$  can be obtained by multiplying the breakup time scale,  $t_b$ , with the injection velocity,  $v_j$ , as:

$$y_b/d = C_y \sqrt{\bar{q}}, \quad (12)$$

where  $C_y$  is a proportionality constant. Equation (12) indicates that the normalized distance,  $y_b/d$ , to the fracture point is a function of  $\bar{q}$  alone. Present measurements of  $y_b$  are plotted in terms of the variables of Eq. (12) in Fig. 12. These results include  $y_b$  for several liquids and for a large range of jet conditions, and the prediction agrees reasonably well with the data in view of the relatively large experimental uncertainties. The power of  $\bar{q}$  for the correlation of the data is not 0.5 as suggested by Eq. (12), however, and can be represented better by the empirical fit that is shown in Fig. 12:

$$y_b/d = 3.07\bar{q}^{0.53}, \quad (13)$$

The correlation coefficient for the fit is 0.94. The increase in the power of the  $\bar{q}$  from 0.50 in Eq. (12) to 0.53 in Eq. (13) is statistically significant but is not large in view of the approximations used to develop the correlating expression and experimental uncertainties.

A second approach was employed to correlate  $y_b$ . The power of  $\bar{q}$  was fixed at 0.5 and the values of  $y_b/\bar{q}^{0.5}$  were averaged to yield the proportionality constant  $C_y$ .  $C_y$  was found to be 3.6, 3.02, 3.14, and 4.49 for water, the 30% alcohol/water solution, the 40% glycerol/water solution, and ethyl alcohol, respectively; and standard deviations for these liquids were 0.73, 0.28, 0.27, and 0.32. These values indicate a weak effect of the  $y$  distances on liquid properties, although a wider range of liquid properties should be studied to confirm their effects. An overall mean value was obtained to be 3.44, which was used for the theoretical prediction in Fig. 12. The standard deviation of this mean value is 0.71.

The  $x$  distance from the nozzle exit to the column fracture point can then be calculated by substituting Eq. (12) into Eq. (5):

$$x_b/d = C_y^2 C_D / \pi = C_x, \quad (14)$$

where  $C_x$  is a proportionality constant. Present measurements of  $x_b/d$  are plotted in terms of  $\bar{q}$  in Fig. 13.  $x_b/d$  is relatively independent of  $\bar{q}$  and agrees with the prediction of Eq. (14). The mean value of  $x_b/d$  is 8.06 with a standard deviation of 1.46. Variations in averaged  $x_b/d$  of different liquids are around 7%, which is not significant. Measured  $x_b/d$  is about 25% larger than the prediction obtained by substituting the values of  $C_y$  and  $C_D$  into Eq. (14): the discrepancy is primarily due to uncertainties in measurements and correlation processes. A linear regression was made to check the dependence of  $x_b/d$  with respect to  $\bar{q}$ , and the slope of the best fit was 0.07, which is negligible. Therefore, it is concluded that the liquid column always breaks at a distance of  $8.06 \pm 1.46$  jet diameters downstream of the nozzle.

Inamura et al.<sup>11,15</sup> used a contact needle probe to identify the column breakup location and also found that  $x_b$  is not sensitive to  $\bar{q}$  and liquid jet properties. This phenomenon can be explained by the cancellation of aerodynamic effects on the liquid acceleration and on the column fracture time scale. A larger aerodynamic force increases the liquid acceleration (Eq. (3)), however, it also reduces the time required for the column to fracture (Eq. (11)). These two effects cancel each other, resulting in a constant  $x_b$ . On the other hand, the variation of the liquid injection velocity only affects the liquid jet penetration and does not have significant effects on  $x_b$ . The fracture point marks the boundary between the liquid column and the dispersed-phase regimes. Each regime has its own flow dynamics and a successful spray analysis should consider these differences.

### Summary of correlations

The correlations of the column trajectory and cross fracture locations may be summarized with measured values as follows:

- liquid column trajectory [Eq. (5)]:

$$y/d = 1.37\sqrt{\bar{q}(x/d)}$$

- transverse height of the column fracture point [Eq. (12)]:

$$y_b/d = 3.44\sqrt{\bar{q}}$$

- axial distance to the column fracture point [Eq. (14)]:

$$x_b/d = 8.06$$

### SUMMARY AND CONCLUSIONS

The breakup processes of liquid jets injected into subsonic crossflows were experimentally studied using a pulsed shadowgraphy technique, considering liquid jets of water, ethyl alcohol, a 30% alcohol/water solution, and a 40% glycerol/water solution in subsonic air crossflows. Jet breakup processes, liquid column trajectories before column fracture points, and the distances to column fracture points were investigated. The major conclusions of the study are as follows:

1. The liquid column breakup processes in a crossflow are similar to those of the aerodynamic secondary breakup of a spherical droplet. The liquid column undergoes deformation first and is then flattened and disintegrated by aerodynamic forces. At  $We_{gd}$  of about 60, the liquid column breaks into several bag-shaped membranes, similar to the multimode breakup of droplets. At larger  $We_{gd}$  conditions, acceleration waves break the column with a shearing process similar to droplet shear breakup.
2. When  $\bar{q}$  is large, the liquid jet undergoes surface breakup as droplets are stripped off from the deflected edges of the liquid column before the development of large-scale column waves. For more viscous liquids, these surface waves are more prominent and have very long threads.
3. A momentum analysis was developed to correlate column trajectories by equating the liquid velocity change in the airstream direction due to the aerodynamic drag. The predictions agree with experimental measurements reasonably well within measurement uncertainties. Earlier correlations based on results for far downstream locations were found to be inappropriate for the description of liquid column trajectories before the fracture point.
4. Drag coefficients were inferred by comparing the column trajectory predictions with measured



results. Drag coefficients were larger for jets of more viscous liquids. This phenomenon is attributed to the thicker boundary layer on the windward side surface of the liquid column.

5. The column fracture locations were identified by measuring the distances from the nozzle exit to the fracture points. The transverse distances to the fracture point were correlated using the secondary breakup time of a spherical droplet because of the close analogy between the breakup processes of a droplet and those of a liquid column.
6. The  $x$  distances to the column fracture point were found to be a constant for the present test conditions. Liquid jets always break at a location of about eight diameters downstream from the nozzle exit, independent of jet injection conditions. The fracture point marks the boundary between the liquid column and the dispersed-phase regimes.

The present results are primarily limited to the liquid jet breakup processes caused by aerodynamic forces. The effects of liquid turbulence and cavitation, and their interactions with aerodynamic effects, were not considered in the present study and should be resolved in the future. Drop sizes after the breakup should also be studied because of their importance for injector designs and spray model validation.

#### ACKNOWLEDGMENTS

This work was sponsored by and performed at Wright Laboratory, Wright-Patterson AFB, Ohio, under contract number F33615-93-C-2300. Assistance from the air facility group of Wright Lab. is acknowledged. The authors would also like to thank Dr. T. H. Chen and Dr. M. R. Gruber for helpful discussion, Dr. C. D. Carter for lending the Nd:YAG laser for the present shadowgraph study, Mr. W. F. Terry and S. A. McAlpine for helping with tunnel installation, and Dr. A. E. S. Creese for editing this paper.

#### REFERENCES

1. Hojnacki, J. T., "Ramjet Engine Fuel Injection Studies," AFAPL-TR-72-76, Aero Propulsion Laboratory, Wright-Patterson AFB, 1972.
2. Wotel, G. J., Gallagher, K. E., Caron, S. D., Rosfjord, T. J., Hautman, D. J., and Spadaccini, L. J., "High Speed Turboramjet Combustor Technology Program," WL-TR-91-2043, Wright Laboratory, Wright-Patterson AFB, OH., 1991.
3. Yates, C. L., "Liquid Injection into a Supersonic Stream," AFAPL-TR-71-97, Vol. 1, Aero Propulsion Laboratory, Wright-Patterson AFB, OH., 1972.
4. Kush, E. A. and Schetz, J. A., "Liquid Jet Injection into a Supersonic Flow," *AIAA Journal*, Vol. 11, No. 9, 1973, pp. 1223-1224.
5. Schetz, J. A., Kush, E. A., and Joshi, P. B., "Wave Phenomena in Liquid Jet Breakup in a Supersonic Crossflow," *AIAA Journal*, Vol. 18, No. 7, 1980, pp. 774-778.
6. Ingebo, R. D., "Aerodynamic Effects of Combustor Inlet-Air Pressure on Fuel Jet Atomization," AIAA Paper 84-1320, Cincinnati, OH., 1984.
7. Schetz, J. A. and Padhye, A., "Penetration and Breakup of Liquids in Subsonic Airstreams," *AIAA Journal*, Vol. 15, No. 10, 1977, pp. 1385-1390.
8. Ingebo, R. D., "Penetration of Drops into High-Velocity Airstreams," NASA TM X-1363, 1967.
9. Chelko, L. J., "Penetration of Liquid Jets into a High-Velocity Air Stream," NACA RM E50F21, 1950.
10. Baranovsky, S. I. and Schetz, J. A., "An Experimental Investigation of Methods to Increase the Liquid Jet Penetration into Supersonic Flow," AFOSR-78-1300, Air Force Office of Scientific Research, Bolling AFB, DC., 1978.
11. Inamura, T., Nagai, N., Hirai, T., and Asano, H., "Disintegration Phenomena of Metalized Slurry Fuel Jets in High Speed Air Stream," Proceedings of the Fifth International Conference on Liquid Atomization and Spray System, Gaithersburg, MD., 1991, pp. 839-846.
12. Chen, T. H., Smith, C. R., Schommer, D. G., and Nejad, A. S., "Multi-Zone Behavior of Transverse Liquid Jet in High-Speed Flow," AIAA Paper 93-0453, Reno, NV., 1993.
13. Chen, T. H., Roe, L. A., and Nejad, A. S., "Multifunction Droplet Imaging and Velocimetry System for Spray Jets," *Journal of Propulsion and Power*, Vol. 10, No. 6, 1994, pp. 798-803.
14. Chen, T. H., Nejad, A. S., Carter, C. D., and Goss, L. P., "A Technique for Simultaneous Velocity Measurement of Liquid and Gas Phases," AIAA Paper 94-0494, Reno, NV., 1994.
15. Inamura, T., Nagai, N., Watanabe, T., and Yatsuyanagi, N., "Disintegration of Liquid and Slurry Jets Traversing Subsonic Airstreams," Proceedings of third World Conference on Experimental Heat Transfer, Fluid Mechanics and Thermodynamics, Honolulu, HI., 1993.
16. Nejad, A. S. and Schetz, J. A., "Effects of Properties and Locations in the Plume on Droplet Diameter for Injection in a Supersonic Stream," *AIAA Journal*, Vol. 21, No. 7, 1983, pp. 956-961.
17. Nejad, A. S. and Schetz, J. A., "Effects of Viscosity and Surface Tension on a Jet Plume in

- Supersonic Crossflow," *AIAA Journal*, Vol. 22, No. 4, 1984, pp. 653-659.
18. Reichenbach, R. E. and Horn, K. P., "Investigation of Injectant Properties on Jet Penetration in a Supersonic Stream," *AIAA Journal*, Vol. 9, No. 3, 1971, pp. 469-472.
  19. Faeth, G. M., "Structure and Atomization Properties of Dense Turbulent Sprays," Twenty-Third Symposium (International) on Combustion, The Combustion Institute, Pittsburgh, 1990, pp. 1345-1352.
  20. Wu, P.-K. and Faeth, G. M., "Onset and End of Drop Formation Along the Surface of Turbulent Liquid Jets in Still Gases," *Physics of Fluids*, Vol. 7, No. 11, 1995, pp. 2915-2917.
  21. Wu, P.-K., Miranda, R. F., and Faeth, G. M., "Effects of Initial Flow Conditions on Primary Breakup of Nonturbulent and Turbulent Round Liquid Jets," *Atomization and Sprays*, Vol. 5, No. 2, 1995, pp. 175-196.
  22. Wu, P.-K., Hsiang, L.-P., and Faeth, G. M., "Aerodynamic Effects on Primary and Secondary Breakup," *Liquid Rocket Engine Combustion Instability*, ed. V. Yang and W. Anderson, Vol. 169, Progress in Astronautics and Aeronautics, AIAA, Washington, DC, 1995, pp. 247-279.
  23. Hsiang, L.-P. and Faeth, G. M., "Near-Limit Drop Deformation and Secondary Breakup," *International Journal of Multiphase Flow*, Vol. 18, No. 5, 1992, pp. 635-652.
  24. Krzeczkowski, S. A., "Measurement of Liquid Droplet Disintegration Mechanism," *International Journal of Multiphase Flow*, Vol. 6, No. 2, 1980, pp. 227-239.
  25. Hinze, J. O., "Fundamentals of the Hydrodynamic Mechanism of Splitting in Dispersion Processes," *AIChE Journal*, Vol. 1, No. 3, 1955, pp. 289-295.
  26. Raffoul, C. N., Nejad, A. S., Gould, R. D., and Spring, A. S., "An Experimental and Numerical Study of the Isothermal Flowfield Behind a Bluff Body Flameholder," ASME Paper 95-GT-102, Houston, TX., June, 1995.
  27. Less, D. M. and Schetz, J. A., "Transient Behavior of Liquid Jets Injected Normal to a High-Velocity Gas Stream," *AIAA Journal*, Vol. 24, No. 12, 1986, pp. 1979-1986.
  28. Kitamura, Y. and Takahashi, T., "Stability of A Liquid Jet in Air Flow Normal to the Jet Axis," *Journal of Chemical Engineering of Japan*, Vol. 9, No. 4, 1976, pp. 282-286.
  29. Kuethe, A. M. and Chow, C.-Y., *Foundations of Aerodynamics, Bases of Aerodynamic Design*, 4th ed., John Wiley & Sons, New York, 1986, p. 381.
  30. Adelberg, M., "Breakup Rate and Penetration of a Liquid Jet in a Gas Stream," *AIAA Journal*, Vol. 5, No. 8, 1967, pp. 1408-1415.
  31. Nguyen, T. T. and Karagozian, A. R. "Liquid Fuel Jet in Subsonic Crossflow," *Journal of Propulsion and Power*, Vol. 8, No. 1, 1992, pp. 21-29.
  32. Geery, E. L. and Margettes, M. J., "Penetration of a High Velocity Gas Stream by a Water Jet," *Journal of Spacecraft*, Vol. 6, No. 1, 1969, pp. 79-81.

Table 1 Summary of test conditions<sup>a</sup>

Liquids	water	ethyl alcohol	30% alcohol/water	40% glycerol/water
$\rho_f$ (kg/m <sup>3</sup> )	996	781	958	1113
$\mu_f \times 10^4$ (kg/m/s)	8.65	9.57	18.4	36.6
$\sigma \times 10^3$ (N/m)	63.5	21.7	34.6	65.9
d (mm)	0.5, 1.0, 2.0	0.5	0.5, 1.0	0.5, 1.0
$v_j$ (m/s)	8.9 - 37.7	32.0	17.0 - 38.5	15.7 - 35.4
$u_\infty$ (m/s)	70.2 - 141	69.2, 107	71.5 - 107	68.1 - 106
$\bar{q}$	3.38 - 148	39.9, 98.7	14.0 - 147	14.5 - 185
$We_{gd}$	71 - 1179	186, 461	140 - 594	57 - 287
$We_{fd} \times 10^{-3}$	0.76 - 11.3	18.4	8.04 - 20.5	4.16 - 10.6
$Re_{gd} \times 10^{-3}$	5.72 - 30.3	13.0	8.87 - 14.0	4.77 - 7.56
$Re_{fd} \times 10^{-3}$	3.38 - 28.4	3.16, 5.08	3.58 - 10.4	3.00 - 9.81
$Oh_d \times 10^3$	2.4 - 4.9	10.4	10.1, 14.3	13.5, 19.1

<sup>a</sup> Air was at  $140 \pm 4$  kPa and  $306 \pm 3$  K in the test section of the wind tunnel, resulting in a density of  $1.76 \pm 0.05$  kg/m<sup>3</sup>.

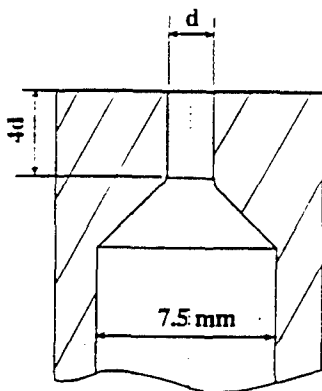


Fig. 1 Nozzle geometry of the present injectors.



WATER:  $d = 0.5 \text{ mm}$ ;  $V_j = 30 \text{ m/s}$

Fig. 2 Injection of a water jet without crossflow ( $d = 0.5 \text{ mm}$ ,  $v_j = 30 \text{ m/s}$ ).



(a)  $d = 0.5 \text{ mm}$ ,  $\bar{q} = 9.9$ ,  
 $We_{gd} = 71$



(b)  $d = 1.0 \text{ mm}$ ,  $\bar{q} = 9.4$ ,  
 $We_{gd} = 139$



(c)  $d = 2.0 \text{ mm}$ ,  $\bar{q} = 10.0$ ,  
 $We_{gd} = 281$

WATER:  $M_{\text{air}} = 0.2$ ;  $\rho_g = 1.76 \text{ kg/m}^3$

Fig. 3 Injection of water jets from nozzles of various injector diameters: (a)  $d = 0.5 \text{ mm}$ , (b)  $d = 1.0 \text{ mm}$ , and (c)  $d = 2.0 \text{ mm}$ .

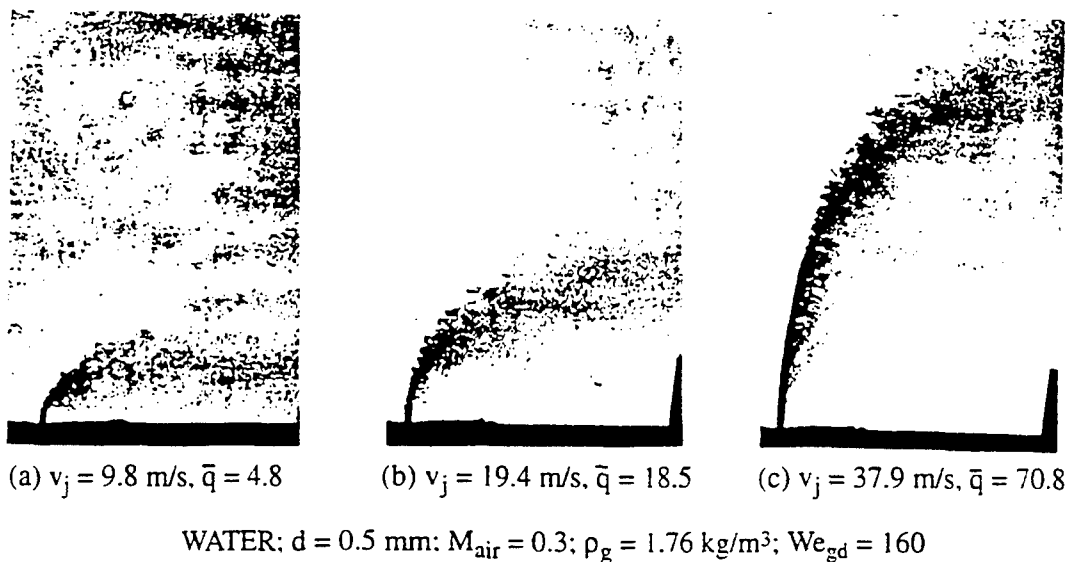


Fig. 4 Injection of water jets at various injection velocities: (a)  $v_j = 9.8 \text{ m/s}$ , (b)  $v_j = 19.4 \text{ m/s}$ , and (c)  $v_j = 37.9 \text{ m/s}$ .

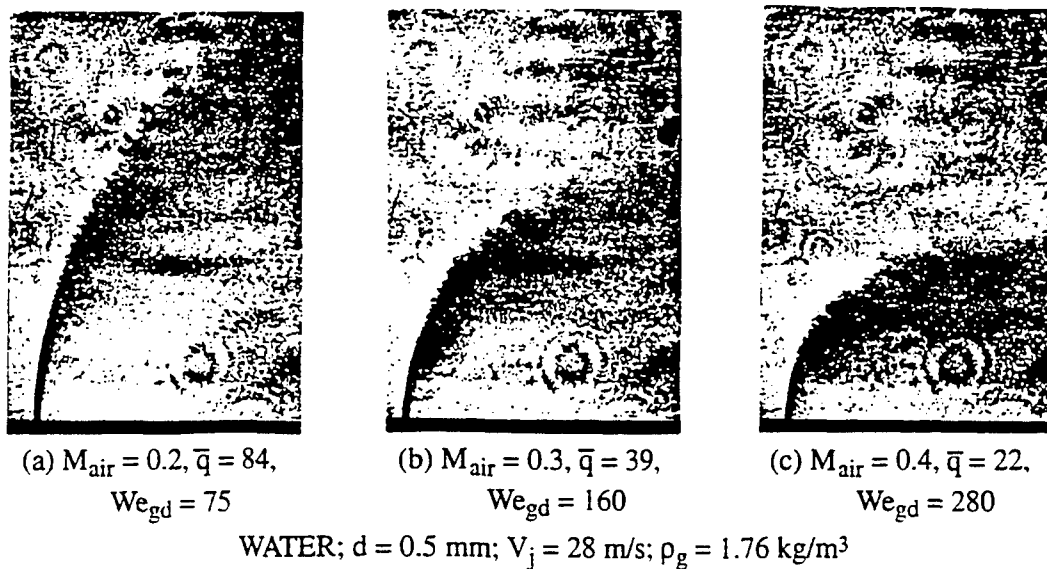
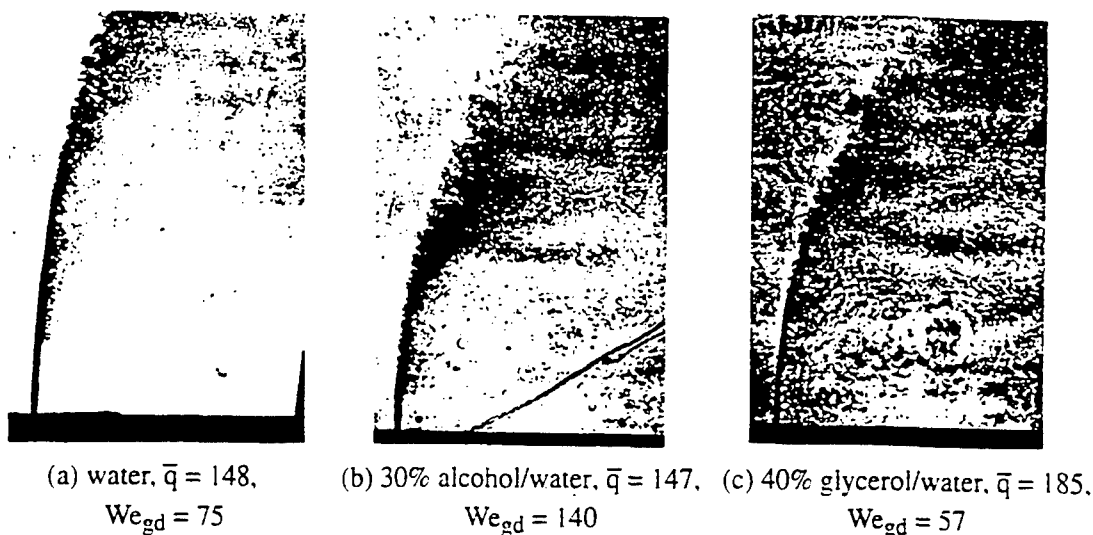


Fig. 5 Injection of water jets into crossflows at various Mach numbers: (a)  $M_{\text{air}} = 0.2$ , (b)  $M_{\text{air}} = 0.3$ , and (c)  $M_{\text{air}} = 0.4$ .



$$d = 0.5 \text{ mm}; V_j \approx 37 \text{ m/s}; M_{\text{air}} = 0.2; \rho_g = 1.76 \text{ kg/m}^3$$

Fig. 6 Injection of various liquids: (a) water, (b) 30% alcohol/water, and (c) 40% glycerol/water.

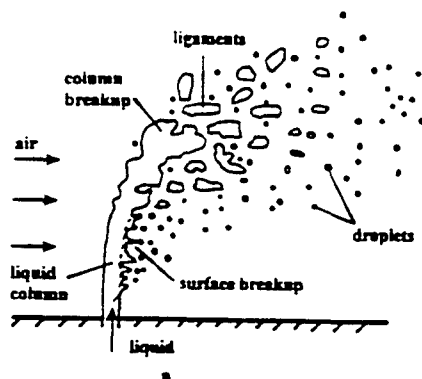


Fig. 7 Sketch of a typical liquid breakup process in an air crossflow.

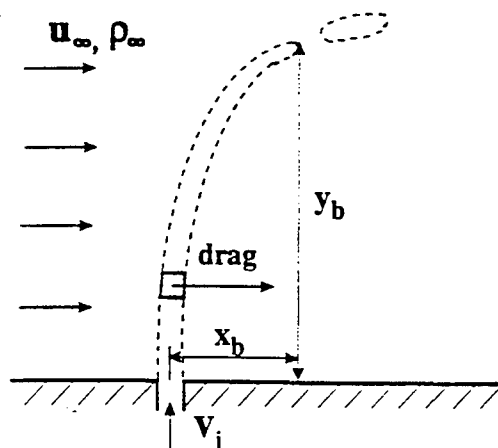


Fig. 9 Sketch of the force diagram for the present phenomenological analysis.

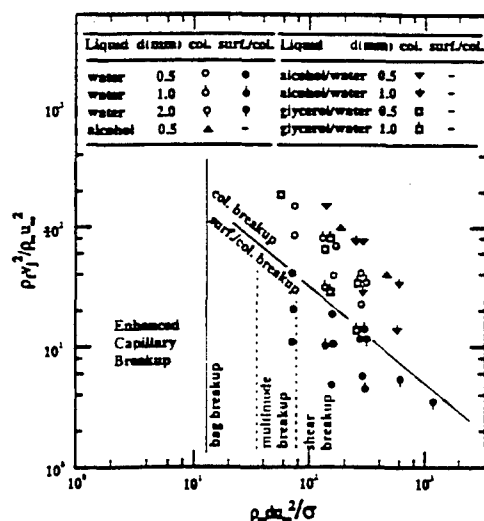


Fig. 8 Regime map of column waves and breakup processes in crossflows.

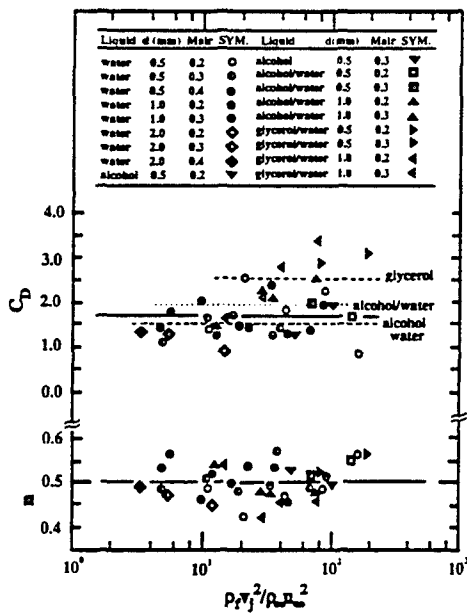


Fig. 10 Drag coefficients ( $C_D$ ) and exponents ( $n$ ) of the fit according to the trajectory analysis.

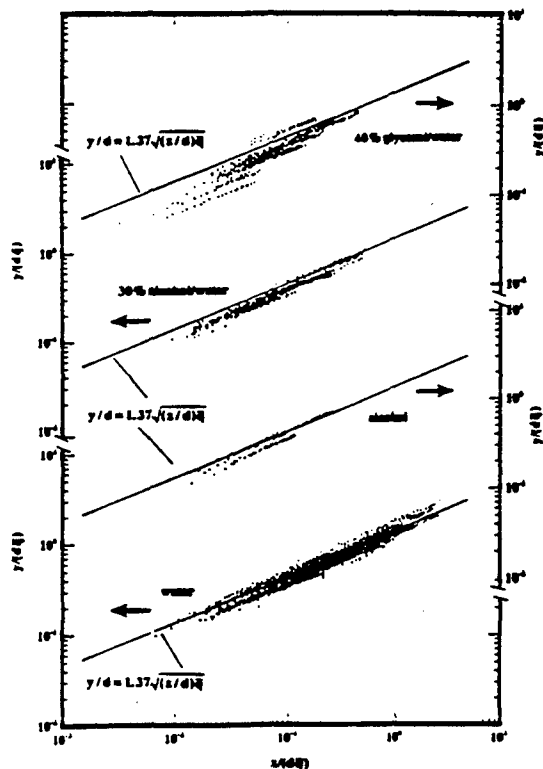


Fig. 11 Comparison of liquid column trajectories of different liquids with the correlation (Eq. (5)).

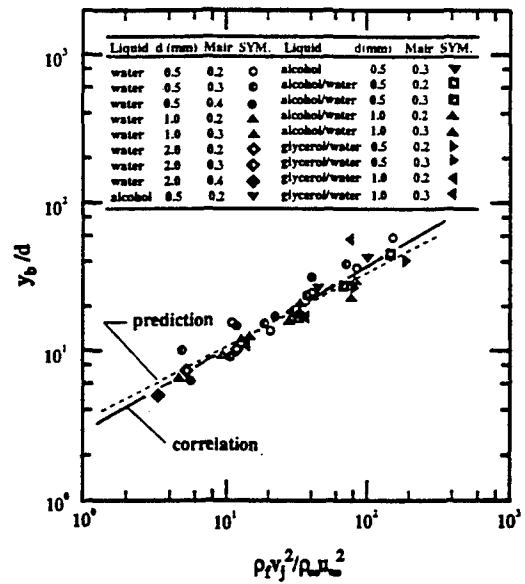


Fig. 12 Column fracture heights ( $y_b/d$ ) of liquid jets in air crossflows.

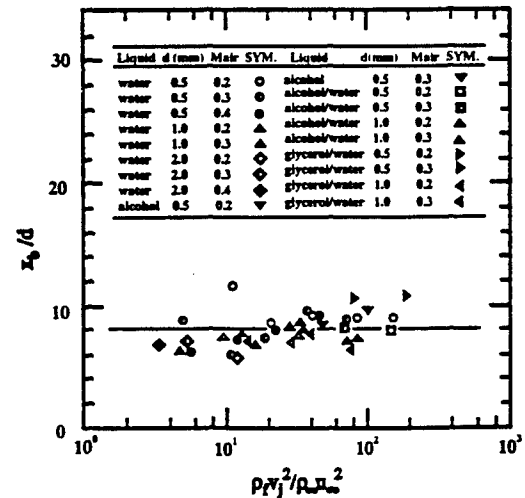


Fig. 13 Column fracture distance ( $x_b/d$ ) of liquid jets in air crossflows.